Theoretical and Experimental Analysis of an Electrostatically Actuated Multi-stage Micropump with Active Valves

By

Karthik Kumar

A dissertation submitted in partial fulfillment
of the requirements for the degree of
Doctor of Philosophy
(Aerospace Engineering)
in The University of Michigan
2013

Doctoral Committee:

Associate Professor Luis P Bernal, Chair
Professor Yogesh B. Gianchandani
Professor Khalil Najafi
Associate Research Scientist Rebecca L. Peterson
Associate Professor Peter D. Washabaugh

DEDICATION

To my wonderful and loving parents who gave me life, a desire to learn and the strength to never give up.

ACKNOWLEDGEMENTS

I would like to thank the following individuals who have in one way or another contributed to this work. I will forever be grateful for their help and would like to acknowledge what they have done.

Firstly, I would like to thank my parents for giving me the opportunity to travel far away from home to pursue a dream I never thought I could achieve. I would sincerely like to thank my mom for the effort she put in, to make me realize the importance of education while still giving me the freedom to choose my profession. I would like to thank my dad for being my source of inspiration and the epitome of hard work. I would like to thank my sister for providing the ever-cheerful laughter that always lifted my spirits.

This work could not have been possible without Dr. Luis P. Bernal. I would like to thank him sincerely for believing in me to achieve goals that I set, which was sometimes overambitious. His vast knowledge in every subject and his motivating spirit has enabled me to learn how to tackle problems and solve them. I will forever be grateful to him for providing me with the opportunity to work on this project.

This work would have been impossible without the help of Seow Yuen Yee. Thank you for helping me to grow as a researcher and a student. I will always cherish the innumerable days spent discussing the project and the problems associated. I would also

like to thank Ali Besharatian, for his unbelievable effort in fabricating the devices despite the challenges posed.

I would like to thank Dr. Washabough, Dr. Najafi, Dr. Peterson, and Dr. Gianchandani for their willingness to serve on my committee, their patience in receiving this dissertation and their accommodation in scheduling.

I would like to thank all my current and ex-room mates, Kumar Sricharan, Gowtham Bellala, Gandharav Kashinath, Karthik Anantharaman, and everyone from 'hello children' for all their help and making my stay in Ann Arbor a memorable one. I would also like to thank Siddharth Sundar and Vignesh Suresh for helping me complete this thesis. Finally, I would like to thank Daniel Cooper, Pradeep Rawat and Seshagopal Manasvi for their help to solve the challenges I faced using STARCCM+.

Thank you all – Karthik Kumar

TABLE OF CONTENTS

LIST OF TABLES

LIST OF FIGURES

LIST OF SYMBOLS

μ	Viscosity
A S	Area
ε	Permittivity
f	Frequency
γ	Specific Gas Constant
Q	Flow Rate (sccm)
P_{in}	Pressure at the inlet of each stage
P_{out}	Pressure at the outlet of each stage
V	Volume Ratio
n	Gas Constant = 1
P_s	Atmospheric Pressure
u_e	Velocity through each valve
L_E	Inertial length
L_v	Viscous Length
ρ	Density in the cavity
h_g	Electrode Gap
H	Valve open =1, Valve Close = 0
α	Speed of Sound
ω	Vorticity
P	Pressure in the given stage
A_E	Area of Valve Holes
h_D	Displacement of center of the membrane
t_D	Thickness of the membrane
τ	Tension Force
σ	Stress in the diaphragm
ω_D	resonant frequency of the membrane
P_e	Electrostatic Pressure
A_D	Area of Membrane
V_C	Cavity Volume
V_D	Volume change due to diaphragm motion
V_V	Volume due to valve membrane motion
ρ_D	Density of the Membrane
t	Time
T	Time Period
h_o	Initial Gap between membrane and electrode
ν	Damping
P_b	Pressure in gap between membrane and electrode
V_b	Volume in gap between membrane and electrode
N_H	Number of holes on Pump Electrode
A_H	Area of Hole on the Pump Electrode

h_{Dio}	Displacement of the center of the inlet/outlet valve
h_{Dtv}	Displacement of the center of the transfer Valve
t_{op}	Valve Open time
t_{cl}	Valve Close time

ABSTRACT

Micropumps are required for various applications such as gas sensing, micro cooling and biological applications. A number of micropumps have been reported in the literature utilizing different actuation methods and flow controls. Designing these pumps requires mathematical models to determine the effect of parameters that affect their performance. Models proposed in the literature are applicable only to specific micropumps, which are generally operated at low frequency. While some models are applicable for operation at high frequency, they require experimentally evaluated parameters. Hence, these models cannot be used for designing and analyzing the performance of electrostatic micropumps.

The goal of the research reported in this thesis is to develop mathematical tools for the design of multi-stage vacuum micropumps operated at high frequency utilizing electrostatic actuation and active valves for flow control. The model should capture the resonance characteristics that govern micropump operation. Two mathematical models are developed in this work. The first is a reduced-order acoustic model used to study the effect of operating frequency, volume ratio, valve leakage, valve timing, dynamic valve timing and transient performance on a multistage vacuum micropump. Using this model the impact of dynamic valve timing and novel multi-stage designs are analyzed and optimized to achieve vacuum efficiently. The second model is a multiphysics model,

which accounts for active valve pumping, membrane deflection and electrostatic actuation. Inertial and resistance length relations are proposed using computational fluid dynamics analysis of the given valve design. Static and eigen-frequency analysis is carried out using Finite Element Analysis (FEA) for a stacked membrane. This model is verified using experimental and computational techniques. The flow performance determined using the multiphysics reduced order model is compared to measured results for a 4-stage micropump. The model predicts three resonant points with an error of 7 to 21%. Due to the difficulty in measuring the pressure and flow fields inside the micropump, a high fidelity CFD model which incorporates membrane motion and cavity acoustics is used to validate pressure and flow fields assumptions used in the reduced order model. Pressure and flow rate performance determined using the reduced order model compare well with high fidelity CFD results for a 3-D device that includes pump and valve membrane motions. The reduced order model suggests for the first time the dominance of valve pumping that has been experimentally observed. Based on these results, a novel micropump design is proposed that can produce high flow rate.

Chapter 1

Introduction

Requirement and Current State of Micropumps

In today's world of miniaturization, MEMS devices play an important role in sensing (Bogue 2007), drug delivery (Nisar et al. 2008) and chemical/biological analysis systems (Hanseup et al. 2007). Reduction in size allows smaller sample volume, reduced cost and short analysis time. Micropumps, when introduced in the 1980's, gained significant interest to control insulin delivery (Santiago 2004). More recently, several microsystems require small fluid volumes of the order of 1 cm^3 to be transferred for biological/medical analysis, space exploration sensors, microelectronics cooling and environmental sensing applications. Micropumps are used to dispense engineered macromolecules into tumors or the blood stream (Dash and Cudworth 1998, Coll et al. 1999). Low volumetric flow rate (less than a milliliter a day), low power consumption (Dash and Cudworth 1998, Allen and Sefton 1986) and controlled delivery makes them ideal candidates for dispensing insulin. Miniature roughing pumps are required for use in mass spectrographs to be carried on lightweight spacecraft (Wiberg et al. 2001). These pumps are required to achieve a vacuum of approximately 0.1 Pa. For ion based propulsion micropumps are required to deliver gases at 1ml/min (Micci and Ketsdever 2000, Bruschi, Diligenti and Piotto 2002, Lozano and Courtney 2010). Micropumps have been developed for use in single and two phase cooling of electronic devices (Zhang et al.

2002), which require flow rates of nearly 10 ml/min. Recently, GE has developed a new piezoelectric micro cooling device, based on jet flow that could be employed for cooling Intel i7 processors (De Bock et al. 2012). Micro-gas chromatography systems developed by Zellers et al. (2007), require pumps to sample gas at high flow rates and consume low power. Hanseup et al. (2007) showed for the first time an integrated micro chromatography system that can analyze 11 organic compounds in 78 seconds. The micropump used by Hanseup et al. (2007) could produce a flow rate of 4 sccm and consumed <100 mW of power. The micro GC when operated in sampling mode requires a flow rate of 25 sccm and pressure differential of 22 kPa, while in the analysis mode requires flow rate at 2 sccm and differential pressure of 50 kPa.

Different actuation mechanisms such as electrostatic, electromagnetic, piezoelectric, thermo-pneumatic and molecular transpiration (Knudsen) are employed to produce pumping. Except for the latter, pumping membranes that drive the fluid and valves that control the transfer of fluid, make up a micropump. Cabuz et al. (2001) showed that electrostatic actuation could produce high flow rate (30 sccm) when operated at high frequency while consuming low power. The most efficient multistage electrostatically driven micropump was reported by Kim et al. (2007) and Astle et al. (2005). It produced a flow rate of 4 sccm, a pressure differential of 12.8 kPa and consumed 57 mW of power. Electrostatic micropumps consist of a thin membrane, made up of a dielectric material coated with conducting metal, spaced a small distance from a stiff and perforated conductive electrode. When a large enough voltage potential is applied between the metalized membrane and electrode, the force is able to overcome the tensile forces and collapse the membrane on the electrode.

Electromagnetic actuation is produced by creating a time varying magnetic field using a coil (Pan et al. 2005), to attract or repel a magnetically coated membrane. While this actuation mechanism can provide large deflection, greater pressure rise and flow rate, it suffers from complex fabrication and high power consumption. Kim et al. (2011) reported an electromagnetic pump that could produce an absolute pressure of 424 Torr when operated at 1 Hz while consuming 3.6 W of power.

Piezoelectric membranes are the most commonly reported method of actuation in the literature (Koch et al. 1999, Woias 2005, Smits 1990). In this case the voltage applied to the membrane causes strain changes in the membrane, which in turn produce the membrane deflection. The advantages of this method are high frequency, high flow rate and large pressure rise. Complex fabrication and high power consumption are the primary disadvantages. The thinXXs (2008) (model MDP1304) micropump produces a flow rate of ~22 sccm and a pressure differential of 10 kPa while consuming ~230 mW of power.

Thermo-pneumatic actuators use a fluid reservoir covered with a membrane to compress the gas in the pumping cavity. A resistive heater that expands the membrane heats the fluid in the reservoir. The advantages of this actuation method are large membrane deflection and pressure rise. The disadvantages are low flow rate, complex fabrication and high power consumption. Lung-Jieh and Tzu-Yuan (2011) report a thermo pneumatic pump that could produce a flow rate of 3.5-12 μl/min when operated between 0.3–3 kHz.

Knudsen pumps are thermally driven transpiration pumps that require no mechanical moving parts. These pumps operate at length scales, which are at the order of

the molecular free path allowing flow to take place from a cold to a hot chamber while consuming high power and producing large pressure differentials. A 9-stage micropump developed by Naveen (2011) could produce a maximum pressure head of 12 kPa, flow rate of 3.7 μl/min while consuming 3.5 W of power. A 48-stage micropump developed by Naveen (2012) consumes 1350 mW and produces a maximum compression ratio of 50. In Table 1.1 we compare the advantages and disadvantages of these actuation techniques.

Transferring of gas in micropumps is achieved using passive and active valves. Passive valves, like macroscopic check valves, open only in one direction when the pressure gradient is favorable and greater than the restoring force of the check valve. These valves provide low sealing and cannot be operated at high frequency. Active microvalves used by Kim et al. (2006) utilize an actuation mechanism similar to the one used to actuate the pumping membranes. These valves are operated at high frequency and allow dynamic control of valve timing to achieve high vacuum.

	Flow rate (sccm)	**Pressure (kPa)**	**Power**	**Fabrication**	**Displacement (μm)**
Electrostatic	< 30	< 12	Low	Simple	< 5
Piezoelectric	< 22	<10	Low	Complex	< 3
Electromagnetic	< 1.2	<35	High	Complex	30
Thermo-pneumatic	< 0.1	<3.8	High	Complex	30
Knudsen	< 0.1	<21	High	Simple	N/A

Table 1.1: Characteristics of different actuation methods employed in micropumps.

Theoretical Modeling

A variety of mathematical models have been developed to analyze micropumps. Models include: lumped-component electrical analog, theoretical (thermodynamic) models, reduced order models and CFD. In this section, the advantages and disadvantages of these different modeling techniques are discussed.

Lumped-component electrical analog models consist of describing the micropump system by a network of mechanical impedances, possibly nonlinear, and subsequently carrying out analysis with an electrical simulation tool like SPICE. Modeling of micropumps using lumped modeling is highlighted by Bourouina and Grandchamp (1999). The equivalent network is built by dividing the micropump into lumped components, which are described by the corresponding electrical analog. The correspondence between electrical and mechanical parameters is shown in Table 1.2.

Φ flow rate	i current
P pressure	e voltage
m/S^2 (where m is mass)	L inductance
α/S^2 (where α is the friction coefficient)	R resistance
k/S^2 (where k is the stiffness)	C Capacitance

Table 1.2: Fluidic and mechanical parameters and their electric analogs.

Hence the equation governing a mechanical system can be rewritten in terms of the equivalent electrical analogs, which simplifies to an RLC electrical circuit as shown in equation 1.1. Any complex fluidic device can then be modeled with an equivalent

network by linking lumped elements in accordance with Kirchhoff's laws adapted to mechanical and fluidic systems.

$$\begin{cases} F = m\frac{dv}{dt} + \alpha v + k\int v dt \\ P = \left(\frac{m}{S^2}\right)\frac{d\phi}{dt} + \left(\frac{\alpha}{S^2}\right)\phi + (k/S^2)\int \phi dt \\ e = L\frac{di}{dt} + Ri + \frac{1}{C}\int i dt \end{cases} \quad \textbf{1.1}$$

Fluidic modeling in these microscale devices assumes the dominance of the viscous losses in the small passages, which allows simplification to a Hagen-Poiseuille law. The mechanical impedance Z for a circular section passage is given by equation 1.2. The mechanical impedance appears as a resistance R_c

$$Z = \frac{\Delta P}{\phi} = \frac{8\eta l}{\pi R^4} \equiv R_c \quad \textbf{1.2}$$

For a system that includes inertia and compressibility effects, the fluidic system can be modeled using equation 1.3.

$$\Delta p = \left(R + jL\omega + \frac{1}{jC\omega}\right)\phi = (Z_{visc} + Z_{inert} + Z_{elastic}) \quad \textbf{1.3}$$

The pressure drop due to inertia in a channel of constant cross section and length, l, can be written as shown in equation 1.4, where L_m is the self-inductance. For compressible systems, the elastic behavior can be deduced from the compressibility factor χ. The capacitance, C_c, is defined as the product of $\chi, l, and\ S$.

$$\Delta p = \rho\frac{l}{S}\frac{d\phi}{dt} \equiv L_m\frac{d\phi}{dt} \quad \textbf{1.4}$$

$$\Delta p = \frac{1}{\chi l S}\int \phi dt \equiv \frac{1}{C_c}\int \phi dt \quad \textbf{1.5}$$

Effects due to the behavior of structural elements dominate due to high stiffness and inertia. The corresponding impedance is derived from a load deflection relation as

shown in equation 1.6. Here, ϕ is the flow due to the structural element motion: $\phi = dS < x > /dt$ and the capacitance $C_S = \frac{S^2}{K}$ describes the elastic behavior. For clamped membranes many nonlinear models have been developed.

$$\boldsymbol{p = \frac{K}{S} < x > = \frac{K}{S^2} \int \phi dt \equiv \frac{1}{C_S} \int \phi dt} \qquad \textbf{1.6}$$

Electrostatic actuation can be modeled as a variable capacitor consisting of two electrodes separated by a fluid gap of height H. One electrode is constituted by a membrane and is able to deflect when subjected to a pressure.

Bourouina and Grandchamp (1999) break down the pump described by Zengerle and Richter (1999) and shown in Figure 1.1 into equivalent electric circuits and models the system using the equations described above. The model results compare well with experimental data. The drawback of this model is the need to compute all the impedances beforehand. These are estimated either using FEM calculations or experimental results. In Figure 1.2, the resistors/inductors, capacitor and diode represent the channels, membrane stiffness and specific valve characteristics respectively. The simulation parameters used in this work are described in Bourouina and Grandchamp (1999).

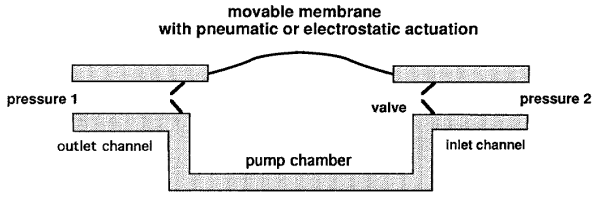

Figure 1.1: Model setup proposed by (Bourouina and Grandchamp 1999), consisting of an electrostatic membrane and two check valves.

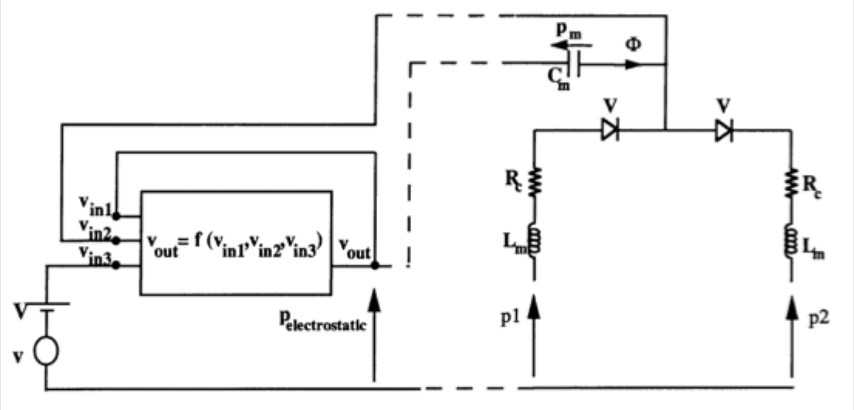

Figure 1.2: Equivalent network for the micropump operated electrostatically.

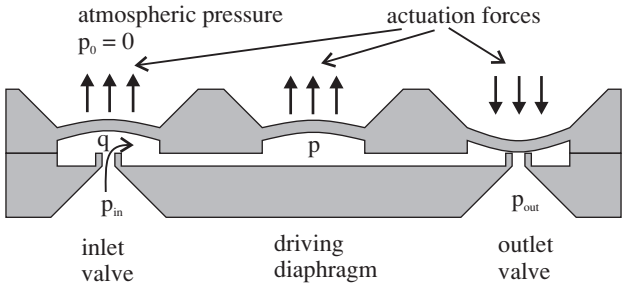

Figure 1.3: Schematic of the design proposed by (Goldschmidtböing et al. 2005) which incorporates active valves.

Goldschmidtböing et al. (2005) describe a micropump for medical applications with active valves, as shown in Figure 1.3. They proposed a lumped model that uses fluidic and structural analogies similar to Table 1.2. The pump consists of a piezoelectric driving membrane and two active microvalves. They assume that the fluidic resistance of the valves is higher than the flow resistance inside the pump chamber and, therefore, pressure losses in the pump are neglected. Since the deflection of the membrane is less than the thickness of the membrane, linear theory can be used to model the volume change. The volume displacement and pressure difference across the membrane is

linearly related as shown in equation 1.7, where ΔV_D, is the volumetric displacement of the driving diaphragm and C_D is a constant parameter.

$$\boldsymbol{\Delta V_D = \Delta V_D|_{p=0} + C_D.p} \quad \textbf{1.7}$$

The change in volume of the valves is also modeled in a similar manner as shown by equation 1.8. Here, C_V is the capacitance due to the membrane deflection and $p^{\pm}{}_{vc}$ is the pressure at which the valve touches the sealing lip. The closed and open positions are represented by – and + respectively. The outer region of the diaphragm is deflected by the pressure difference (p-p_{Vc}^{-}) with a fluidic capacitance C_{Vc}. The fluidic capacitance is much smaller than the corresponding capacitance of the membrane since the diaphragm is much stiffer when the sealing lip supports it.

$$\boldsymbol{\Delta V_v = \Delta V_v|_{p=0} + C_v.p + C_{Vc}(p - p_{Vc}^{\pm})} \quad \textbf{1.8}$$

In the gap between the valve lip and diaphragm, the flow is dominated by viscous losses. Assuming a parabolic flow velocity profile between the lip and the diaphragm, the resistance is inversely proportional to the cube of the valve gap, h_v.

$$\boldsymbol{p_p - p = R_v.q} \quad \textbf{1.9}$$

$$\boldsymbol{R_v = \frac{6.\eta}{\pi h_V^3} ln\left(\frac{r_2}{r_1}\right)} \quad \textbf{1.10}$$

Fast diaphragm and slow diaphragm actuation are the two operating modes of this pump. When the actuation is fast, pressure waves damp quickly since the pressure oscillation frequency is much higher than the frequency of fluctuations of the flow through the outlet and inlet valves. In slow actuation, the pressure inside the pump varies slowly. For these two operating modes the pressure inside the cavity is constant. A system of 13 unknowns reduces to 5 unknowns by operating the pump at low frequency.

The parameters can be estimated using ANSYS, but due to the inaccuracies of FEA modeling, an experimental setup was used.

Goldschmidtböing et al. (2005) model predicts the performance of the pump when operated at low frequencies with the optimum frequency at ~17 Hz. Though this is one of the first models for active valve pumping, it cannot be used to analyze high frequency systems and requires estimations of at least 5 parameters from experiments or FEA analysis.

Qiao Lin et al. (2007) and Lin et al. (2006) proposed a flow model for peristaltic micropumps involving coupled fluid flow and structural motion. Analysis is carried out on a micropump that consists of three compliant diaphragms located in a thin pumping cell, electrostatically actuated in a peristaltic sequence to move fluid, as shown in Figure 1.4.

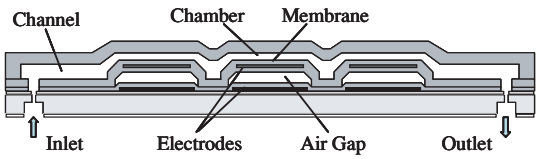

Figure 1.4: Schematic of the peristaltic micropump proposed by (Lin et al. 2006).

The diaphragm is assumed to be a plate with spring constant K vibrating elastically under the action of electrostatic and hydrodynamic forces. The diaphragm inertia is assumed to be negligible since the actuation frequency is below 100 Hz. The spring constant K is derived from the pull-in voltage. Equations 1.11–1.14 are used to estimate the deflection of the membrane coupled with electrostatics and hydrodynamics. Here, δ is the displacement, V is the voltage and A is the area.

$$K\delta = F^{elec} + F^{hydro} \quad \textbf{1.11}$$

$$F^{elec} = \frac{\varepsilon_o V^2 A}{2(d_{eff}-\delta)^2} \quad \textbf{1.12}$$

$$d_{eff} = d + t_p/\varepsilon_p \quad \textbf{1.13}$$

$$K = 16.4N/\lambda \quad \textbf{1.14}$$

Squeeze film damping due to the interactions of viscous fluid flow and diaphragm motion, and the hydrostatic effects of inlet and outlet pressures are modeled as shown in equation 1.15.

$$F^{hydro} = \frac{\alpha\mu l^2 A}{(h+\delta)^3}\dot{\delta} + \frac{1}{2}\beta(p_i + p_{i+1})A \quad \textbf{1.15}$$

The flow rate from each valve is estimated using the relation shown in equation 1.16. The system level model is shown in Figure 1.5. Here, $-p_1 = R_{in}Q_1$ and $p_4 - p_{back} = R_{out}Q_4$.

$$Q = \frac{1}{2}A\dot{\delta} + \frac{\gamma(h+\delta)^3}{12\mu}(p_i - p_{i+1}) \quad \textbf{1.16}$$

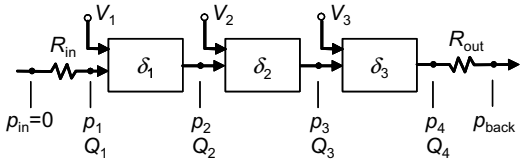

Figure 1.5: System-level model for the entire peristaltic pump.

Equations 1.11, 1.16 and pressure flow rate relations are solved in MATLAB using a three phase square wave. The model has been used to analyze the effect of geometry on the performance of the pump and the results were compared to the experimental data available from a previously constructed micropump. The model suggests that with an increase in the height of cavity, flow rate first increases and then decreases after an optimum height due to the effect of competition between the reduced

damping on the membrane vibrations and backflow. Decreasing the electrode gap increases the flow rate without increasing the optimum frequency. Though this model does not require experimentally estimated parameters, it cannot be used for operation of high frequency micropumps using active valves.

Gerlach (1997) presents a thermodynamic analysis to predict the performance of a valveless piezo-micropump. The net flow rate is related to the stroke volume, frequency and the efficiency. Gerlach (1997) also developed the thermodynamic relation between the pressure in the pumping cavity and the volume of the oscillating chamber shown in equations 1.17 to 1.19.

$$\boldsymbol{Q = f\varepsilon\Delta V} \qquad \textbf{1.17}$$

$$\boldsymbol{P(t) = \left[\left(\frac{1}{\frac{V_M(t)}{V_i}+1}\right)^{\gamma} - 1\right] P_M} \qquad \textbf{1.18}$$

$$\boldsymbol{\frac{P_1}{P_2} = \left(\frac{1}{V}\right)^{\gamma}} \qquad \textbf{1.19}$$

where V is the volume ratio (V_{min}/V_{max}). P(t) is the time-varying pressure in the cavity, V_M(t) is the oscillating chamber volume, V_i is the mean chamber volume and P_M is the mean cavity pressure. To obtain the maximum pressure relation, equation 1.18 is simplified to equation 1.19. While the model correlates with experimental data for flow rate it overpredicts the pressure rise. Astle et al. (2002) proposed a thermodynamic model, shown in equation 1.20, similar to Gerlach (1997) to model a multistage micropump. The model relates the flow rate to the operating frequency, compression ratio and pressure rise across each stage. It is solved iteratively to predict the flow rate and pressure rise across each stage, with the inlet/outlet pressure and operating frequency being known. This enables the design of a membrane that can withstand the predicted

pressure load. Simplifying this model allows prediction of the minimum compression ratio required to achieve a given pressure rise, as shown in equation 1.21. The disadvantage of these thermodynamic models is their inability to predict resonance effects. However, at frequencies lower than the resonance frequency, they correlate well with experimental data.

$$\frac{\dot{Q}}{f(V_{max}-V_{min})} = \frac{1}{1-V}\left(\frac{(P_{in})_j}{P_s}\right)^{1/n}\left[1 - V\left(\frac{(P_{out})_j}{(P_{in})_j}\right)^{1/n}\right] \quad \textbf{1.20}$$

$$\left(\frac{(P_{in})_j}{(P_{out})_j}\right) = V^n \quad \textbf{1.21}$$

$$\dot{Q} = f(V_{max} - V_{min}) \quad \textbf{1.22}$$

Equation 1.20–1.22 are the thermodynamic relations proposed by Astle et al. (2002) to study the performance of a dual chamber, electrostatically actuated micropump. Equation 1.21 is the minimum attainable pressure by the micropump, which is obtained by setting the flow rate ($\dot{Q}$) to zero. Equation 1.21 is the maximum attainable flow rate which occurs when P_{in}=P_{out}. Using the thermodynamic model, Astle et al. (2002) found that when the volume ratio is >0.98, it produces equal pressure difference pumping across each stage, while the opposite occurs when the volume ratio is <0.98. For lower volume ratios, pumping is found to occur in the stages closer to atmospheric pressure.

Goldschmidtböing et al. (2005) suggests that there are many commercially available CFD tools such as ANSYS, Flotran, COMSOL etc. to simulate fluid structure interaction and actuation methods. Due to the limitations of computational resources, as well as stability and convergence problems, CFD is applicable only to solving valve flow characteristics but not the entire pumping process. Nabity (2004) uses ANSYS to solve for coupled fluid structure interaction problem in a micropump. A SIMPLEF fluid solver,

moving mesh algorithm, contact analysis and a quadrilateral mesh were used to study the performance of the micropump. The peak displacement was 33 μm, maximum peak frequency performance was found to vary between 100–1000 Hz. Three-dimensional models developed in ANSYS and other CFD software packages also have limitations compared to reduced order models for performing parametric analysis mainly because of long computational time.

Astle et al. (2003) proposed a dual chamber system for maximum packaging efficiency with dual electrodes to electrostatically actuate the membranes driving the gas and active checkerboard valves for fluid transfer, as shown in Figure 1.6. To model and design this device, Astle et al. (2003) proposed a 1-D reduced order model based on conservation of mass and momentum in the pumping cavities.

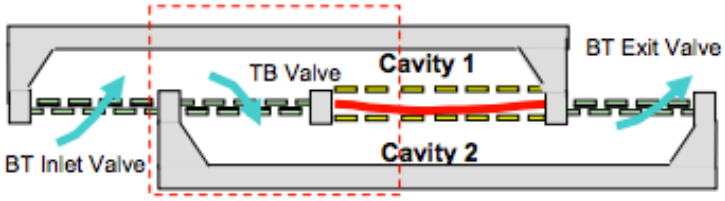

Figure 1.6: Schematic of a working dual stage micropump proposed by Astle et al. (2003).

A single micropump contains inlet/outlet valves and transfer valves. The operation of the pump is shown in Figure 1.7. The first trace is the position of the pump membrane between the top and bottom electrodes. The second and third traces represent the state of the valve, a high state indicates open valve, a low state indicates closed valve. The total duration during which the valves are opened is the Valve open time (t_{op})+Valve close time (t_{cl}).

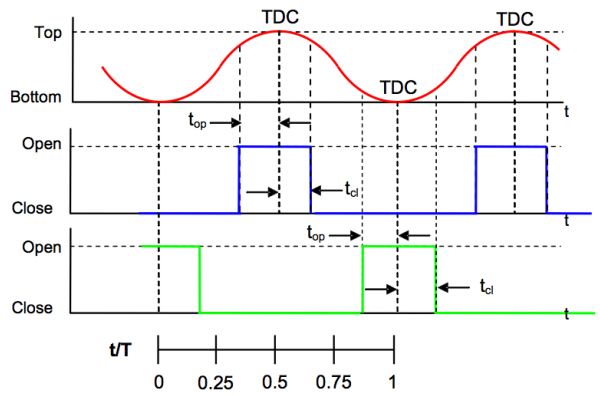

Figure 1.7: Valve operation with respect to the position of the pump membrane. The red blue and green lines represent the pump, transfer and inlet/outlet valve membranes respectively.

Astle et al. (2003)'s model assumes that the acoustic wavelength is much larger than the cavity size and hence the pressure distribution in the pumping cavities is uniform. Damping and inertial effects are entirely due to the flow through the valves and not the cavity. The volume variation in time, which drives the fluid, is assumed to be sinusoidal. The valves membranes do not displace fluid and are assumed to be ideal.

Equations of conservation of mass and momentum along a streamline are reduced to equation 1.23.

$$\frac{du_e}{dt} = \frac{1}{L_E}\frac{\Delta P}{\rho} - 8\frac{\mu}{\rho}\frac{u_e}{h_g^2}\frac{L_V}{L_E}H \qquad \textbf{1.23}$$

The pressure change in each cavity is due to flow through each valve and the volume change is as shown in equation 1.24.

$$\frac{dP}{dt} = -\rho\alpha^2\frac{n}{\gamma}\frac{uA_E}{V}H + \rho\alpha^2\frac{n}{\gamma}\frac{uA_E}{V}H - \rho\alpha^2\frac{n}{\gamma}\frac{1}{V}\frac{dV}{dt} \qquad \textbf{1.24}$$

The density change in each stage is given by the relation between the pressure change and the speed of sound as shown in equation 1.25.

$$\frac{d\rho}{dt} = \frac{\gamma}{n\alpha^2}\frac{dP}{dt} \quad \textbf{1.25}$$

The viscous length (L_v) and inertial length (L_e) are estimated using a laminar steady flow calculation in a commercial CFD package (FLUENT). They account for the resistance and inertial effects in the pump. This model was then used to estimate the resonant frequency for prescribed geometric dimensions. The effect of L_v and L_e on the resonant frequency was analyzed. The main drawbacks of this model are its inability to predict the membrane deflection, effect of electrostatic force of attraction, behavior of active valves and effect of multiple stages.

Table 1.3 summarizes the highlights of each of the modeling techniques discussed. While these tools have been successful in modeling certain characteristics of different kinds of existing micropumps, their application for more generic and detailed analysis of high frequency, electrostatically driven peristaltic micropumps is limited.

	Lumped Modeling	Thermodynamic modeling	CFD	Reduced Order Modeling
High Frequency	Mostly Low Frequency	No	Yes	Yes
Resonance effects	Cavity/ Membrane Resonance	No	Yes	Cavity Resonance
Requirement of experimental data	Yes	No	No	No
Computational time	Analytic/ Fast	Analytic/Fast	Computationally Intensive	Fast
Stability/Convergence	Yes	Yes	Not necessarily stable/convergent for all solutions	Yes
Active Valve pumping	Yes	No	Yes	No
Structural Membrane deflection	Yes	No	Yes	No

Table 1.3: Advantages and disadvantages of current models applicable for the design and analysis of micropumps.

Proposed Micropump

A new and innovative multistage vacuum peristaltic micropump based on the design proposed by Kim et al. (2007) is being developed at the University of Michigan. The goal of this micropump is to produce high-pressure difference in a vacuum system comprising of two other micropumps (Knudsen and Sputter Ion), as shown in Figure 1.8. Review of the literature suggests the use of electrostatic actuation and flow control using active micro-valves for the required applications. Salient features of this design are:

- Multiple stages comprising of dual (top/bottom on a pumping membrane) hexagonal shaped cavities for modular and efficient packaging
- Utilization of metalized oxide-nitride-oxide membrane for increased frequency of operation, electrostatic actuation and ease of fabrication
- Single electrode design for increased volume compression and ease of fabrication
- Checkerboard valve design for optimum valve timing and leakage reduction

Figure 1.9 illustrates a 3-D flow pattern in a single pump cavity present in a multistage device. The flow takes place through the inlet valve into the cavity below where it is compressed and pushed by the pump membrane through the transfer valve. The gas then flows through the exit valve into the atmosphere or the next pumping stage. For ease of fabrication only a single electrode is used for actuation.

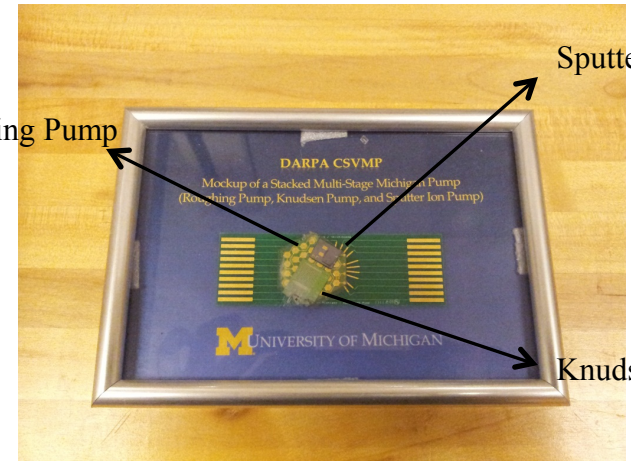

Figure 1.8: Stacking of the roughing, Knudsen and sputter ion pump.

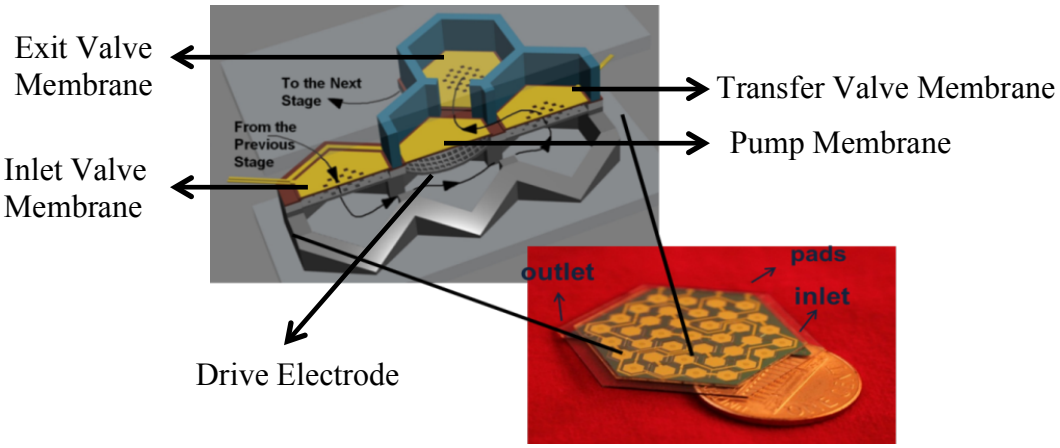

Figure 1.9: The new 3-dimensional concept drawing and actual multistage micropump. The 3-D drawing shows the presence of a single electrode, valve and pump membranes along with the direction of flow of gas from one cavity to another.

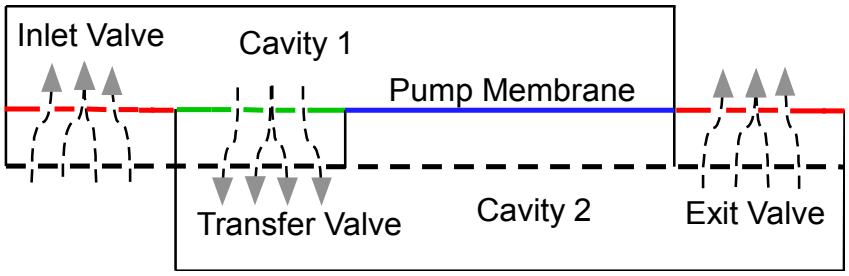

Figure 1.10: Schematic showing the flow direction through each valve. The valve membranes in red, green and blue represent the inlet/exit valves, transfer valve and the pump membrane respectively. The black dotted line represents the electrode.

Figure 1.10 is the schematic of a two stage vacuum micropump. The micropump consists of two sets of active microvalves, inlet/exit valves and transfer valves. The membranes for the valves and the pump are made up of a stack of oxide-nitride-oxide chromium and gold. A voltage difference is applied between the electrode and the membranes to drive the pump as well as to close/open the valves.

Figure 1.11 shows the operation of the micropump during a cycle. A voltage is applied to the valve's electrode to close each of the valves as shown in Figure 1.11(h). As shown in Figure 1.11(a), the inlet/exit valves open when the pressure at the inlet is greater than the pressure in cavity 1 and the pressure in cavity 2 is greater than the outlet pressure. Flow takes place from the inlet into the cavity 1 and from cavity 2 to the outlet. At this condition the pump membrane is at an intermediate position as illustrated in Figure 1.11(a). When the pump is operated at low frequency, the inlet/exit valves should close when the membrane collapses on the electrode as shown in Figure 1.11(b). At high frequency due to the fluid inertia, the valves should remain open until the pump membrane reaches the position as shown in Figure 1.11(c). The upward motion of the pump membrane increases the pressure in cavity 1 and decreases pressure in cavity 2. The transfer valves open when the pressure in cavity 1 is greater than the pressure in

cavity 2 and flow takes place from cavity 1 to 2. The displacement of the membrane in the upward direction is constrained due to the mechanical tension of the membrane as shown in Figure 1.11(f). The change in direction of the membrane causes the pressure in cavity 1 and 2 to decrease and increase respectively. The transfer valves close as shown in Figure 1.11(g) to prevent any loss in flow rate performance from backflow in the valves. The cycle begins all over again as illustrated by Figure 1.11(h).

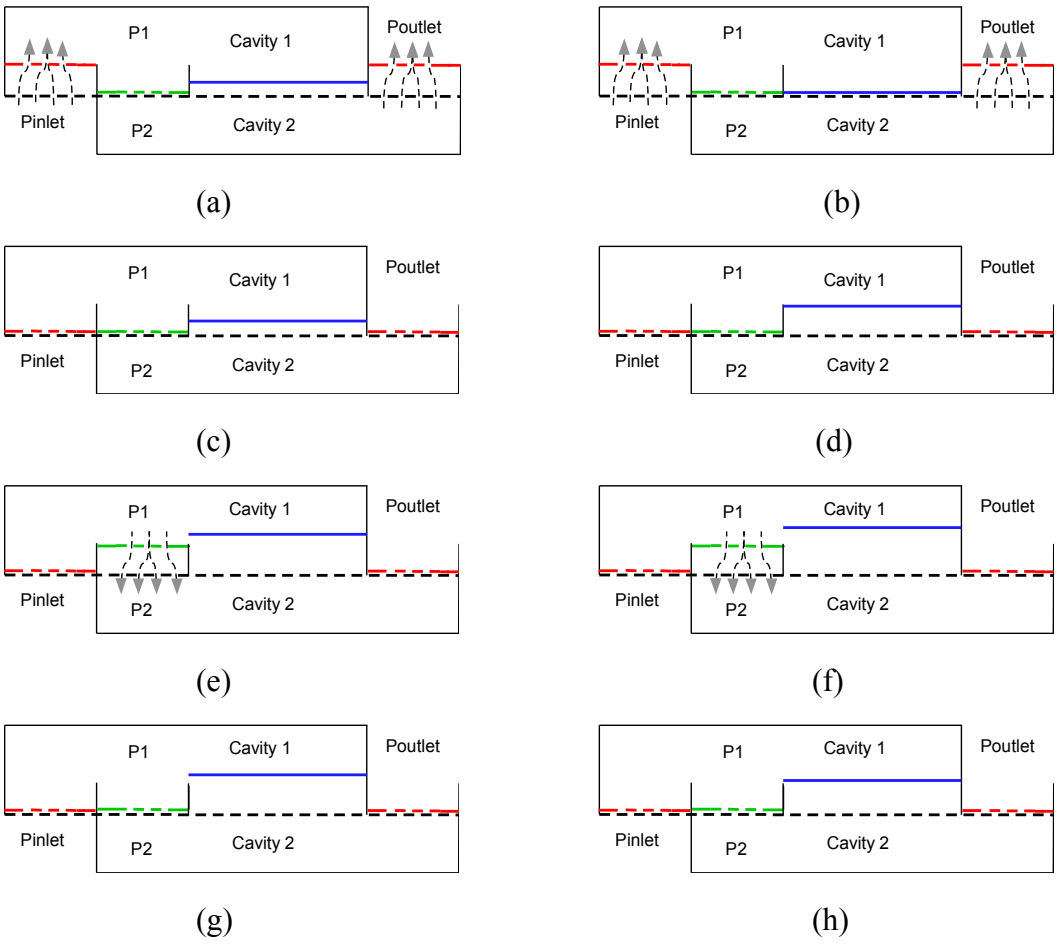

Figure 1.11: Schematic showing the pumping procedure. The pump membrane, inlet/exit valves and transfer valves are shown in blue, red and green respectively.

Checkerboard, electrostatically actuated microvalves are designed to regulate the flow through the micropump. The membrane and the electrode are perforated such that the pattern of holes on the electrode is offset from that on the membrane. When the

electrostatic force collapses the membrane on the electrode, the shifted pattern closes the perforations and prevents flow. Opening the valve is achieved by releasing the membrane from the electrode.

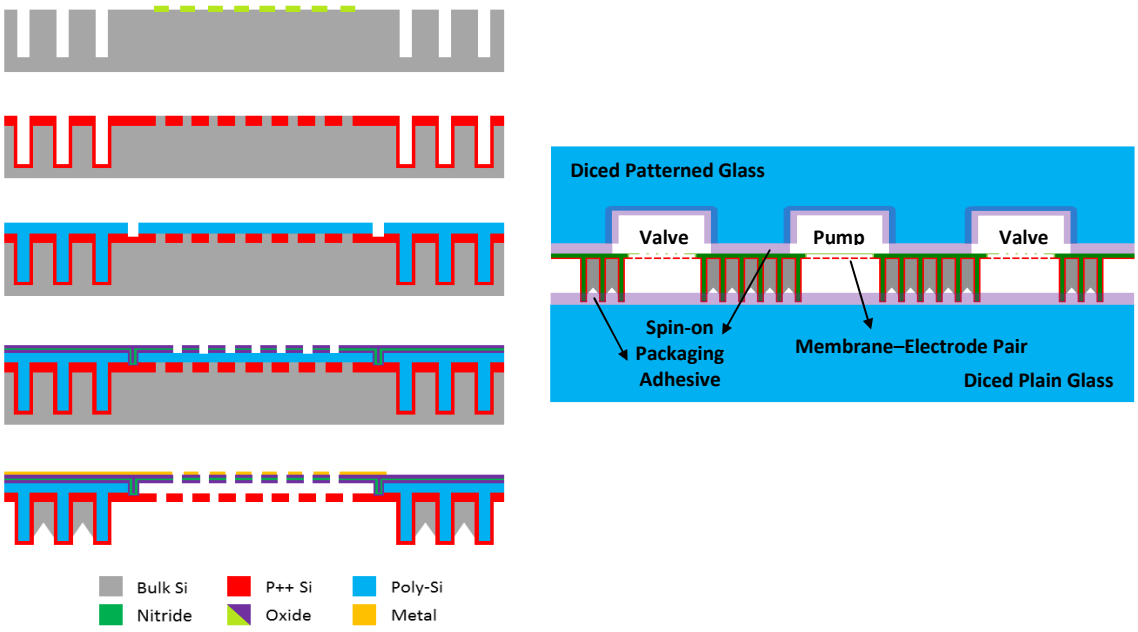

a) b)

Figure 1.12: Fabrication procedure for a dual stage micropump developed by Besharatian et al. (2012). In figure a), first trace is the thermal oxidation to form the doping mask followed by DRIE trenches; the second is boron doping and stripping; third is polysilicon doping and patterning; fourth is O-N-O membrane deposition and patterning; fifth is metal deposition and patterning followed by DWP in EDP. Figure b is the assembly procedure for packaging the pump.

Figure 1.12(a) shows the fabrication procedure of the mechanical resonator part of the micropump proposed by Besharatian et al. (2012). This is done using a six mask process. First Silicon wafers are thermally oxidized to form a mask for boron doping after which deep trenches are etched using DRIE process to define pumping cavities and form vertical stiffeners. Wafers are then boron doped to improve the level of conductivity of the electrode areas. Next an LPCVD, polysilicon sacrificial layer is deposited and

patterned, followed by deposition and patterning of an LPCVD oxide-nitride-oxide membrane and a thin sputtered Cr-Au layer for electrostatic actuation. Finally the resonators are released through DWP and surface micromachining process using EDP solution. In Figure 1.12(b) the acoustic resonator part of the micropump is fabricated in a single mask process by etching pumping cavities in glass wafers using HF and evaporated Cr-Au as the mask. Upon dicing the packages, Su-8-20101 is spun on glass packages and soft baked. The mechanical resonator is then sandwiched between and aligned to the acoustic resonator and the whole stack is heated up to reflow the SU-8 and seal the cavities. UV exposure and post exposure bake follow to cure the polymer and prevent it from time degradation.

Scope of this Work

Mathematical models reported in the literature can be used to study the performance of specific micropumps. Most of these models cannot be used for general applications. While lumped modeling is accurate, it relies on experimentally evaluated parameters to predict the performance of low frequency pumps. Thermodynamic models are good for estimating the maximum flow rate or achievable pressure based on geometric parameters, but cannot capture resonance. Reduced order models, like that developed by Astle et al. (2003), only captures resonance of the cavity but do not model the effects of membrane deflection or valve pumping. Current modeling tools can also predict only one operating resonant point but cannot predict multiple resonant points. These drawbacks demonstrate the need for developing a more generic model that can be used to predict the performance of a micropump more accurately.

The main objective of the research reported in this thesis is to develop new multiphysics mathematical tools which can overcome the drawbacks present in available models and can be used to design and analyze the performance of micropumps including the design proposed by Besharatian et al. (2012). The model builds on the mathematical tools developed by Astle et al. (2003) and Müller et al. (2000) (Müller et al. 2002). The transient performance, effect of operating frequency, valve timing, volume ratio, valve leakage, valve pumping and applied voltage are very important design considerations for high vacuum multistage micropumps. Estimation of the different operation modes will allow simpler experimental characterization of the pump. To ensure correctness of these

predictions, the model is verified with experimental results to ensure that all modes of operation are captured. While this model is developed for a particular design, it can easily be modified to study the performance of other electrostatically actuated micropumps.

Structure of this Work

In Chapter 2, the reduced order model for a dual stage micropump proposed by Astle et al. (2003) is extended to a multistage device having fixed membrane displacement and ideal valves. The effect of valve timing, leakage, operating frequency on a multistage design is analyzed for both steady and transient pumping states. Three new designs are proposed and their performances are compared. The influence of volume ratio and leakage is evaluated for obtaining a desired vacuum.

Chapter 3 discusses improvements to the reduced order model proposed in chapter 2 by incorporating structural deflection and electrostatic effects. The novelty of a single electrode micropump is evaluated and the transient performance for a 4-stage micropump is estimated. The valves are then modeled as active valves, no longer ignoring deflection, viscous and inertial effects. New viscous and inertial models are estimated for these valves. Finally, the behavior of the different resonant performance points is analyzed. A new design is presented for valve only pumping.

Chapter 4 discusses the development of a new experimental setup for the measurement of the performance of a micropump. First, the resonant frequency and pump membrane deflection are measured for different frequencies and voltages. Next, 4-, 12- and 24-stage micropumps are analyzed under high flow rate conditions. The effect of valve timing on 12 and 24-stage micropumps is also measured. The flow rate vs.

frequency characteristics is then compared between the experimental and predicted results.

Chapter 5 compares the theoretical reduced order model with computational fluid dynamics results to further validate the reduced order model assumption. Pressure distribution inside the micropump and flow rates through the transfer and exit valves are compared when only the pump membrane is actuated as well as when both the pump and valve membranes are actuated. The performance of the proposed resistance and inertial model in chapter 3 is compared to CFD results.

Chapter 6 summarizes the modeling and experimental analysis performed to characterize and study the performance of multistage vacuum micropumps. The main conclusions of the research are summarized and topics for further research are highlighted.

Chapter 2

Multistage Reduced Order Modeling

Extension of Reduced Order Model

Lumped modeling is capable of analyzing acoustic devices operated at high frequency but requires experimental data to estimate performance of a given system. CFD analysis is time consuming and the complex geometries with moving walls involved result in grid generation challenges, stability and convergence problems. The deficiencies of these models make them unsuitable for modeling the multistage peristaltic micropump. The thermodynamic model discussed in Chapter 1 serves as an initial guess to estimate the volume ratio needed to achieve the target vacuum pressure and flow rate based on the gap between the electrode and membrane. Lack of viscous and inertial effects render this model incapable of predicting resonance effects. This information is obtained from the reduced order model. The goal in this chapter is to estimate the necessary volume ratio required across each stage along with the effect of valve timing, frequency and leakage for a 16-stage micropump designed to achieve a vacuum of 250 Torr. To achieve this, the thermodynamic model is first used to evaluate the size of each stage followed by performance analysis using the reduced order model. In this section, the reduced order model proposed for a 2-stage micropump by Astle et al. (2003) is extended to a multistage device.

The thermodynamic model is a highly idealistic method of modeling micropumps. It assumes equal flow rate through every valve with the outlet pressure of one stage being equal to the inlet pressure in the next stage. The expansion and compression ratio follow a polytropic law, with a constant power law exponent n. Equation 2.1 relates the flow rate with the frequency of operation, volume ratio, change in volume and inlet and outlet pressures at each stage. The change in volume is due to membrane deflection, which is fixed and equal in each direction. The input pressure in each stage is estimated based on the flow rate and the outlet pressure.

$$\frac{\dot{Q}}{f(V_{max}-V_{min})} = \frac{1}{(V-1)}\left(\frac{(P_{in})_j}{P_s}\right)^{1/n}\left[1 - V\left(\frac{(P_{out})_j}{(P_{in})_j}\right)^{1/n}\right] \quad \textbf{2.1}$$

$$j = 1 \dots M \; (P_{out})_k = (P_{in})_{k+1} \; k = 1 \dots M-1 \; P_{out} = P_s$$

Equation 2.1 is solved iteratively for the pressure in each stage. It is observed that volume ratio affects the pressure rise in each stage. High volume ratios (>0.98) produce nearly equal pressure rise across each stage, and lower pressure differences when operated as a vacuum micropump. Volume ratios <0.98 produce unequal pressure rise each stage which results in a small pressure increase at the stages closer to the inlet and a large increase at the high pressure stages. Despite this they produce a higher vacuum.

To design a multistage pump capable of producing a desired vacuum, equation 2.1 can be used to study necessary cavity volume required across each stage. The flow rate to be produced at the required vacuum is zero. In equation 2.1, Q is set to zero which results in equation 2.2.

$$\frac{P_{in}}{P_{out}} = V^{n.M} \quad \textbf{2.2}$$

Equation 2.2 relates the volume ratio with the required target vacuum, the outlet pressure and the number of stages.

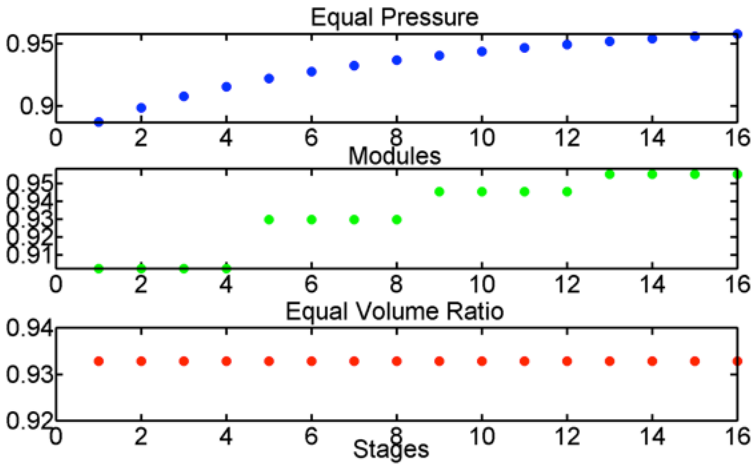

Figure 2.1: Volume ratio across each stage to achieve a target vacuum of 250 Torr. Top, middle and bottom traces are equal pressure, modular and equal volume ratio design respectively.

Three different approaches are presented based on certain design criteria as shown in Figure 2.1. The most important criterion while designing a multistage vacuum pump is the distribution of the pressure difference equally across each stage. This is because this pressure difference determines the force acting on the pumping and valve membranes. The goal is to minimize the pressure across each membrane. The top trace in Figure 2.1 shows the volume ratio across each stage required to achieve the target vacuum while achieving an equal pressure rise across each stage. For a 16-stage design the volume ratio in each of the stages 1-12 differ widely. Stages 13-16 have nearly equal volume ratio. Fabricating cavities, though challenging, is done using a new modular approach proposed by Besharatian et al. (2012)

A simpler procedure to achieve the equal pressure design is to divide the 16 stages into groups of 4 stages, each group having the same volume ratio. The volume ratio

across each stage is designed such that equal pressure difference is obtained across each module. The equal pressure difference is based on zero flow rate and the required target vacuum. The middle trace in Figure 2.1 quantifies this design. In this case the volume ratio is minimum for first module and maximum for the last module.

The easiest and simplest method of achieving the target vacuum is a constant volume ratio design. The bottom trace in figure 2.1 suggests that a volume ratio of 0.9329 across each stage can achieve the target vacuum. The advantages, disadvantages and performance of each of these designs are analyzed in subsequent sections.

In Chapter 1 the reduced order model proposed by Astle et al. (2003) was briefly described and is now extended to analyze the performance of a multistage vacuum micropump. The details of the model are highlighted in significant detail in this section. The model is based on conservation of mass and momentum along streamlines passing through a valve. The streamline originates at one cavity and ends in the cavity at the downstream side of the valve as shown in Figure 2.2. The model assumes uniform pressure distribution in the pumping cavities, which implies that the acoustic wavelength of pressure fluctuations at the pump operating frequency is much greater than the size of the cavity.

Figure 2.2 illustrates the flow through the valves. Two electrodes are depicted to represent a fixed membrane displacement. This assumption is used through this entire chapter. This allows the membrane to collapse on both electrodes assuming fixed displacement in each direction. The red arrows indicate the flow path from the inlet to the outlet. The enlarged sketch of the transfer valve in Figure 2.2 shows the mismatch in

holes positions between the membrane and bottom electrode, which allows sealing in the closed state when the membrane is collapsed against the lower electrode. The holes on the bottom and top electrodes are misaligned to allow for opening/closing of the valve in the appropriate direction relative to the pressure rise direction. For the inlet and outlet valves, the hole pattern on the bottom and top electrode is reversed compared to the transfer valves.

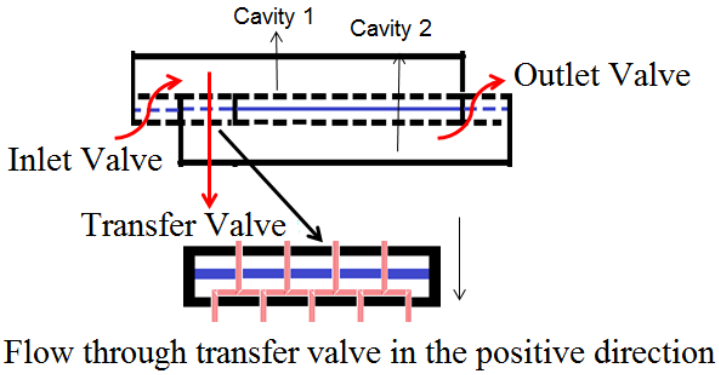

Figure 2.2: Illustration of the flow through a 2-stage micropump. The blue continuous line represents the pump membrane; the dotted blue line represents the valve membranes and the two types of valves are shown.

Equation 2.3 is the mathematical expression for conservation of momentum in integral form.

$$\rho \frac{d}{dt} \int \vec{u}.ds + \rho \int \nabla \left[\frac{\vec{u^2}}{2} + \frac{P}{\rho} \right].ds = \mu \int [\nabla.\vec{\omega}].ds \qquad 2.3$$

The viscous rotational term in equation 2.3 can be simplified as shown in the last term in equation 2.4. In equation 2.4 u_e is the mean flow velocity in the valve, Δp is the pressure difference between adjacent cavities, ρ is the density of the gas flowing from the corresponding cavity, L_E is the inertial length, L_V is the viscous length, h_g is the electrode

gap and C_D is the coefficient of drag. The quadratic term in u_e should be small and can be neglected.

$$\frac{du_e}{dt} = \frac{1}{L_E}\frac{\Delta P}{\rho} - \frac{{u_e}^2}{2C_D L_E} - 8\frac{\mu}{\rho}\frac{u_e}{h_g^2}\frac{L_V}{L_E} \quad \textbf{2.4}$$

The system of Ordinary Differential Equations (ODE) describing the flow through the different valves is shown in equation 2.6. The flow through the inlet valve depends on the pressure difference between the inlet and first stage, and viscous losses through the valves (L_V). The inertial length, L_E, accounts for the flow acceleration, which is obtained by integrating along a streamline originating from one stage and terminating in the other as shown in equation 2.5. In equation 2.6, j represents the valve number and varies from 2 to M, where M is the number of stages.

$$L_E = \frac{1}{u_e}\int u_e ds \quad 2.5$$

$$\begin{cases} \frac{du_{e1}}{dt} = \frac{1}{L_E}\frac{(P_{inlet}-P_1)}{\rho_{amb}}H_{inlet} - 8\frac{\mu}{\rho_{amb}}\frac{u_{e1}}{h_g^2}\frac{L_V}{L_E}H_{inlet} & Inlet\ Valve \\ \frac{du_{ej}}{dt} = \frac{1}{L_E}\frac{(P_{j-1}-P_j)}{\rho_j}H_j - 8\frac{\mu}{\rho_j}\frac{u_{ej}}{h_g^2}\frac{L_V}{L_E}H_j & Interior\ Valve \\ \frac{du_{eM+1}}{dt} = \frac{1}{L_E}\frac{(P_M-P_{outlet})}{\rho_M}H_M - 8\frac{\mu}{\rho_M}\frac{u_{eM}}{h_g^2}\frac{L_V}{L_E}H_M & Exit\ Valve \end{cases} \quad \textbf{2.6}$$

The viscous term is estimated using CFD and assuming steady flow as shown by Astle et al. (2003). The steady state assumption on equation 2.6 reduces it to the algebraic relation in equation 2.7. In these computations a pressure difference is applied across a section of the valve and calculating the flow rate, which gives the average velocity. Equation 2.7 is used to determine L_v the open state of the valve.

$$\Delta P = 8\frac{\mu u_e L_V}{h_g^2} \quad \textbf{2.7}$$

The opening and closing of the valves are governed by changing the H term in equations 2.6. H is set to zero when the valves are closed and one when open. In the closed state, setting H to zero, results in infinite resistance to flow.

The conservation of mass, equation 2.8, is used to estimate the pressure and density change in each of the stages. The pressure and density are related using equation 2.9, derived from the speed of sound. Substituting equation 2.9 in equation 2.10, the pressure in each stage can be determined. The volume change is assumed to be sinusoidal with fixed membrane displacement.

$$\frac{d(\rho V)}{dt} = -\rho u_E A_E \qquad \textbf{2.8}$$

$$\frac{d\rho}{dt} = \frac{\gamma}{n\alpha^2}\frac{dP}{dt} \qquad \textbf{2.9}$$

$$\frac{dP}{dt} = -\rho\alpha^2\frac{n}{\gamma}\frac{uA_E}{V} - \rho\alpha^2\frac{n}{\gamma}\frac{1}{V}\frac{dV}{dt} \qquad \textbf{2.10}$$

Similar to the relations for the flow through the valves, the pressure equation in 2.10 is organized to represent the pressure change in each stage, as shown in equation 2.11.

$$\begin{cases} \frac{dP_1}{dt} = -\rho_1\alpha^2\frac{n}{\gamma}\frac{u_{e2}A_E}{V_1}H_2 + \rho_{inlet}\alpha^2\frac{n}{\gamma}\frac{u_{e1}A_E}{V_1}H_1 - \rho_1\alpha^2\frac{n}{\gamma}\frac{1}{V_1}\frac{dV_1}{dt} \\ \frac{dP_j}{dt} = -\rho_{j+1}\alpha^2\frac{n}{\gamma}\frac{u_{ej+1}A_E}{V_j}H_{j+1} + \rho_j\alpha^2\frac{n}{\gamma}\frac{u_{ej}A_E}{V_j}H_j - \rho_j\alpha^2\frac{n}{\gamma}\frac{1}{V_j}\frac{dV_j}{dt} \\ \frac{dP_k}{dt} = -\rho_{k+1}\alpha^2\frac{n}{\gamma}\frac{u_{ek+1}A_E}{V_k}H_j + \rho_{k+1}\alpha^2\frac{n}{\gamma}\frac{u_{ek+1}A_E}{V_k}H_{k+1} - \rho_k\alpha^2\frac{n}{\gamma}\frac{1}{V_k}\frac{dV_k}{dt} \end{cases} \qquad \textbf{2.11}$$

Where j =3, 5, 7, …M-1 and k= 2, 4, 8…M.

In the system of ODE equations in 2.11, the pressure changes in the first stage, the odd and even stages are represented by the first, second and third equations respectively. In the first equation, the pressure decrease due to the flow through the transfer valve, pressure increase due to the flow through the inlet valve and pressure change due to the

membrane deflection are represented by the first, second and third terms respectively. The second equation is arranged similarly to the first equation. In the third equation, the decrease in pressure due to the flow through the exit valve, increase in pressure through the transfer valve and pressure change due to membrane deflection are represented by the first, second and third terms respectively. The density used in these equations is based on the positive direction of flow. If flow reversal takes place, the density from the corresponding stage is substituted.

The density change in each stage is given by equation 2.9, with the corresponding pressure change shown in equation 2.11. To analyze the effect of steady state inlet pressure and multiple stages, the systems of ODE equations 2.6, 2.9 and 2.11 are solved using MATLAB's ode45 solver. Initially the stage pressure is atmospheric and velocity through each valve is zero. The set of equations are solved until the cycle to cycle variation of the pressure in each stage is below 10^{-5}. Similarly the mass flow rate through each valve should also agree within an error less than 1%.

In reality, a micropump is required to evacuate gas from a fixed known volume. The pressure in this volume changes with time due to the pumping. This is implemented using equation 2.12. For transient performance analysis equations 2.6, 2.9, 2.11 and 2.12 are solved. Steady state is obtained when the cycle-to-cycle change in inlet pressure is less than 10^{-5}.

$$\frac{dP_{inlet}}{dt} = -\rho_{inlet}\alpha^2 \frac{n}{\gamma}\frac{u_{e1}A_E}{V_{inlet}} \qquad 2.12$$

Steady State Operation

In the previous section, a reduced order model is developed for analyzing a multistage vacuum micropump. Astle et al. (2003) showed the effect of operating frequency on steady state performance while the effect of other parameters such as valve timing, leakage etc. were not explored. Currently, there is limited information on the performance of a multistage vacuum micropumps. In this chapter we assume a square membrane instead of a hexagonal membrane with fixed displacement where the volume change is sinusoidal. Although this model does not account for the structure dynamics of the membranes the goal of this analysis is quantify the effect of other aspects like multi-staging, valve leakage and give good relative performance estimates

For the different design parameters shown in table 2.1, the analysis is carried out assuming steady state inlet pressure conditions. Two operating conditions are outlined in table 2.1. Conditions 1 and 2 are governed by the volume ratio. In the previous section, the reason for valve flipping by Astle (2006) was explained. Fabricating the device using the current procedure does not allow for valve flipping. Therefore, the volume ratio computation should not take into account the displacement of the valves. Figure 2.3 outlines the maximum and minimum volume in stage 1. Volume ratio is the ratio of minimum volume to maximum volume.

Operating Conditions 1	
Target Pressure	334 Torr
Volume Ratio	0.95
Cavity Volume	0.8 mm^3
Operating Conditions 2	
Target Pressure	250 Torr
Volume Ratio	0.93
Cavity Volume	0.365 mm^3
Pump Dimensions	
Area of Valves	1 mm^2
Membrane Area	4 mm^2
Holes in Valve	110
Electrode Gap	3.5 µm
L_v	30 µm
L_E	200 µm
Stages	16

Table 2.1: Operating and design parameters for design analysis.

a) b)

Figure 2.3: Schematic showing the computation of the volume ratio. Figure a, is the maximum volume in stage 1 and figure b is the minimum volume in stage 1.

Two volume ratios are used for the current analysis, 0.93 and 0.95. A lower vacuum pressure is obtained by the lower volume ratio and vice versa. In the current analysis, parameters similar to the ones used by Astle et al. (2003) are incorporated. The valve area is smaller than the current design used by Besharatian et al. (2012). Despite a smaller valve area, a significant amount of information regarding the operation of the pump is obtained. Using equation 2.2 a 16-stage vacuum micropump was calculated to have a minimum volume ratio of 0.9329 to achieve the target vacuum of 250 Torr. Here

we use a volume ratio of 0.93 to account for the loss in performance due to leakage. The system of equations 2.6, 2.9 and 2.11 are solved using MATLAB's ode45 solver for the operating conditions and pump parameters shown in Table 2.1, as illustrated in Figure 2.4.

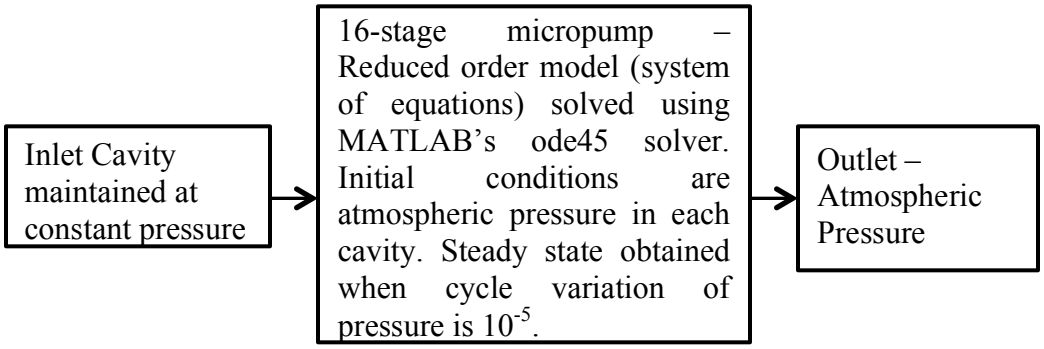

Figure 2.4: Schematic showing the setup for solving the equation in MATLAB

Lee et al. (2009) showed the impact of valve timing on the performance of the pump. Different t_{op} and t_{cl} values are chosen using operating conditions 1 in Table 2.1, to compute the flow rate. The inlet pressure is maintained at 0.9 atm. and the pump is operated at 50 kHz. Figure 2.5 shows contour lines representing the flow rate for the corresponding t_{op} and t_{cl}. In this case, it was found that the optimum valve timing producing the maximum flow occurred when t_{op} /T was 0.26 and t_{cl} /T was 0.245. This procedure is followed for all further analysis. In the open state, L_V is assumed to be 30 μm and L_E to be 200 μm.

Since, the micropump is operated at high frequency, analysis is carried out at 10 and 50 kHz. To first study vacuum operation, pressure performance is evaluated at steady

state inlet pressures of 0.4 and 0.9 atm. At these operating conditions, the effects of valve timing and resonance are studied in detail.

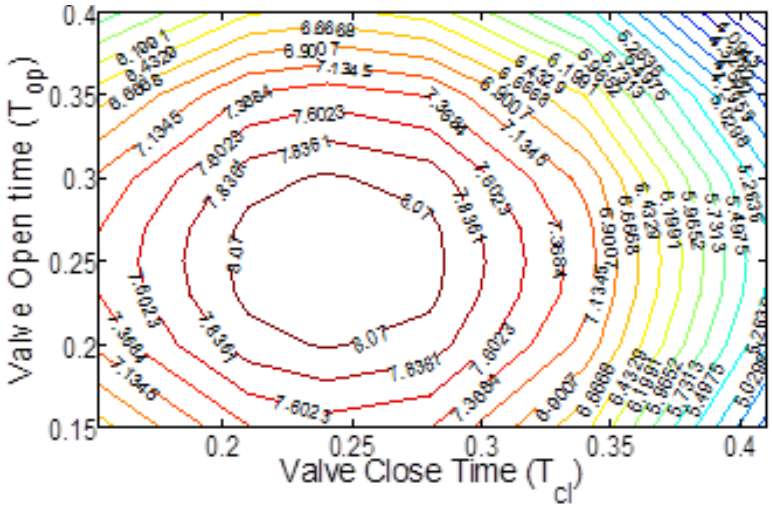

Figure 2.5: Flow rate produced by the pump for operating conditions 1 for different valve open time (t_{op}) and valve close time (t_{cl}).

Figure 2.6a and Figure 2.6b illustrates the velocity through each valve when the pump is operated at steady state inlet pressures of 0.4 and 0.9 atm. respectively. A high flow is expected at inlet pressures closer to the atmospheric pressures. It is expected that operation of this pump at high frequencies should produce maximum flow rate. At 50 kHz, the velocity through each valve is significantly higher that when operated at 10 kHz. Figure 2.6a indicates that the valves are opened and closed earlier when operated at lower frequencies. However, the total time for which these valves are opened is nearly equal. The valve timings utilized for each case is optimized to produce maximum flow.

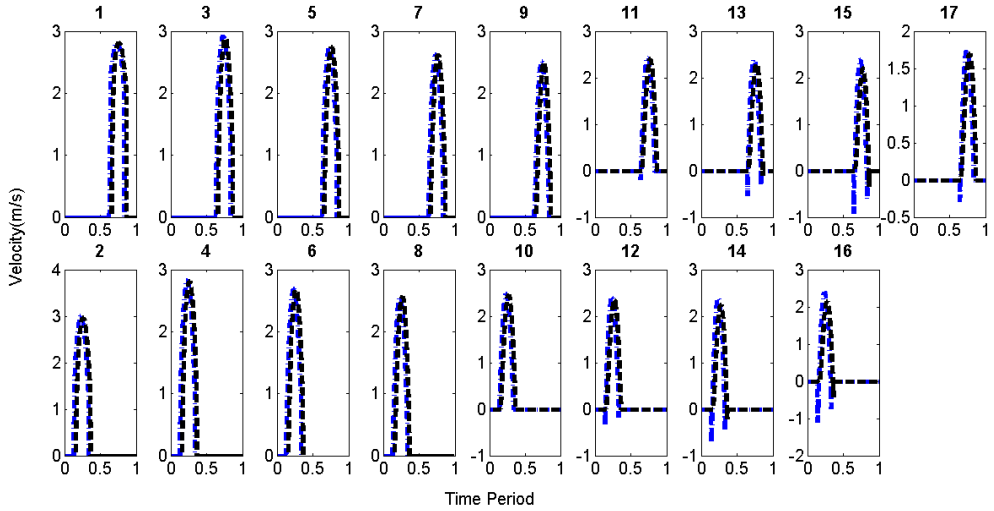

a)

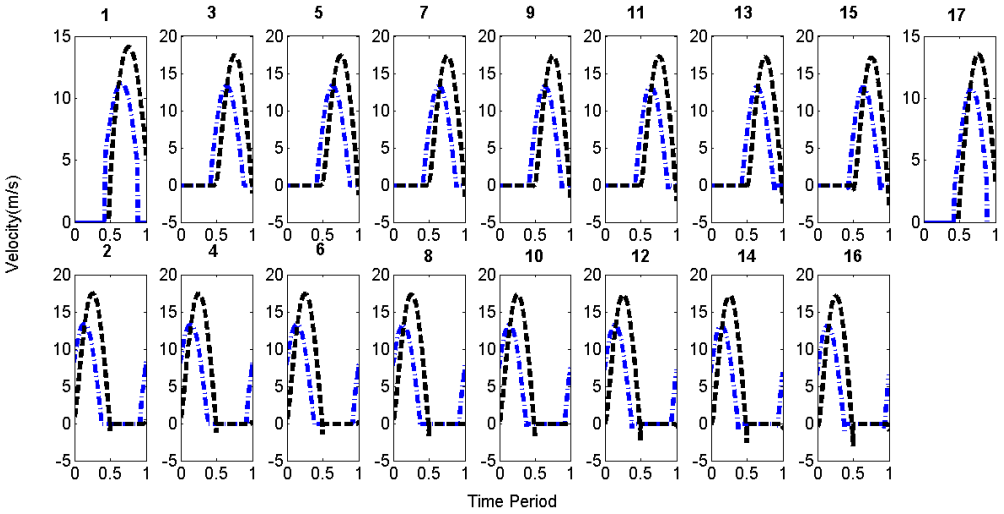

b)

Figure 2.6: Velocity profile through each valve. Figure a) and figure b) are the operations at 0.4 and 0.9 atm. inlet steady state pressure. Odd and even numbered figures represent flow through the inlet/exit and transfer valves respectively. -.- and – is the operation of pump at 10 and 50 kHz respectively.

At lower inlet pressures, the flow rate is expected to decrease. A negligible disparity in performance is noticed at these frequencies. In Figure 2.6b, 10 and 50 kHz produce nearly the same flow rate through each valve. The duration for which the valves are opened for a given cycle is nearly equal. Thus, the valve timing at different operating pressures and frequencies are significantly different.

Figure 2.7a and Figure 2.7b illustrates the pressure distribution in each stage when the pump is operated at 10 and 50 kHz respectively. Figure 2.7a shows that that there is negligible change between the pressure distribution in each cavity when the pump is operated at 10 and 50 kHz. However, in Figure 2.7b there is a noticeable change between the pressure distribution in each cavity when the pump is operated at 10 and 50 kHz. A larger variation in pressure magnitude occurs when the pump is operated at 50 kHz. In Figure 2.7a the difference between the minimum and maximum pressure for a given cycle increases from 20 to 40 Torr from the 1^{st} to the last stage, which is due to the equal volume ratio across each stage. This difference across stages follows the same trend when the inlet pressure is 0.9 atm., as shown in Figure 2.7b. The difference between the minimum and maximum pressure varies from 40 – 60 Torr.

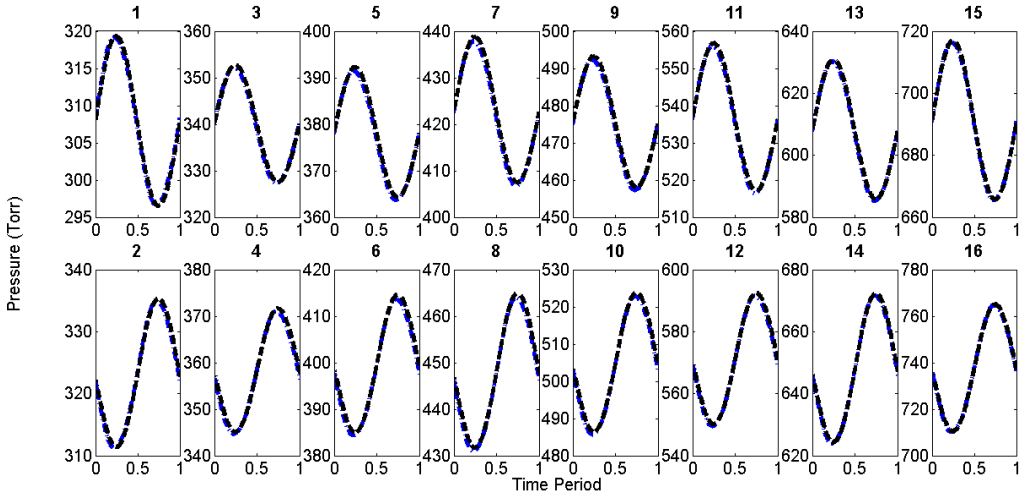

a)

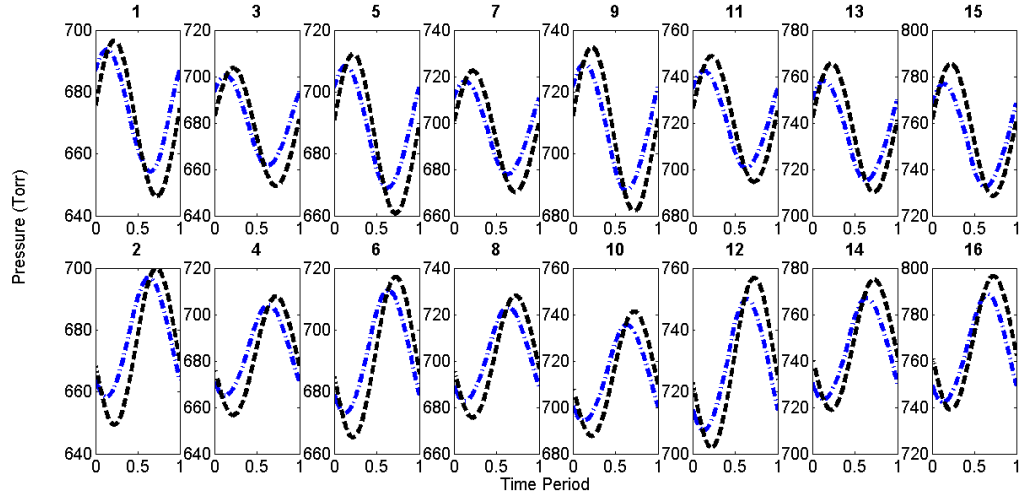

b)

Figure 2.7: Pressure distribution in each stage when the pump is operated at 0.4 and 0.9 atm. steady state inlet pressure shown in figure a) and b) respectively. The numbers on each trace represent the corresponding cavity. -.- and – represent the operation at 10 and 50 kHz respectively.

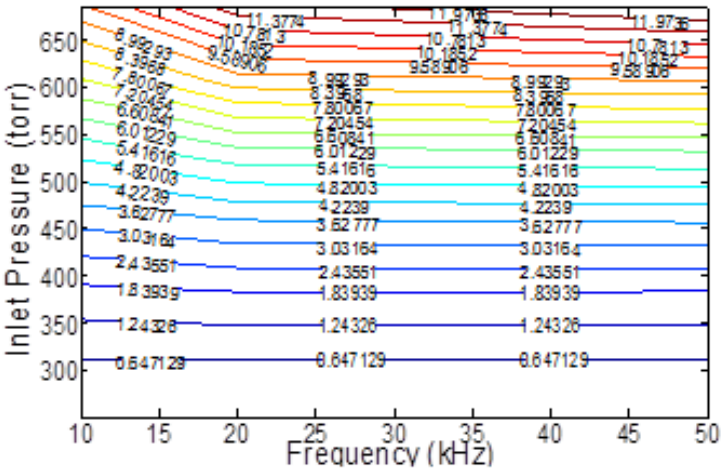

Figure 2.8: Contours of flow rate (sccm) for corresponding operating frequencies and inlet pressures.

Figure 2.8 analyzes the performance of the pump when operated at different steady state inlet pressures and frequencies. The contour lines represent the flow rate for optimized performance at each frequency and pressure. Optimum valve timing is used to achieve maximum performance for each case. At inlet pressures above 450 Torr, the frequency that produced maximum performance was estimated to be 50 kHz. As the steady state inlet pressure is decreased, the disparity in flow performance between these frequencies becomes smaller. The flow rate is nearly constant for the operating range of frequencies at inlet pressures less than 450 Torr. Closer examination of the performance suggests that the optimum operating frequency decreased from 50 to 20 kHz when the pressure dropped from 760 to 250 Torr. At lower inlet pressures, the difference in volume flow rate for the operating range of frequencies was negligible (<0.01 sccm). Although operating frequency can result improved performance as the inlet pressure decreases, development and implementation of such system would be expensive. Hence, further analysis has not been carried out.

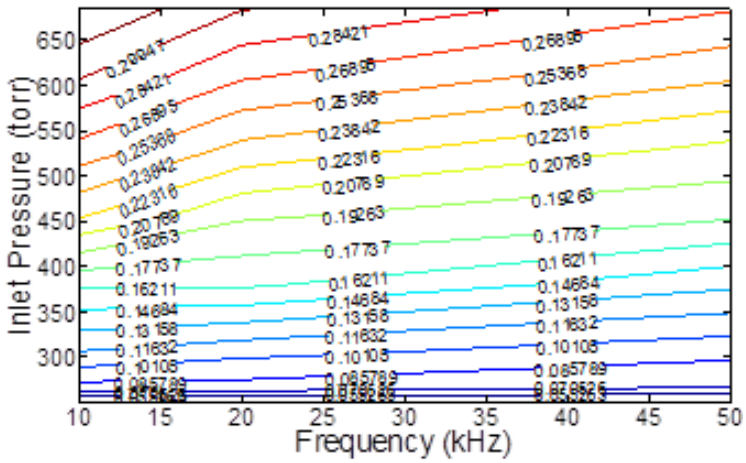

Figure 2.9: Contours of valve open time, t_{op}, for corresponding operating frequencies and inlet pressures.

The time parameters that control the opening and closing of the valves are Valve Open and Valve Close time, described in chapter 1. In Figure 2.9, the contour lines represent the optimized valve open time. The numbers on these lines depict the fraction of a cycle for which the valves are open. The data is computed at steady state inlet pressures for a given frequency. When the inlet pressure is high, the valve open time is small for higher frequency and vice versa. At low inlet pressures, the valve open time becomes nearly equal for all the frequencies. Since the flow rate is small, the valves need to be open only for a small duration. Larger valve duration would result in back flow thereby hindering the performance of the pump.

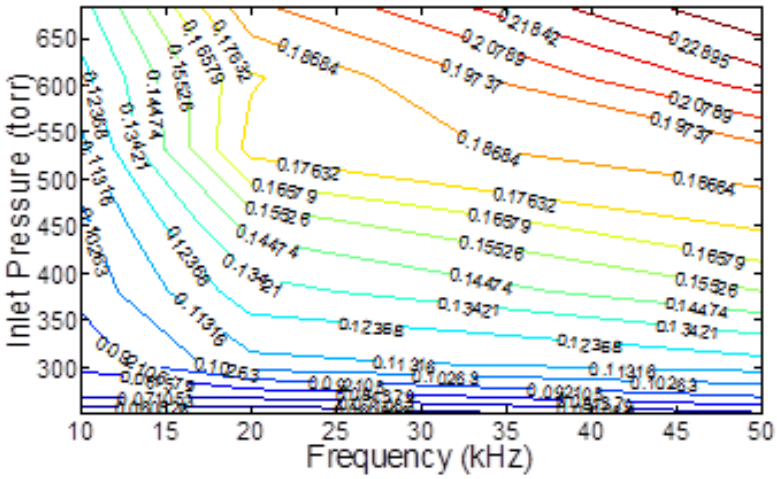

Figure 2.10: Contours of valve close time, t_{cl}, for corresponding operating frequencies and inlet pressures.

The Valve Close time is the fraction of time required to close the valve. Contour lines in Figure 2.10 represent the Valve Close time for the corresponding inlet pressure and frequency. Inlet pressures close to atmosphere (i.e. is outlet pressure) produce high flow rate. The duration for which these valves are open is longer. Low frequencies have a larger valve open time in comparison to that at higher frequencies. Since the fraction of a given cycle for which these valves are opened are nearly the same for a given inlet pressure at any operating frequency, the valve close time is directly related to the valve open time. Therefore, at high inlet pressures, the valve close time is small for low frequencies and larger for higher frequencies. With the decrease in inlet pressure, due to the smaller flow, Valve Close time is nearly the same.

Dynamic Valve Timing

In the previous section, the impact of optimized valve timing is described. Valves opened for too long period could result in back flow, reducing performance of the pump. A smaller valve open time period could result in very little flow, increasing the time taken to evacuate the gas from a given chamber. The goal in this section is to develop a method that can operate the pump efficiently. Figure 2.6 suggests that changing the valve timing when the pump is transitioning from atmospheric pressure to target vacuum. This section investigates the development of a control system that can produce maximum performance by changing valve timing as the inlet pressure decreases.

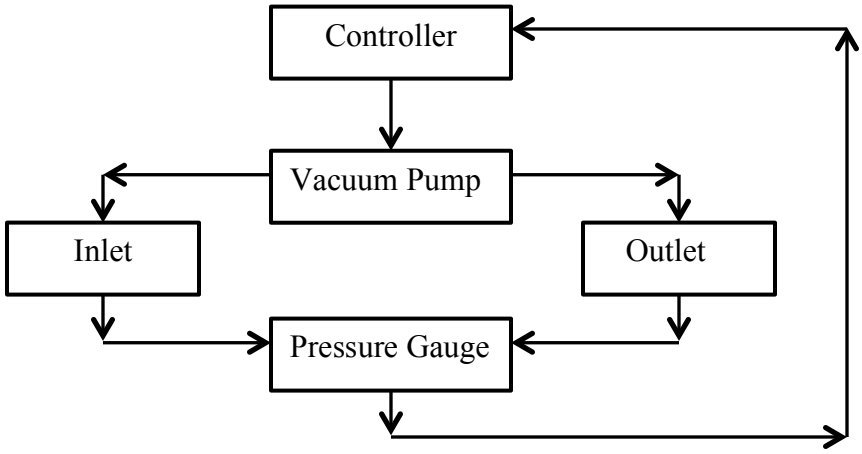

Figure 2.11: Schematic of the proposed method to control the valve timing.

Figure 2.11 is a proposed scheme to control the pump more effectively. The micropump is connected to an inlet volume ($1cm^3$) initially maintained at atmospheric pressure, while the outlet is exposed to the atmosphere. At any given instant the pressure difference between the inlet and outlet is measured using a pressure gauge. The

information obtained from the gauge, is sent to a controller, which modifies the valve signals. The analysis carried out is only a theoretical evaluation and has not been implemented experimentally. In the subsequent chapters the implementation aspects of such a system is evaluated.

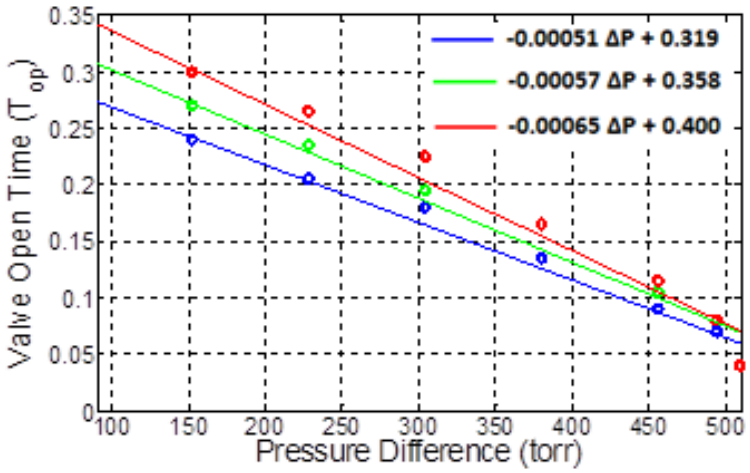

Figure 2.12: Linear relation between the valve open time and the pressure difference across the pump. The red, green and blue lines show the operation of the pump at 10, 20 and 50 kHz respectively. The legend shows the mathematical relation between the valve open time and pressure difference.

Steady state analysis is first used to determine how the valve open/close time is affected by the pressure difference across the pump and operating frequencies. Figure 2.12 shows the relationship between the Valve Open time, t_{op}, and the pressure difference across the pump. The analysis shown above is similar to that in the previous section. The Valve Open time is optimized to obtain maximum flow rate for a given pressure difference and operating frequency. The figure shows a linear relationship between the pressure difference and t_{op}. Since the linear relation breaks down close to the target vacuum, better mathematical correlations can be used. But as an initial estimate, the linear relation is implemented to evaluate performance improvement. The mathematical

relationship between t_{op} and the pressure difference is shown in Figure 2.11, which is obtained using MATLAB's curve fit toolbox. As expected, t_{op} is larger at lower pressure differences and vice versa when operated at high frequency. Around the target vacuum, t_{op} used for the range of frequencies is nearly equal.

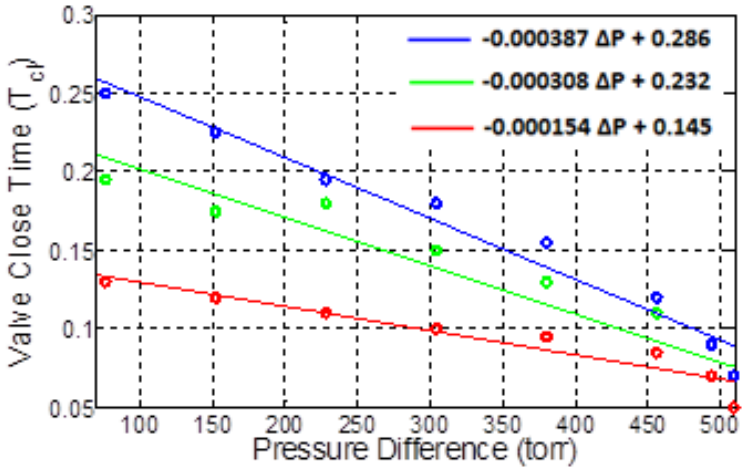

Figure 2.13: Linear relation between the valve close time and the pressure difference across the pump. The red, green and blue lines show the operation of the pump at 10, 20 and 50 kHz respectively. The legend shows the mathematical relation between the valve close time and pressure difference.

Figure 2.13 shows the analysis of t_{cl} and pressure difference across the pump for different operating frequencies 10, 20 and 50 kHz. Similar to the analysis of t_{op}, a linear relation exists between t_{cl} and the pressure difference, which breaks down near the target vacuum. However as mentioned earlier, the linear relationship provides a good initial estimate to evaluate the performance improvement. In concurrence with previous analysis, lower pressure differences across the pump require a smaller t_{cl} and vice versa when operated at lower frequencies. This difference between the frequencies reduces when the target vacuum is approached, becoming nearly equal at the target vacuum.

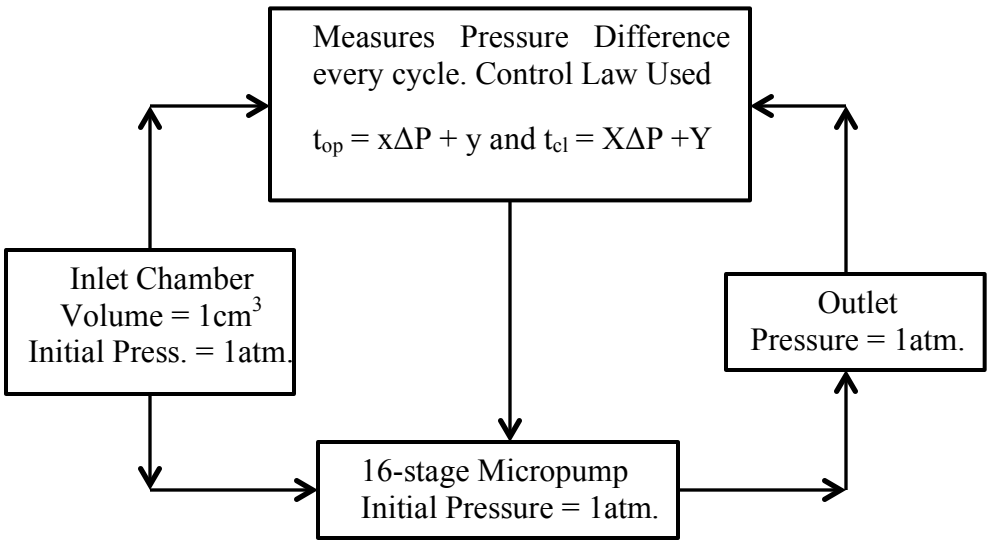

Figure 2.14: Schematic showing the implementation of dynamic valve timing in a 16 stage vacuum micropump.

The process of transient adjustment of the valve timing during the operation of the pump is known as dynamic valve timing (DVT), as shown in Figure 2.14. A 16-stage micropump initially maintained at atmospheric pressure, evacuates gas from the volume, while the outlet is maintained at atmospheric pressure. Equations 2.6, 2.9, 2.11 and 2.12 are now solved in MATLAB. At every time instant, the pressure difference across the pump is measured and the corresponding t_{op} and t_{cl} is computed based on the relationships shown in Figure 2.12 and Figure 2.13. These valve timings now adjust the open time of the valves, maximizing performance as the inlet pressure decreases.

For examining the advantage of this system, two fixed valve times are compared with DVT. The first fixed valve timing (case 1) has $t_{op}/T = 0.04$ and $t_{cl}/T = 0.07$, while the second (case 2) has $t_{op}/T = 0.12$ and $t_{cl}/T = 0.12$. Steady state analysis shows that for a micropump operated at 50 kHz, the first fixed valve timing produces maximum flow rate at 250 Torr and is opened for a short duration only. Valves are opened for a longer duration using the second fixed timing, which results in a higher flow rate. They are also

chosen as these numbers are in between the range of valve timings shown in Figure 2.12 and Figure 2.13, for the corresponding frequency.

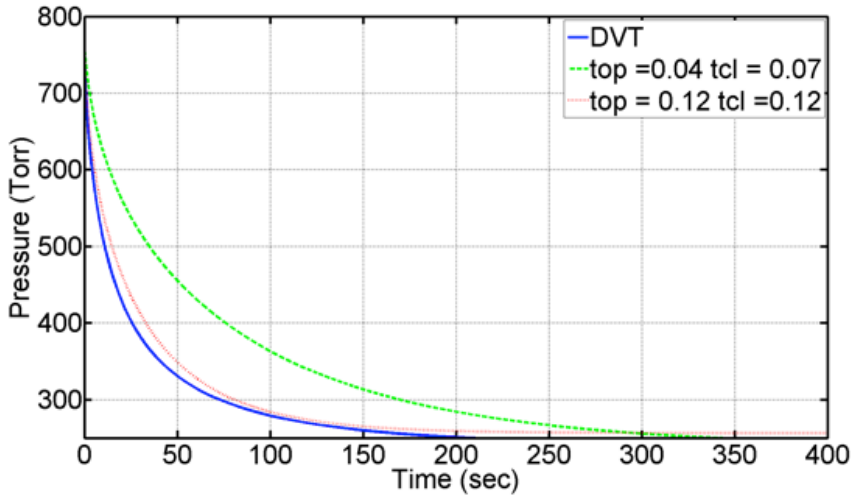

Figure 2.15: Comparison of pumps performance using dynamic valve timing and a constant valve timing. The pump is operated at 50 kHz. The green, red and blue lines represent the first, second fixed valve timing and dynamic valve timing respectively.

Figure 2.15 is a comparison of pressure performance of the pump when operated at 50 kHz. Using the fixed valve timings in case 1, the pressure decreased from atmospheric pressure to 250 Torr in nearly 350 seconds. The fixed valve timing conditions in case 2 could not achieve the target pressure of 250 Torr. Dynamic valve timing reduced the pressure in the chamber to 250 Torr in 200 seconds. The performance improvement produced by DVT is nearly 40%. Hence, it is important to analyze this system in greater detail by studying the velocity distribution through each valve.

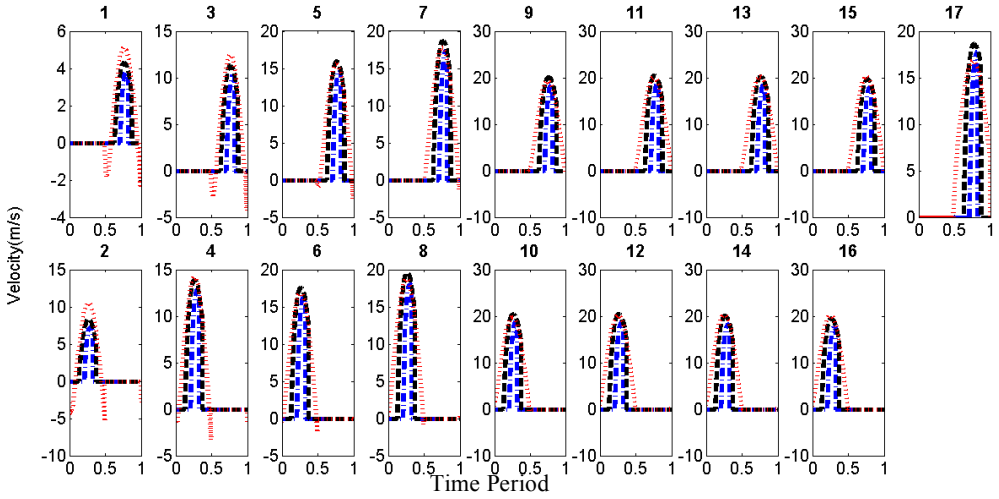

Figure 2.16: Velocity profiles through each valve when inlet pressure is 650 Torr and the operating frequency is 50 kHz. -.-, -- and : represent the case 1, case 2 fixed valve timings and dynamic valve timings respectively. Even and odd numbered figures represent flow through the transfer and inlet/exit valves respectively.

A snapshot of the velocity distribution through each valve at 650 Torr is shown in **Figure 2.16**. The pump is operated at 50 kHz and the impact of the three different valve timings is compared. The fixed valve timings do not have reverse flow and allow gas transfer for shorter durations. Dynamic valve timing allows gas transfer for a longer duration resulting in higher flow and faster decrease in inlet pressure. **Figure 2.16** suggest valves 1-8 allow reverse flow when operated using dynamic valve timing. However, the backflow produced is significantly smaller in comparison to the positive flow. Hence, the linear relation between the valve timing and pressure difference does hold reasonably well when the pump is evacuating gas at high inlet pressures.

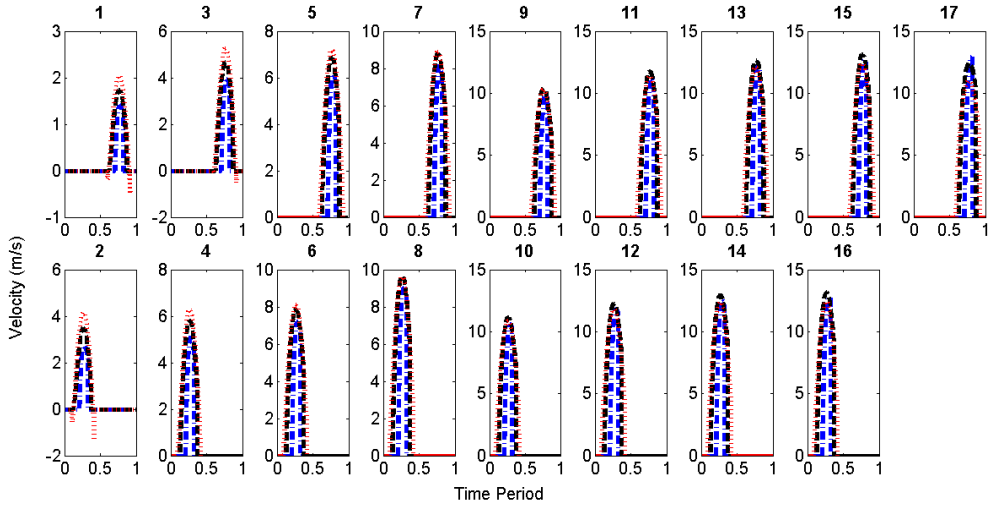

Figure 2.17: Velocity profiles through each valve when inlet pressure is 450 Torr and the operating frequency is 50 kHz. -.-, -- and : represent the case 1, case 2 fixed valve timings and dynamic valve timings respectively. Even and odd numbered figures represent flow through the transfer and inlet/exit valves respectively.

A snapshot of the velocity distribution through each valve at 450 Torr is shown in Figure 2.17. Case 1 and case 2 of the fixed valve timing do not produce back flow. Stages 1-4 allow small flow reversal when operated using dynamic valve timing. This reversed flow is significantly smaller than the positive flow rate. Since the valves are opened for a longer duration when the dynamic valve timing is used, a larger flow rate is obtained through each valve. Coincidently the valve timings for the dynamic valve timing and case 2 (fixed valve timing) are nearly equal at this operating inlet pressure. Hence, at intermediate inlet vacuum pressures the dynamic valve timing still preforms significantly better than the case 1 (fixed valve timing).

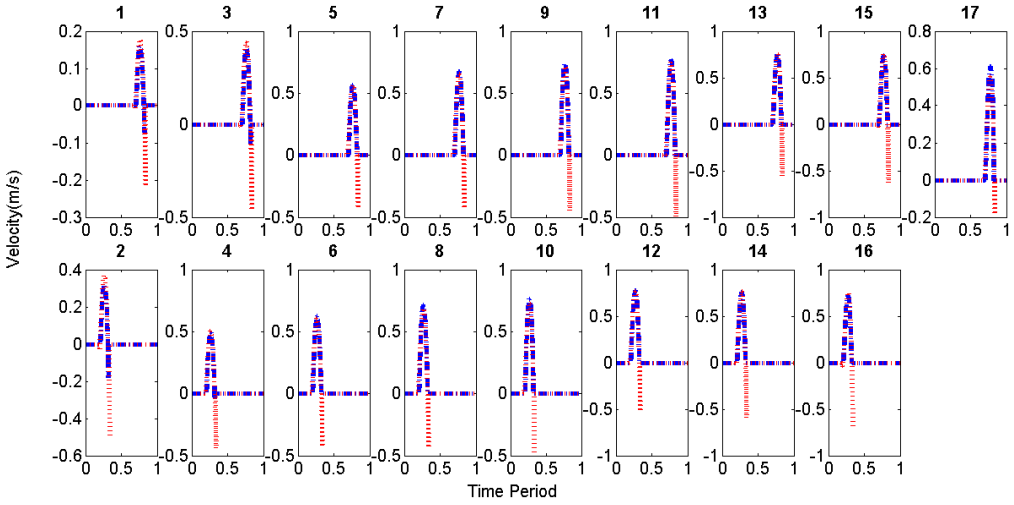

Figure 2.18: Velocity profiles through each valve when inlet pressure is 450 Torr and the operating frequency is 50 kHz. -- and : represent the case 1 fixed valve timings and dynamic valve timings respectively. Even and odd numbered figures represent flow through the transfer and inlet/exit valves respectively.

Figure 2.18 is a snapshot of the velocity distribution through each valve when the inlet pressure is 250 Torr. The second fixed valve timing is not included in the above figure as the target vacuum is not achieved. Reverse flow is observed for dynamic valve timing through each valve. When operated using DVT, the target vacuum is achieved despite reduction in the pump's performance. The linear relationship between the pressure difference and valve timing produces a significant improvement in the performance of the pump. Hence, better mathematical correlations are not required.

Figure 2.19 compares the DVT operation of the pump at frequencies 10, 20 and 50 kHz. Initially, the maximum pressure performance is achieved when operated at 50 kHz as shown in Figure 2.19a. When the inlet pressure approaches the target vacuum, the maximum performance occurs at 20 kHz, as shown in Figure 2.19b. The target vacuum is first achieved when the pump is operated at 20 kHz as shown in Figure 2.19c. Though a

frequency shift in performance occurs, the time difference in obtaining the vacuum is negligible.

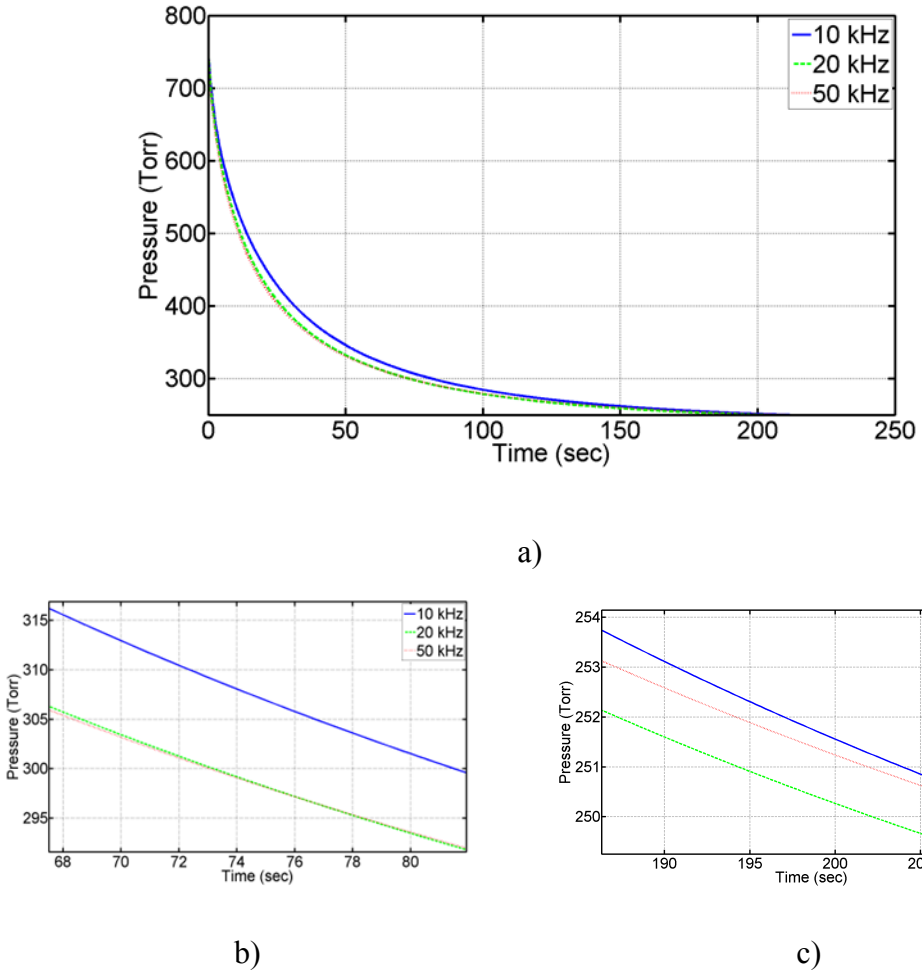

Figure 2.19: Comparison of dynamic valve timing for different operating frequencies. The blue, green and red lines are for operating frequencies of 10, 20 and 50 kHz respectively. Figure b and c are enlarged sections of figure a.

Transient Analysis of Multistage Designs

In the first section, the thermodynamic model predicted that three different designs that could be used to achieve the target vacuum. The three designs were equal volume ratio, equal pressure and modular design. The volume ratio for each design is illustrated in Figure 2.1. The equal volume ratio design has the same compression ratio across each stage. Equal pressure design has a volume ratio designed to produce equal pressure difference across each stage. The modular design is a combination of the equal volume ratio and equal pressure design. In this section transient analysis is carried out on all three designs to study the pressure difference across the membrane at a given instant. The goal in this section is to identify the design that is easy to fabricate and has an equal pressure rise across stages.

Transient analysis is similar to the procedure outlined in the previous section. In this section, a valve timing having t_{op}/T =0.04 and t_{cl}/T = 0.07 and a frequency of operation equal to 50 kHz are used to analyze the behavior of a 16-stage vacuum micropump which evacuates the given volume.

The transient performance of the equal pressure design is analyzed in Figure 2.20. The pump starts evacuating gas from the volume. When the pressure in this volume reaches 650, 450 and 250 Torr, a snapshot of the pressure distribution in each stage for the given cycle is recorded. From the data, the mean, maximum and minimum pressure in each stage is computed. In Figure 2.20, at 650 Torr, the first few stages have significantly

higher pressure rise in comparison to those closer to the outlet. The mean pressure rise from one stage to another is nonlinear, increasing in those nearer to the inlet and decreasing as the outlet is approached. The difference between the maximum pressure and the mean pressure is < 35 Torr in stages 1-6, < 20 Torr in stages 7-12 and <10 Torr in stages 13-16. A pressure buildup in the middle stages is observed.

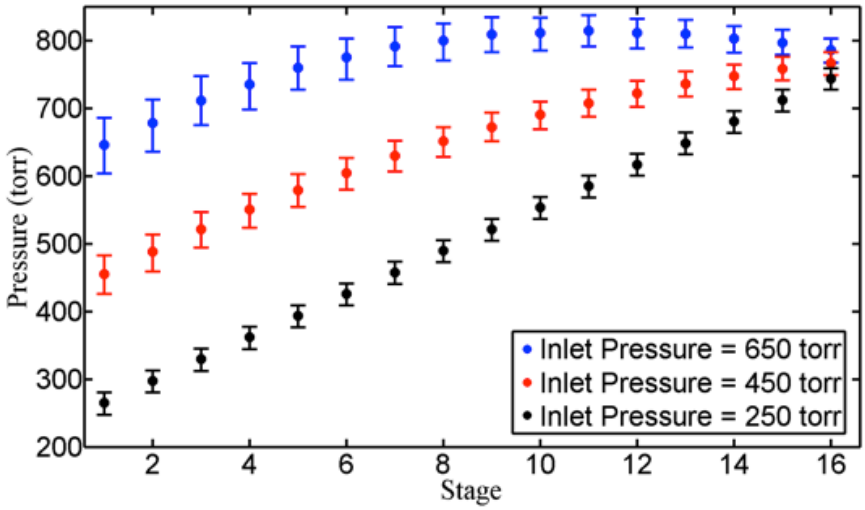

Figure 2.20: Pressure distribution in each stage at inlet pressures of 650,450 and 250 Torr using the equal pressure design. The error bars depict the maximum, minimum and mean pressure in the given cycle

At 450 Torr, the difference between maximum pressure and the mean pressure across each stage is nearly equal (<15 Torr). The pressure build up in the middle stages has disappeared. A mean pressure rise from one stage to another now approaches a linear increase. At an inlet pressure of 250 Torr, the pressure rise across each stage is the same. The difference between the maximum and mean pressure is <10 Torr. The initial deviation from linear pressure rise across each stage is unexpected and can be attributed to the fixed valve timing. DVT can prevent the pressure build up in the middle stages and excessive pumping in the initial stages. Figure 2.21 shows the pressure difference across

the membrane. The small fixed valve timing produces a large pressure difference across the membrane, which may not be realistic for electrostatically actuated membranes. At 650 Torr, the maximum pressure difference across the first few membranes is >100 Torr. This begins to decrease as the inlet pressure decreases. At steady state, the maximum pressure difference is ~70 Torr and equal across each membrane.

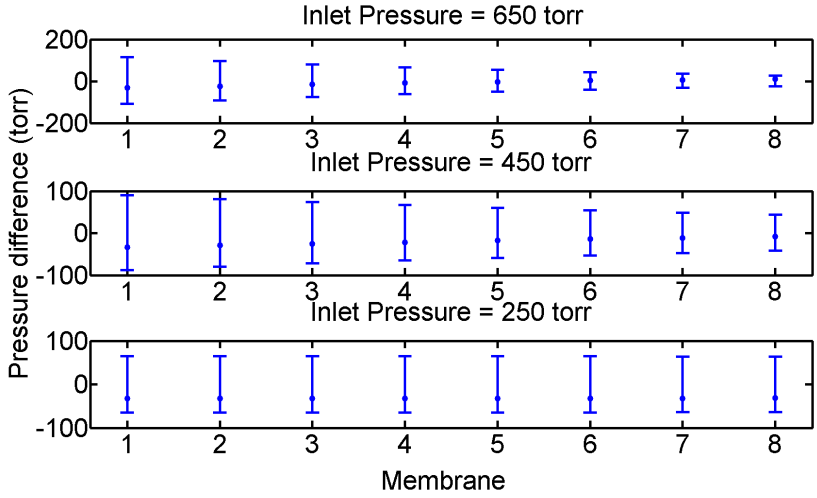

Figure 2.21: Pressure difference across each membrane at different inlet pressures. Analysis was performed on equal pressure design. The error bars represent the minimum, maximum and average pressure difference across each membrane.

Designing a micropump with the same volume ratio across each stage simplifies fabrication. The thermodynamic model developed by Astle et al. (2002) states that a multistage micropump having volume ratio < 0.98 will result in unequal pumping. Stages close to the outlet are expected to do most of the pumping compared to the rest of the stages. In Figure 2.22 the pressure distribution in each stage of this design for inlet pressures 650, 450 and 250 Torr is shown. When the inlet pressure is 650 Torr, the mean pressure rise in each stage follows a linear trend. The difference between the maximum and mean pressure in each stage is maximum in the last few stages suggests that the last few stages are over performing. The decrease in inlet pressure destroys the linear trend in

the pressure rise across each stage. It is evident that at 450 Torr that the mean pressure rise in stages 12-16 is significantly higher than that in 1-11. The difference between the maximum and mean pressure rise in stages 12-16 is significantly higher than in other stages. At 250 Torr, Figure 2.22 suggests that the evacuation from the chamber is essentially produced in the last few stages. The difference between the maximum and mean pressure in the initial stages is <10 Torr, while increasing to levels <50 Torr in the latter stages. The pressure difference across the membranes in the final stages is abnormally high, which may not be realistic for electrostatic actuation. Figure 2.23 suggests that the membranes in the final stages initially experience a maximum pressure difference of ~50 Torr. A reduction in the inlet pressures increases this maximum pressure difference to ~120 Torr.

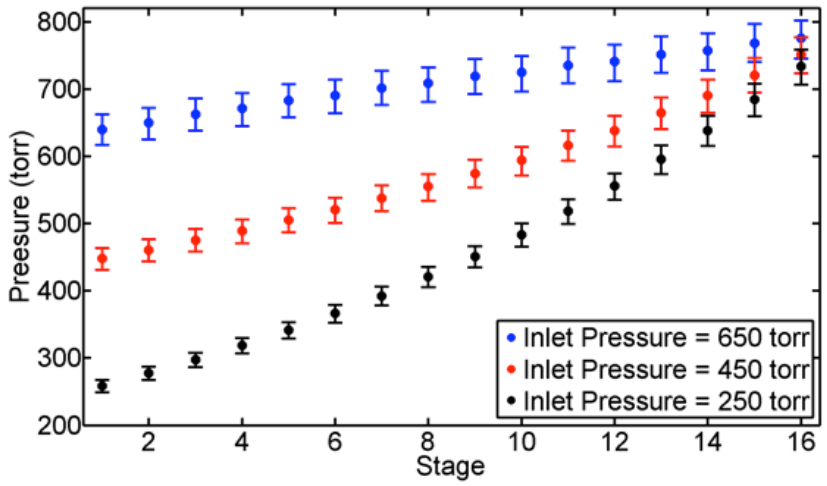

Figure 2.22: Pressure distribution in each stage at inlet pressures of 650,450 and 250 Torr using the equal volume ratio design. The error bars depict the maximum, minimum and mean pressure in the given cycle

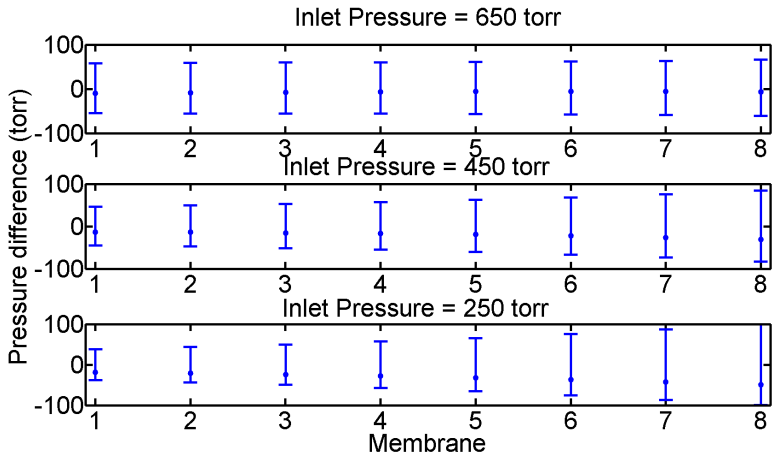

Figure 2.23: Pressure difference across each membrane at different inlet pressures. Analysis was performed on equal volume ratio design. The error bars represent the minimum, maximum and average pressure difference across each membrane.

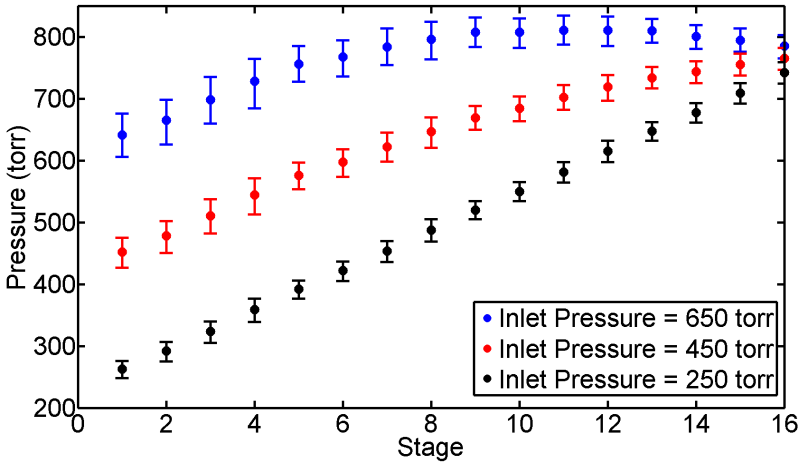

Figure 2.24: Pressure distribution in each stage at inlet pressures of 650,450 and 250 Torr, using the modular design. The error bars depict the maximum, minimum and mean pressure in the given cycle.

The modular design exhibits the advantages of both the equal pressure and equal volume designs. The 16-stages are divided into 4 groups, each group having 4 stages and equal volume ratio. The volume ratio is chosen to produce equal pressure difference across each module. The transient behavior of the pump is similar to the equal pressure

design. Initially, the stages closer to the inlet are producing a higher pressure rise than the stages closer to the outlet. A pressure buildup is observed in the middle stages. With the decrease in inlet pressure, the pressure buildup disappears and the stages now start performing equally. At steady state, all the stages exhibit nearly the same performance. Figure 2.25 suggests that the pressure difference across the membranes is numerically equal to the equal pressure design. Since the volume ratio across each module is <0.98, a small increase in pressure difference is obtained. This analysis suggests that the modular design is the most effective design in terms of fabrication and pressure difference across the pump stages.

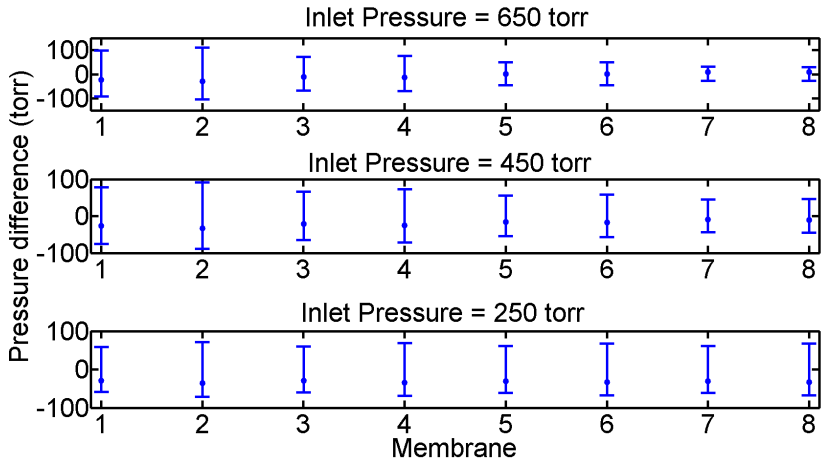

Figure 2.25: Pressure difference across each membrane at different inlet pressures. Analysis was performed on the modular design. The error bars represent the minimum, maximum and average pressure difference across each membrane.

Non Ideal Valves

Analyses in the previous sections are based on operation of the pump using ideal valves, which assume no flow through the valves when they are closed. While the assumption is justified for the analysis performed, models need to be developed to study the operation of the pump more realistically. The goal in this section is to study the impact of leakage on the performance of the micropump.

In the first section, the system of equations 2.6 and 2.11 capture the ideal operation of the valves. The H function governs the opening and closing of the valves. When valves are opened, H = 1, and when closed, H = 0. Equations 2.6 and 2.11are modified by dropping the H term as shown in the systems of equations 2.13 and 2.14.

$$\begin{cases} \frac{du_{e1}}{dt} = \frac{1}{L_E}\frac{(P_{inlet}-P_1)}{\rho_{amb}} - 8\frac{\mu}{\rho_{amb}}\frac{u_{e1}}{h_g^2}\frac{L_V}{L_E} & \textbf{Inlet Valve} \\ \frac{du_{ej}}{dt} = \frac{1}{L_E}\frac{(P_{j-1}-P_j)}{\rho_j} - 8\frac{\mu}{\rho_j}\frac{u_{ej}}{h_g^2}\frac{L_V}{L_E} & \textbf{Interior Valve} \\ \frac{du_{eM+1}}{dt} = \frac{1}{L_E}\frac{(P_M-P_{outlet})}{\rho_M} - 8\frac{\mu}{\rho_M}\frac{u_{eM}}{h_g^2}\frac{L_V}{L_E} & \textbf{Exit Valve} \end{cases} \quad \textbf{2.13}$$

Where j = 2,3,…M.

$$\begin{cases} \frac{dP_1}{dt} = -\rho_1\alpha^2\frac{n}{\gamma}\frac{u_{e2}A_E}{V_1} + \rho_{inlet}\alpha^2\frac{n}{\gamma}\frac{u_{e1}A_E}{V_1} - \rho_1\alpha^2\frac{n}{\gamma}\frac{1}{V_1}\frac{dV_1}{dt} \\ \frac{dP_j}{dt} = -\rho_{j+1}\alpha^2\frac{n}{\gamma}\frac{u_{ej+1}A_E}{V_j} + \rho_j\alpha^2\frac{n}{\gamma}\frac{u_{ej}A_E}{V_j} - \rho_j\alpha^2\frac{n}{\gamma}\frac{1}{V_j}\frac{dV_j}{dt} \\ \frac{dP_k}{dt} = -\rho_{k+1}\alpha^2\frac{n}{\gamma}\frac{u_{ek+1}A_E}{V_k} + \rho_{k+1}\alpha^2\frac{n}{\gamma}\frac{u_{ek+1}A_E}{V_k} - \rho_k\alpha^2\frac{n}{\gamma}\frac{1}{V_k}\frac{dV_k}{dt} \end{cases} \quad \textbf{2.14}$$

Where j =3, 5, 7, …M-1 and k= 2, 4, 8…M.

The system of equations 2.11, 2.12, 2.13 and 2.14 are solved using MATLAB's ode45 solver in the same manner as has been done in the previous analyses. Adjusting the viscous length accordingly captures the valve open and close states. In the open state, L_V is set to 30μm. In the closed state, L_V in the open state is multiplied by a factor referred to as the sealing factor ($L_{Vclosed}$=L_{Vopen}x Sealing factor). To estimate this sealing factor, the flow rate is measured by applying a steady pressure difference across the pump in the open and closed states of the valves. In these states, we assume that the flow is steady and the same in all the valves. Equations 2.13 and 2.14 reduce to equation 2.15, where N is the number of valves and V_{flow} is the flow rate through each valve in sccm.

$$\Delta \boldsymbol{P} = \frac{\boldsymbol{8\mu N L_V V_{flow}}}{\boldsymbol{60X10^6 A_E h_g^2}} \qquad \textbf{2.15}$$

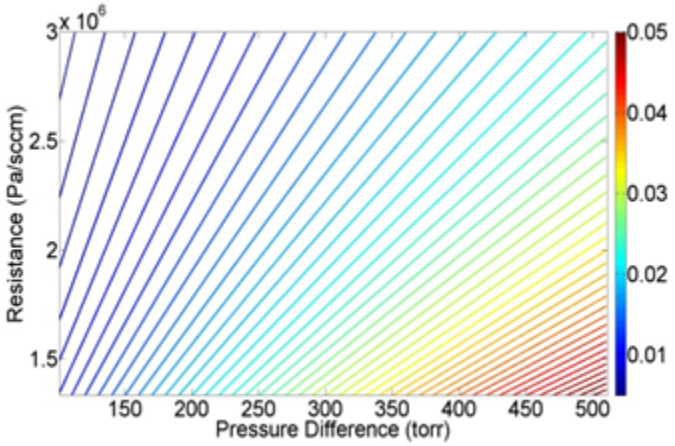

Figure 2.26: Contours of backflow for a specified resistance and pressure difference across the pump.

Steady state analysis at 250 Torr predicts a 16–stage micropump having parameters listed in Table 2.1 would produce a flow rate of 0.05 sccm, which was estimated using optimized valve timing. Thus, the valves should produce sealing such that the maximum backflow is 0.05 sccm at the target vacuum. Equation 2.15 is used to

estimate the sealing factor required to achieve the target vacuum. Figure 2.26 shows contours of the estimated backflow rate for a given resistance and pressure difference across the pump. The minimum allowable sealing factor required for these conditions outlined is ~880 or a resistance of $2x10^6$ Pa/sccm in the closed state.

The impact of sealing on flow rate justifies the need to study the pressure performance of the pump. Three sealing factors are considered, 10, 100 and 880. Sealing factors of 10 and 100 are chosen to determine the impact of low sealing on the performance of the pump. The pump is operated at 50 kHz to evacuate a volume of 1 cm^3 using a valve timing of t_{op}=0.04 and t_{cl}=0.07.

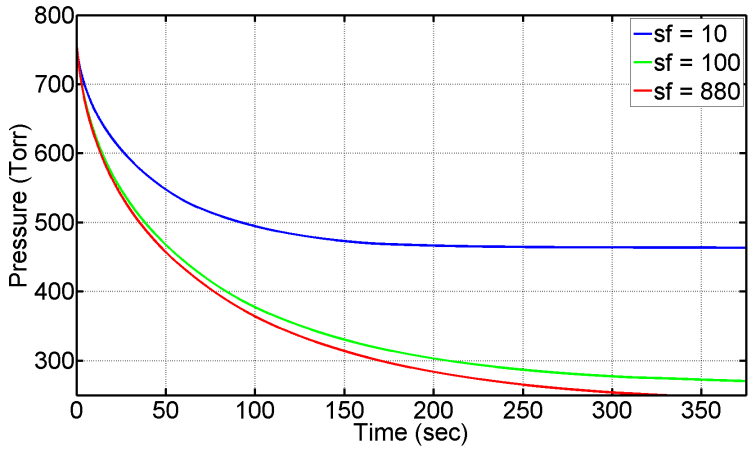

Figure 2.27: Transient performance of the pump using non-ideal valves. The blue, green and red lines represent the sealing factors 10, 100 and 880 respectively.

Figure 2.27 shows the comparison of pressure performance results for the three sealing factors. A sealing factor of 10 is able to evacuate the volume down to a pressure of ~ 450 Torr only; while a sealing factor of 100 brings the pressure down to 264 Torr. As expected, the sealing factor of 880 generates the desired vacuum. The sealing factors

between 100 and 880 produce a significant change in the minimum pressure that can be achieved due to extremely small flow rate at these pressures.

Figure 2.28 compares the behavior of ideal and non-ideal valves. The non-ideal valves are operated with a sealing factor of 880. There is no change in the pressure performance due to the leakage through the valves, which suggests ideal behavior.

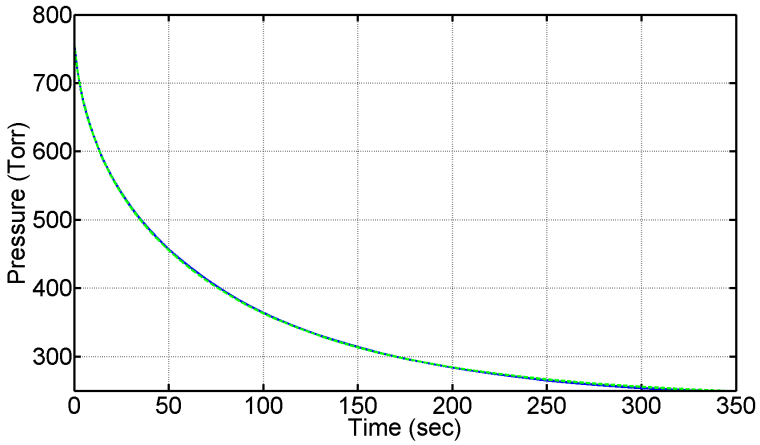

Figure 2.28: Comparison of ideal and non-ideal valves for pressure performance. The green and blue lines represent the performance for ideal and non-ideal behavior respectively.

To study the impact of leakage through the valves, a snapshot of the velocity through each valve for different sealing factors was taken, as shown in Figure 2.29. A significantly large leakage through the valves is observed in the closed state when a sealing factor of 10 is used. Using a sealing factor of 100, very small flow reversal through the closed valves is observed. However, as the inlet pressure decreases, the flow reversal through each of the valves increases in the closed state. A sealing factor of 880 produces an ideal behavior and no flow reversal is observed even as the inlet pressure decreases.

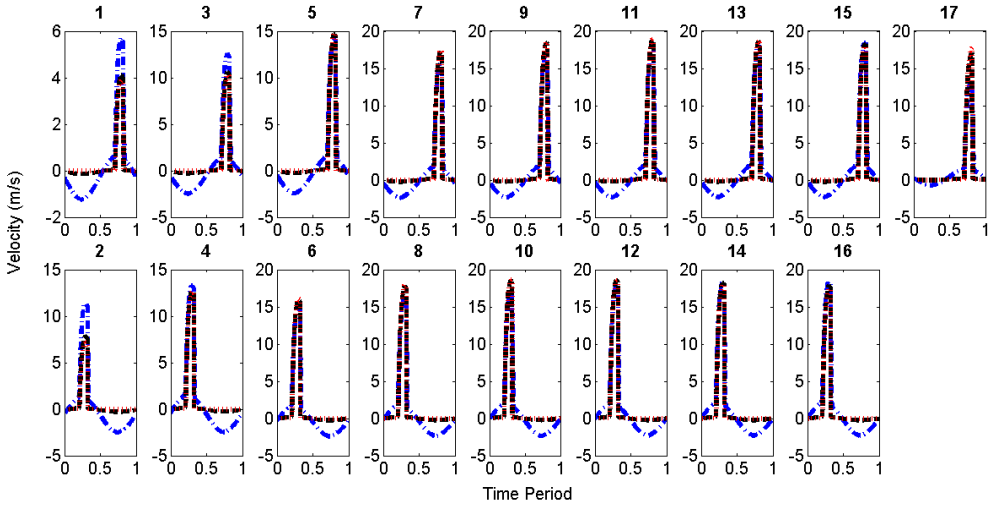

Figure 2.29: Performance comparison of different sealing factors when the pump is operated at 50 kHz using the snapshot of the velocity through each valve. Odd and even numbered figures represent the inlet/exit and transfer valves respectively. -.-, -- and : represent sealing factors of 10, 100 and 880 respectively.

Effect of Resistance and Volume Ratio

Analyses carried out in this chapter show that the governing factors for achieving a desired vacuum are volume ratio, operating frequency, valve timing and leakage. In-depth analyses have been carried out to study the effect of frequency and valve timing. The detrimental effects of inappropriate valve timings have been studied. In this section the goal is to the study the effect of volume ratio and resistance on the performance of the pump.

The first step in designing a micropump is defining the appropriate volume ratio to achieve the target vacuum. The system of equations 2.11, 2.12, 2.13 and 2.14 are used to solve the effect of volume ratio and valve resistance. The volume ratio is varied from 0.70 to 0.98 and the valve close sealing factor is varied from 10 to 1000. Each 16-stage micropump is operated at 50 kHz with a valve timing of t_{op}=0.04 and t_{cl}=0.07 and evacuates a volume equal to the number of stages times the cavity volume for each stage. The optimum frequencies and valve timings have not been evaluated.

In Figure 2.30, the contour lines represent the steady state inlet pressure produced by the micropump. The L_v in the open state is 30μm. Along a contour line, a system with a lower volume ratio and lower sealing produces the same performance as a system with a higher volume ratio and higher sealing. For a sealing factor greater than 100, the performance of the pump improves only slightly for a higher sealings. Thus, a system having a higher volume ratio will require a sealing factor of at least 100 to approach the

desired target vacuum. This shows that the main governing factor influencing the pressure performance is the volume ratio.

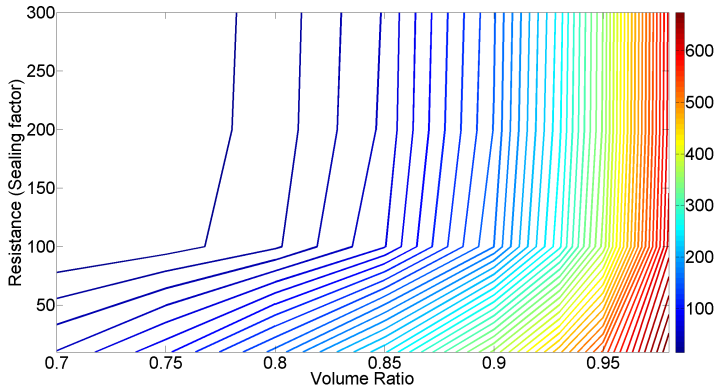

Figure 2.30: Effect of Volume ratio and Resistance on the performance of the micropump. The contours depict the steady state inlet pressure in Torr.

The analyses in this and the previous sections have used L_v in the open state to be 30μm. If a blockage occurs in the system, the resistance in the open state would increase, in turn affecting the flow rate. To increase the open state resistance, L_v is 300μm as shown in In Figure 2.31. The contour lines represent the steady state inlet pressure obtained by the micropump. The behavior is similar to that shown in Figure 2.30. Figure 2.31 indicates that the steady state pressure obtained by the micropump with the higher resistance is marginally higher than one with lower open resistance.

Figure 2.31 does not show in detail the effect of open state resistance on the pressure performance. Figure 2.32 analyzes the performance of a 16-stage micropump having a volume ratio of 0.7. When the sealing factor is 10, the pump having an open state resistance of 30μm reaches steady state in less than 1500 time steps while the open state resistance of 300μm causes the pump to achieve steady state in 4500 time steps. The pressure attained by the two cases is nearly the same. Thus if the open state resistance

increases by a factor of 10, the performance of the pump should not be significantly hampered. Similar behavior is observed when the sealing factor is increased by a factor of 100. Thus the controlling parameters that influence the performance of the pump are volume ratio and sealing factor.

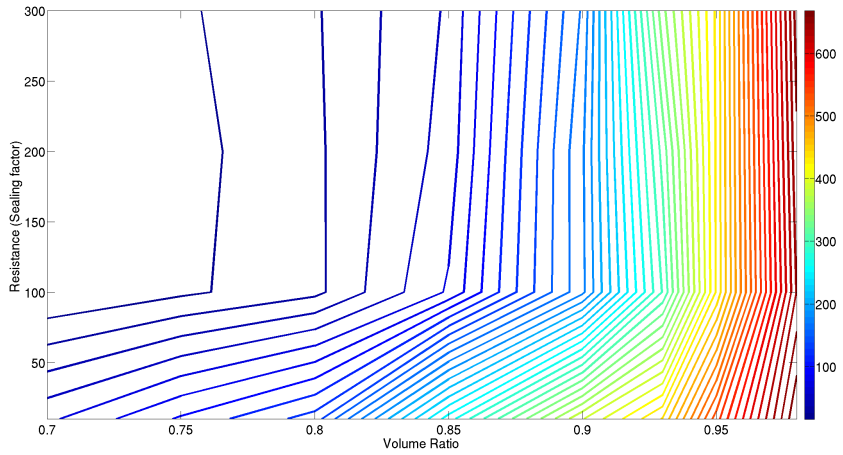

Figure 2.31: Effect of Volume ratio and Resistance on the performance of the micropump. The contours depict the steady state inlet pressure in Torr. L_v in the open state is 300μm.

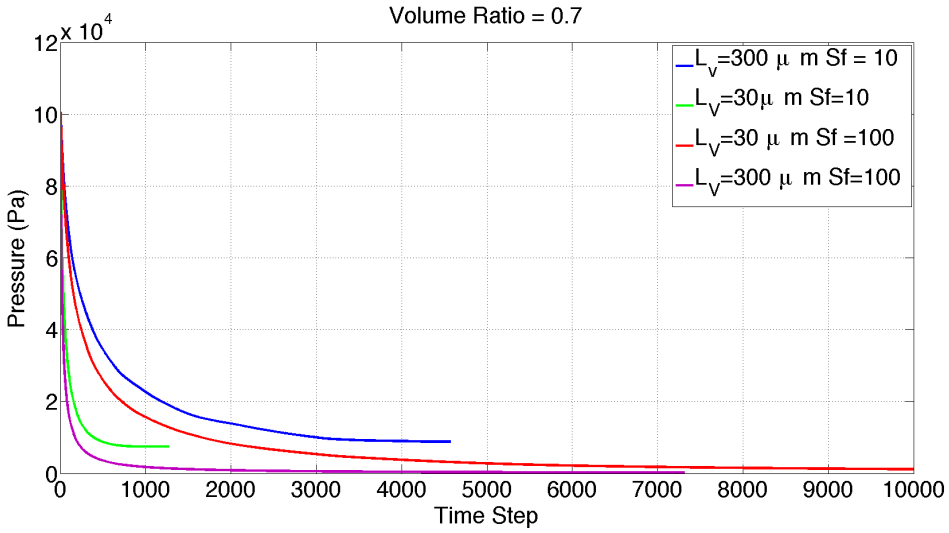

Figure 2.32: Transient inlet pressure performance for a 16 stage having a volume ratio of 0.7. Comparison is made for different sealing factors and open state resistance.

Chapter 3

Multiphysics Modeling

Improvements to Reduced Order Modeling

In the previous chapter, the reduced order model developed by Astle et al. (2003) is extended for multistage analyses of micropumps. This provided an in-depth understanding of volume ratio, valve timing, frequency of operation and leakage. Figure 3.1 illustrates the arrangement of a dual stage micropump, where the membrane deflection opposite to the electrode (dotted line) is not constrained. It depends on the structural resonance, acoustic and the electrostatic pressure acting on it. The membrane deflection from the initial position in the direction opposite to the electrode can be greater, lesser, or equal to the gap. In this chapter, the reduced order model is improved to study the coupled effect of membrane deflection, acoustics and electrostatic effects.

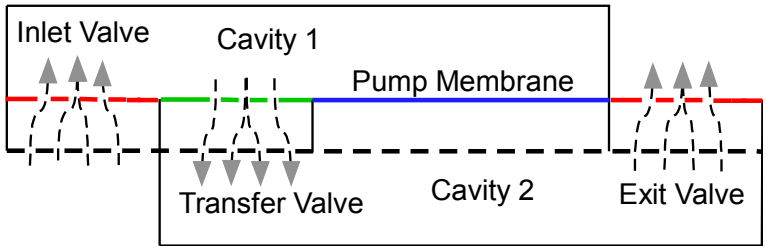

Figure 3.1: Single electrode arrangement for a dual stage micropump. Arrows show the flow direction while the red green and blue lines represent the inlet/outlet, transfer valves and pump membranes respectively.

Structural & Electrostatic Model

As discussed earlier, a hexagonal membrane is used to drive the gas as well as transfer air from one stage to another. The modularity of the hexagonal membrane allows for a compact design. Mathematically modeling a hexagonal membrane is challenging and complex. To simplify this, a square membrane, having the same surface area is modeled. This assumption, though radical, serves as a good first order model to predict the performance of the pump.

A square membrane is assumed to have a sinusoidal deformation with maximum displacement at the center. The simplest model for the diaphragm is a second order dynamical system characterized by resonant frequency and apparent mass. At any given instant, the position of a point on the diaphragm is given by equation 3.1, which depends on the central point of the membrane. h_D(t) is the distance between the center of the membrane and the electrode at any given instant.

$$\boldsymbol{\eta(x,y,t) = h_D(t) sin\left(\frac{\pi x}{L_D}\right) sin\left(\frac{\pi y}{L_D}\right)} \quad 0 < x < \mathbf{L_D},\ 0 < y < \mathbf{L_D} \qquad \mathbf{3.1}$$

The inertia of the diaphragm is found by integrating equation 3.1 over the area of the membrane. The acceleration of the membrane at any given instant is given by the double differential of equation 3.1 with respect to time.

$$\iint \boldsymbol{\rho_D t_D \frac{\partial^2 \eta}{\partial t^2} dxdy = \rho_D t_D \frac{d^2 h}{dt^2} \iint_0^{L_D} \sin\left(\frac{\pi x}{L_D}\right) \sin\left(\frac{\pi y}{L_D}\right) dxdy = \rho_D t_D \frac{4A_D}{\pi^2} \frac{d^2 h}{dt^2}} \qquad \mathbf{3.2}$$

Compliance of the diaphragm can be due to the bending (plate behavior) or tension. For very thin membranes, when the thickness of the diaphragm is smaller than the length, tension influences the deflection. This tension force acting on the diaphragm depends on the inclination made with the edge. The integral along the perimeter is the tension force acting on the membrane at a given instant. Since, $h_d/L_D << 1$, the force due to tension is shown in equation 3.3.

$$\int \tau sin\Theta dl = 4 \int_0^{L_D} \tau \frac{\partial \eta}{\partial x}|_{x=0} = 8\tau h_D \quad \textbf{3.3}$$

The acoustic pressure and electrostatic pressure govern the motion of the membrane. The pressure from the top stage in Figure 3.1 pushes the membrane down, while that from the bottom stage pushes the membrane upwards. The electrostatic pressure always pulls the membrane towards the electrode. Hence, the displacement of the center of the membrane at any given instant is given by equation 3.4.

$$\rho_D t_D \frac{4A_D}{\pi^2} \frac{d^2h}{dt^2} = -8\tau h_D - P_1 A_D + P_2 A_D - P_e A_D \quad \textbf{3.4}$$

To incorporate the resonant term, equation 3.4 is rearranged to equation 3.5 and the residual stress in the membrane is accounted for. The resonant frequency of the membrane is governed by the stress and area of the membrane.

$$\rho_D t_D \frac{4A_D}{\pi^2} \left(\frac{d^2h}{dt^2} + \omega^2{}_D h_D\right) = -P_1 A_D + P_2 A_D - P_e A_D \quad \textbf{3.5}$$

$$\omega_D = \pi \sqrt{\frac{2\tau}{\rho_D t_D A_D}} = \pi \sqrt{\frac{2\sigma}{\rho_D A_D}} \quad \textbf{3.6}$$

where $\sigma = \frac{\tau}{t_D}$ is the stress in the diaphragm.

In the previous chapter, the acoustic equations were driven by the sinusoidal volume change. The motion of the diaphragm is now coupled to the acoustic equations as

shown in equation 3.4. The volumetric change due to the membrane deflection is the integral of the membrane motion, as shown in equation 3.7.

$$\mathbf{V_D(t)} = \int_0^{L_D}\int_0^{L_D} \boldsymbol{\eta}(\mathbf{x,y,t})\mathbf{dxdy} = \frac{4}{\pi^2}\mathbf{A_D h_D(t)} \quad \textbf{3.7}$$

The volume change in stages 1 and 2 are shown in equation 3.8 and 3.9 respectively.

$$\mathbf{V(t)} = \mathbf{V_C} - \mathbf{V_D(t)} = \mathbf{V_C} - \frac{4}{\pi^2}\mathbf{A_D h_D(t)} \quad \textbf{3.8}$$

$$\mathbf{V(t)} = \mathbf{V_C} + \mathbf{2}V_v + V_M + \mathbf{V_D(t)} = \mathbf{V_C} + \mathbf{2}V_v + V_M + \frac{4}{\pi^2}\mathbf{A_D h_D(t)} \quad \textbf{3.9}$$

In equation 3.5, the electrostatic force is estimated using Coulomb's law, shown in equation 3.10.

$$p_e A_D = \frac{1}{4\pi\varepsilon_o}\iint \frac{q(\xi,\zeta),q(x,y)}{\vec{r^2}}\cos(\alpha)dxdyd\xi d\zeta \quad \textbf{3.10}$$

where x, y define the position of a charge on the diaphragm; ξ, ζ define the position of a charge in the electrode; q(x, y) and q(ξ, ζ) give the distribution of electrical charge per unit area on the diaphragm and electrode, respectively; $\vec{r}$ is the vector joining points x, y and ξ, ζ; and α is the angle formed by $\vec{r}$ and the normal to the electrode at point x, y. The first integral is over the electrode, while the second is over the diaphragm.

The electrical charge, shown in equation 3.11, at a point on the diaphragm or electrode is determined by the local electric field strength, Φ, and ε_o, the permittivity of air ($\varepsilon_o = 8.45\times10^{-12}$ in SI units).

$$q(x,y) = \varepsilon_o \Phi(x,\ y) \quad \textbf{3.11}$$

Using the standard method to calculate the distance for a given vector, $\vec{r}$, the distance between the electrode and membrane is shown in equation 3.12.

$$\overrightarrow{r^2} = (x-\xi)^2 + (y-\zeta)^2 + (h_o-\eta)^2 \quad \textbf{3.12}$$

The angle, α, is estimated using the standard trigonometric operations shown in equation 3.13.

$$\cos(\alpha) = \frac{h_o + \eta(x,y,t)}{\sqrt{\left(x-\xi\right)^2 + \left(y-\zeta\right)^2 + \left(h_o + \eta(x,y,t)\right)^2}} \quad \textbf{3.13}$$

Substituting equations 3.11, 3.12 and 3.13 in 3.10, the electrostatic force acting on the membrane is shown in equation 3.14.

$$p_e A_D = \frac{\varepsilon_o}{4\pi}\int_0^{L_D}dx\int_0^{L_D}dy\int_0^{L_D}d\xi\int_0^{L_D}d\zeta\left[\Phi(x,y)\Phi(\xi,\zeta)\right.$$
$$\left.\times\frac{h_o+\eta(x,y,t)}{\left(\left(x-\xi\right)^2+\left(y-\zeta\right)^2+\left(h_o+\eta(x,y,t)\right)^2\right)^{3/2}}\right] \quad \textbf{3.14}$$

Equation 3.14 is rearranged to allow further simplification as shown in equation 3.15 and equation 3.16. The prime variables in these equations can be non-dimensionalized with the length of the membrane as shown in equation 3.17.

$$p_e A_D = \frac{\varepsilon_o A_D}{2} F\left(\frac{h_o}{L_D}, \frac{h_D}{h_o}\right) \quad \textbf{3.15}$$

$$F = \frac{1}{2\pi}\int_0^1\int_0^1\int_0^1\int_0^1 \frac{\Phi\left(x',y'\right)\Phi\left(\xi',\zeta'\right)\frac{h_o}{L_D}\left(1+\frac{h_D}{h_o}\sin(\pi x')\sin(\pi y')\right)d\xi' d\zeta' dx' dy'}{\left(\left(x'-\xi'\right)^2+\left(y'-\zeta'\right)^2+\left(\frac{h_o}{L_D}\right)^2\left(1+\frac{h_D}{h_o}\sin(\pi x')\sin(\pi y')\right)^2\right)^{3/2}} \quad \textbf{3.16}$$

$$x' = \frac{x}{L_D},\ y' = \frac{y}{L_D},\ \xi' = \frac{\xi}{L_D},\ \zeta' = \frac{\zeta}{L_D} \quad \textbf{3.17}$$

Since the gap between the electrode and the membrane is smaller than the length of the membrane, the integral is evaluated as shown in equation 3.18.

$$F\left(0,\frac{h_D}{h_o}\right)=\int_0^1\int_0^1 \Phi^2(x',y')\,dx'\,dy' \qquad \textbf{3.18}$$

Assuming straight field lines, the electric field is the ratio of the potential difference and the distance between the membrane and electrode at any given instant. The electrostatic pressure force acting on the diaphragm is simplified to equations 3.20 and 3.21.

$$\Phi=\frac{E}{h_o+\eta} \qquad \textbf{3.19}$$

$$p_e=\frac{\varepsilon_o}{2}\left(\frac{E}{h_o}\right)^2 f\left(\frac{h_D}{h_o}\right) \qquad \textbf{3.20}$$

$$f\left(\frac{h_D}{h_o}\right)=\int_0^1\int_0^1 \frac{dx\,dy}{\left(1+\frac{h_D}{h_o}\sin(\pi x)\ \sin(\pi y)\right)^2} \qquad \textbf{3.21}$$

The integral is numerically evaluated resulting in the analytical equation shown in equation 3.23.

$$f\left(\frac{h_D}{h_o}\right)=\frac{1}{\left(1+\frac{h_D}{h_o}\right)^{0.846}} \qquad \textbf{3.22}$$

The orifices present on the electrode reduce the force acting on the diaphragm. Assuming the characteristic dimension of the metal surface of the electrode to be large compared to the distance between the electrode and membrane, the force acting on the membrane reduces to equation 3.23.

$$p_e A_D=\frac{\varepsilon_o\left(A_D-N_H\,A_H\right)}{2}\left(\frac{E}{h_o}\right)^2 f\left(\frac{h_D}{h_o}\right) \qquad \textbf{3.23}$$

Finite Element Modeling of Static Membrane deflection

The membranes for the valves and pumps are composed of a stack of oxide, nitride, oxide gold and chromium. The oxide-nitride-oxide layer acts as an insulating layer to prevent shorting when the membrane collapses on the electrode. The resonant frequency of a membrane depends on the residual stress as shown in equation 3.6. The residual stress and thickness of each layer used in the membrane is shown in

Table 3.1.

Material	Thickness (μm)	E (GPa) - Elasticity	ρ (kg/m^3) - Density	ν –Poisson's Ratio	σ (MPa) – Residual Stress
SiO_2	0.5	250	2200	0.17	-150
Si_3N_4	0.25	70	3100	0.23	1100
Cr	0.1	279	7150	0.21	450
Au	0.5	70	19300	0.44	-100
Avg	1.85	105	7210.8	0.2532	65

Table 3.1: Thickness, material properties and residual stress of each layer used in the membrane.

$$\beta_{avg} = \frac{\sum_{i=1}^{i=5} \beta_i t_i}{t_D} \qquad 3.24$$

To estimate the resonant frequency of the membrane, the average residual stress is used in equation 3.6. The average residual stress is estimated using equation 3.24, where β is the property under evaluation. The thickness of each layer is used as the weighting factor. The estimated resonant frequency is 33.8 kHz.

Deflection of the membrane is assumed to be linear. While the assumption is valid for small deflections, for large deflections, the displacement will be nonlinear. The model developed, does not account for these effects. These effects are accounted for by estimating the average properties for the elasticity, Poisson's ratio, residual stress and density using equation 3.24 and

Table 3.1. A square membrane having a side length of 2mm, thickness of 1.85μm and average properties listed in

Table 3.1 is solved for resonant frequency and static deformation using COMSOL Multiphysics. To create the mesh, 10 node points along each side are chosen. The mesh was chosen based on a refinement study that produced an error of less than 1kHz for the first mode eigen frequency. The estimated first mode resonance was 35.8 kHz as shown in Figure 3.2, which is close to the theoretically predicted frequency. For all analyses performed in COMSOL, the large deflection model is chosen.

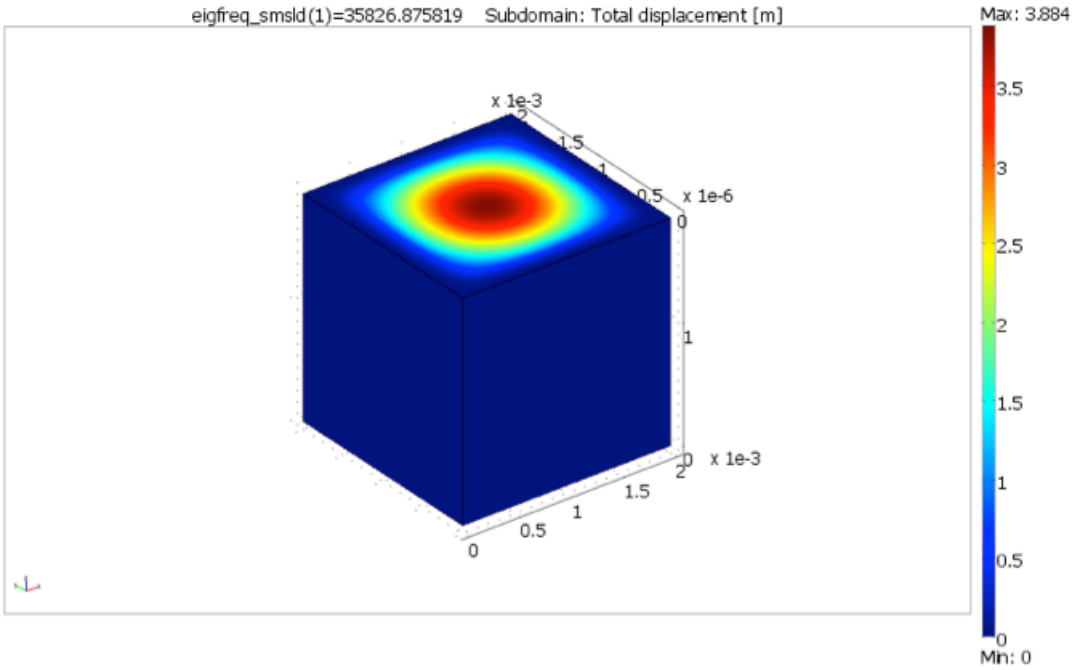

Figure 3.2: Estimated resonant frequency of the square membrane having properties shown in

Table 3.1.

Analysis of large membrane deflection is performed by applying a pressure load on the top surface of the membrane, acting in the negative z direction. When a uniform pressure load of 0.01 Pa is applied, the displacement at the center of the membrane is

estimated to be 2.292×10^{-11} m. Figure 3.3 illustrates the location of maximum displacement, which as predicted occurs in the center of the membrane.

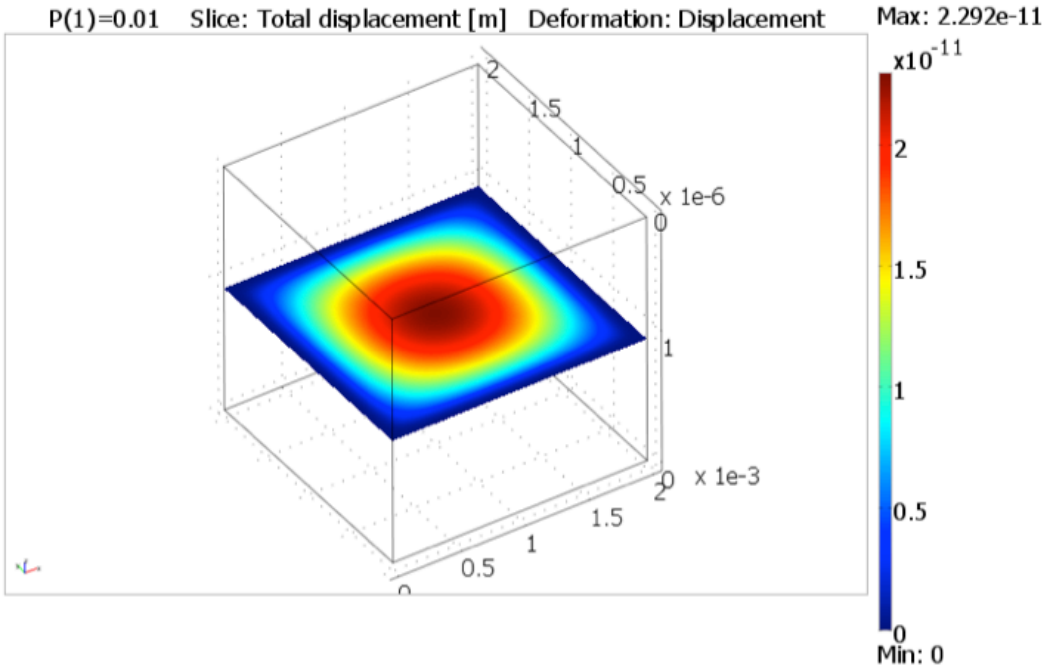

Figure 3.3: Contours of the displacement of the membrane when a uniform load of 0.01 Pa is applied on the top surface. The maximum displacement occurs at the center.

A parametric study is carried out for different pressure loads and the displacement at the center of the membrane is estimated. Pressures larger than the fractural stress of the membrane are applied only to develop a mathematical relation between the force and the estimated displacement. The mathematical relation between the pressure and displacement includes a linear and cubic term. The cubic term accounts for the hardening properties of the membrane. This relation is obtained from a custom code developed in MATLAB. The higher order nonlinear terms are neglected. Figure 3.4 illustrates the relationship between the estimated displacement and the applied uniform pressure load. The linear relation is only valid at pressures below 3 kPa. Since the displacements in the

system can be greater than 5μm, the non-linear relation, shown in equation 3.25 is used for analysis.

$$P = 5.33X10^{17}h_D^3 + 4.34X10^8 h_D \quad \textbf{3.25}$$

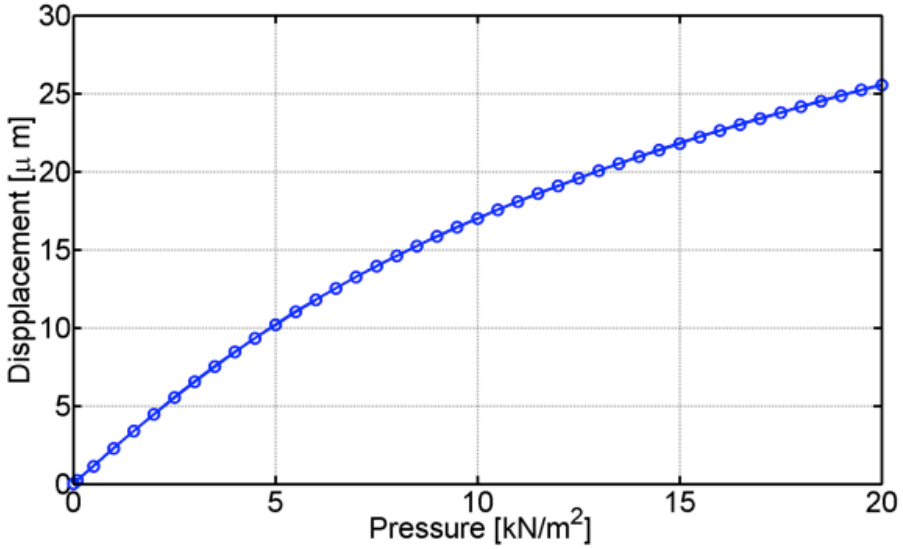

Figure 3.4: Static Displacement vs. Pressure for a diaphragm modeled as single element. The blue dots represent the estimated displacement while the line represents the curve fit obtained from MATLAB.

Dropping the second term to include the effects of hardening as shown in equation 3.26 modifies equation 3.5. This equation includes the inertial effects, spring hardening, acoustic and electrostatic pressures. In subsequent sections, the effect of holes on the valve is analyzed and found to be negligent.

$$\rho_D t_D \frac{4A_D}{\pi^2}\frac{d^2h}{dt^2} = -PA_D - P_1A_D + P_2A_D - P_eA_D \quad \textbf{3.26}$$

Analysis of the Multiphysics Model

Models for acoustic behavior, membrane deformation and electrostatics have been developed in the previous chapter and sections. The first step in analysis is to estimate the pull-in voltage by solving equation 3.5 using MATLAB's ode45 solver. The effects of acoustic pressure and nonlinear displacement are ignored. The system for analysis is shown in Figure 3.5.

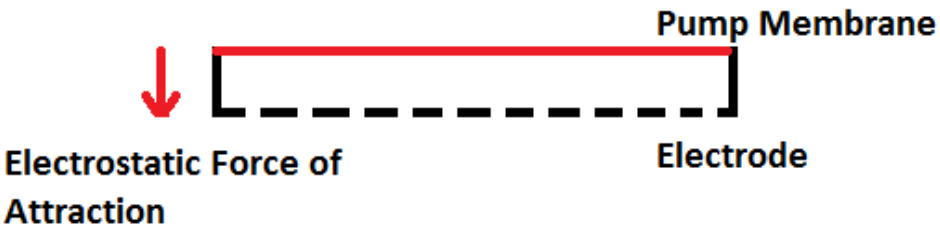

Figure 3.5 Theoretical setup for pull-in voltage estimation.

Pull-in voltage is generally estimated using a constant voltage. However, for the present system, to prevent any inertial effects, the pull-in voltage is estimated using an exponential function as shown in Figure 3.6.

Figure 3.7 shows the pull-in voltage when the membrane gap is 3.5 and 4 μm. The maximum voltage is increased in steps until the membrane collapses on the electrode. For a gap of 3.5 μm, the pull-in voltage is 26V and occurs at a distance 1.89 μm from the initial position. For the 4 μm gap, the pull-in voltage is 31V and the instability point occurs at a distance 2.16 μm from the initial position. To check the validity of these results, analytical relations for the pull-in voltage are developed using standard procedures.

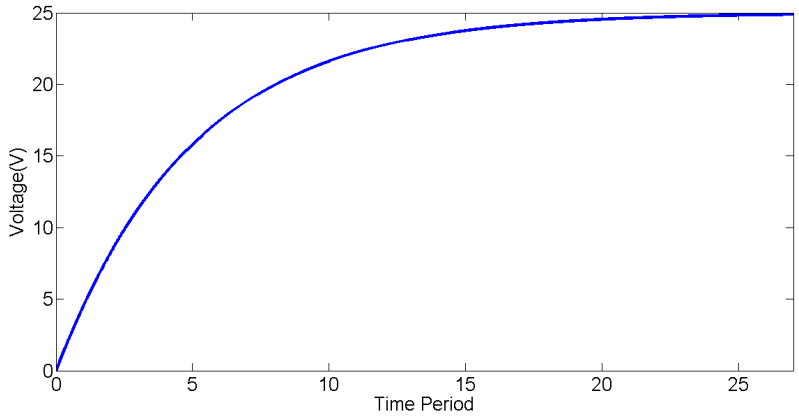

Figure 3.6: Exponential voltage applied to study pull-in voltage, E_0=E (1 - $e^{-t/T}$).

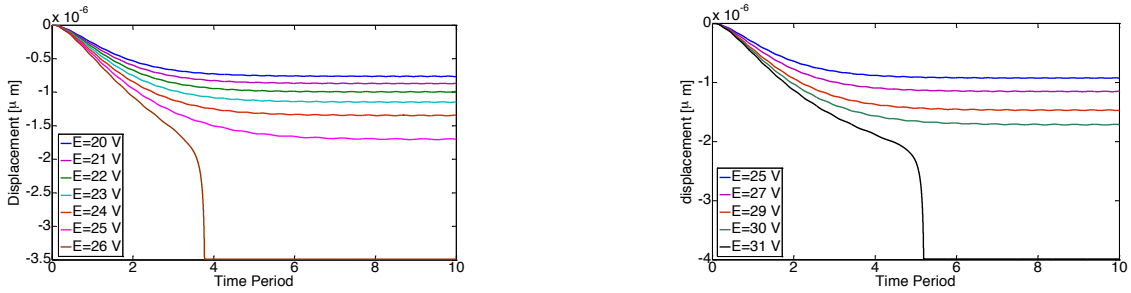

a) b)

Figure 3.7: Estimation of pull-in voltage for different gaps. Figures a and b represent the deflection of the membrane when the gap is 3.5 and 4μm respectively.

$$F = -kh_D - C\frac{1}{\left(1+\frac{h_D}{h_o}\right)^{0.846}} \quad \textbf{3.27}$$

$$\frac{dF}{dh} = -k - C\frac{0.846}{h_0\left(1+\frac{h_D}{h_o}\right)^{1.846}} \quad \textbf{3.28}$$

$$h_{pull-in} = -\frac{h_o}{1.846} \quad \textbf{3.29}$$

Equation 3.5 is rearranged to give equation 3.27 where the constant C represents the geometric and material properties. At the instability point, F=0 and $\frac{dF}{dh}$ = 0. Combining equations 3.27 and 3.28, at the instability point, the estimated pull-in distance is shown in equation 3.29. The analytical relation for the pull-in distance is the equal to that estimated from the system shown in Figure 3.7.

Damped and Non-damped System Response

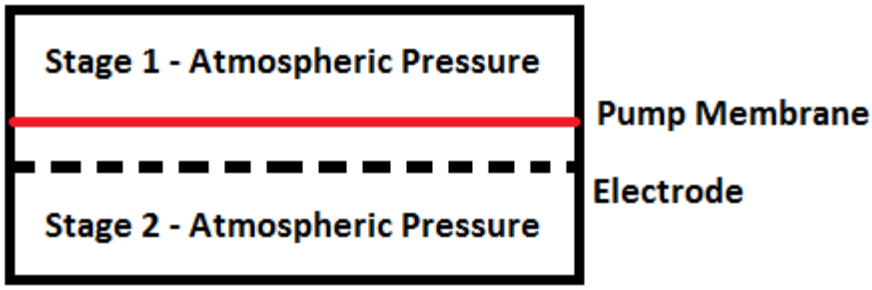

Figure 3.8: Schematic showing the system used to study the effect of forced and damped oscillations.

When the system is non-damped, the membrane will behave as a harmonic oscillator. In a damped system, the amplitude of oscillation of the membrane decreases with time. The system shown in Figure 3.8 contains two stages separated by a pump membrane and electrode. The perforations on the electrode allow compression in the bottom stage. When the ratio of the open area to the closed area is greater than 1/3, the system is considered to be non-damped. Due to an increase in resistance to the flow, viscous losses dominate in such a system.

$$\frac{dh^2}{dt^2} + \nu\frac{dh}{dt} + \omega^2 h = 0 \qquad \textbf{3.30}$$

The 1-D equation 3.30 is used to model the behavior of a spring. Inertia, damping and resonance behavior of the membrane are represented by the first, second and third terms respectively.

Comparing equation 3.5 with 3.30, it is observed that the pressure terms, at any given instant, do not depend on the rate of change of the membrane deflection. Equations 3.31 and 3.32 represent the deflection and pressure change in each stage for a non-damped system.

$$\frac{d^2h_D}{dt^2} = -\omega^2 h_D + \frac{\pi^2}{\rho_D t_D A_d}(-P_e A_D - P_1 A_D + P_2 A_D) \quad \textbf{3.31}$$

$$\frac{dP}{dt} = -\rho\alpha^2 \frac{n}{\gamma}\frac{1}{V}\frac{dV}{dt} \quad \textbf{3.32}$$

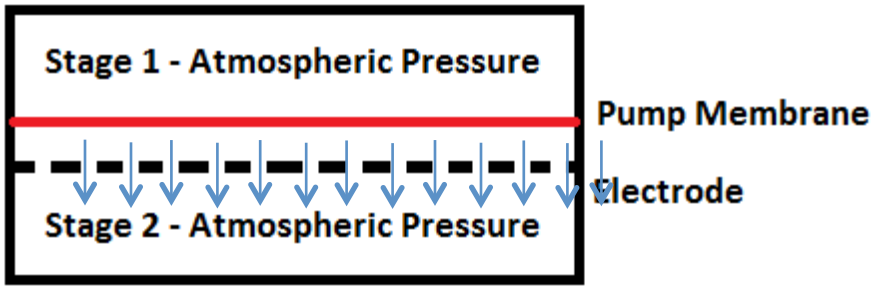

Figure 3.9: Damping effect due to the flow through the holes. The pressure change in stage 2 is due to flow in and out through the valves.

Figure 3.9 describes a damped system in which the pressure change in stage 2 is due to the flow through the perforations unlike in a non-damped system. To model this system, the gap between the membrane and electrode can be considered to be an additional stage (stage 3). The pressure change in this stage is due to the volumetric change produced by the membrane and the flow through the valves as shown in equation 3.33.

$$\frac{dP_b}{dt} = -\rho_b\alpha^2 \frac{u_b N_b A_e}{V_b} + \rho_b\alpha^2 \frac{1}{V_b}\frac{dV_b}{dt} \quad \textbf{3.33}$$

The pressure change in stage 2 and velocity through the perforation are shown in equations 3.34 and 3.35.

$$\frac{dP}{dt} = \rho_b \alpha^2 \frac{n}{\gamma} \frac{u_b A_E}{V_b} \quad \textbf{3.34}$$

$$\frac{du_b}{dt} = \frac{1}{L_E} \frac{(P_b - P_2)}{\rho_b} - 8 \frac{\mu}{\rho_b} \frac{u_b}{h_g^2} \frac{L_V}{L_E} \quad \textbf{3.35}$$

$$\frac{d^2 h_D}{dt^2} = -\omega^2 h_D + \frac{\pi^2}{\rho_D t_D A_d} (-P_e A_D - P_1 A_D + P_b A_D) \quad \textbf{3.36}$$

The membrane motion is coupled with the pressure change in the gap between the membrane and electrode as shown in equation 3.36 while accounting for damping. The system of equations for the corresponding setup is solved using MATLAB's ode45 solver. The initial pressure in each stage is atmospheric pressure and the velocity is zero through the perforations. The analysis for membrane deflection in this section uses the analytical model for resonance frequency and not FEM.

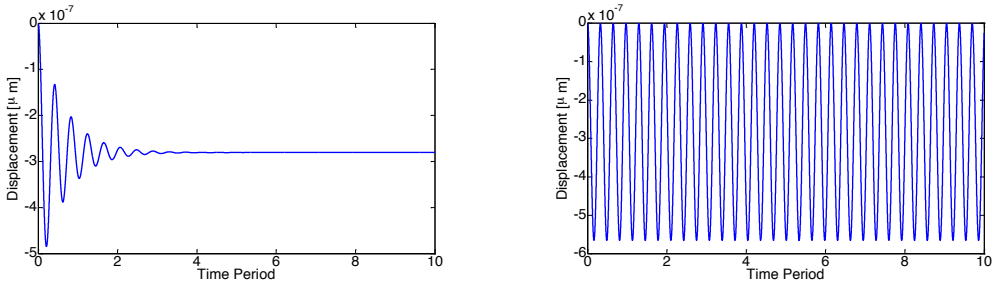

a) b)

Figure 3.10: Motion of the membrane in damped and non-damped systems. A constant voltage of 25V is applied. Figures a and b are the damped and non-damped systems respectively.

The two systems are operated at constant voltage of 25V. Figure 3.10 compares the behavior of damped and non-damped systems. Figure 3.10a states that the maximum displacement of the membrane is 0.48μm. For the non-damped system, the maximum membrane displacement is 0.55 μm as shown in Figure 3.10b. As expected, in a damped system, with time, the amplitude of oscillation decreases and becomes constant as seen in

Figure 3.10a. For a non-damped system, the oscillations do not reduce with time and follow a sinusoidal displacement, as seen in Figure 3.10b. The pushing force on a membrane moving downwards is the sum of the restoring mechanical force and acoustic pressure, in stage 3 for a damped system or in stage 2 for a non-damped system. The pulling force on the membrane is the sum of the electrostatic pressure and the acoustic pressure acting on the membrane from the top cavity. The direction of a membrane moving downwards changes when the pushing force is greater than the pulling force. In the damped system, L_V= 30μm and L_E= 200μm. These values are chosen only to compare the behavior of damped and non-damped systems. In an actual system the deflection of the membrane will cause L_V to change. The analyzed system assumes L_V to be constant until it collapses on the electrode. When collapsed, L_V changes to 1000 times the initial L_V. More sophisticated unsteady models need to be developed to model the system more accurately.

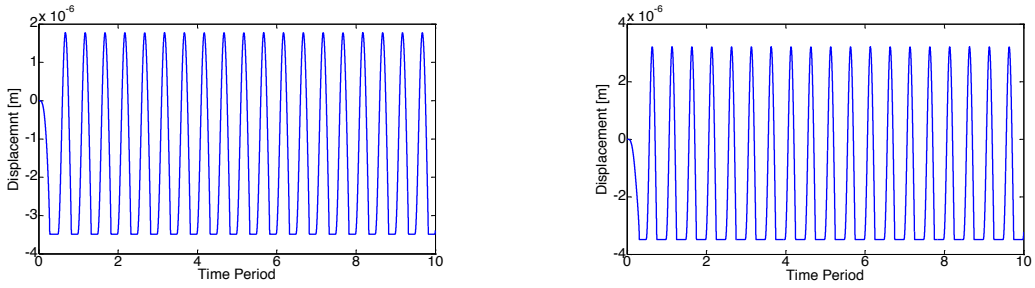

a) b)

Figure 3.11: Displacement of the membrane when driven by a sinusoidal waveform (100 Vp-p) in damped and non-damped systems. Figures a and b represent the damped and non-damped systems respectively.

When the membrane collapses on the electrode, the velocity and acceleration of the membrane is zero until the sum of the pushing force is greater than the pulling force.

These are the boundary conditions used when the membrane collapses on the electrode. The zero velocity and acceleration ensures that the position of the membrane is fixed until it is released from the electrode.

Energy possessed by the membrane is lost in overcoming the viscous effects due to the flow through the perforations. This loss in energy will prevent the membrane from reaching its maximum displacement. Figure 3.11 compares the displacement of damped and non-damped membranes. The displacement of the damped membrane in the direction opposite to the electrode is smaller than that in the non-damped system. The membrane displacement in Figure 3.11b represents an ideal model, which predicts the displacement to be nearly 3.5μm. The difference in displacement is significantly large, but the resistance model used to analyze the system is not accurate. The system currently under fabrication has 3000 holes (area ratio 0.5), which would result in a significantly lower L_v and hence ideal behavior. Therefore, the displacement predicted by the non-damped model is not over estimated.

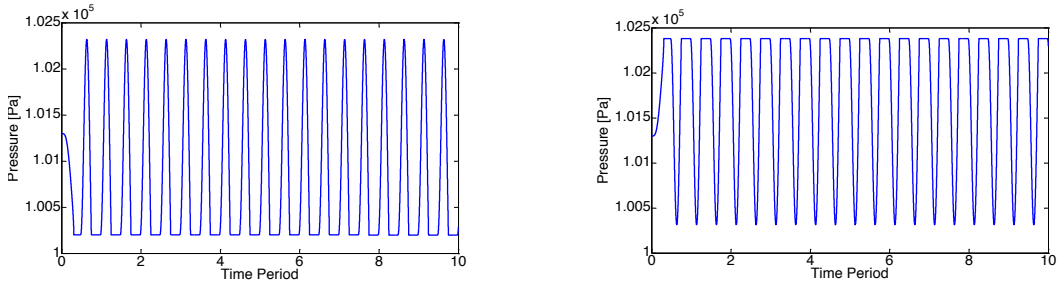

a) b)

Figure 3.12: : Pressure distribution in each stage while using the non-damped system. Figures a and b show the pressure distribution in stages 1 and 2 respectively.

The resulting pressure distribution in a non-damped system is shown in Figure 3.12. The sinusoidal membrane displacement results in the corresponding pressure changes in each stage as shown in Figure 3.12a and b. When the membrane is collapsed on the electrode, the absence of volume change results in constant pressure. The pressure difference in each stage is nearly 0.02×10^5Pa.

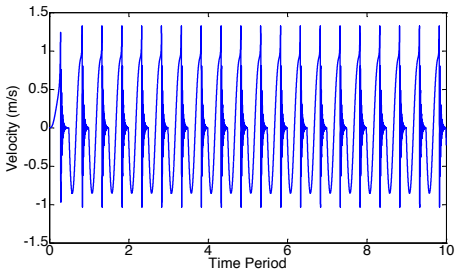

Figure 3.13: Velocity distribution through the holes in the electrode of the damped system.

Figure 3.13 shows the velocity distribution through the holes in the electrode. Oscillations in the flow appear when the membrane collapses on the electrode. This is due to the resistance model chosen. Unsteady models need to be developed and this is discussed in Chapter 5. The corresponding pressure changes in stages 1, 2 and 3 are shown in Figure 3.14 a, b and c respectively. The pressure change in stage 3 is large due to the small volume while that in stage 1 is similar to the non-damped system. The pressure in stage 2 decreases or increases due to the flow in and out of stage 3 resulting in smaller variations.

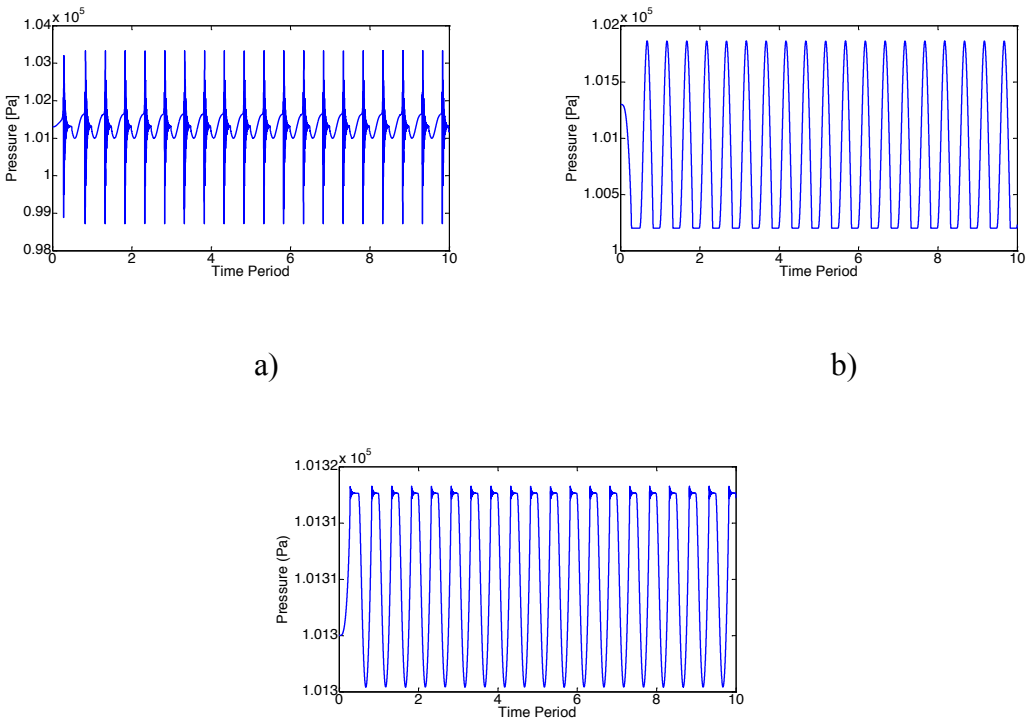

Figure 3.14: Pressure distribution in each stage when using the damped system. Figures a, b and c show the pressure distribution in the stages 3, 1 and 2 respectively.

Multiphysics modeling of a 4 stage micropump

The mathematical models for acoustic, structural deflection and electrostatic behavior are combined to form a new multiphysics model. A 4-stage micropump comprises of two membranes that drive the flow. In this section, the following assumptions are made:

1) The behavior of the valves is ideal and do not contribute to the volume displacement.
2) The damping on the pump membrane is negligible.
3) The damping in the system is due to the flow through the valves.

The operation of the valves is passive. The valves are opened when pressure difference across them is favorable to allow flow in the positive direction, while they are closed when flow takes place in the negative direction. The schematic for the operation of the valves in this system is shown in Figure 3.15. In Figure 3.15a, the valve is opened due to the favorable pressure gradient (P1 > P2), while in Figure 3.15b the valve is closed due to the adverse pressure gradient (P1 < P2). The required gas transfer should be from stage 1 to 2 and not reverse.

In the previous section, the damping of the pump membrane is analyzed with a simple resistance model. The number of valve holes on the electrode is 3183. The ratio of the open area to the closed area is ~ 0.5. Damping is considered to be minimum when this ratio is >0.33. The non-damped model is used to study the performance of a 4-stage micropump. The system of equations 2.6, 2.9, 2.11,3.22, 3.23 and 3.26 is solved using MATLAB's ode45 solver for the geometric parameters of the pump shown in Table 3.2.

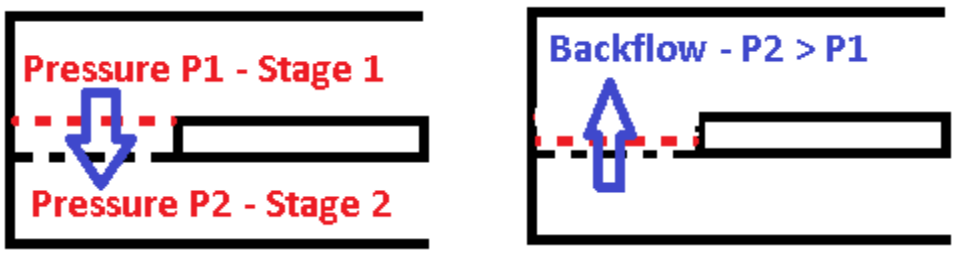

a) b)

Figure 3.15: Schematic showing the operation of the valves. In figure a, the valve is open since P1 > P2, which results in flow from stage 1 to 2. In figure b, the valve is closed since P1 < P1 that would result in backflow.

A_D	4 mm^2	L_V Open	30μm
h_o	3.5μm	L_V Closed	30X1000μm
N_H	3183	Cavity Volume	0.8983 mm^3
A_H	$4X10^{-10}$ m^2	L_E	200μm

Table 3.2: Geometric parameters used to model a 4-stage micropump.

In Chapter 1, the behavior of the membrane in a similar system is studied using lumped modeling for low frequency operation. Now, the displacement of the membrane will be analyzed in a 4-stage micropump operated at high frequency. As mentioned earlier, a single electrode is used to produce a higher compression in the top stages. To check the validity of this idea, a 4-stage micropump is maintained at a steady state inlet pressure of 0.97 atm. The pump is operated until steady state is obtained in each stage. The initial conditions are atmospheric pressure, zero velocity through each valve and zero displacement of the pump membrane. The pump membrane is driven using a sinusoidal waveform. The sine waveform is chosen as the appropriate driving signal as it does not induce additional complications in analyzing the system.

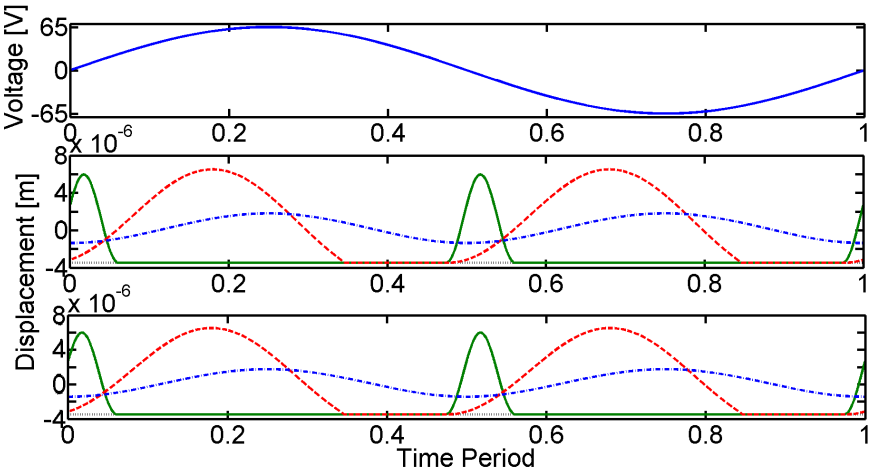

Figure 3.16: Displacement of the pump membrane when a sinusoidal waveform having 130 Vp-p is applied. The top trace is the input driving waveform; middle is the displacement of the membrane in pump 1 and bottom trace is the displacement of the membrane in pump 2. The green, red and blue lines in the middle and bottom trace are for operating frequencies of 5, 26 and 35 kHz respectively.

A sinusoidal waveform having amplitude of 130 V is used to drive the pump membrane. Figure 3.16 shows the corresponding displacement of the membranes when the pump is operated at different frequencies. The second and third trace represents the displacement of the first and second membrane respectively. Operating the pump at 5 kHz produces a displacement where the membrane is collapsed on the electrode for most of the cycle. The membrane is released from the electrode when the voltage goes to zero. The compression produced by operating the pump at 5 kHz is for a very small duration. At 26 kHz, the displacement of the membrane is nearly sinusoidal and spends a significantly smaller time collapsed on the electrode. The maximum displacement of these membranes at the two operating frequencies is ~7μm, which is nearly twice the membrane gap. A sinusoidal waveform having a frequency of 35 kHz does not have sufficient energy to collapse the membrane on the electrode. As expected, the pump membrane oscillates at twice the signal frequency.

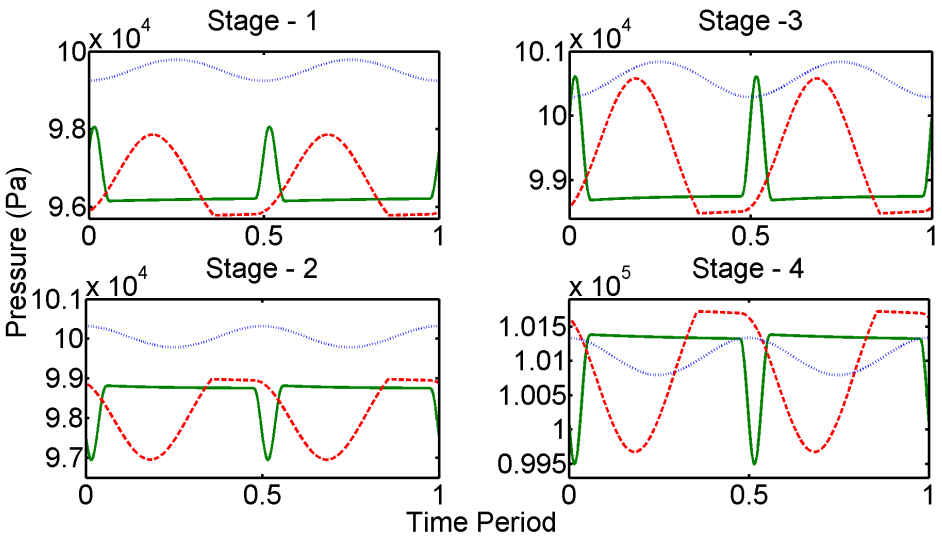

Figure 3.17: Pressure distribution in each stage when the inlet pressure is 0.97 atm. The green, red and blue lines represent the operating frequencies 5, 26 and 35 kHz respectively.

When the pump is operated at 5 kHz as shown in Figure 3.17, sharp variations in the pressure in each cavity are observed. This pressure distribution is expected due to the corresponding membrane deflection. When the pump is operated at 26 kHz, the change in pressure in each stage is nearly sinusoidal and similar to that observed by the reduced order acoustic model in Chapter 2. The inability of the membrane to collapse on the electrode results in a smaller compression, which prevents the pump from achieving positive flow. Figure 3.17 shows that the pressure in each stage is higher than the inlet pressure of 0.97 atm.

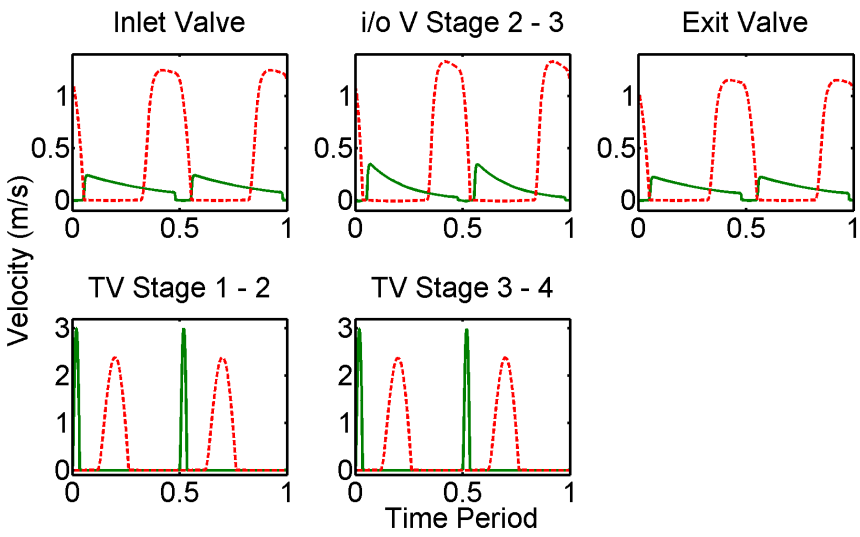

Figure 3.18: Velocity distribution through each valve. The top traces show the flow through each i/o valve and the bottom traces show the flow through the transfer valves. The green and red lines show the flow distribution when the pump is operated at 5 and 26 kHz respectively.

Figure 3.18 shows the velocity distribution through each valve for the corresponding operation. Operation of the pump at 5 kHz results in a significant difference between the durations for which the inlet/outlet and transfer valves are opened. The pulsed pressure change in each stage, results in the transfer valves being opened for a small duration. The consequence of the membrane collapsed on the electrode is the large open duration for the inlet/outlet valves. In reality, operating the valves to behave this way would be impossible. At 26 kHz, the duration for which the valves are opened is nearly the same for the inlet/outlet and transfer valves. The flow through each valve is similar to that observed by the acoustic model, where the driving force was the sinusoidal volume change. The valve open duration for the inlet/outlet is slightly larger than that for the transfer valves. This results in a higher velocity to maintain the same flow rate through each valve.

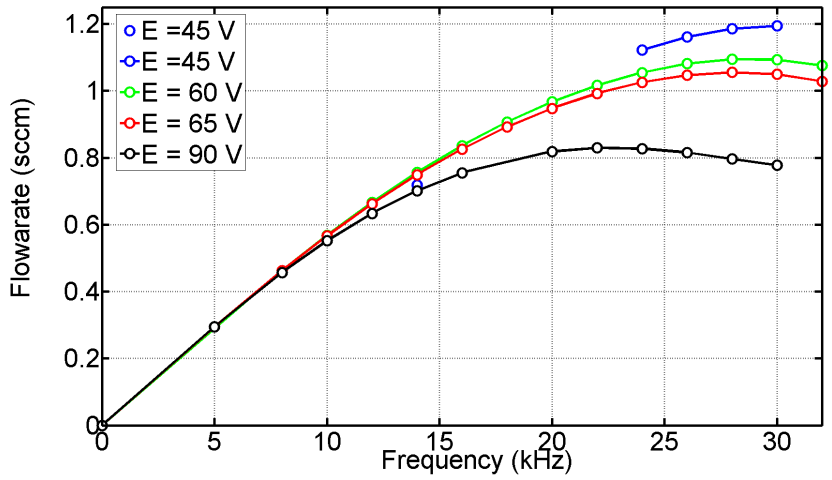

Figure 3.19: Flow rate vs. Frequency for a 4-stage micropump when using a sinusoidal waveform at different amplitudes.

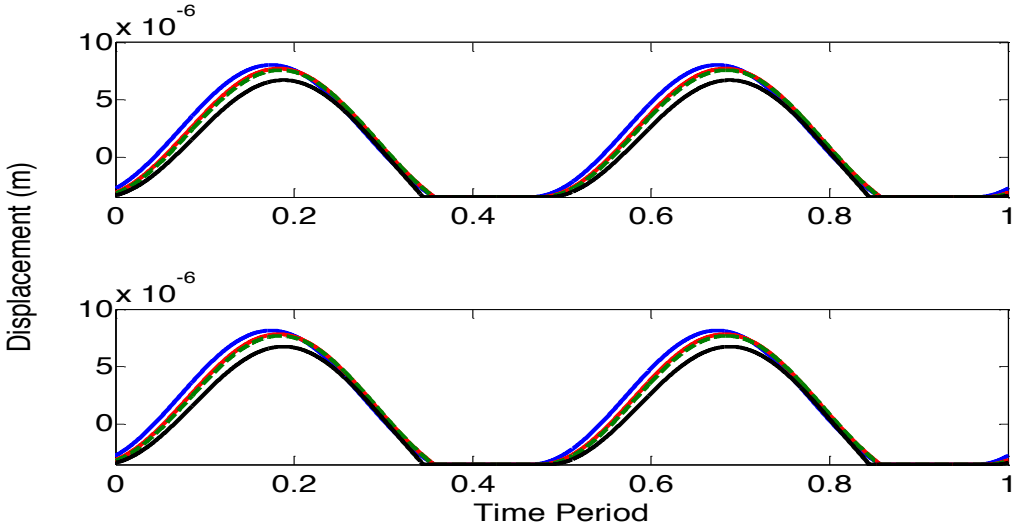

Figure 3.20: Displacement of the membrane at frequency 26 kHz for different voltages. The blue, red, green and black lines represent peak voltages of 45, 60, 65 and 90 V respectively.

The amplitude and frequency of the sinusoidal waveform play a vital role in controlling the performance of the micropump. Figure 3.19 illustrates the effect of

operating frequency and amplitude. The acoustic model predicts an increase in flow rate until a maximum is reached, after which the flow rate decreases with frequency. The maximum flow rate is obtained around the resonance frequency of the cavity. In Figure 3.19, an amplitude of 180 V increases the flow rate until 22 kHz and then the flow rate decreases. It was found that, after 32 kHz no flow rate is achieved for any amplitude. The energy at this frequency is either too large or too small to achieve positive flow at an inlet pressure of 0.97 atm. Decreasing the amplitude of the driving signal increases the operating resonant frequency. When the amplitudes are 120 and 130 V, the resonant frequency is estimated to be 28 kHz. When the amplitude is decreased, the flow rate is found to increase since the membrane deflects more in the direction opposite to electrode. The electrostatic force of attraction is not strong enough to constrain the deflection. When the voltage amplitude decreases to 90 V, flow performance is estimated only at 14 kHz or in range of frequencies between 24-30 kHz. There is sufficient energy only in this range of frequencies to operate the pump at 0.97 atm. Performance is estimated at 14 kHz due to the membrane resonance and between 24-30 kHz due to cavity resonance.

This phenomenon is illustrated in Figure 3.20. The displacement for both the pump membranes is nearly the same for the above-mentioned operating frequencies and amplitude. Increasing the amplitude decreases the deflection of the membrane in the opposite direction due to the electrostatic force of attraction. Providing more energy should produce more flow; but the designed device can produce maximum flow at a lower amplitude and higher resonant frequency.

Steady state analysis showed the operation of the pump at different frequencies and voltages. The transient analysis of the pump at these voltages and frequencies has not

been explored. To study transient performance of this device with design parameters shown in Table 3.2, the transient model proposed in Chapter 2 is combined with the multiphysics model. The inlet volume and the pump are initially maintained at atmospheric pressure and operated with a sinusoidal waveform of frequency 30 kHz and amplitude 90 V.

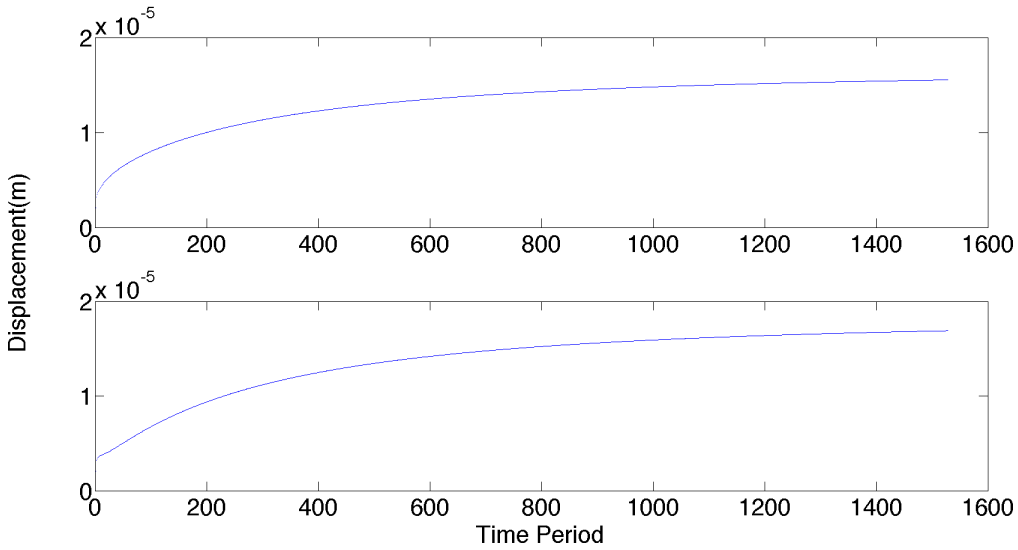

Figure 3.21 Transient maximum displacement of the pumping membranes in a 4-stage micropump. Top and bottom traces represent the displacement of membranes 1 and 2 respectively.

Figure 3.21 is the transient maximum displacement of the membranes. Top and bottom traces are the displacement of the membranes 1 and 2 respectively. A 4-stage pumps consists of two membranes numbered from the inlet. The time period shown on the x-axis is the time taken for the pump to decrease the pressure from atmospheric to the steady state pressure for an inlet volume equal to the dead volume of the device. The actual time obtained is the time period times the frequency. It is observed that, with a decrease in inlet pressure, the maximum displacement of the membrane increases from the initial position to ~15μm. The maximum displacement of the membrane is computed when the deflection of the membrane is in the direction opposite the electrode; the

minimum displacement is equal to the initial gap. With decreasing inlet pressure, the deflection of the membrane increases. Increase in the deflection of the membrane increases the volume ratio and hence the maximum attainable steady state pressure.

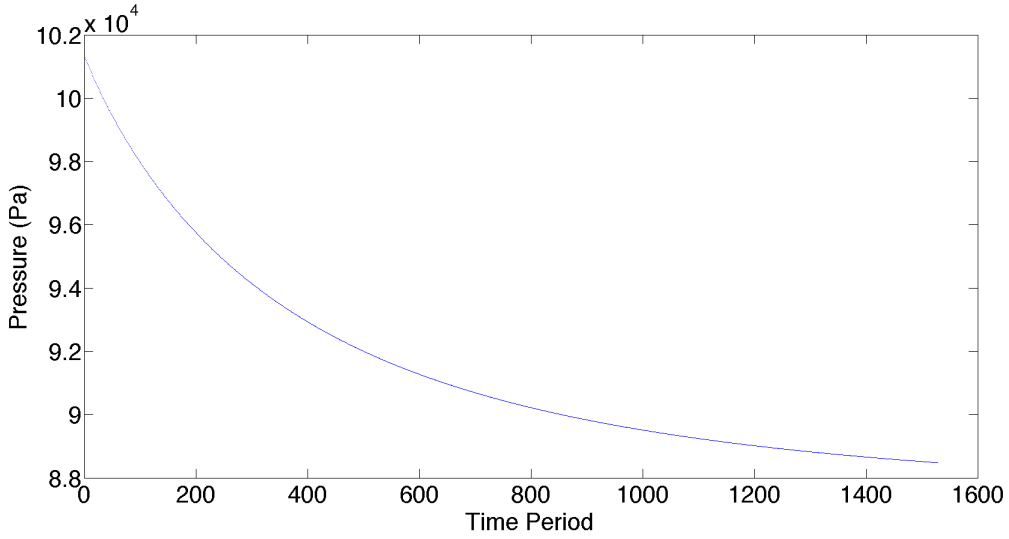

Figure 3.22: Decrease in inlet pressure for a 4-stage vacuum micropump operated using the transient model.

The advantage of the increase in membrane deflection is the decrease in volume ratio. The volume ratio determines the maximum attainable steady state pressure for a given micropump. The two electrode design has a fixed membrane deflection in both directions and hence a fixed volume ratio. The increase in deflection of the membrane with time decreases the volume ratio, which increases the maximum attainable vacuum. In Figure 3.22, the steady state pressure is estimated to be 88.5 kPa. This is significantly higher than the predicted pressure attainable for a dual electrode design. For a dual electrode design, the volume ratio is estimated to be 0.97 and the predicted thermodynamic attainable pressure is 90 kPa. This would be slightly lower for the reduced order model due to damping and inertial effects. The single electrode design is therefore more advantageous than the dual electrode design. However this system does

not take into account the effect of valve pumping. This could either increase or decrease the performance of the system.

Impact of Valve Membrane deflection

In the previous sections and chapters, the deflection of the valves has been ignored. They are assumed to operate passively and do not contribute to pumping. This assumption is only valid when the area of the valve is smaller than the area of the pump membrane or when the volume displaced by the valve membrane is lower than that displaced by the pump membrane. Astle (2006) showed that pumping could be achieved with only valves. When the deflection of the membrane is not constrained, it results in larger volume changes as seen in the previous section. Since the area of the valve membrane is equal to that of the pump membrane in the proposed device, it is important to model the valve membranes and study their impact on pumping.

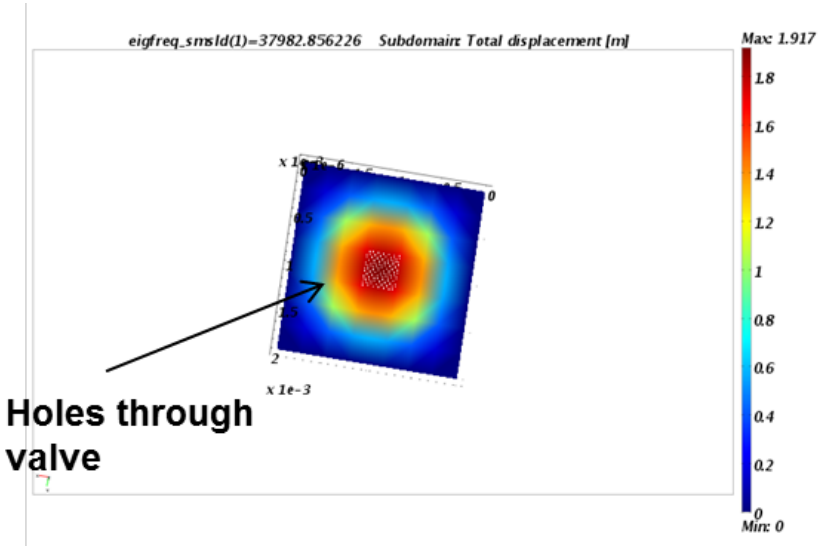

Figure 3.23: Resonant frequency analysis of the valve membrane using COMSOL Multiphysics.

A pattern of holes is applied on a valve membrane having properties shown in

Table 3.1. The holes are square and have dimensions of length 20x20 μm. The spacing between the holes from center to center is 70 μm. The holes on the electrode and membrane are arranged to have a checkerboard pattern as shown in Figure 3.24. The membrane has 169 holes in total. Using a mesh similar to the one that was used for the pump membrane, the resonant frequency of the membrane is estimated to be 37.9 kHz as shown in Figure 3.23. The resonant frequency of the pump membrane is estimated to be 35.8 kHz. Thus, the holes do not change the resonant frequency significantly.

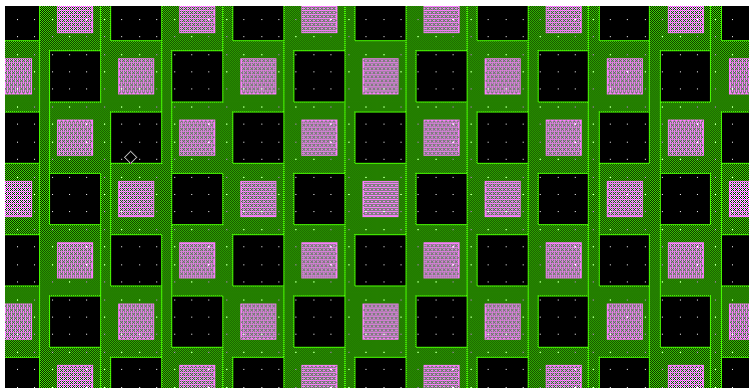

Figure 3.24: Arrangement of holes on the valve membrane and electrode. The pink and black colors represent the holes on the membrane and electrode respectively.

As observed in the previous section, the deflection of the membrane is > 10 μm. Beyond this, the deflection of the membrane with respect to the force acting on the membrane is no longer linear. Using COMSOL's static structural module with large deflection, the maximum displacement of the membrane for an applied force is estimated. The maximum displacement occurs at the center of the membrane. Figure 3.25 illustrates the relation between the deflection of the membrane and the applied pressure. The deflection of the membrane has been normalized with the gap length and the pressure has been normalized with the residual stress. The linearity in the deflection of the membrane disappears when the normalized pressure is greater than 0.5×10^{-4}.

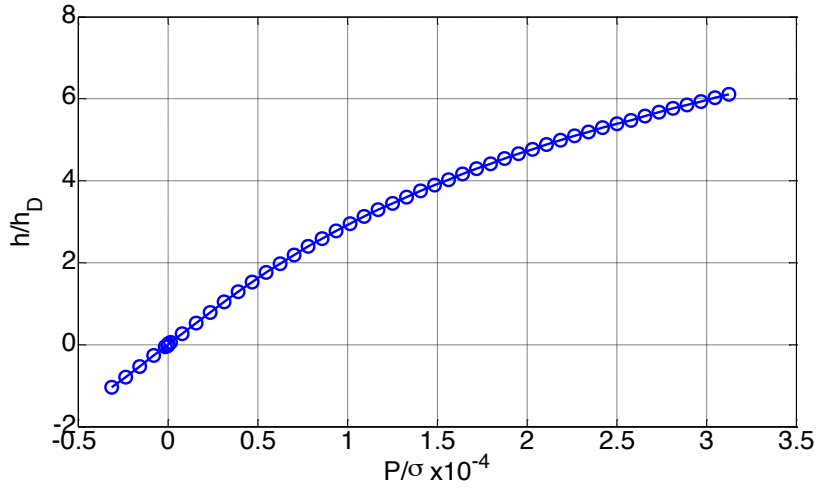

Figure 3.25: Static deflection of the valve membrane when a uniform pressure is applied on the surface. The blue circles and the line represent the evaluated maximum deflection and the mathematical fit respectively.

Using a custom code built in MATLAB, a nonlinear relation between the deflection of the membrane and the applied pressure is evaluated. The mathematical relation between the applied pressure and deflection of the membrane consists of a linear term, which accounts for the softening effects, and a cubic term, which accounts for the hardening effects, as shown in equation 3.37. Higher nonlinear terms are neglected. The mathematical relation is similar to equation 3.25 with a small change in the coefficients.

$$\mathbf{P = 5.8295e^{17}X\,h_D^3 + 4.6756e^{6}Xh_D} \qquad \mathbf{3.37}$$

The volume change in cavity 1 and 2, shown in equations 3.38 and 3.39, is due to the deflection of the pump and valve membranes. The initial dead volume in stage 2 is the cavity volume and the volume between the membrane and the electrodes for the transfer, outlet valves and pump.

$$\mathbf{V(t) = V_C - V_D(t) - V_{Dio}(t) - V_{Dtv}(t) = V_C - \frac{4}{\pi^2}A_D h_D(t) - \frac{4}{\pi^2}A_D h_{Dio}(t) - \frac{4}{\pi^2}A_D h_{Dtv}(t)} \qquad \mathbf{3.38}$$

$$\mathbf{V(t) = V_C + V_D(t) + V_{Dio}(t) + V_{Dtv}(t) + V_M + V_{io} + V_{tv} = V_C + \frac{4}{\pi^2} A_D h_D(t) + \frac{4}{\pi^2} A_D h_{Dio}(t) + \frac{4}{\pi^2} A_D h_{Dtv}(t)} \quad \textbf{3.39}$$

Combining the acoustic, structural and electrostatic equations, the flow rate performance of a 4-stage micropump is evaluated at atmospheric steady state conditions. As the valve membrane deflects, the gap between the valve membrane and electrode changes, increasing the resistance to flow. In the analysis presented here, the resistance is assumed to be constant and increases only when the membrane collapses on the electrode. This assumption though drastic, serves as an initial estimate to study the resonant effects present in the pump. The geometric parameters used for the 4-stage modeling is shown in Table 3.3. All other properties used are shown in Table 3.2.

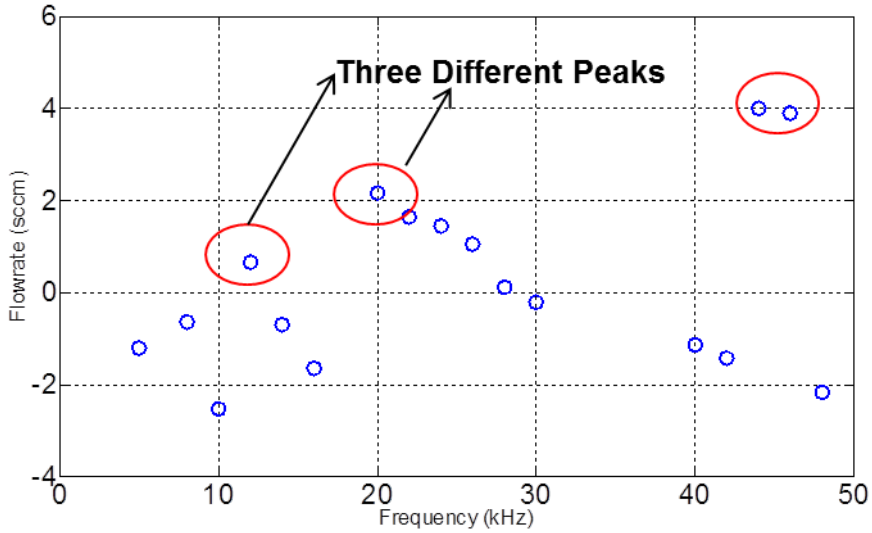

Figure 3.26: Flow rate vs. driving frequency for a 4-stage micropump. Sinusoidal and trapezoidal waveforms are used to drive the pump and valve membranes. The valve timing is not optimized for each frequency.

Properties	Value
Cavity Volume	1.1021 mm^3

Pump Membrane Gap	4 µm
Valve Membrane Gap	6 µm

Table 3.3: Geometric parameters of the 4-stage micropump used for analysis.

The 4-stage micropump is operated by applying a sinusoidal and trapezoidal waveform on the pump and valve membranes respectively. The trapezoidal signal given to the two valves are different as shown in Figure 3.27. In Figure 3.26, the flow rate is estimated for the corresponding operating frequency. The amplitude of each waveform is shown in Figure 3.27. The valves are not optimized to produce maximum flow rate. Three operating frequencies 12, 20 and 44 kHz produce flow, which is maximum for each of the observed peaks. Since the valve timing is not optimized, some of the frequencies produce negative flow. The frequency points that produce maximum flow correspond to the cavity resonance and the resonant frequency of the membrane. The cavity resonance is 31.4 kHz and is estimated from the cavity volume.

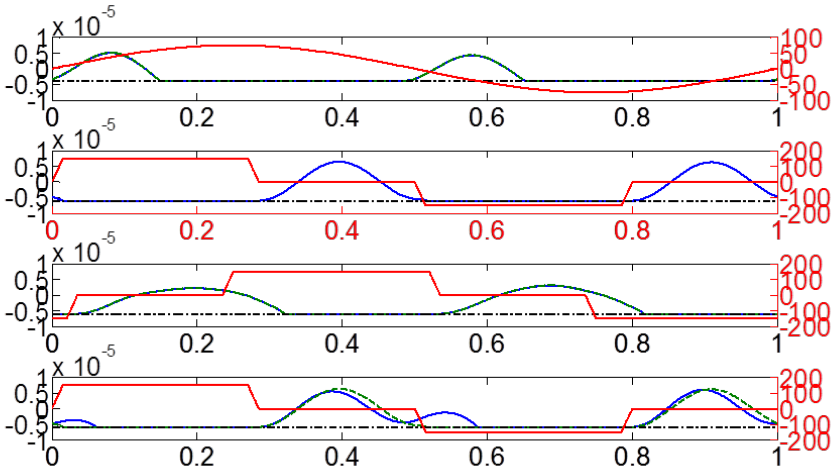

Figure 3.27: Displacement of the pump and valve membrane for a 4-stage micropump operated at 12 kHz. The first, second, third and fourth traces correspond to the pump, inlet, transfer and outlet valves respectively. The blue and green lines represent the membranes in pumps 1 and 2 respectively.

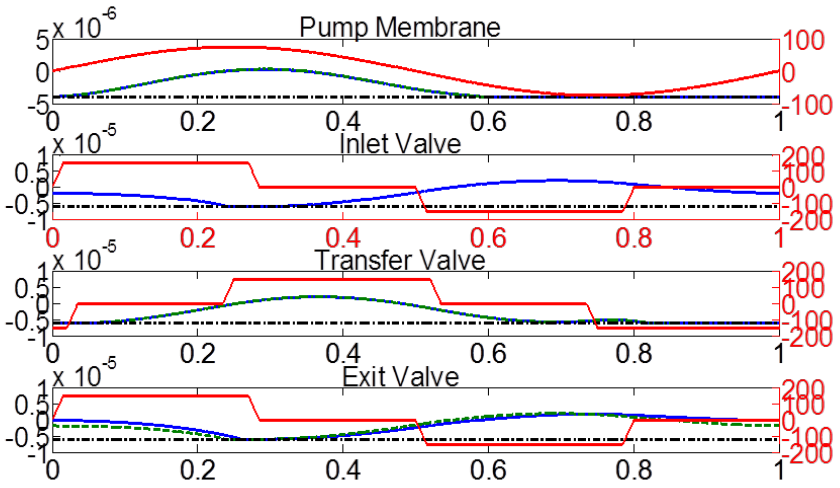

Figure 3.28: Displacement of the pump and valve membrane for a 4-stage micropump operated at 44 kHz. The first, second, third and fourth traces correspond to the pump, inlet, transfer and outlet valves respectively. The blue and green lines represent the membranes in pump 1 and 2 respectively.

The waveforms used to actuate the pump and valve membranes are shown in Figure 3.27 and Figure 3.28. Alternating positive and negative amplitudes are chosen for the trapezoidal waveform to prevent charge accumulation over the membrane. This is explained in detail in Chapter 4. The valve membrane deflection is significantly larger than the pump membrane, which indicates that the valves produce significant pumping. The volume displaced by the valves is large enough to hinder the performance of the pump. The transfer valves are open for a longer duration than the inlet/exit valves when operated at 12 kHz. The pump membrane does not experience frequency doubling when operated at 44 kHz. The trapezoidal waveform for the two valves are created so as to adjust the opening and closing of the valves in accordance with the theory proposed in Chapters 1 and 2. In Figure 3.29 the valve timing is optimized to produce maximum performance and eliminate negative flow rate. This also results in the offset of the three peaks that were observed in Figure 3.26.

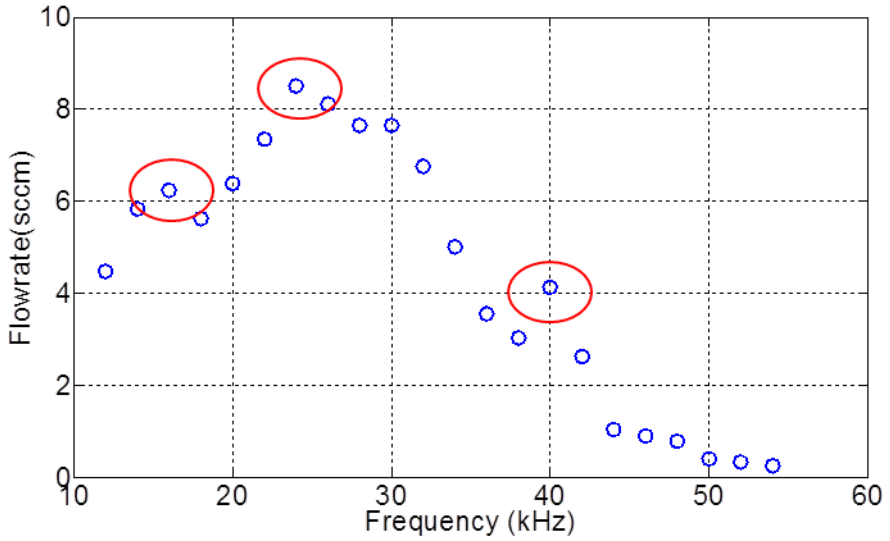

Figure 3.29: Flow rate vs. frequency for optimized valve timing. The three red circles indicate the resonant peaks.

Resistance model for valve modeling

In the previous section, the opening and closing resistances of the valve do not change with the deflection of the membrane. Analysis suggests that the valve membrane deflection can no longer be ignored. The behavior of the membrane was previously assumed to be ideal, completely open or completely closed. The resistance and inertial effects through the valves, which are influenced by the membrane motion, influence the operating frequencies. New models for resistance and inertial effects need to be developed to improve the modeling of the micropump.

Two new holes patterns on the valve membrane and electrode are proposed as shown in Figure 3.30a (design a) and Figure 3.30b (design b). In Figure 3.30a, the spacing of the holes on the electrode and membrane are not equal as it follows a checkerboard design. Due to the unequal spacing on the electrode, a stress gradient appears which results in electrode curving. In Figure 3.30b, the holes on the membrane are rotated to allow for equal spacing between the holes on the electrode and the membrane.

To analyze the fluidic resistance and inertial effects, a section of the valve is modeled in Fluent. The boundary conditions used are shown in Figure 3.31. Symmetric boundary conditions are used on the surfaces shown. A pressure inlet is applied on the top surface and an outlet exists on the bottom surface. The two channels above and below the electrode and membrane are designed to be considerably long to prevent any near

boundary effects. The mesh is created using GAMBIT and the number of tetrahedral cells used for each simulation is as shown in Table 3.4.

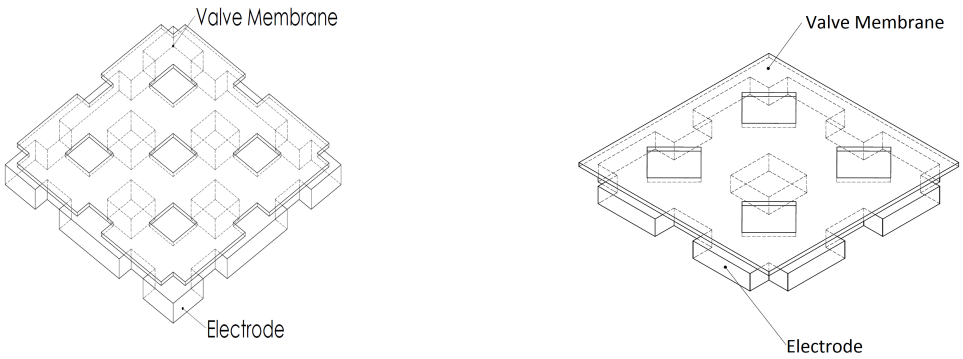

a) b)

Figure 3.30: Two proposed designs for arrangement of the holes on the valve membrane and electrode. The dashed and the solid lines represent the holes on the electrode and valve membrane respectively.

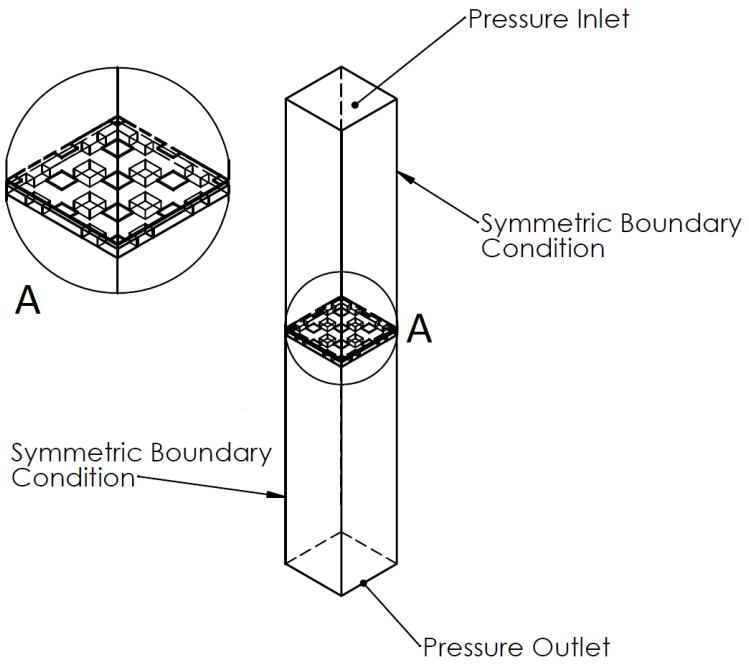

Figure 3.31: Boundary conditions applied to a section of the valve used for modeling.

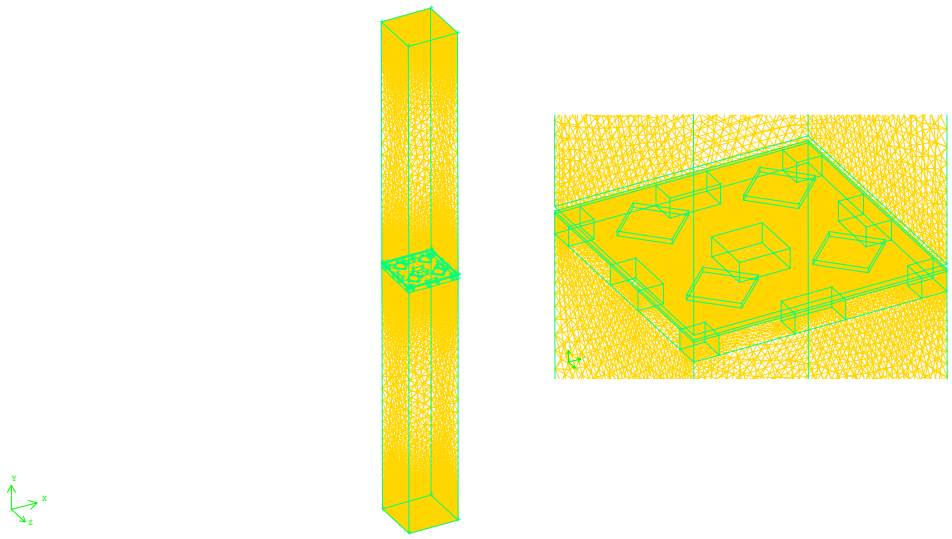

Figure 3.32: Meshing setup when the gap between the electrode and membrane is 1μm. The expanded section represents the mesh setup used in the valve area.

Gap Distance μm	Mesh count
1	272414
2	130656
3	158885
4	135202

Table 3.4: Tetrahedral mesh count used for the corresponding gap between the electrode and the membrane.

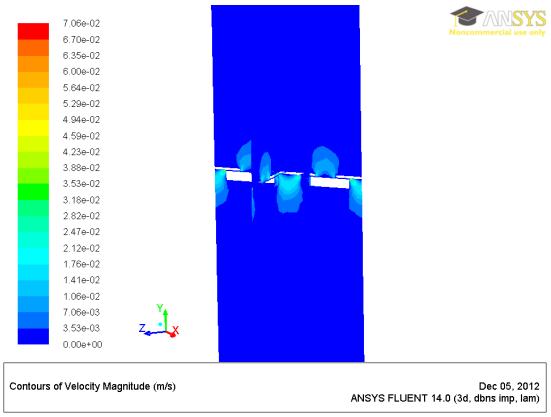

a)

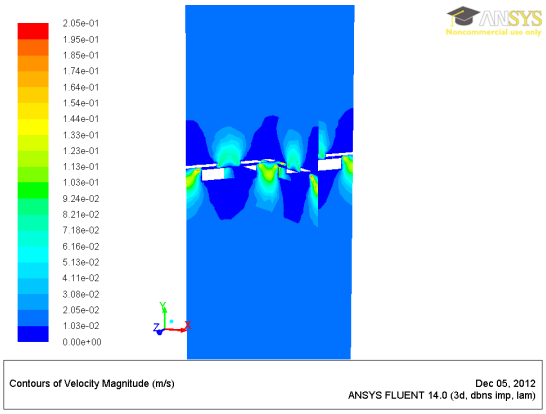

b)

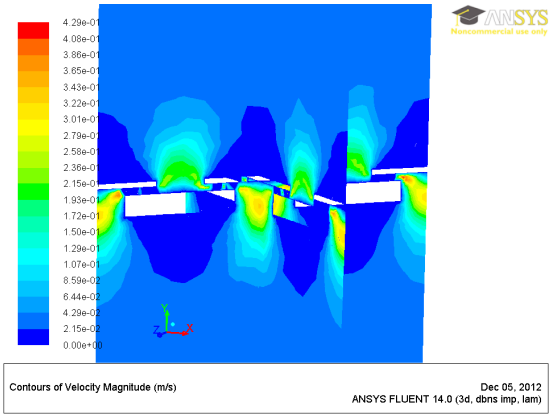

b)

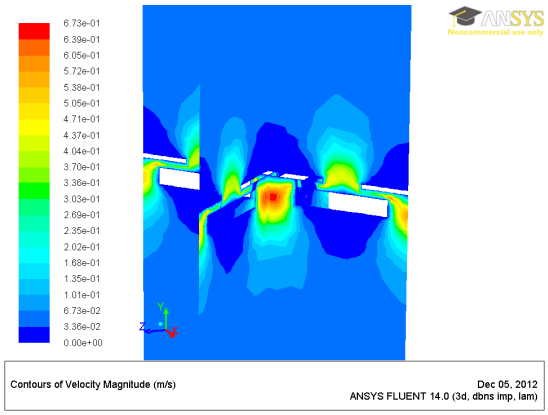

d)

Figure 3.33: Contours of velocity magnitude over two cross sectional planes. Figures a, b, c and d represent the flow for gaps 1, 2, 3 and 4 ***μ***m respectively.

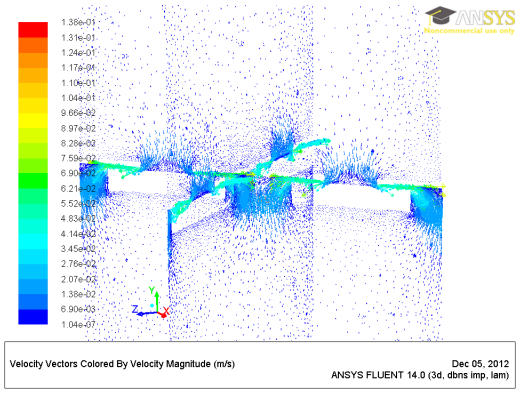

a)

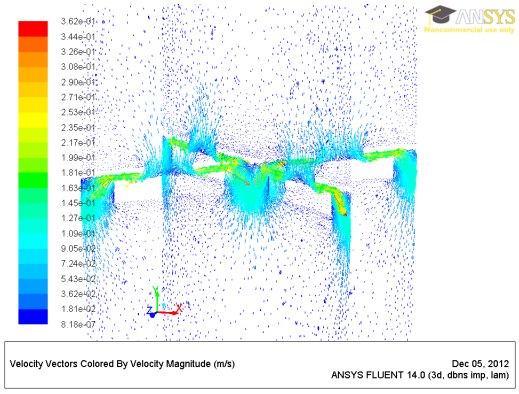

b)

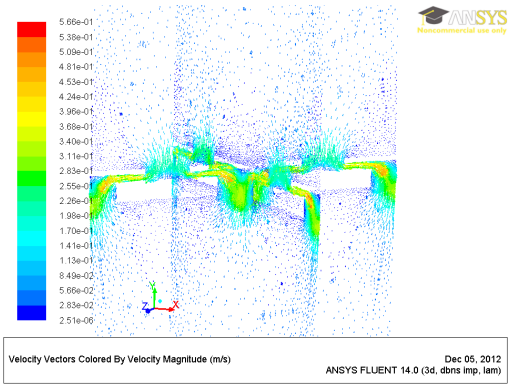

b)

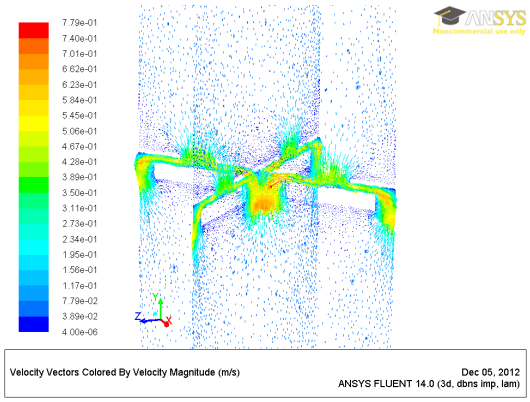

d)

Figure 3.34: Contours of velocity vectors over two cross sectional planes. Figures a, b, c and d represent the flow for gaps 1, 2, 3 and 4 $\boldsymbol{\mu}$m respectively.

To study the flow pattern through the valve section, the mesh created in GAMBIT is imported into FLUENT. A pressure difference of 100 Pa is applied between the inlet and outlet and the flow is estimated numerically using an implicit Roe solver and a second order upwind scheme. The initial conditions are zero flow and atmospheric pressure everywhere. The solver is run until the flow reaches a steady state. Steady state is achieved when the difference in average pressure in a given cross section plane between

two iterations does not change by 10^{-5}. The standard residuals are also monitored to ensure that steady state is achieved.

Figure 3.33 and Figure 3.34 illustrate the velocity magnitude on two cross sectional planes for different gap distances using contour and vector plots. The velocity distribution when the gap between the electrode and membrane is 1μm is as shown in Figure 3.33a and Figure 3.33b. The contours suggest that flow acceleration is through the valve holes. The rest of the system has nearly zero velocity. The velocity magnitude increases when the gap between the membrane and electrode increases. This suggests that the resistance is lower for larger valve gaps. The vectors in Figure 3.34 show the direction of flow through the valves. The velocity in the gap is nearly zero for smaller valve gaps because the flow from the membrane to the electrode holes occurs in only one direction. For larger gap distances, the velocity in this region increases significantly.

$$\boldsymbol{\Delta P = 8\frac{\mu u_e L_V}{h_g^2}} \qquad \textbf{3.40}$$

Equation 3.40 is used to evaluate the resistance to the flow for the given electrode gap. For designs a and b at the given pressure difference, the average velocity is estimated at the inlet and outlet planes. Viscous length, L_V, estimated for designs a and b is 187 and 189 μm with the gap between the electrode and membrane being 4μm. This suggests that the orientation of the holes do not influence the resistance. Thus the governing factors that affect the resistance are the gap and hole size.

$$\boldsymbol{L_v = 10^{-17.03} h_g^{-2.46}} \qquad \textbf{3.41}$$

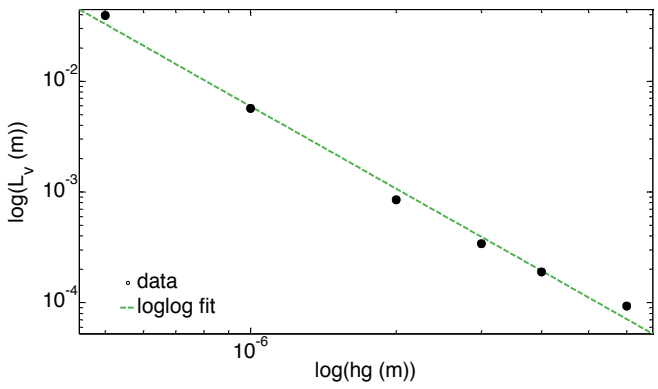

Figure 3.35: Relationship between the viscous length, $\boldsymbol{L_V}$, and the gap between the membrane and electrode, for design b.

Equation 3.41 is the mathematical relation between the gap and the viscous length. This relation is obtained by using a linear fit between the logarithm of the viscous length and the gap. A custom code was developed in MATLAB to estimate the slope and the interception of the linear line shown in Figure 3.35. The viscous length is seen to vary inversely with the cube of the electrode gap.

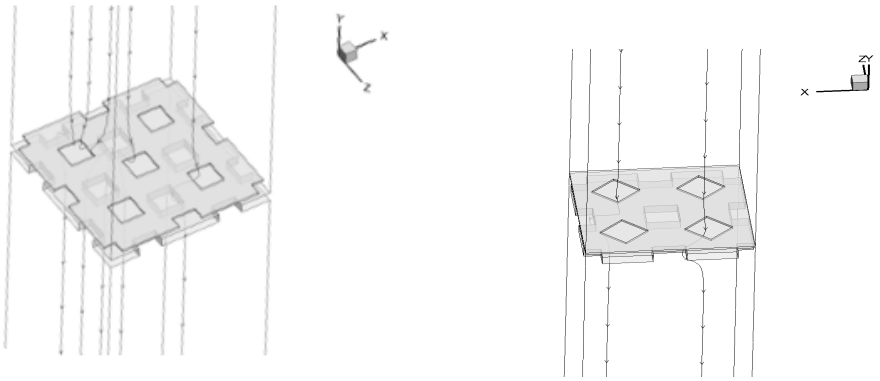

a) b)

Figure 3.36: Streamline originating from the inlet and terminating at the outlet. Figures a and b are the streamlines for designs a and b respectively.

$$L_e = \frac{1}{u_e}\int u_e ds \qquad 3.42$$

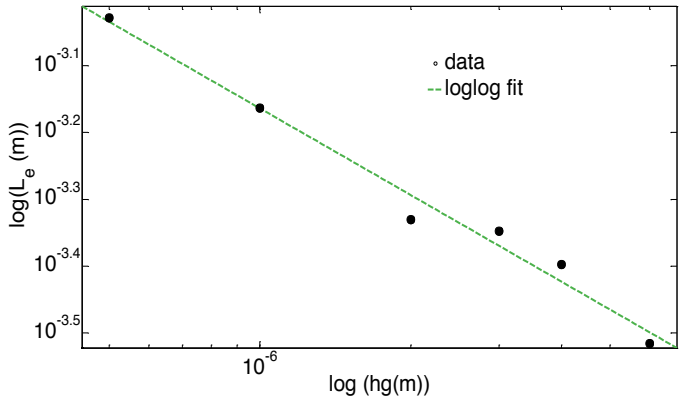

Figure 3.37: Relationship between the inertial length, L_E, and the gap between the membrane and electrode for design b.

$$L_e = 10^{-5.74} h_g^{-0.4309} \qquad 3.43$$

Similar to the estimation of the viscous length, the inertial length is obtained by integrating equation 3.42 along a streamline originating from the inlet and terminating at the outlet as shown in Figure 3.36. The average inertial length is estimated by integrating along different streamlines. For designs a and b having a gap of 4 μm, the inertial lengths are ~380 and 370 μm respectively. These lengths do not vary significantly for the two designs. Using a linear fit between the logarithm of the inertial length and gap, the slope and intercept are computed as shown in Figure 3.37. The inertial length is found to vary inversely with the square root of the gap.

The relations 3.41 and 3.42 along with acoustic, structural and electrostatic equations are used to model a 4-stage micropump as described in the previous sections. The dimensions used for this purpose are shown in Table 3.5. The flow rate is measured at atmospheric pressure conditions (maximum flow rate).

Properties	Values
Square Membrane length	2mm
Top Cavity Height	65 µm
Bottom Cavity Height	90 µm
Gap (Membrane/electrode) h_g	4 µm
N_H (pump electrode)	3200
N_H (valve electrode)	1600
Valve Holes Length	20 µm
Number of Valve Holes	169

Table 3.5: Geometric parameters used for a modeling a 4-stage micropump to evaluate flow rate performance.

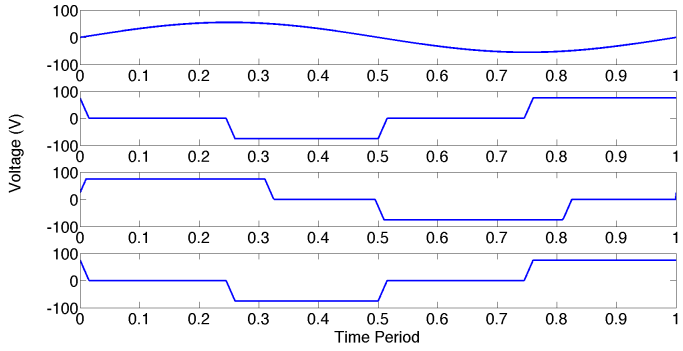

Figure 3.38: Signals used to operate the 4-stage micropump. The first, second, third and fourth trace represent the signals used to actuate the pump, inlet, transfer and outlet valves respectively.

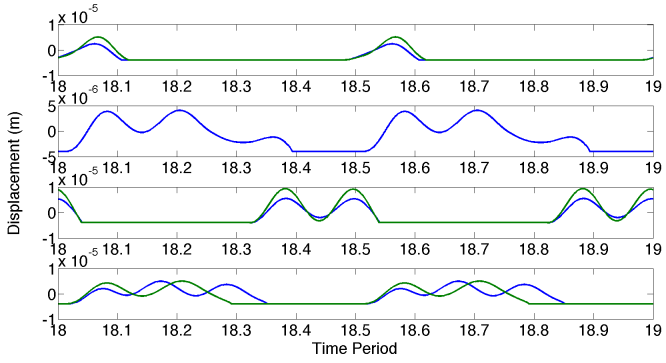

Figure 3.39: Displacement of the membranes for a 4-stage vacuum micropump operated at 7kHz. The first, second, third and fourth trace represents the displacement of the pump, inlet, transfer and outlet valve membranes respectively.

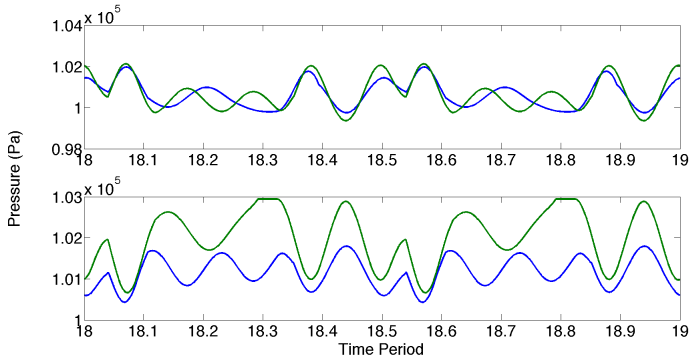

Figure 3.40: Pressure distribution in a 4-stage vacuum micropump operated at 7kHz. The first and second traces represent the pressure distribution in stages 1 and 2 respectively.

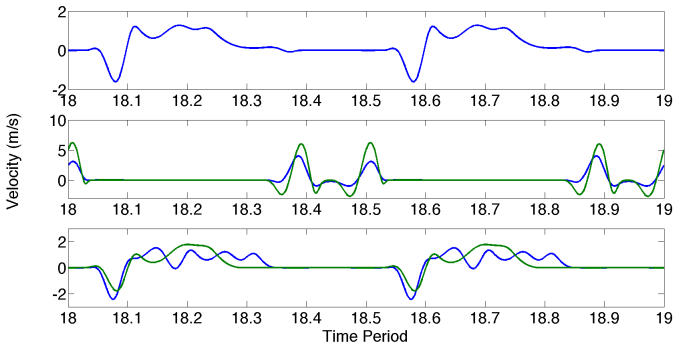

Figure 3.41: Velocity distribution through each valve in a 4-stage micropump operated at 7 kHz. The first, second and third traces represent the flow through the inlet, transfer and outlet valves respectively.

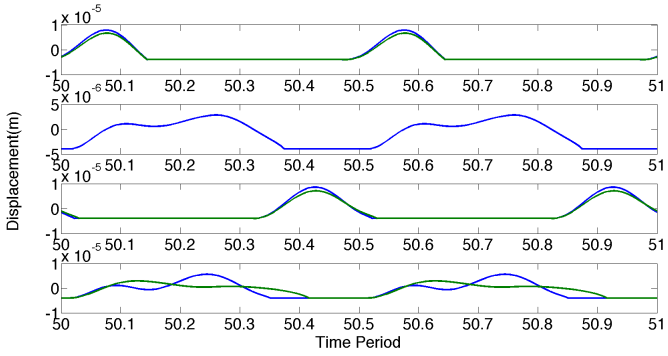

Figure 3.42: Displacement of the membranes for a 4-stage vacuum micropump operated at 12kHz. The first, second, third and fourth traces represent the displacement of the pump membrane, inlet, transfer and outlet valve membranes respectively.

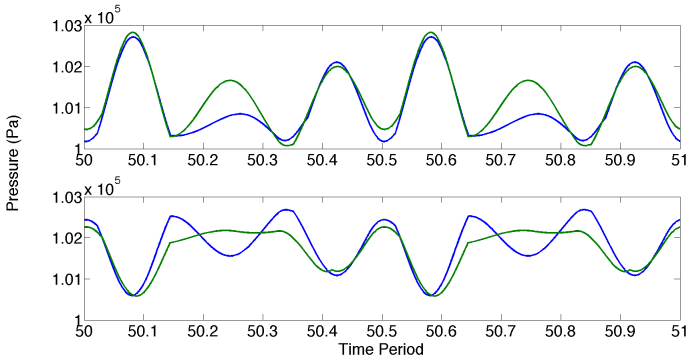

Figure 3.43: Pressure distribution in a 4-stage vacuum micropump operated at 12kHz. The first, and second traces represent the pressure distribution in stages 1 and 2 respectively.

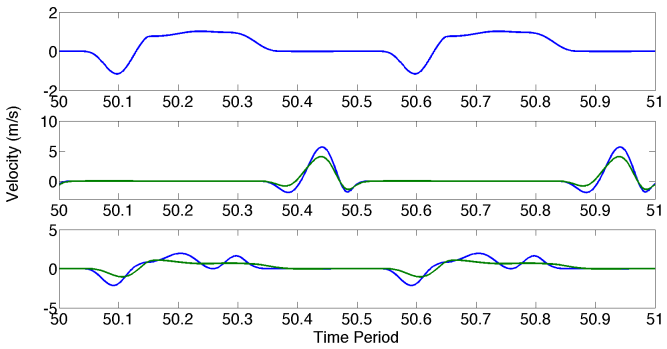

Figure 3.44: Velocity distribution through each valve in a 4-stage micropump operated at 7 kHz. The first, second and third traces represent the flow through the inlet, transfer and outlet valves respectively.

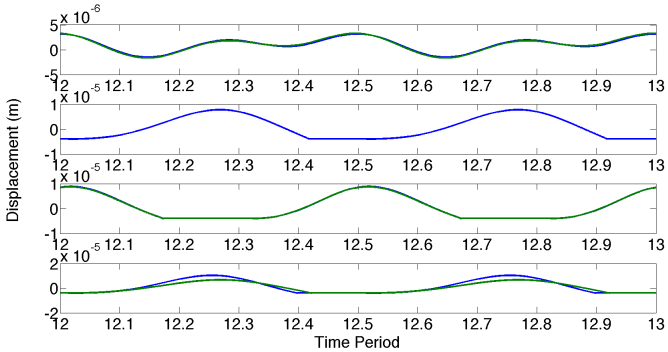

Figure 3.45: Displacement of the membranes for a 4-stage vacuum micropump operated at 22kHz. The first, second, third and fourth traces represent the displacement of the pump membrane, inlet, transfer and outlet valve membranes respectively.

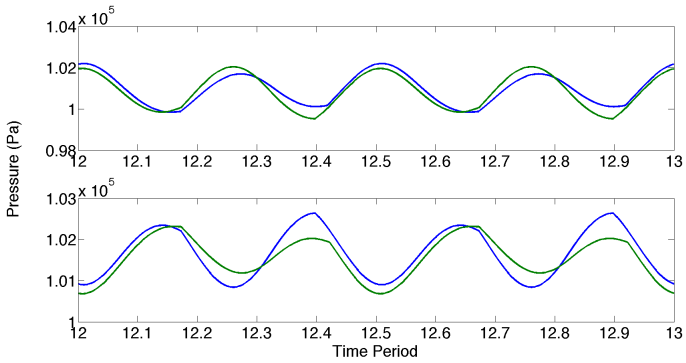

Figure 3.46: Pressure distribution in a 4-stage vacuum micropump operated at 12kHz. The first, and second traces represent the pressure distribution in stages 1 and 2 respectively.

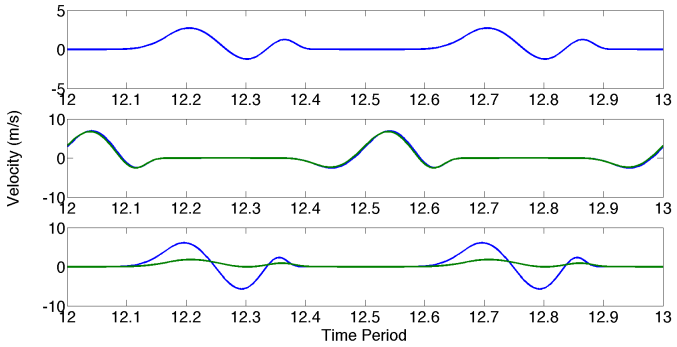

Figure 3.47: Velocity distribution through each valve in a 4-stage micropump operated at 7 kHz. The first, second and third traces represent the flow through the inlet, transfer and outlet valves respectively.

The displacement of each membrane in the 4-stage micropump is shown in Figure 3.39. The signals used to actuate the membranes are shown in Figure 3.38. The comparison of flow rate vs. frequency will be presented in Chapter 4. The displacement of the pump membrane in all the cases suggests that its displacement is equal or less than the displacement of the valves. The pressure distribution in each of the stages, shown in Figure 3.42, Figure 3.43 and Figure 3.44, suggest that the valves contribute significantly to pumping. In the previous chapter, lack of valve modeling suggested that the only reason for the corresponding pressure distribution in each stage is the deflection of the

pump membrane. Since the valves contribute significantly to the pumping, their effect cannot be ignored. Figure 3.43 suggests that the pressure distribution in each stage is only affected by the valve membranes and not by the pump membrane. The velocity distribution through each valve is shown in Figure 3.41, Figure 3.44 and Figure 3.47. Optimizing the valve timing to produce zero back flow through each valve was extremely difficult. This indicates that the system is extremely sensitive to the deflection of the valve membranes. To remedy negative effects brought about by the valve pumping, the valve area and the gap should both be reduced. The theoretically predicted performance is compared with the experimental results in Chapter 4. The advantages and possible drawbacks of the model are also discussed.

Valve Only Pumping

The active valves in this system contribute heavily to pumping. In some cases, as shown, the pump membrane does not do the intended pumping. While the design proposed could be disadvantageous, changes have to be made to reduce this effect. Decreasing the area of the valve membranes or gap can limit this detrimental effect. However, since the valves contribute to the pumping, a new design is conceived to eliminate the pump membrane altogether as shown in Figure 3.48.

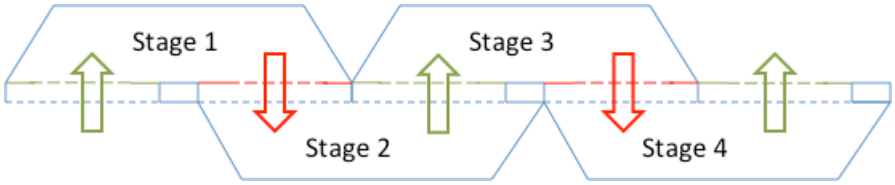

Figure 3.48: Illustration of Valve Only Pumping for a 4-stage micropump. The green and red lines represent the inlet/outlet and transfer valves respectively.

For valve only pumping, the pump membrane is eliminated from the single electrode design. As illustrated in Figure 3.48, the valves perform the required compression/expansion as well as sealing. The flow direction takes place from the inlet into stage 1 then into stage 2 and so on until it reaches the outlet. The working of this device is illustrated in Figure 3.49. The pressure distribution in stage 1 and 2 are normalized as shown in equation 3.44. P_i is the initial pressure in each stage. When the pressure in stage 1 is greater than that in stage 2, the transfer valve is opened and vice versa. When the inlet pressure is greater than the pressure in stage 1, the inlet/outlet valves are open and vice versa.

$$P = \frac{(P_1 - P_i)}{P_{max}} \qquad \textbf{3.44}$$

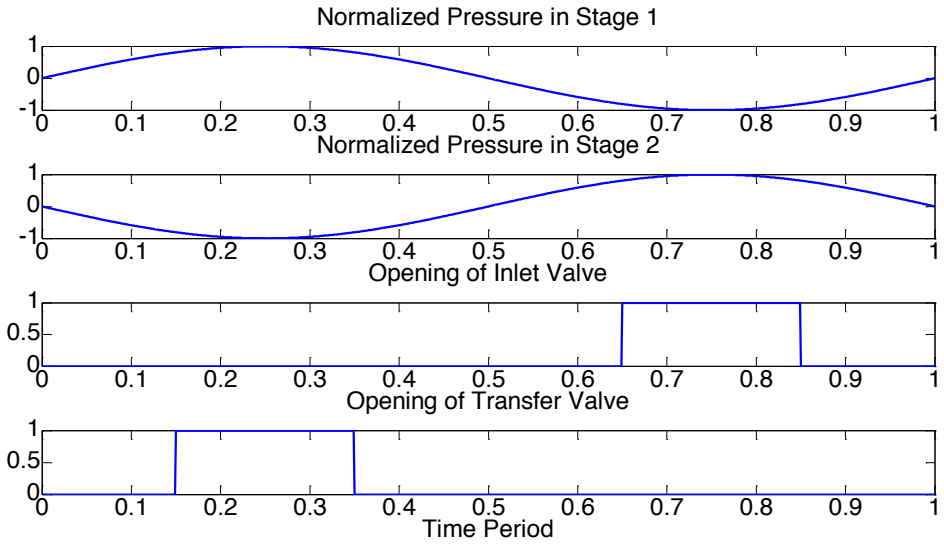

Figure 3.49: Illustration of the working of valve only pumping. First, second, third and fourth traces represent the normalized pressure in stages 1, 2 and the valve timing in inlet and transfer valves respectively.

In this thesis, optimized controlling of the valves for valve pumping is not presented and should be dealt with in the future. The goal in this section is to present a proof of concept of the working of this device. The device under consideration has properties shown in Table 3.5 but the cavity volumes are different. The cavity volume due to the pump membrane is neglected. This makes the volume significantly smaller. The reduction in the dead volume will increase the resonant frequency and decrease damping. The smaller device will be more compact and can be used to house more stages for pressure pumping. Here, the device proposed is analyzed only for high flow rate conditions. The cavity volumes used for the top and bottom stages are 4.8 and 7.2 mm^3 respectively.

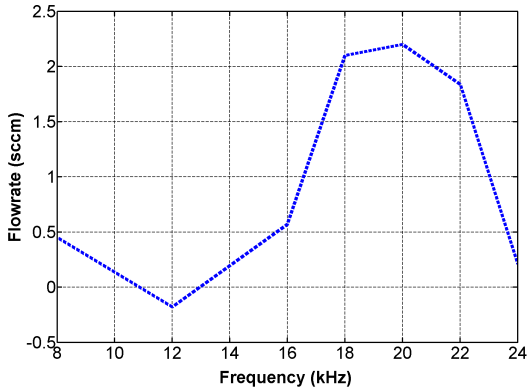

Figure 3.50: Flow rate vs. frequency for valve only pumping for the 4-stage design proposed.

The inlet and transfer valves are operated using sine and cosine waveforms with amplitude of 180V ($\pm 90V$). To model this device, the equations in section 3.8 are used with zero volume displacement by the pump membrane. The dead volume due to the gap between the membrane and electrode is also ignored. Figure 3.50 shows the estimated flow rate vs. frequency sweep. Frequencies other than those presented here did not achieve steady state (convergence). The flow rate for these frequencies was not the same through each valve and changed with each cycle. This has been attributed to the nature of the system. As expected, only certain frequencies produce positive flow rate while others produce negative flow rate. The negative flow rate suggests the bi-directionality of this device. Changing the frequencies will allow use of the device in either direction. The pressure performance of this device is not completely evaluated and should be studied in the future. In Chapter 4, the measured flow rate produced by this device is presented.

Chapter 4

Experimental Analysis & Theoretical Comparisons

Experimental Setup

Performance analysis is carried out on the newly developed test setup illustrated in Figure 4.1. The pump, inlet/outlet and transfer valves are actuated using three different signals as explained in Chapter 3. The electrode is maintained at ground potential. Modeling results recommend the actuation of the pump and valve membranes using sinusoidal and trapezoidal waveforms respectively.

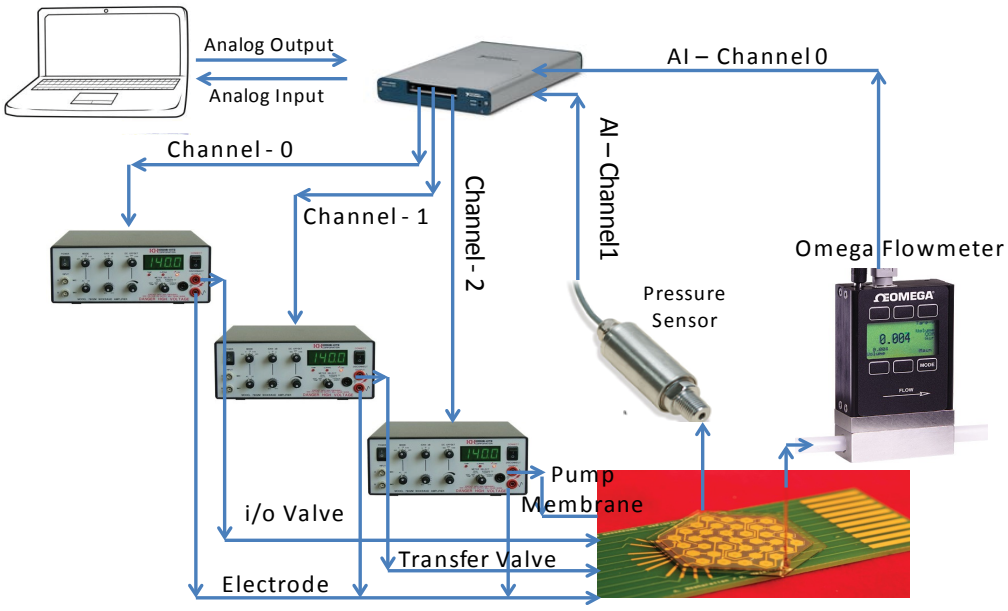

Figure 4.1: Experimental setup used to control the micropump.

The data acquisition card (NI-6353) outputs the analog signals to three amplifiers (Krohn Hite 7602), which are then used to actuate the different membranes. The ground outputs from these amplifiers are combined and connected to the electrode. To prevent damage to the membrane due to very large currents 100-kΩ, resistors are connected between the amplified signal and the membranes. The inlet and outlet ports are connected to an Omega pressure sensor and a flow meter (FMA-1601) respectively. The flow meter and the pressure sensor are connected to the analog input channels of the data acquisition card. These voltage signals are converted to flow rate and pressure using the prescribed calibration from the respective data sheets provided by the manufacturer. This data is processed using MATLAB to study the Flow vs. Frequency and Pressure vs. Time performance.

Analog output signals are generated using MATLAB. To enable easy control of the micropump, a GUI controller is developed in MATLAB as shown in Figure 4.2.

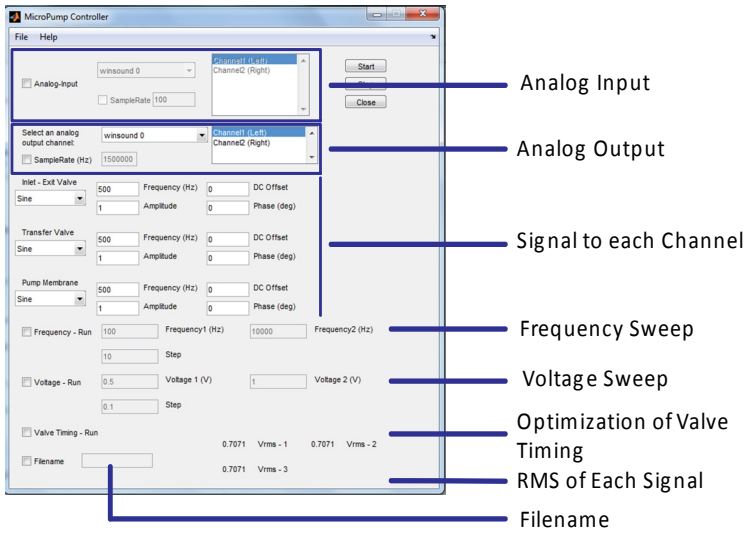

Figure 4.2: Micropump controller developed in MATLAB to generate corresponding signals and interpret flow and pressure data.

Each analog output signal is generated based on the waveform required. The user is allowed three signal options (sine, square and custom), which can be accessed using the drop down menu. Parameters that control a sine wave such as amplitude, phase, frequency and DC-offset can be changed by the user. A square wave depends on parameters such as t_{op}, t_{cl}, amplitude, rise time and frequency. The custom signal allows the user to input a prewritten signal. Each of these signals is generated using a sampling frequency of 1.5 MHz. However, the user is allowed the freedom to change this depending on the number of signals generated. Choice is also provided to the user to enable selection of any of the channels (numbered 0-3). For standard operation, only the first three channels are selected. A sample set of signals chosen for the pump, inlet and transfer valve membranes are shown in Figure 4.3. To analyze the flow performance and valve timing effects, the interface allows the user to scan the performance of the pump over a desired range of frequencies for the selected signals. For single frequency operation, output and input signals are generated and read by MATLAB for 45 seconds. Between two frequency transitions, the pump is rested for 30 seconds to eliminate any persisting transients. These parameters can only be changed in the code and not through the interface. Similar options are provided for the valve timing, where the t_{op} is fixed and t_{cl} is changed or vice versa. In order to read signals from the flow meter and pressure sensor, Channel 1 and Channel 2 need to be selected. These sensors have a sampling rate of 100 Hz. Therefore, the input signals are read at this frequency.

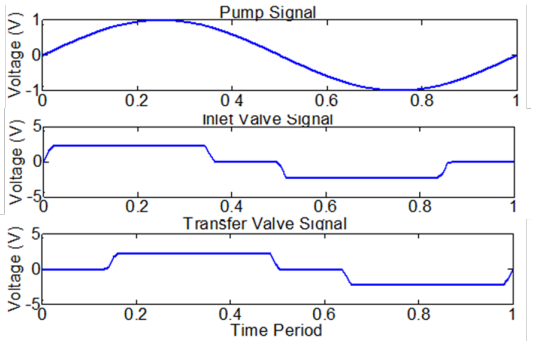

Figure 4.3: Driving signals used to actuate the pump, inlet and transfer valve membranes.

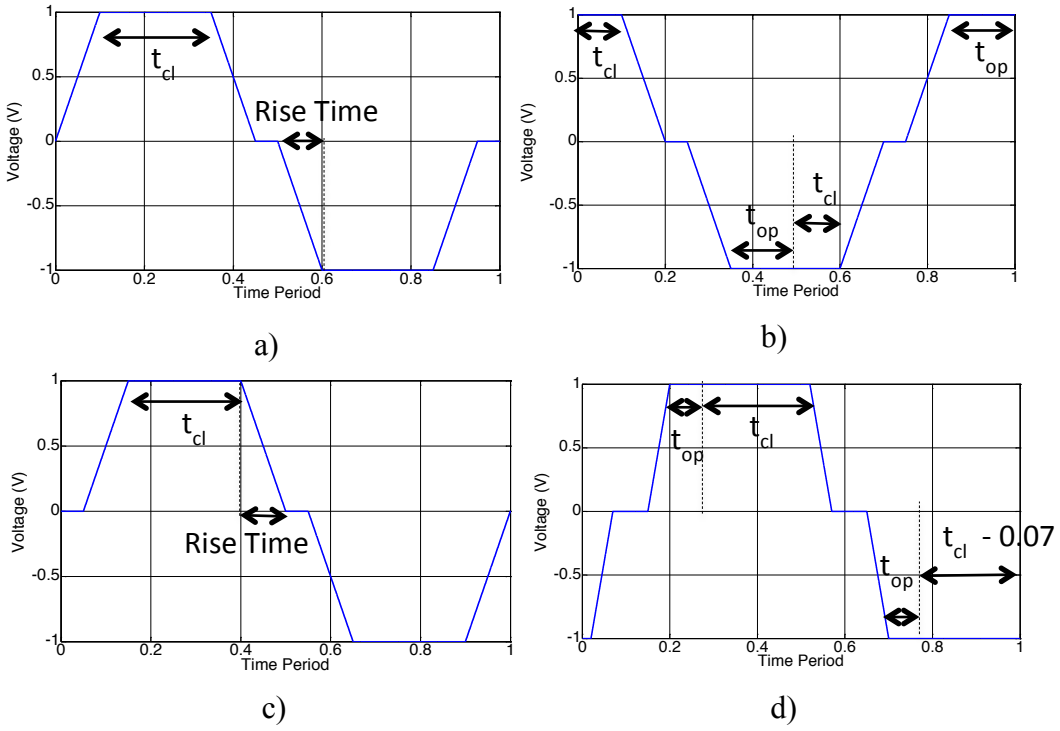

Figure 4.4: Trapezoidal waveforms generated for valve operation. Figures a) (case 1) and b) (case 2) represent the signal generated for the inlet valves while Figures c) (case 3) and d) (case 4) represent those generated for the transfer valve.

Figure 4.4 shows the trapezoidal waveforms generated for the inlet and transfer valves. The trapezoidal signals for the cases 1) (t_{op} =0, t_{cl} = 0.2 and rise time = 0.1), 2) (t_{op}=0.1, t_{cl}=0.15 and rise time = 0.1), 3) (t_{op} =0, t_{cl} = 0.25 and rise time = 0.1) and 4) (t_{op} =0.05, t_{cl} = 0.27 and rise time = 0.1) for a given cycle are shown in Figure 4.4a, Figure 4.4b, Figure 4.4c and Figure 4.4d respectively.

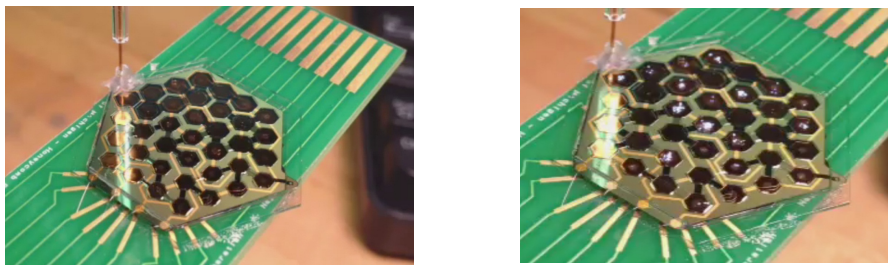

a) b)

Figure 4.5: Operating the pump using a trapezoidal waveform that does not have alternating positive and negative voltages. a and b represent the states of the pump when the pump is not operated and when it is operated using a positive trapezoidal waveform respectively.

Figure 4.4 illustrates the use of alternating positive and negative voltage in a single cycle for a given waveform. The reason for choosing this is shown in Figure 4.5b. Sparks were seen nearly instantaneously when a trapezoidal waveform (same polarity) was applied. This happens due to the charge accumulation on the membrane. To prevent this charge accumulation, the waveform in Figure 4.4 is chosen.

Membrane Characteristics found using Laser Vibrometer

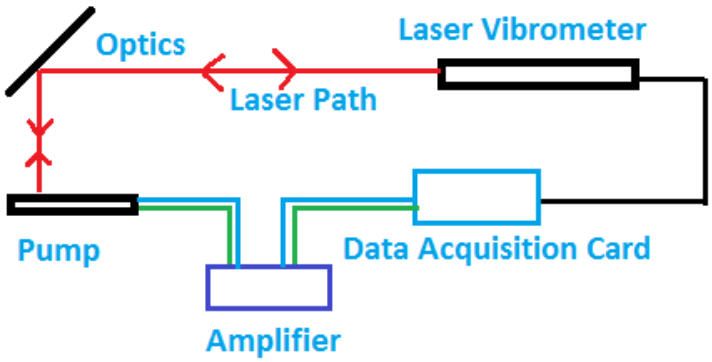

Figure 4.6: Schematic for measuring membrane displacement using laser vibrometer.

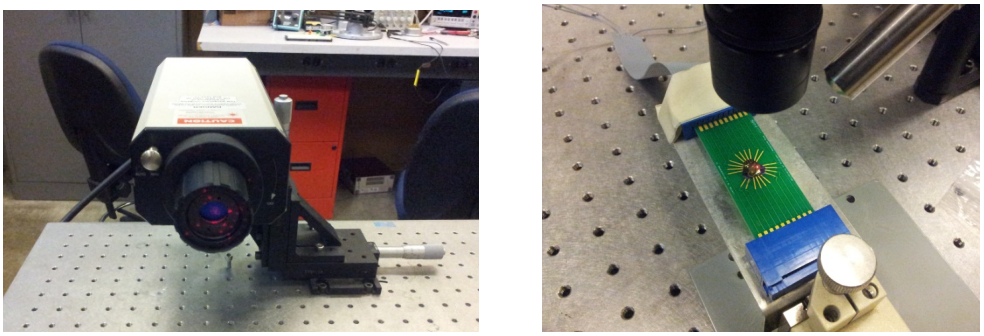

a) b)

Figure 4.7: Laser vibrometer setup to measure the displacement of 4-stage micropump. a and b show the reflection of the laser light from the membrane onto the detector and the focused spot on the pump membrane respectively.

A polytec OFV303.8 laser vibrometer is used to measure the membrane displacement as shown in Figure 4.5. The light from the laser is focused on the membrane using the laser's inbuilt optics. The output signal from the data acquisition

card is processed using a polytec OFV 3001S controller box. This filtered signal is then analyzed using MATLAB.

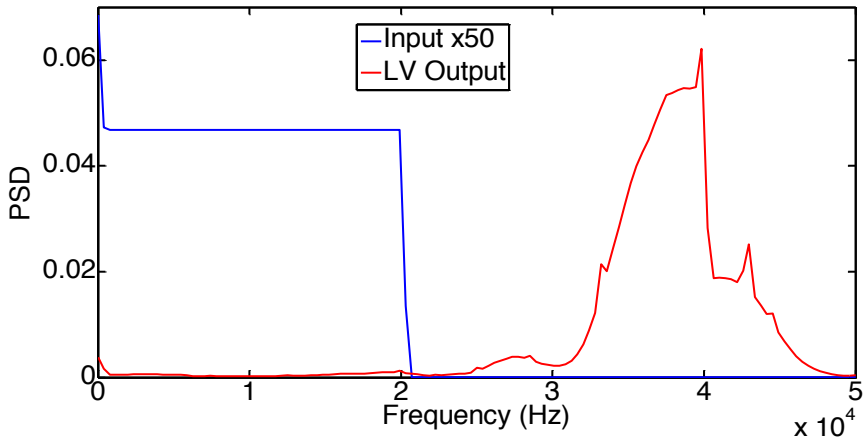

Figure 4.8: Measured resonant frequency of the pump membrane.

Using a chirp function with frequencies varying from 0–50 kHz, the resonant frequency of the membrane was measured to be 38 kHz as shown in Figure 4.8. The predicted theoretical resonant frequency is 35 kHz, which is in good correlation with the measured results.

The reflected laser light was found to form a pattern on the sensor as shown in Figure 4.6a. This pattern is due to the electrode hole pattern embossed on the membrane and is produced when the diaphragm is released. It was initially believed that this could affect the reading but a methodology was devised to eliminate any loss in data.

In Figure 4.6b, the laser light is focused on the center of the membrane using a microscope. Readings obtained using the inbuilt filters in the controller were found to eliminate vital information. To overcome this, the raw data produced by the laser is read and processed in MATLAB using a bandpass filter having limits of 0.5 and 300 kHz. To

estimate the displacement, the velocity is integrated while ensuring that the drift velocity is removed.

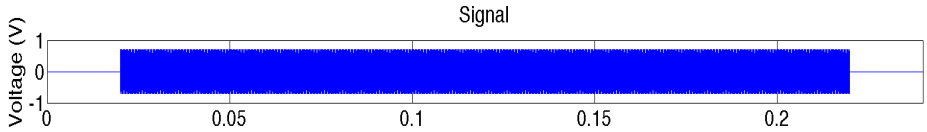

Figure 4.9: Schematic of the operation of the membrane for measuring the displacement of the diaphragm.

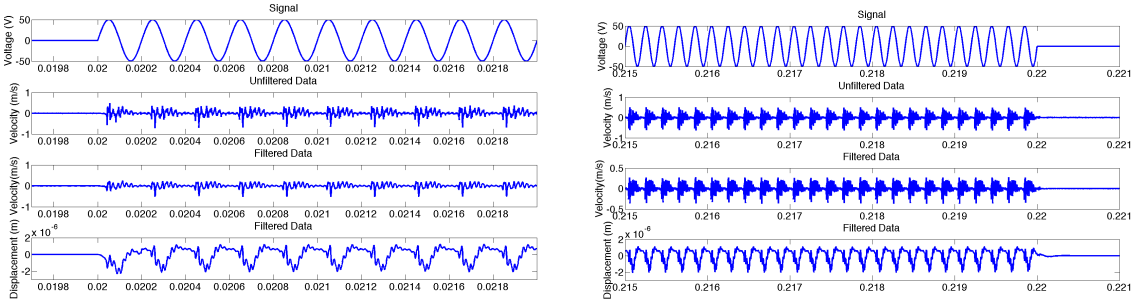

a) b)

Figure 4.10: Measured displacement of a membrane in a 24-stage micropump when operated at a frequency of 5 kHz and amplitude of 50V. Figures a) and b) represent the velocity measured at the beginning and at the end of the data acquisition period. The first, second, third and fourth traces in each figure represent the driving signal, unfiltered measured velocity, filtered velocity and displacement respectively.

The schematic of a three-step procedure followed to measure the displacement is shown in Figure 4.9. Initially, no signal is applied to actuate the membrane and only the output from the laser vibrometer is measured and should be zero. Subsequently, the membrane is actuated to measure velocity using a sinusoidal waveform having a time period of 100 cycles. Finally, no actuating signal is applied while the velocity of the membrane is measured during which the velocity of the membrane should dampen down to zero. The displacement of the membrane is measured by integrating the velocity and

ensuring that the membrane returns to its original position once the voltage is switched off.

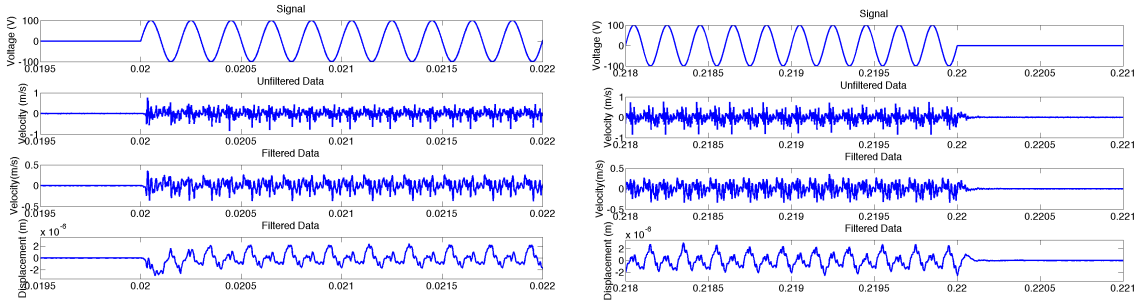

a) b)

Figure 4.11: Measured displacement of a membrane in a 24-stage micropump when operated at a frequency of 5 kHz and amplitude of 100V. Figures a) and b) represent the velocity measured at the beginning and at the end of the data acquisition period. The first, second, third and fourth traces in each figure represent the driving signal, unfiltered measured velocity, filtered velocity and displacement respectively.

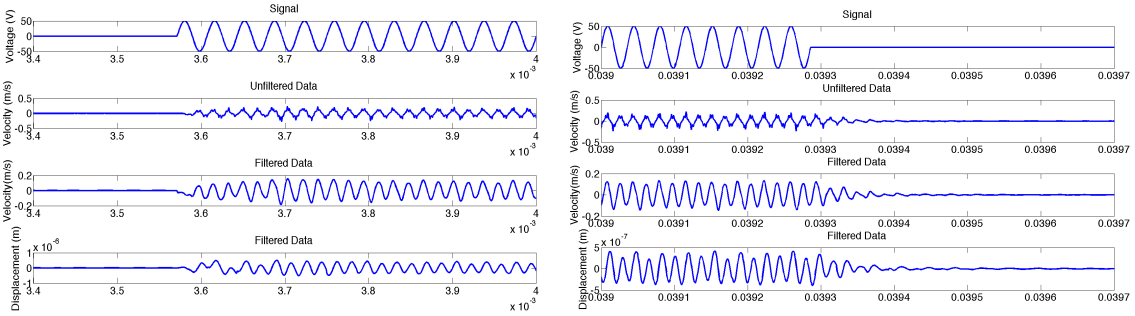

a) b)

Figure 4.12: Measured displacement of a membrane in a 24-stage micropump when operated at a frequency of 28 kHz and amplitude of 50V. Figures a) and b) represent the velocity measured at the beginning and at the end of the data acquisition period. The first, second, third and fourth traces in each figure represent the driving signal, unfiltered measured velocity, filtered velocity and displacement respectively.

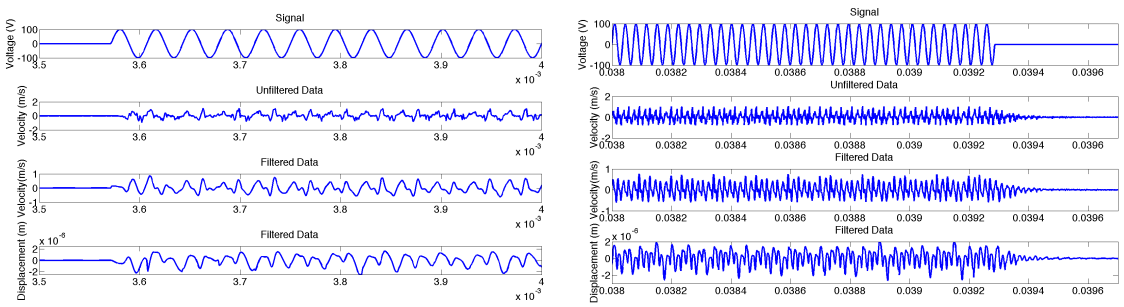

a) b)

Figure 4.13: Measured displacement of a membrane in a 24-stage micropump when operated at a frequency of 28 kHz and amplitude of 100V. Figures a) and b) represent the velocity measured at the beginning and at the end of the data acquisition period. The first, second, third and fourth traces in each figure represent the driving signal, unfiltered measured velocity, filtered velocity and displacement respectively.

Figures 4.10 and 4.11 illustrate the measured displacement of a membrane in a 24-stage micropump when operated at 5 kHz. When the pump membrane is operated at amplitude of 50 V, the maximum displacement estimated is ~$2x10^{-6}$ m and the frequency of oscillation is 5 kHz. The displacement of the membrane in the direction opposite to the electrode is not the same as that towards the electrode. The expected frequency doubling is not observed at these low voltages. When the voltage is increased as shown in Figure 4.12, the frequency of oscillation doubles to 10 kHz. The maximum displacement of the membrane on either side is equal to ~$2x10^{-6}$ m. When the voltage is switched off, the membrane returns back to its initial position, which validates the integration. The reduced order model does not predict the observed loss in frequency doubling. This could be due to the loss in information as a result of the pattern on the membrane. Further analysis needs to be carried out to study this observed behavior using more sophisticated techniques or by polishing the membrane.

Figures 4.12 and 4.13 illustrate the measured displacement of a membrane in a 24-stage micropump driven by a sinusoidal signal having frequency of 28 kHz and amplitudes of 50 and 100 V. It is observed that the signal obtained is less noisy than that measured at 5 kHz. However, the measured membrane displacement is not as high as that measured at 5 kHz. When the voltage is increased to 100 V, the maximum measured displacement is $<2x10^{-6}$m on either side of the initial position of the pump membrane. In comparison to the operation at 5 kHz, due to the inertia possessed by the membrane, the measured displacement of the membrane suggests that it takes longer to dampen down to the initial position. For all voltages and operation at 28 kHz, the membrane oscillates at 56 kHz (twice the driving frequency).

Power spectral density (PSD) for the measured velocity signal at the corresponding operating frequency and voltage is calculated using MATLAB's pwelch function, as shown in Figure 4.14. The maximum PSD was evaluated to be at 4 kHz. In subsequent sections, it will be shown that maximum flow rate was achieved at this frequency.

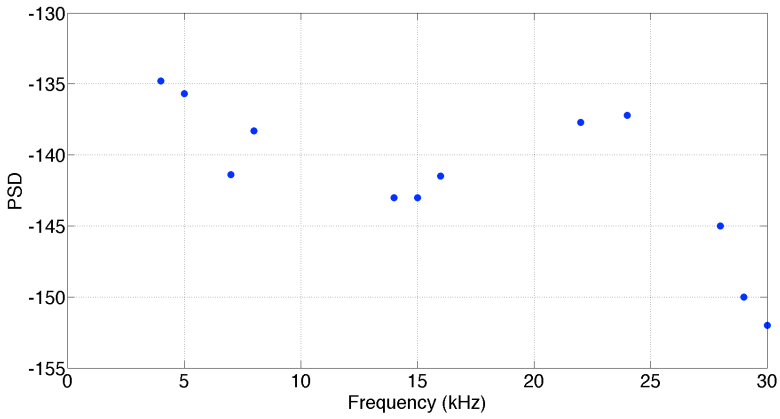

Figure 4.14: Measured PSD for membrane displacement when operated at the corresponding frequency at amplitude of 100 V.

Leakage Estimation

The first step in evaluating the performance of the pump is measuring leakage through the valves. To calculate the resistance of the device, a pressure difference is applied across the pump and the flow rate is measured. To measure the closed and open state resistances, the valves are either actuated or not actuated respectively. To measure the change in resistance with the position of the inlet/outlet valves, a DC voltage that is shown in Figure 4.15 is used to actuate them when a pressure difference is applied across the device.

Figure 4.15 suggests that a voltage of 90V is required to perfectly seal the valves when operated statically. The measured resistance of the valves in the open state is 3.5 kPa. From this, the measured L_v is 338 μm while the estimated value is 187 μm. The estimated value is nearly half that of the measured value. This discrepancy is due to the resistance of the channels, the possible blockage of some of the valve holes and the inlet and outlet capillary tubes. In the closed state, the resistance is 3000 kPa/sccm, which is nearly 1000 times that of the open resistance.

Dynamic performance of these valves has also been estimated as in Figure 4.16. When the valves are opened, the estimated flow rate is 0.12 sccm. A sinusoidal waveform having a frequency 2 Hz and amplitude 300V is applied to the inlet/outlet valves. The measurement indicates a doubling in resistance. This change in resistance will not be sufficient to produce the sealing required to achieve vacuum.

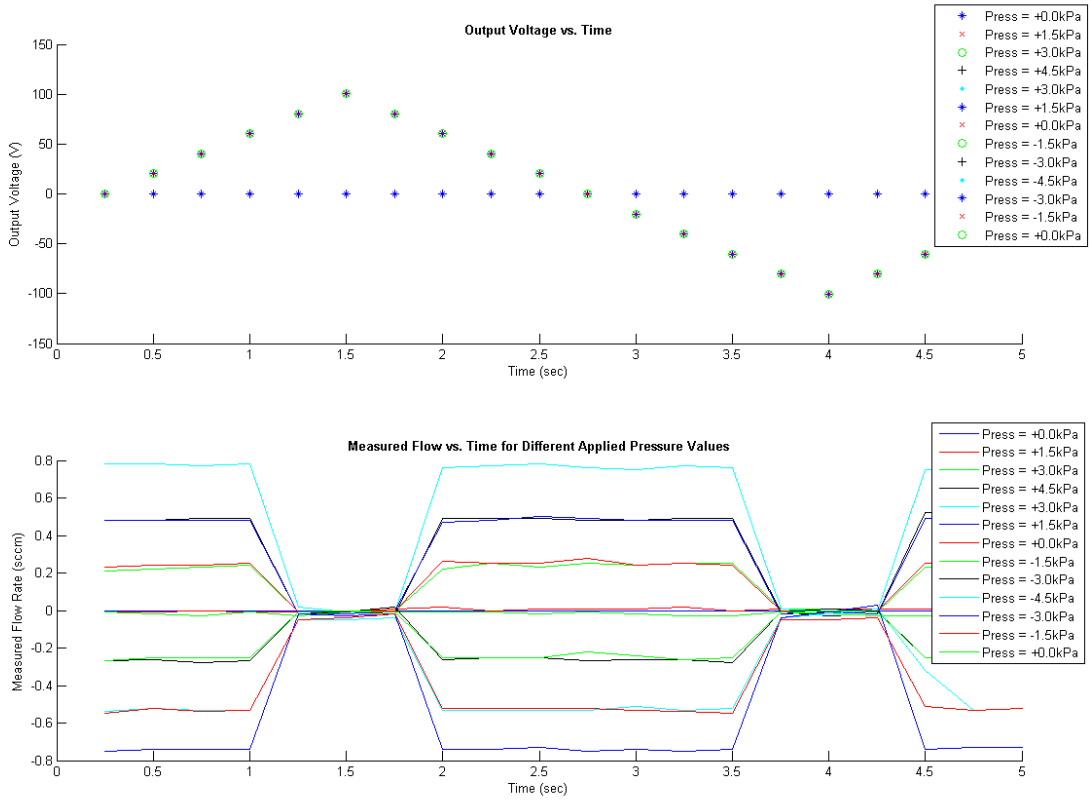

Figure 4.15: Inlet/outlet valve leakage characteristics for a 4-stage micropump. Top trace shows the applied voltage, bottom trace shows the flowrate change.

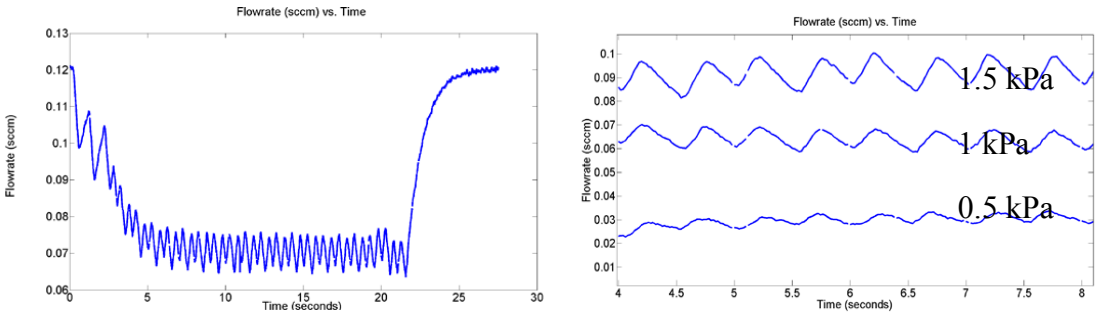

a) b)

Figure 4.16: Dynamic measurement of the change in resistance when the valves are operated using a sinusoidal waveform. Figure b is the enlargement of figure a when the valves are closed.

Measurement of Flow Rate

A setup similar to the one shown in Figure 4.1 is used to measure the flow rates produces by 4-, 12- and 24-stage micropumps. First we will analyze the performance of two 4-stage micropumps. The performance of this device is compared with the theoretical reduced order model.

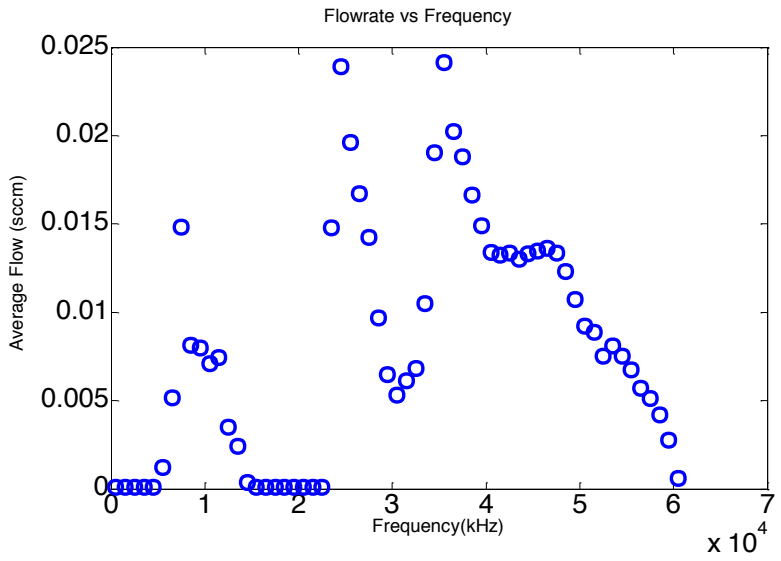

Figure 4.17: Flow rate measured for the corresponding frequencies. Sinusoidal and trapezoidal waveforms having amplitudes of 59Vrms and 115Vrms are used to actuate the corresponding pump and valve membranes respectively.

Figure 4.17 shows the flow rate estimated for a 4-stage micropump having properties shown in Table 3.5. Fabrication challenges and unequal stress gradients resulted in curvature of the valve electrode. Hence, a higher voltage is required to actuate these membranes. Figure 4.19 showed the formation of three peaks whose maxima occurred at 10, 25 and 35 kHz. These peaks correspond to the resonance of the two

cavities and the pump membrane as suggested by the multiphysics model. The cavity heights at the top and bottom were 60 and 90 μm respectively. Due to the inability of the flow meter to transmit negative signals, reverse flow rate is not shown in this figure. The low flow rate could be caused by the curvature of the valve electrode (producing low sealing), the presence of particles blocking the holes either on the valve electrode or membrane, leakage through the sidewalls and valve pumping. This device failed to produce flow after the above frequency sweep analysis had been carried out. A loud noise was heard when the pump produced flow.

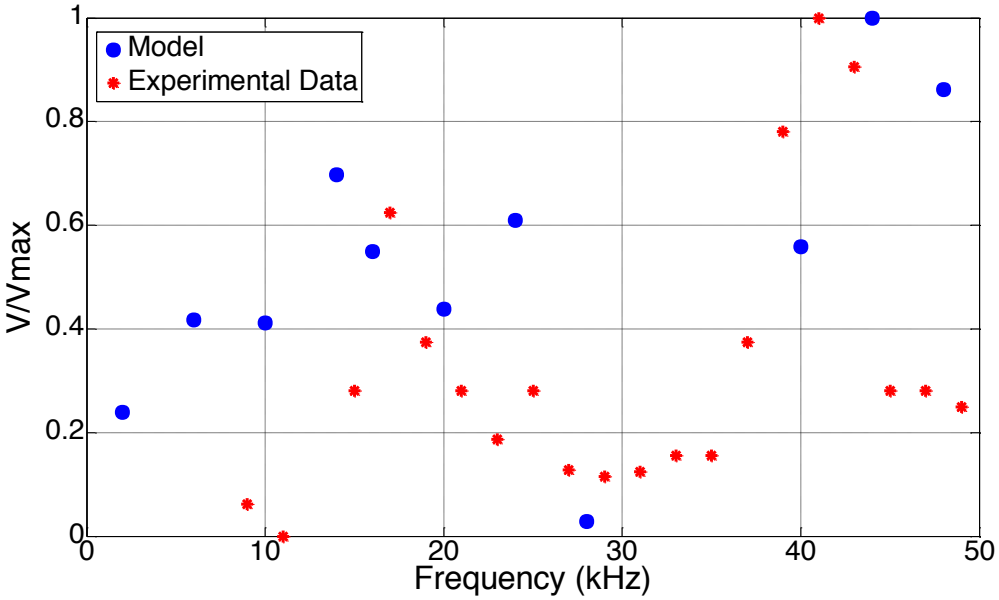

Figure 4.18: Comparison of flow rate vs. frequency between the model and experimental data. The measured flow rate is estimated on a second 4-stage micropump.

In Figure 4.18, the predicted flow rate for the applied frequency is compared with the measured flow rate. The flow rate predicted by the model is nearly double the measured result. Hence, the data presented in Figure 4.18 is normalized with the maximum flow rate. These results show that the three resonant peaks have been captured

fairly accurately. Predicted peaks occur at 14, 22 and 44 kHz, while the measured results show peaks to be at 17, 25 and 41 kHz. The predicted peaks and measured results for the first pump also correlate fairly accurately. These peaks were predicted with an error of 7-21% by the model. The main reason for this deviation is the curvature of the electrode, which introduces a higher volume source (changing the resonant frequency behavior). When the membrane is released from the electrode, nonlinear effects not included in the FEM model could alter the performance of the pump. Hence, the membrane model should be improved as part of future work. The lack of hexagonal modeling can also account for this observed deviation. However, since these peaks are estimated fairly accurately, the model serves as a first order tool to predict the frequency range for which the performance should be expected.

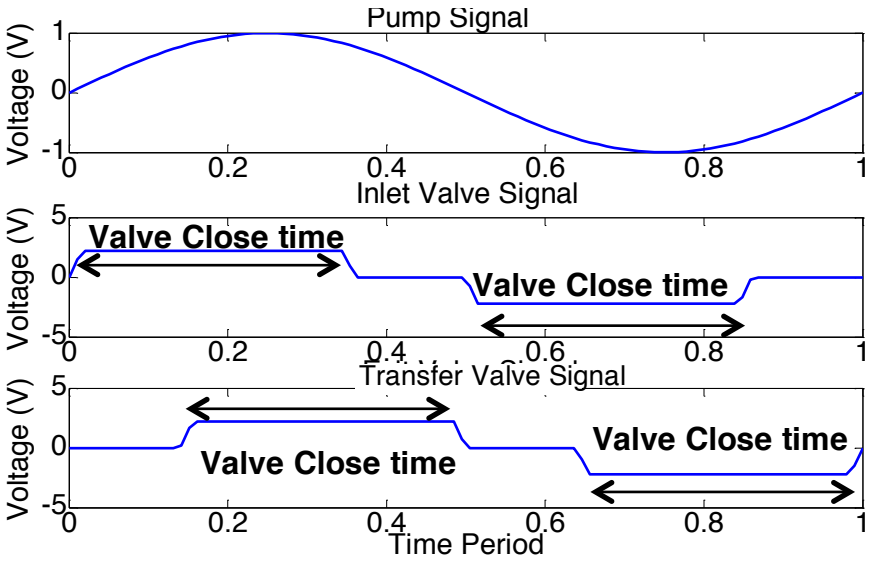

Figure 4.19: Signals used to actuate the pump, inlet/outlet and transfer valves.

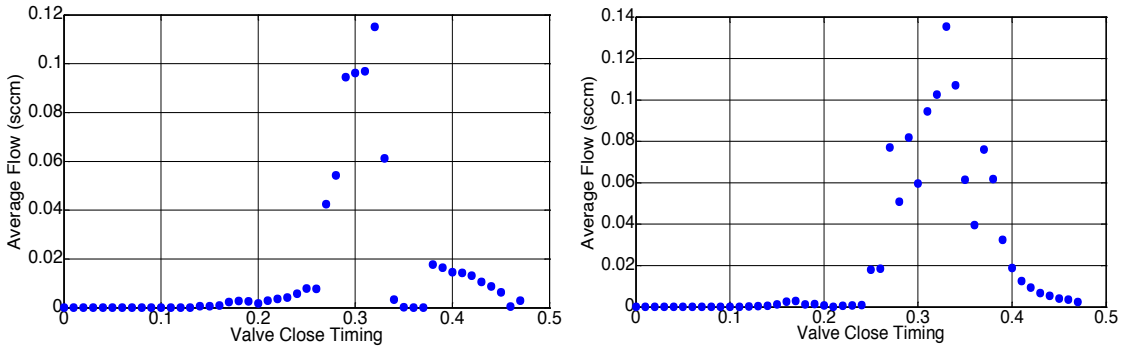

a) b)

Figure 4.20: Valve Timing optimization for a 12-stage micropump. a) and b) represent the optimization at frequencies 12 and 13.5 kHz respectively with t_{op} set to zero.

A 12-stage pump has the same geometric parameters as that of the 4-stage pumps with the only difference being the number of stages. From the analysis on the 4-stage device, the expected frequency is measured to be around 14 kHz. Hence an optimization of valve timing is carried out at 12 and 13.5 kHz as shown in Figure 4.20. Here t_{op} is set to zero and t_{cl} is varied. Valve time optimization showed that the maximum flow rates measured for the 12-stage device are 0.14 and 0.12 sccm when operated at 13.5 and 12 kHz respectively. Valve timing as expected plays a significant role in controlling the performance. The results in Figure 4.20a and b suggest that only a small range of t_{cl} produce flow. When the valves are opened for a very long or short duration, no flow rate is measured. The valves are opened for nearly half the cycle as shown in the Figure 4.19. Further optimization by adjusting t_{op} while maintaining t_{cl} constant was not possible as the device stopped functioning. Therefore, the model was able to predict the performance of the pump at these resonant frequencies fairly accurately.

Analysis was carried out on a variable compression ratio 24-stage micropump. The 24-stage device was divided into 6 modules, with volume ratios of 0.92, 0.94, 0.96

and 0.98. The cavity volume below the pump membrane for each module varies from 0.32, 0.3264, 0.3328 and 0.3392 mm^3 while for the top cavity the volume varies from 0.24, 0.2448, 0.2496 and 0.2544 mm^3.

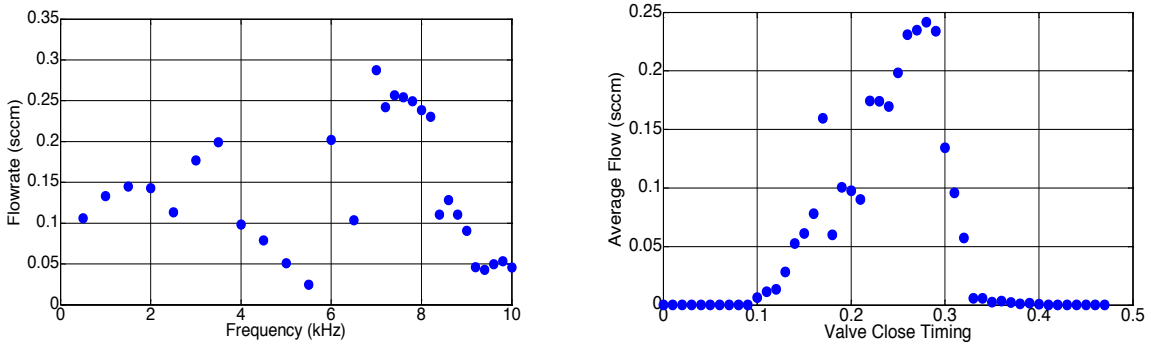

a) b)

Figure 4.21: Flow rate measurements for a 24-stage micropump. Figure a) Measurement of flow rate vs. frequency. Figure b) Optimization of valve timing at 7.5 kHz. A sine wave and trapezoidal waveform with amplitudes 59 Vrms and 150 V respectively are used to operate the pump.

The flow rate performance of a 24-stage micropump is shown in Figure 4.21. First, the flow rate is measured for a given operating frequency using the valve timing shown in Figure 4.19. Figure 4.21 shows the measured flow rate vs. frequency. The maximum performance is estimated to be at 7.5 kHz. A secondary peak performance was also measured at 4 kHz. This is in accordance with the laser vibrometer results in the previous section. The maximum displacement of the membrane was found to occur in the frequency range 4-10 kHz as shown in Figure 4.14. The valve timing is optimized at 7.5 kHz and was found to produce flow in a much larger range of timings in comparison to the 12-stage device due to its modular design. Thus, the volume ratio and valve timing govern the operation of the pump as suggested by previous modeling analyses.

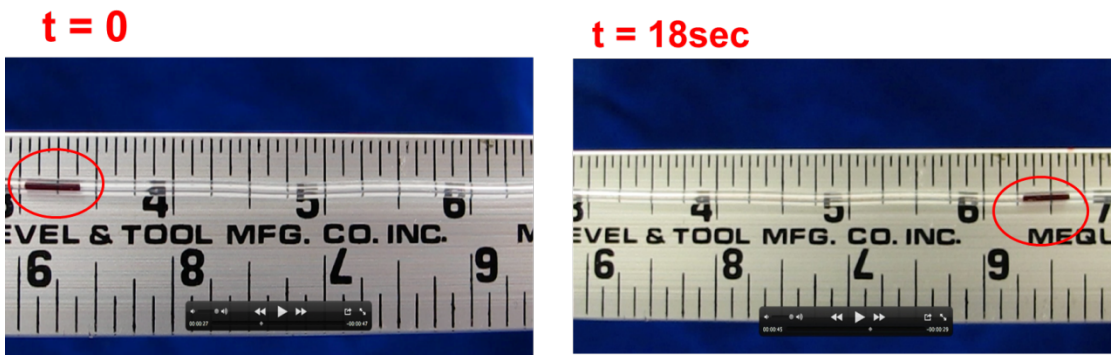

Figure 4.22: Droplet moved by 24-stage micropump when operated at 7.5 kHz.

To visualize the performance of the pump, a drop of ~2 mm length is inserted into a tygon tube and moved by the 24-stage device. The device displaced the droplet by 3 cm in 18 seconds as shown in Figure 4.22. The operating frequency of the device was 7.5 kHz. This experiment suggests that a pressure drop allowed the droplet to be moved. However, none of these devices were able to decrease the pressure in a volume. The pressure would drop by 100 Pa initially and then rise back up to atmospheric. This is believed to be due to low sealing or leakage. The resonant nature of the device and the sensitivity to valve timing stresses the need to implement DVT.

Valve Only Pumping

In Chapter 3, the concept of valve pumping was theoretically analyzed. The analysis showed that just the valve membranes could produce pumping. To experimentally verify this concept, a 12-stage micropump's electrode and pump membranes were broken and sealed with a thin film of epoxy as shown in Figure 4.23. The fluidic path remains the same as before with no contribution to the volume change from the pump membrane.

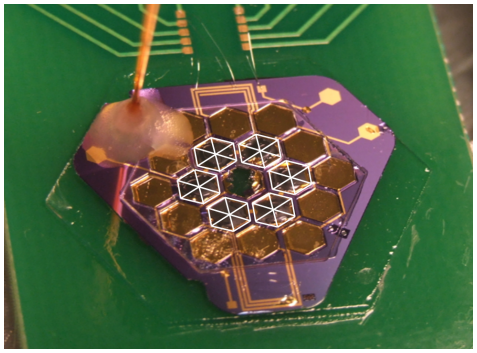

Figure 4.23: Modification to a 12-stage micropump to study the effect of valve only pumping. The hexagonal white lines show the elimination of the pump membranes.

Previous theoretical analysis recommends the use of sine and cosine waveforms for the operation of the inlet/outlet and transfer valves to produce flow. Thus, the device shown in Figure 4.23 is operated using these waveforms each of which have an amplitude 115 Vrms. Figure 4.24 shows that flow rate is produced between 0.5-1 kHz. The flow rate produced when the device is operated at 1 kHz is nearly 0.15 sccm, as seen in Figure 4.24b. When the device is operated at 0.5kHz, a very small flow rate is produced, but with time it decreased to zero, as shown in Figure 4.24a. When a trapezoidal waveform is

used an average flow rate of 0.05 sccm is measured as shown in Figure 4.25. Though the sinusoidal and cosine waveforms produce better performance than the trapezoidal waveform, further analysis needs to be carried to optimize these signals.

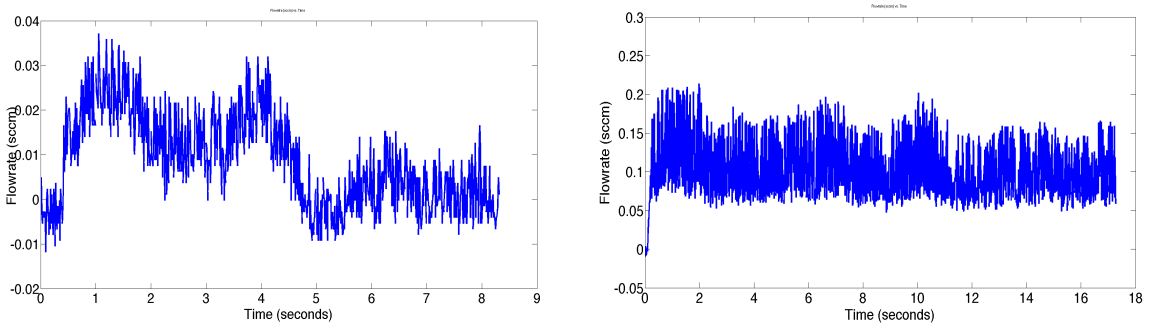

a) b)

Figure 4.24: Valve only pumping flow results for a 12-stage micropump. Figures a and b represent the flow rate when the pump is operated at 0.5 and 1 kHz respectively.

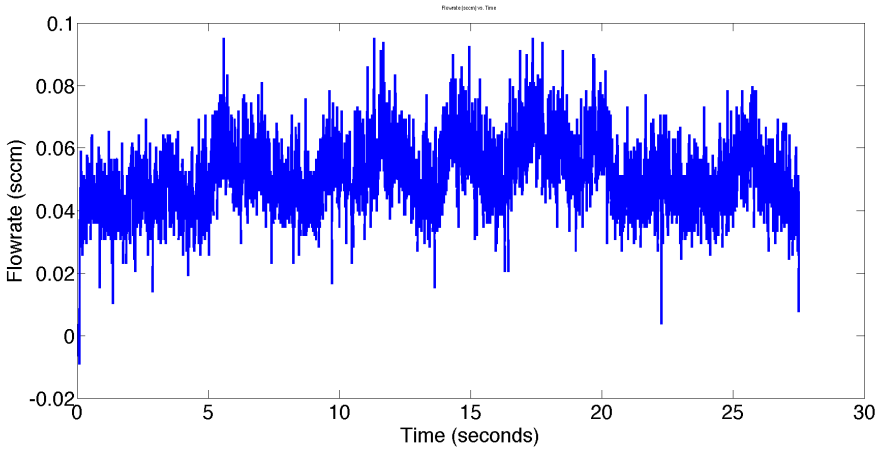

Figure 4.25: Flow rate generated by valve only pumping when a 12-stage micropump is operated using a trapezoidal waveform.

Chapter 5

Computational Fluid Dynamic Modeling

Need for Computational fluid dynamic modeling

The multiphysics model developed, assumes equal pressure distribution in each stage and operation using square membranes instead of hexagonal membranes. Despite these assumptions, it predicted the resonant peaks in experiments accurately. However, the hexagonal shape and the large size of the device could pose acoustic challenges that cannot be captured by the model. Sophisticated experiments like PIV, required to measure inertial and wave propagation effects, are difficult due to the dimensions of the electrode pump system and the size of the device. Measurement of the membrane deflection using the laser vibrometer provided an insight into the velocity and deflection characteristics of the membranes but did not give any information about the acoustic phenomena. Due to the unavailability of experimental techniques, Computational Fluid Dynamics (CFD) is used to study the pressure distribution in each stage.

Finite elemental analysis is required to predict the structural deflection of the membrane. The acoustic pressure in the device is driven by this deflection and hence would require coupling, CFD and FEA. Large computational resources are required for CFD analysis of such devices. This analysis is simplified by assuming that the deflection

of the membrane is similar to that of a piston motion and hence only CFD analysis is required.

The model setup for CFD analysis along with the hole configuration is shown in Figure 5.1. For simplified analysis, only the pressure in the bottom stage is studied. To further reduce computational time, this bottom stage is split into half along the symmetry plane as shown. The model setup also takes into account the transfer and exit valves. The arrangement of the holes on the pump, valve electrode and valve membrane are shown in Figure 5.1.

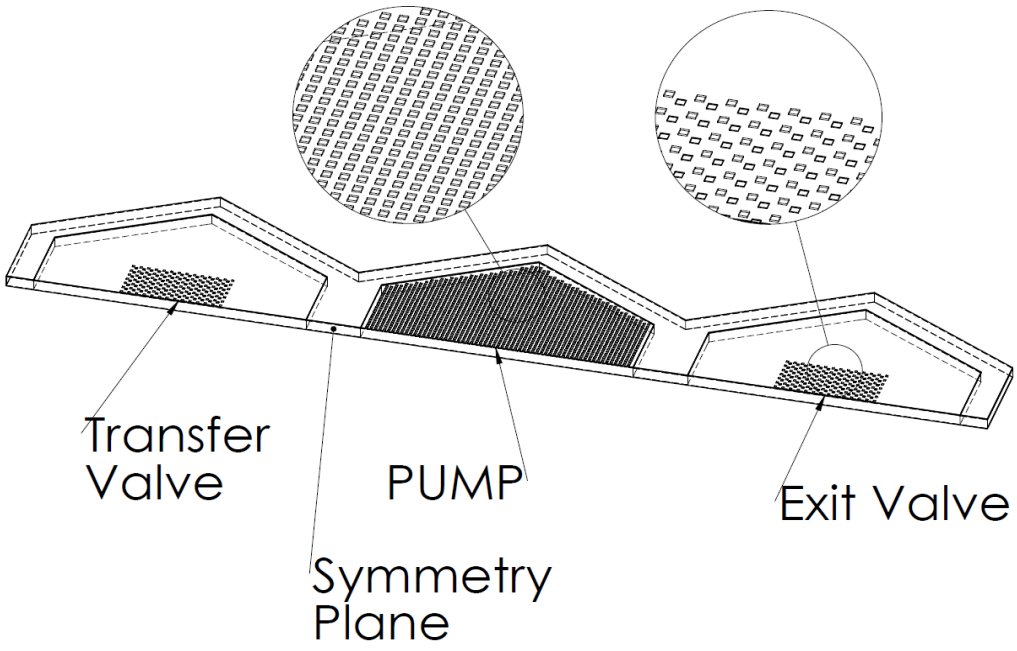

Figure 5.1: Hole Pattern arrangement on the valve and pump electrode membrane system.

Geometric properties of the device are shown in Table 5.1. The dimensions used in this chapter are similar to that used for fabrication of the device (highlighted in chapter 4).

Geometric Parameters	Value
Cavity height	100 µm
Channel Length	50 µm
Membrane Diameter	2.5 mm
Holes – Valve Electrode	196
Holes – Pump Electrode	1600
Holes – Valve Membrane	169

Table 5.1: Geometric parameters used for modeling the micropump using CFD.

STARCCM+ v7.02.008 is used for CFD analysis of the micro pump. Once the model is created in SOLIDWORKS, the fluid volume is extracted using the surface repair tool. The micro pump is broken up into 5 regions, the bottom cavity, pump membrane and electrode, transfer and exit membranes and electrode and finally the holes connecting the bottom cavity to each of the membrane and electrode systems. An ideal gas laminar model along with a segregated implicit unsteady solver is used to study the flow phenomenon. Two different meshes are used to solve the problem. In the bottom cavity, a polyhedral mesh having a base size of 10 µm, and a trimmer mesh in the remaining sections, having a base size of 4µm, is used. Though the polyhedral mesh reduces the mesh count drastically, it provides significant refinement in the process of capturing the necessary flow physics. Figure 5.2 is the mesh used in different sections of the pump setup. The total cell count is 7588234. Figure 5.2a shows the section planes existing in different regions of the pump. Figure 5.2b and c show the mesh in pump and valve regions respectively. In the gap between the membrane and the electrode in the pump and

valves, only two mesh layers are used to prevent the drastic change in aspect ratio when the membranes move. However, the meshes in all the regions are still fine enough to capture the necessary physics.

Based on the size of the device, the acoustic wavelength is estimated to be 17.444 kHz. Preliminary analysis constitutes actuating the pump membrane with the valves kept stationary. The pump membrane oscillates in a sinusoidal manner, changing the volume as if a piston is used to drive the gas. The maximum displacement of the membrane towards the electrode is 3.4 μm and not the entire electrode gap of 4 μm, due to the constraints of the software. Initial position of the membrane is 4 μm from the electrode and later deflects ±3.4 μm from its initial position. Initial conditions are atmospheric pressure and zero velocity everywhere. The pump membrane oscillates at $1/5^{th}$ of the acoustic frequency and the time step is 0.25 μsec in order to capture the propagation of the gas with a high resolution.

Figure 5.3 and Figure 5.4 illustrate the time varying pressure at various points. The pressure at the symmetry plane and interior positions are chosen to study the spatial variation in pressure. Figure 5.3 suggests that the pressure under the valve has a small phase lag in comparison to that below the pump membrane. This is due to the propagation of the pressure wave. However, this lag is insignificant and at this frequency, the pressure is assumed to be uniform. Figure 5.4 does not indicate the existence of any spatial variation in pressure, which is also observed on the symmetry plane. Thus, the hexagonal shape of the valve and pump chambers do not affect the pressure in the cavity. The maximum pressure rise and drop in the cavity is ~900 Pa. Due to the sinusoidal variation in motion of the pump membrane, the flow rate through each valve is equal and

follows the motion of the pump membrane as shown in Figure 5.5. The maximum flow rate in and out of the valve is ~1^{-7} kg/s.

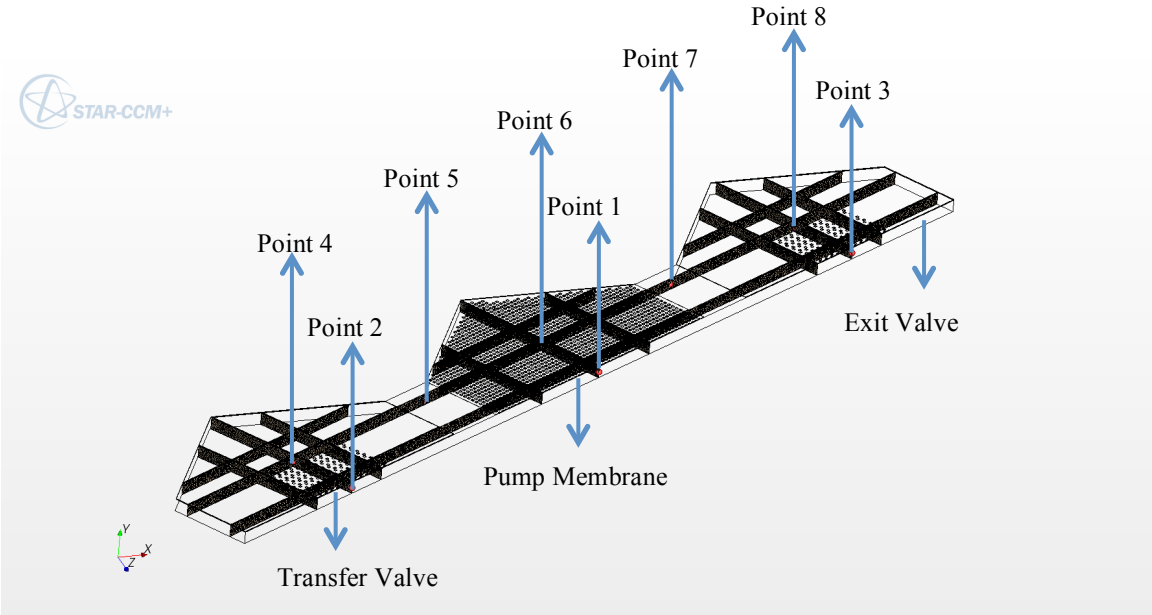

a)

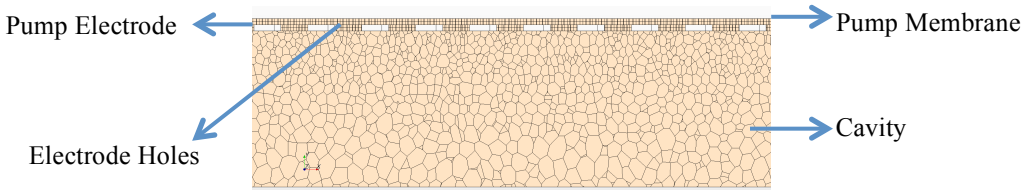

b)

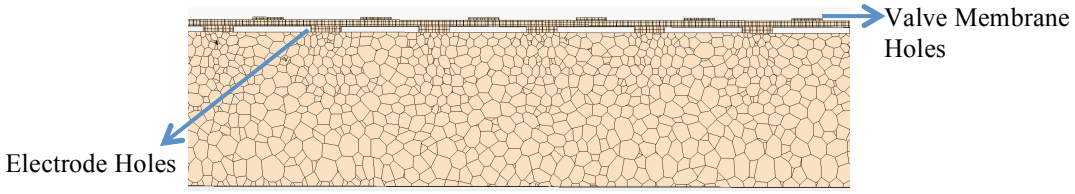

c)

Figure 5.2: Mesh Setup for the model. a) shows the section slices through different parts of the body. b) shows the mesh setup in the pump region while c) shows the mesh setup in the valve region.

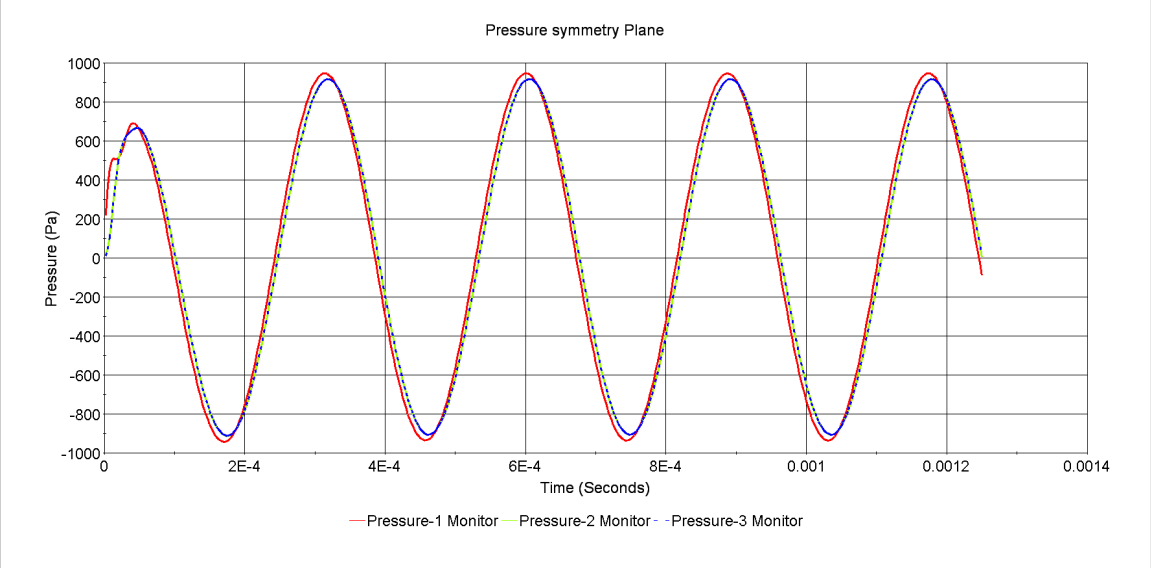

Figure 5.3: Time Variation of the pressure on the symmetry plane at points 1, 2 and 3 respectively (operated at 3.488 kHz).

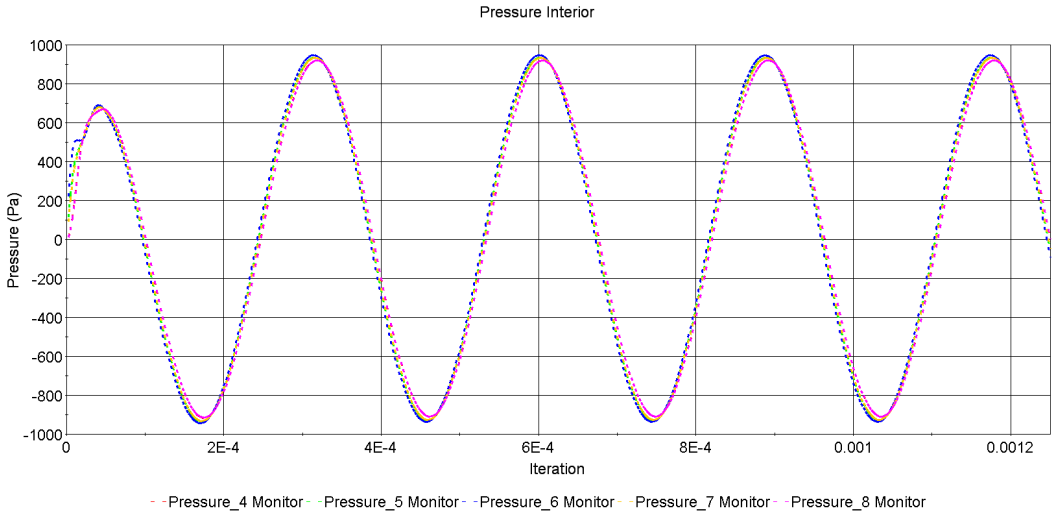

Figure 5.4: Time Variation of the pressure in the interior at points 4, 5, 6, 7 and 8 respectively (operated at 3.488 kHz).

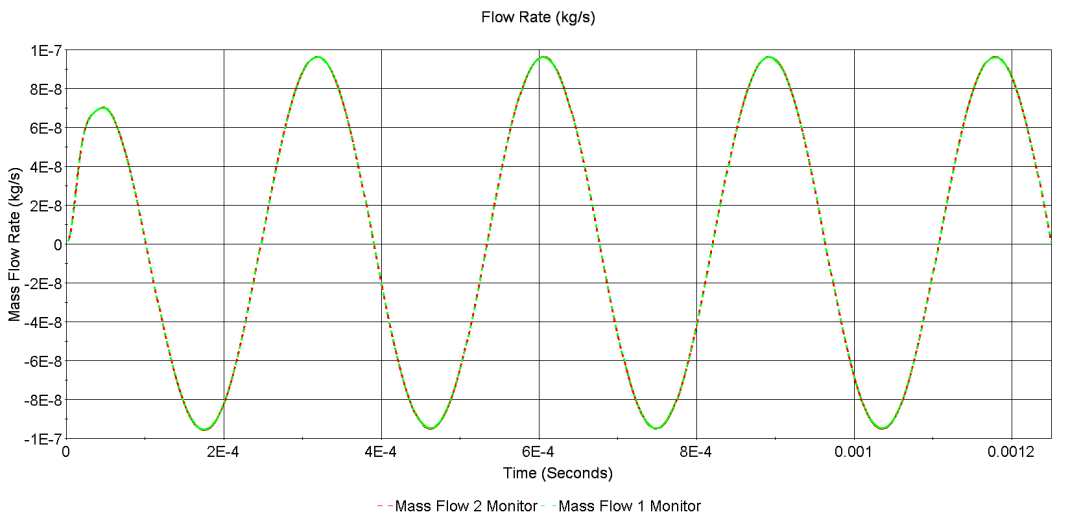

Figure 5.5: Time Variation of the mass flow rate through the transfer and exit valve respectively (operated at 3.488 kHz).

Figure 5.6 shows the contours of the velocity magnitude through the micropump for every given quarter in the third cycle. The contour plots suggest that the maximum flow rate exists between the channel connecting the pump and the valve membranes. Pressure loss due to the channel is smaller than that through the valve holes. Traversing from figures a – e, the effect of the cyclic motion of the membrane on the velocity is observed. Initially when the membrane moves downwards, the velocity increases and then starts decreasing as it moves in the opposite direction and increases again when the membrane starts moving towards the electrode.

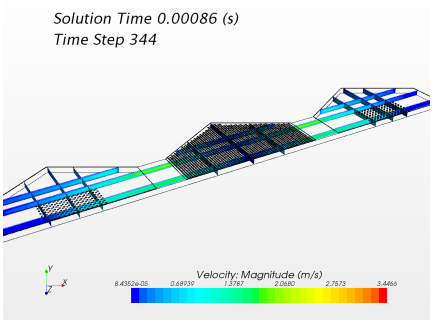

a)

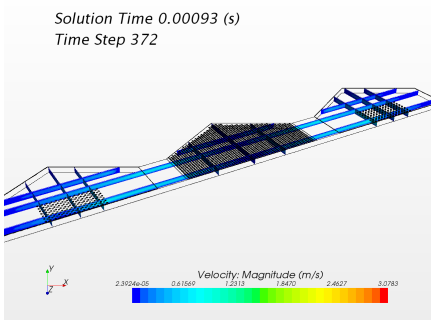

b)

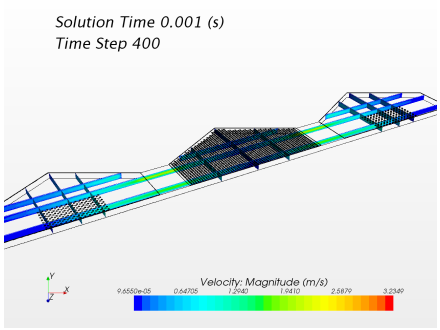

c)

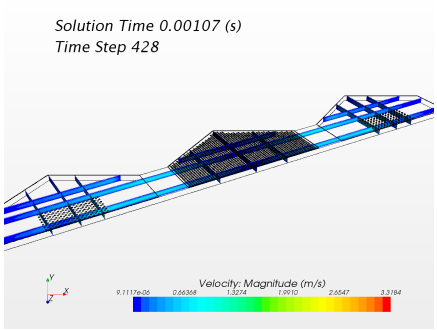

d)

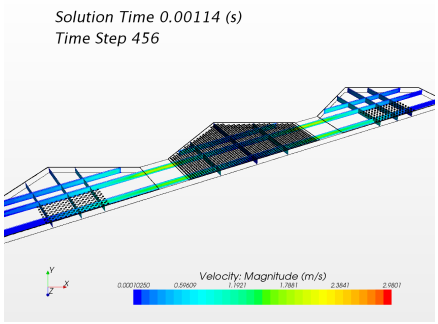

e)

Figure 5.6: Velocity distribution in the pump for each quarter of a cycle. Figures a, b, c, d and e represent the velocity magnitude on the section planes at 3.0, 3.25, 3.5, 3.75 and 4th period of the given simulation time.

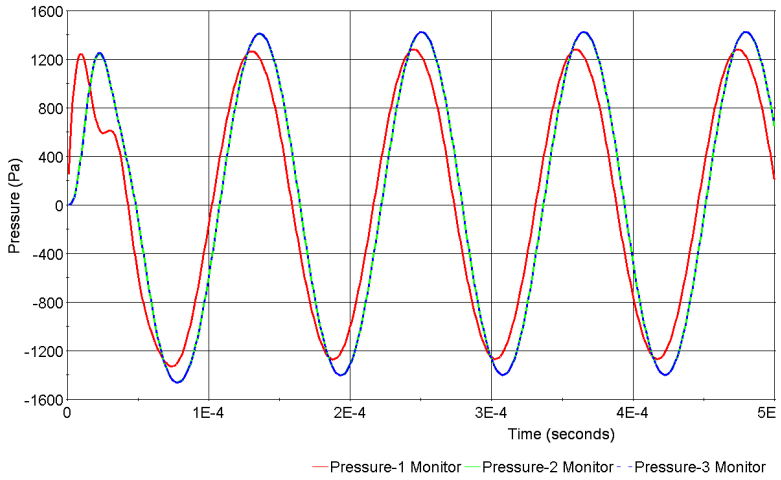

Figure 5.7: Time Variation of the pressure on the symmetry plane at points 1, 2 and 3 respectively (operated at 8.722 kHz).

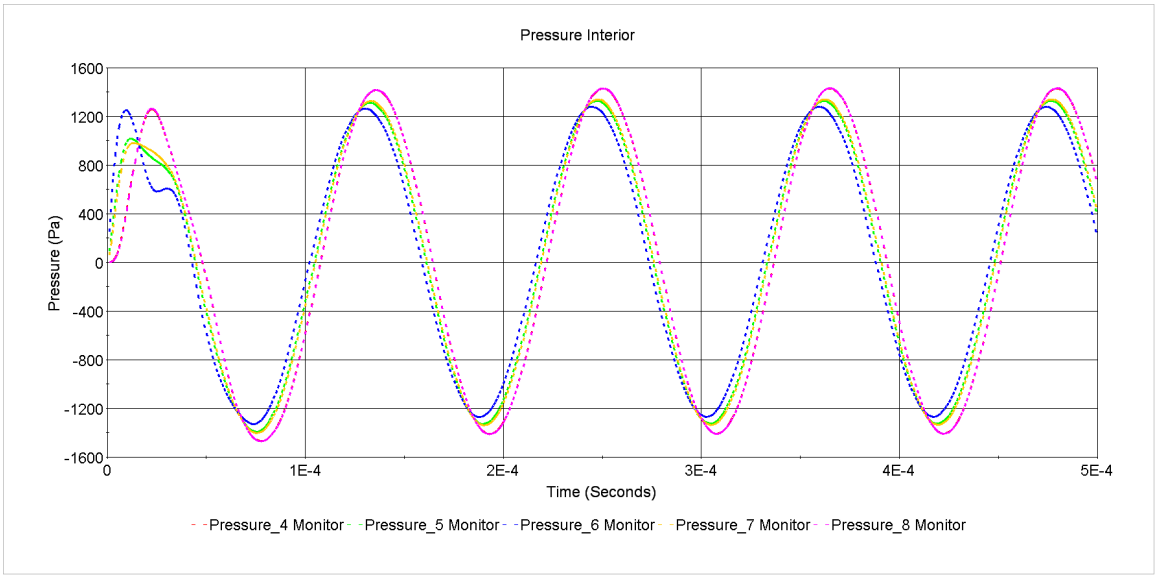

Figure 5.8: Time Variation of the pressure on the symmetry plane at points 4, 5, 6, 7 and 8 respectively (operated at 8.722 kHz).

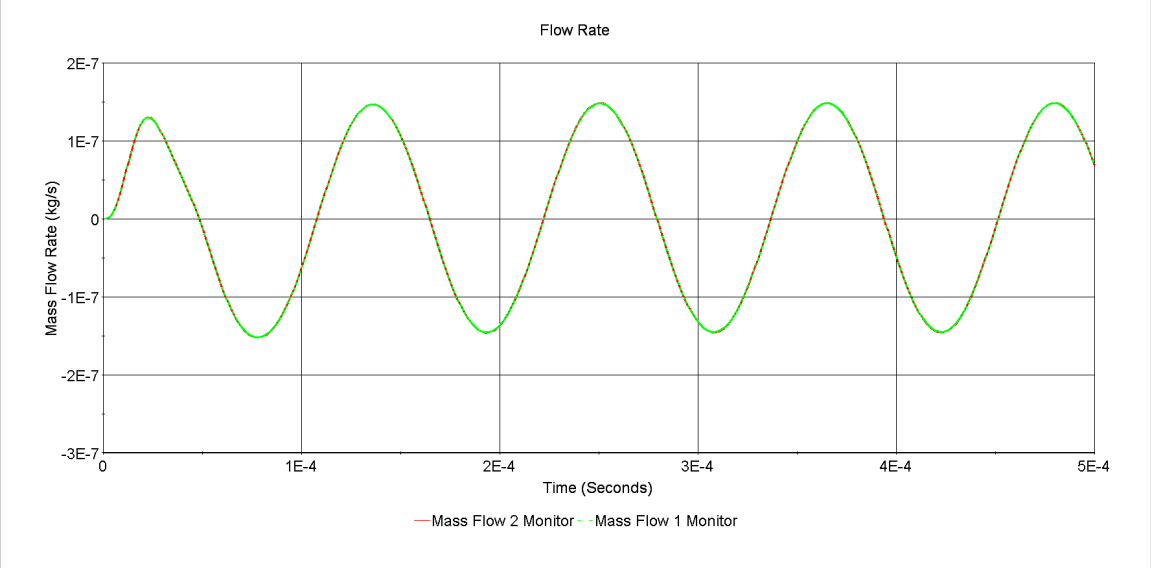

Figure 5.9: Time Variation of the mass flow rate through the transfer and exit valve respectively (operated at 8.722 kHz).

Figure 5.7 shows the pressure distribution at points 1, 2 and 3 on the symmetry plane, while Figure 5.8 shows the pressure distribution at points 4, 5, 6, 7 and 8 located in the interior of the pump. The pump is operated at 8.722 kHz (half the acoustic frequency). The figures suggest that there is a larger phase lag between the points located under the pump membrane and valve membrane in comparison to the operation of the pump at 3.422 kHz. However, this phase lag is not sufficient to affect the performance of the pump. It is also observed that the pressure variation magnitude under the pump membrane is lower than the pressure variation magnitude under the valve membrane. The presence of lesser number of holes on the valves contributes to the increase in pressure. The flow rate shown in Figure 5.9 is predicted to be $>1^{-7}$ kg/s. This variation follows the membrane motion. The velocity contours in Figure 5.10 shows a similar flow performance behavior as that of the 3.422 kHz operation.

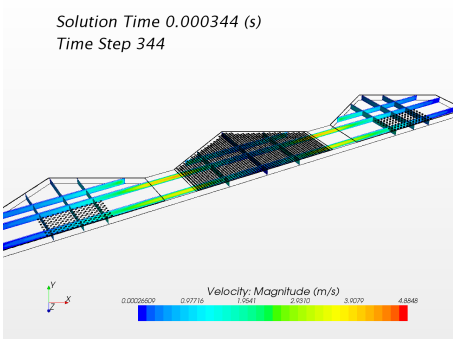

a)

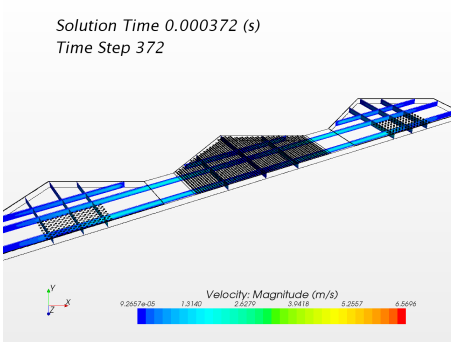

b)

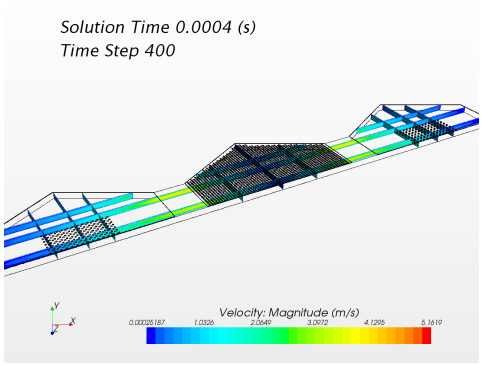

c)

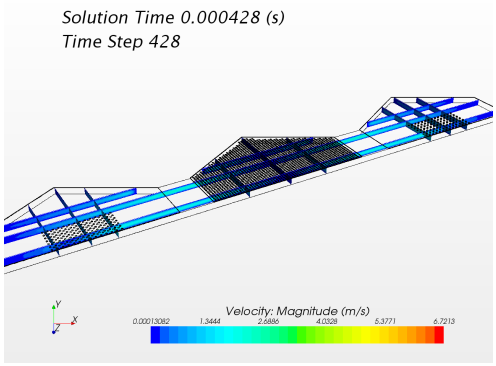

d)

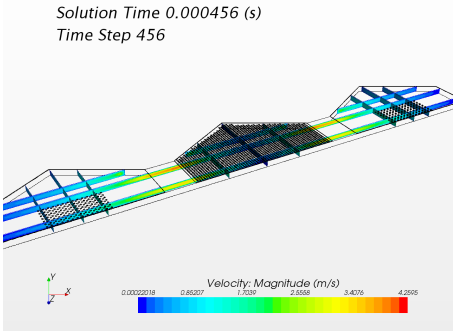

e)

Figure 5.10: Velocity distribution in the pump for different quarters of a cycle when operated at 8.722 kHz. Figures a, b, c, d and e represent the velocity magnitude on the section planes at 3.0, 3.25, 3.5, 3.75 and 4th period of the given simulation time.

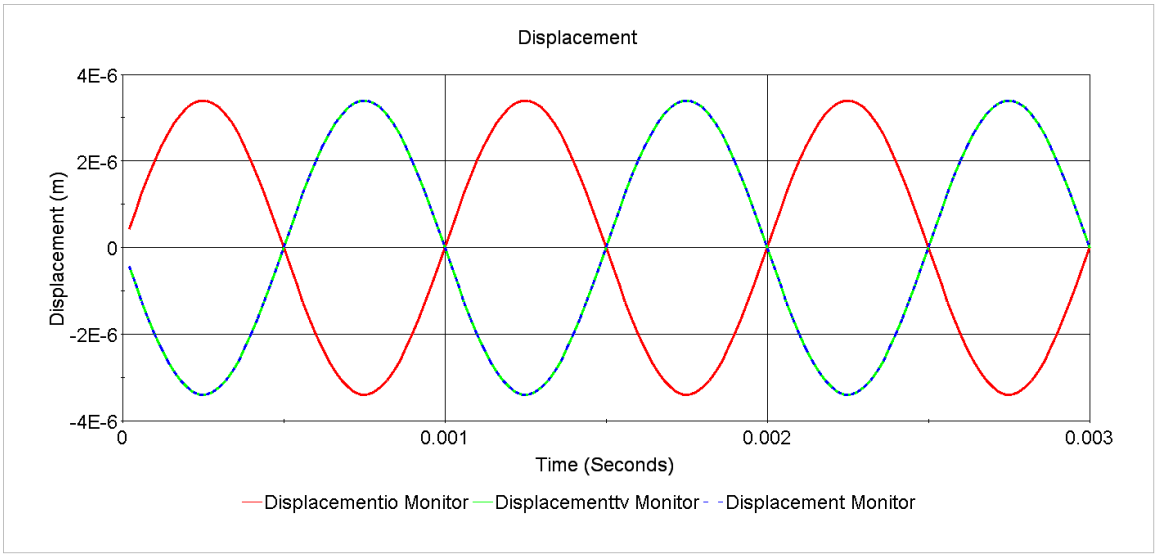

Figure 5.11: Displacement of the exit valve, transfer valve and pump membrane.

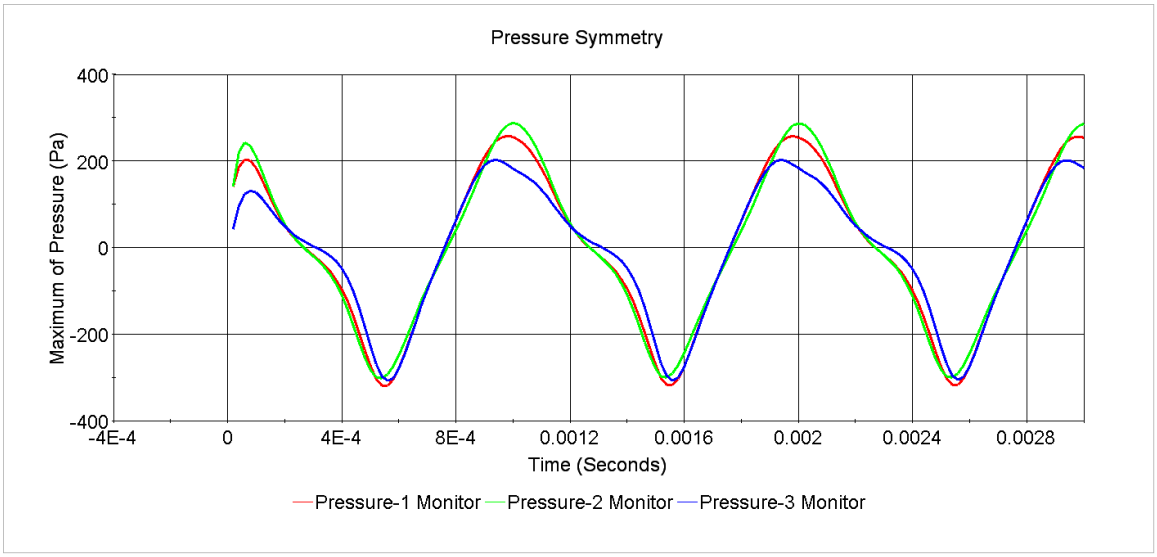

Figure 5.12: Pressure distribution on the symmetry planes for points 1, 2 and 3 when the pump and valve membranes are operated at 1 kHz.

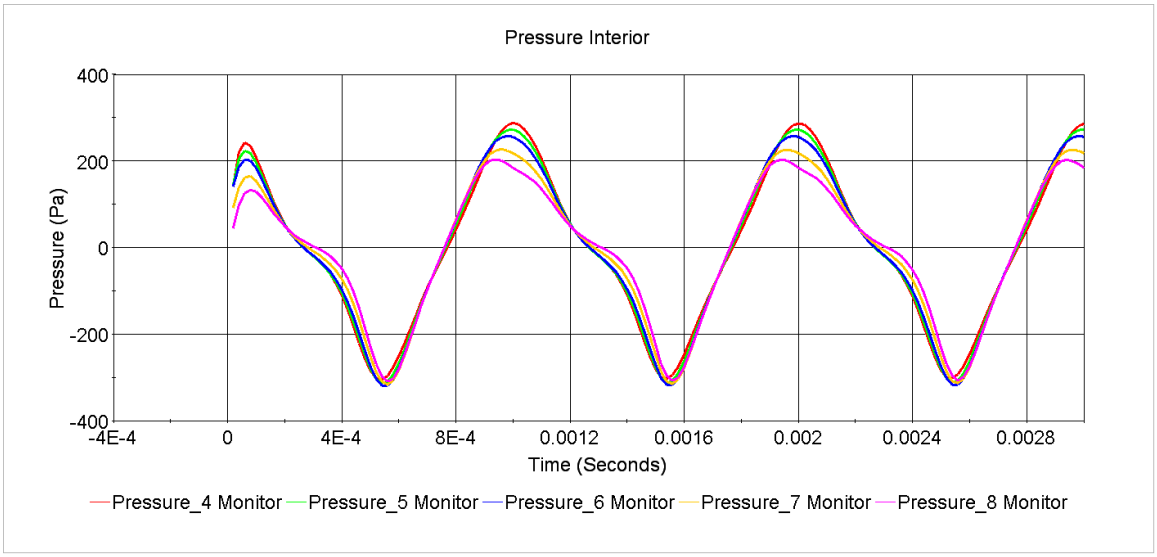

Figure 5.13: Pressure distribution in the interior at points 4, 5, 6, 7 and 8 when the pump and valve membranes are operated at 1 kHz.

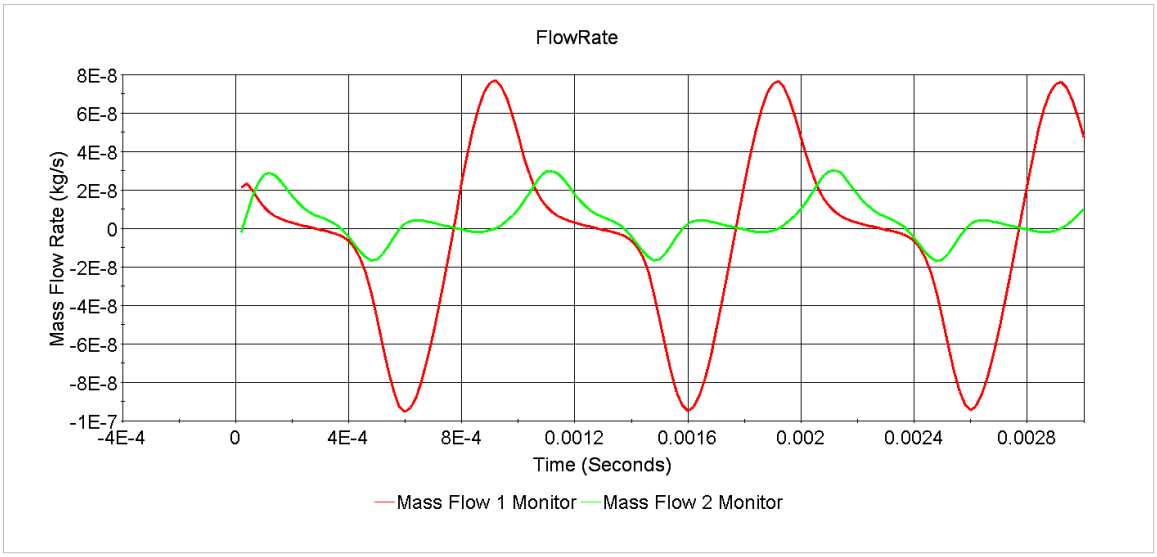

Figure 5.14: Flow rate through the transfer valve and exit valve shown by the red and green lines respectively.

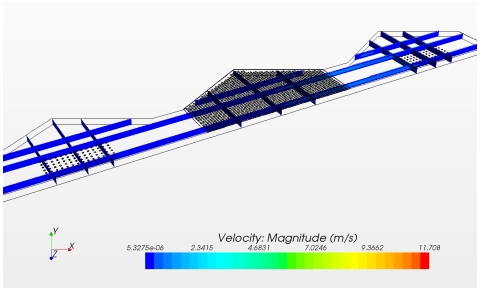

a)

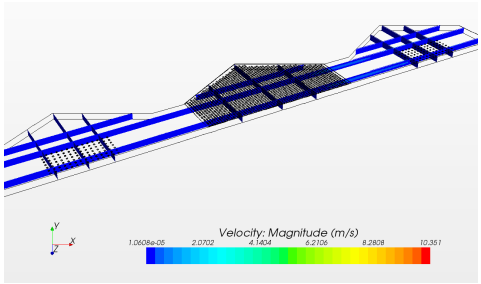

b)

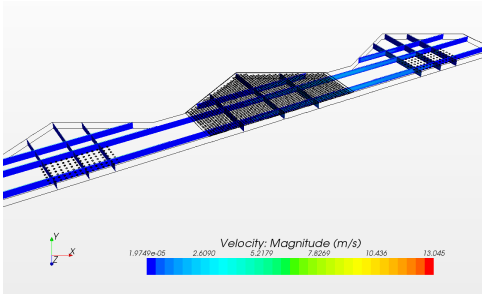

c)

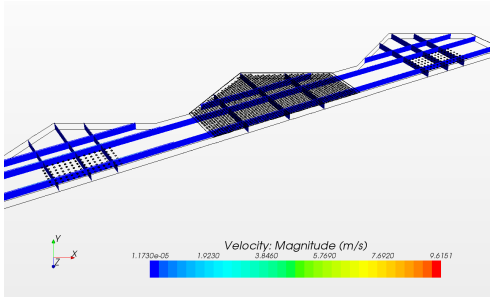

d)

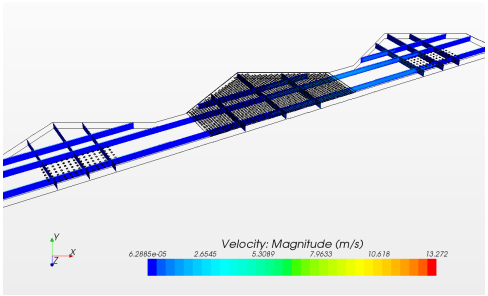

e)

Figure 5.15: Velocity distribution in the pump for different quarters of a cycle when operated at 8.722 kHz. Figures a, b, c, d and e represent the velocity magnitude on the section planes at 3.0, 3.25, 3.5, 3.75 and 4th period of the given simulation time.

Figure 5.11 shows the displacement of the exit, transfer valve membranes and the pump membrane. The exit valve membrane moves in the opposite direction as it follows the procedure outlined in the Chapter 1 and 2. Figure 5.12 and Figure 5.13 show the

pressure distribution at the respective points on the symmetry plane and interior. The pressure distribution on the symmetry plane suggests a nearly insignificant phase difference between the three points. However, there is a magnitude change between the point under the exit valve and the points below the transfer and pump membranes. A similar trend is observed for the interior points as shown in Figure 5.13. Figure 5.14 suggests that the flow rate through the exit valves is lower than the flow rate through the transfer valves.

Figure 5.15 shows the velocity magnitude distribution in the pump. Figures a–e suggest that the maximum velocity no longer occurs in the channel connecting the valves but occurs in the gap between the valve membrane and electrode. Closer examination suggests a pressure build up in this gap for the two valves, which in turn results in the difference in flow rate as observed in Figure 5.14.

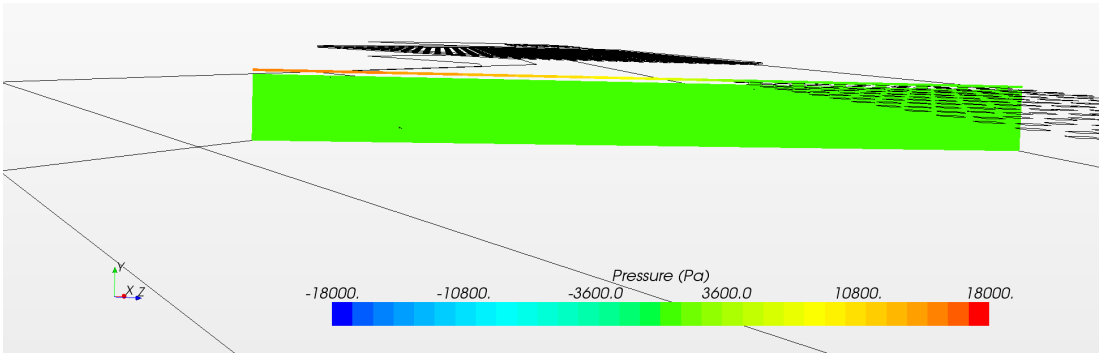

Figure 5.16: Pressure buildup in the gap between the transfer valve membrane and electrode.

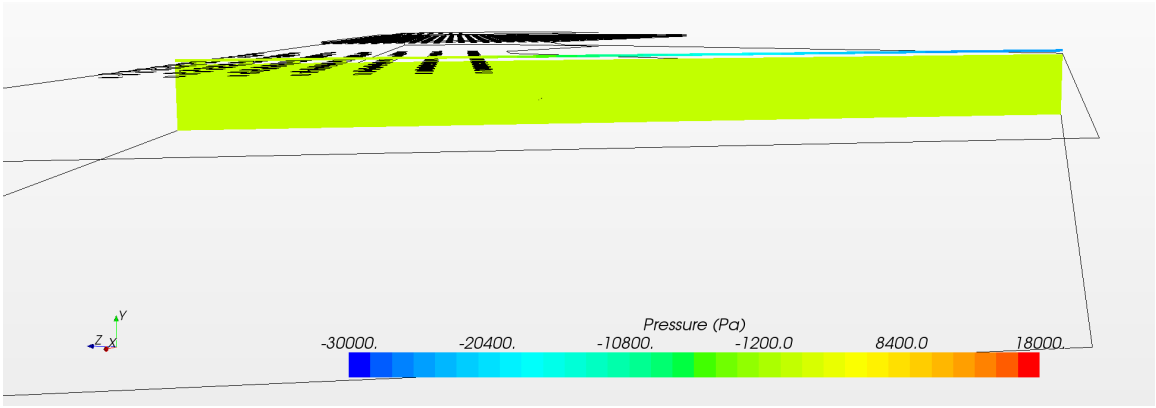

Figure 5.17: Pressure buildup in the gap between the exit valve membrane and electrode.

Figure 5.16 and Figure 5.17 show the pressure distribution in the gap between the membrane and electrode for the transfer and exit valves respectively. The membrane returns to its initial position in each case. The pressure buildup for the two valves is not equal and is significantly larger than the build up in the cavity. The maximum pressure build-ups in the transfer valve, exit valve and the cavity are ~18 kPa, ~ -30 kPa and 200 Pa respectively. These disparities in pressure result in the reduction of the performance of the pump. The number of holes on the electrode was used to observe the acoustic effects in the pump. However, in the actual fabricated micropump, the holes are present all over the electrode as shown in Figure 5.18. In Figure 5.18a and Figure 5.18b the number of holes on the electrode is 196 and ~1000 respectively. In order to improve the performance of the pump, the number of holes is increased to release the pressure buildup.

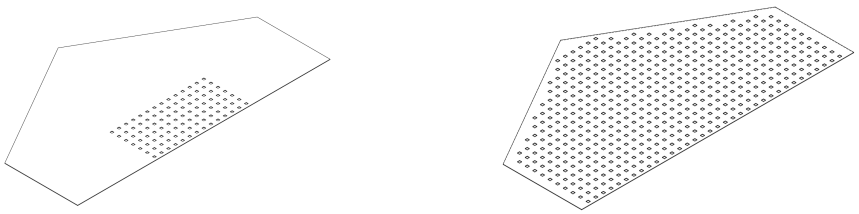

a) b)

Figure 5.18: Hole pattern on the valve electrode. a and b represent the hole pattern used for initial and final analysis respectively.

Figure 5.19 and Figure 5.20 show the pressure distribution of the points on the symmetry and interior planes respectively, when the holes are increased on the electrode. The magnitude change and phase lag between the points is negligible. The pressure variation in this stage is sinusoidal. These phenomena are opposite to those observed in Figures 5.12 and 5.13. The flow rate through the exit and transfer valves are nearly equal as shown in Figure 5.21.

Figure 5.22 and Figure 5.23 show the pressure distribution in the gap between the transfer and exit valve membranes and electrode respectively. The maximum pressure build up is ~500 kPa as opposed to ~30000 Pa, observed when 196 holes are used on the electrode. This suggests that the presence of a larger number of holes on the electrode will improve the performance of the pump. Computationally, the convergence using an increased number of holes was quicker and the residuals decreased to nearly 1^{-5} as opposed to 0.001 using the fewer holes.

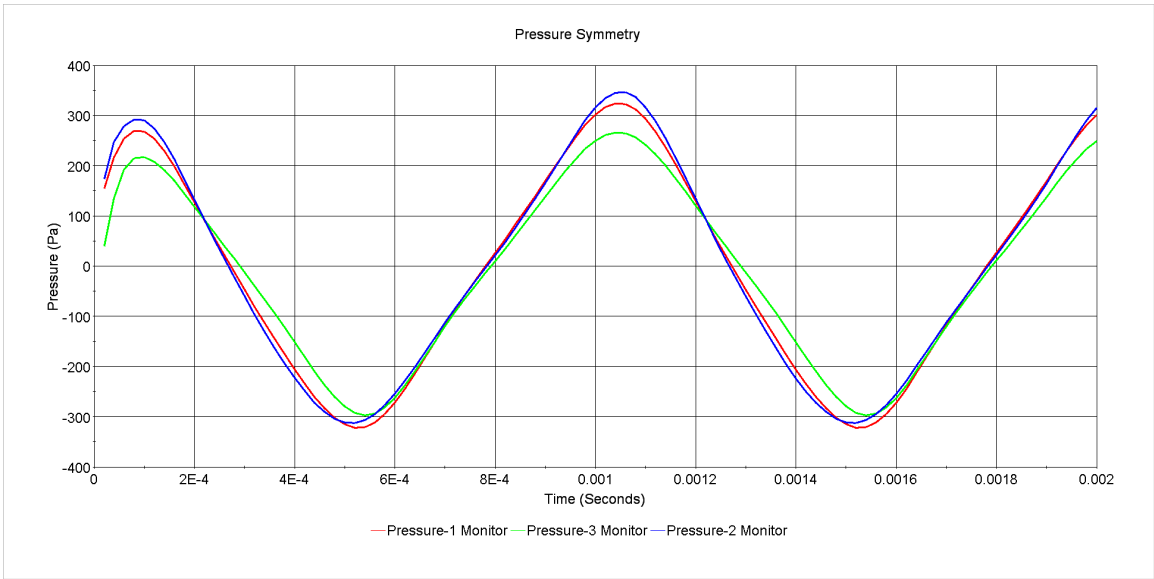

Figure 5.19: Pressure distribution on the symmetry planes for points 1, 2 and 3 when the pump and valve membranes are operated at 1 kHz using the new hole pattern on the valve electrode.

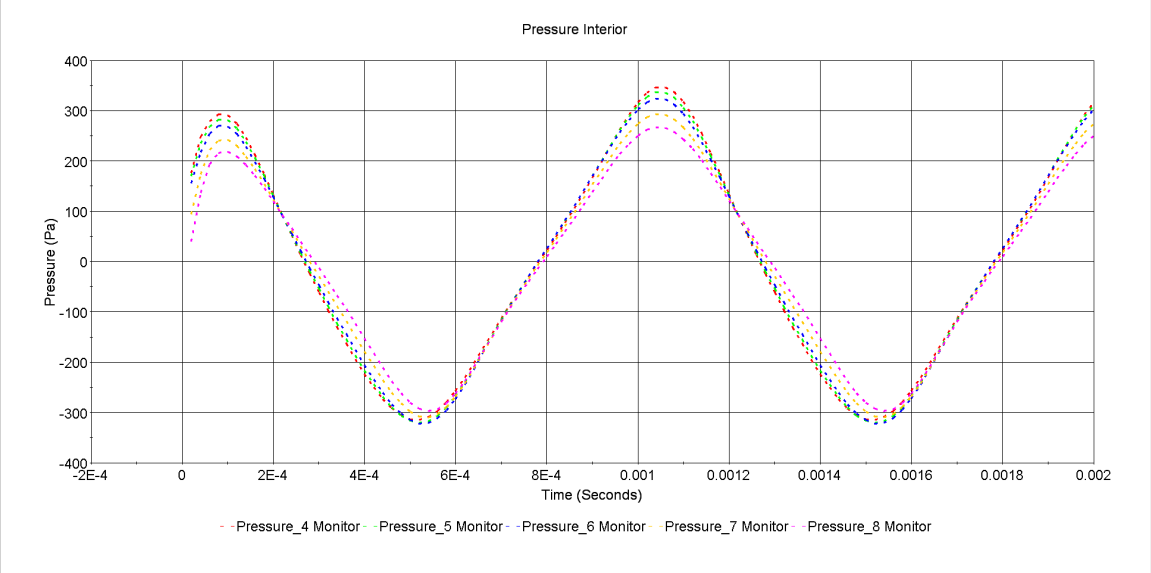

Figure 5.20: Pressure distribution in the interior for points 4, 5, 6, 7 and 8 when the pump and valve membranes are operated at 1 kHz using the new hole pattern on the valve electrode.

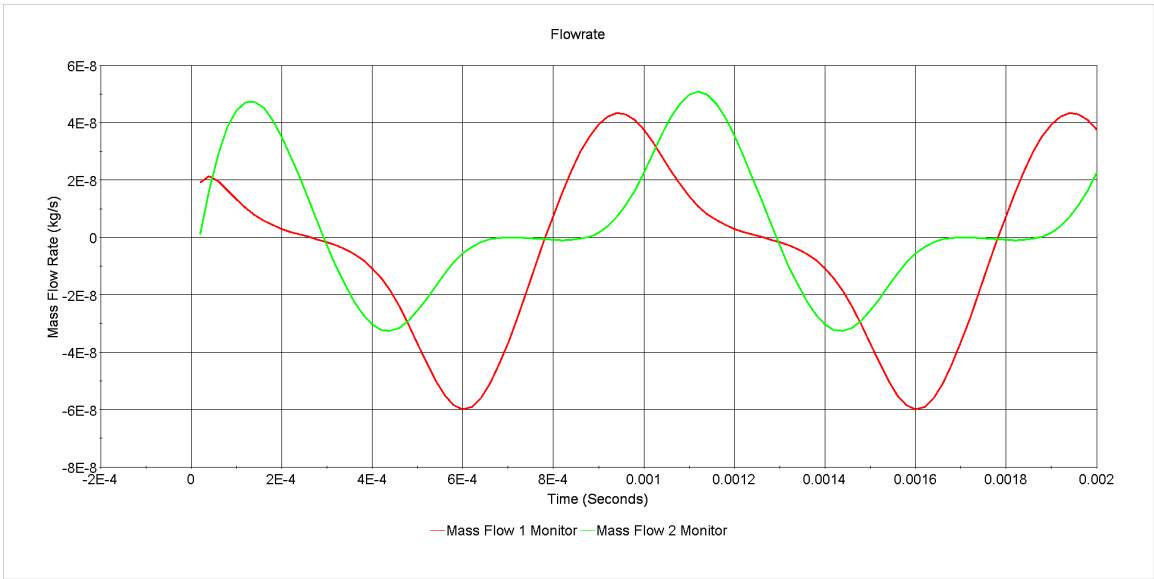

Figure 5.21: Flow rate through the transfer valve and exit valve shown by the red and green lines respectively using the new hole pattern on the valve electrode.

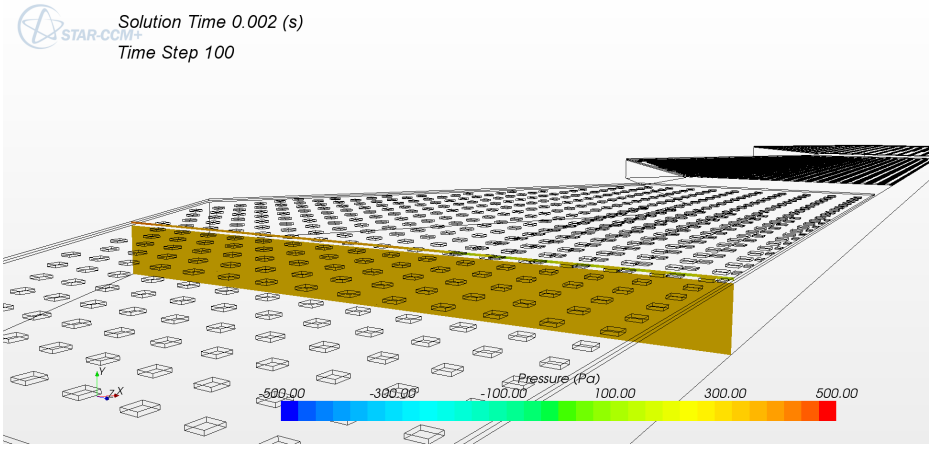

Figure 5.22: Pressure distribution in the gap between the transfer valve membrane and electrode.

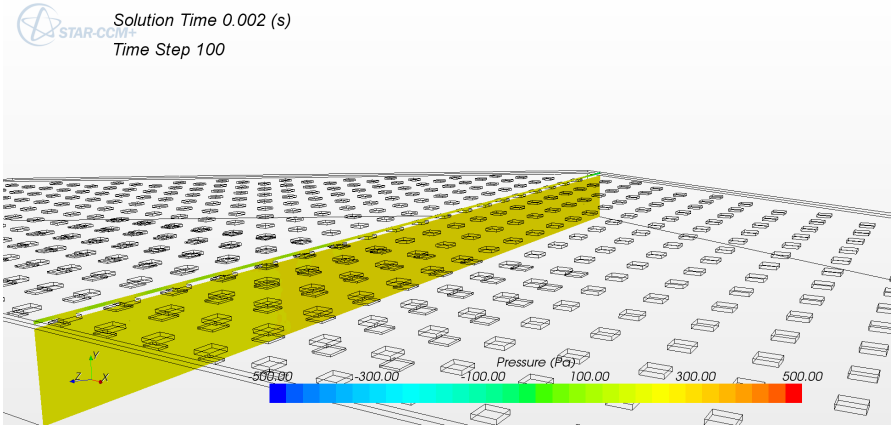

Figure 5.23: Pressure distribution in the gap between the exit valve membrane and electrode.

Comparison of Reduced Order Model with CFD

The geometric properties outlined in Table 5.1 and the equations in Chapter 2 and 3 for reduced order modeling of pump and valve membrane deflection, resistance and inertial lengths are combined to consider sinusoidal volume change for the pump and valve membranes respectively.

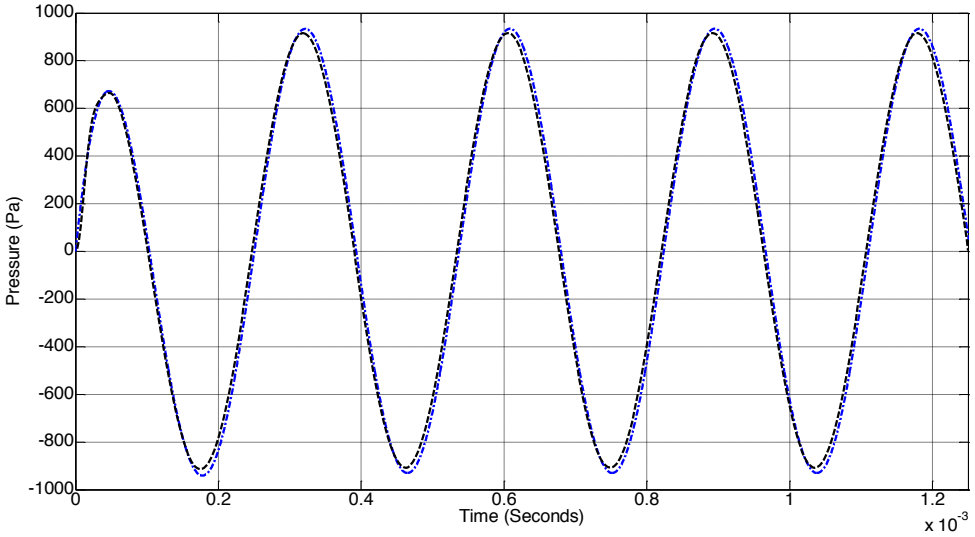

Figure 5.24: Comparison of the pressure in the cavity between the reduced order model and CFD shown by blue and black lines respectively**.** Operation of the pump membrane at 3.488 kHz with valves opened.

Figure 5.24 and Figure 5.25 are a comparison of the pressure distribution at point 1 and flow rate through the transfer and exit valve using the reduced order model and CFD, when the valves are not actuated and the pump is operated at 3.488 kHz. The reduced order model predicts nearly the same pressure distribution in the cavity. The mass flow rate through the transfer and exit valves predicted by both CFD and the

reduced order model are nearly the same. For frequencies closer to the acoustic frequency, the predicted pressure and flow rate are shown in Figure 5.26 and Figure 5.27 respectively with the pump being operated at 8.722 kHz. A phase lag exists between the predicted pressure under the pump membrane using CFD and the reduced order model. However, the magnitude between the two is nearly the same. Thus, the assumption of uniform pressure distribution in the cavity is valid even at pressures close to the acoustic pressure.

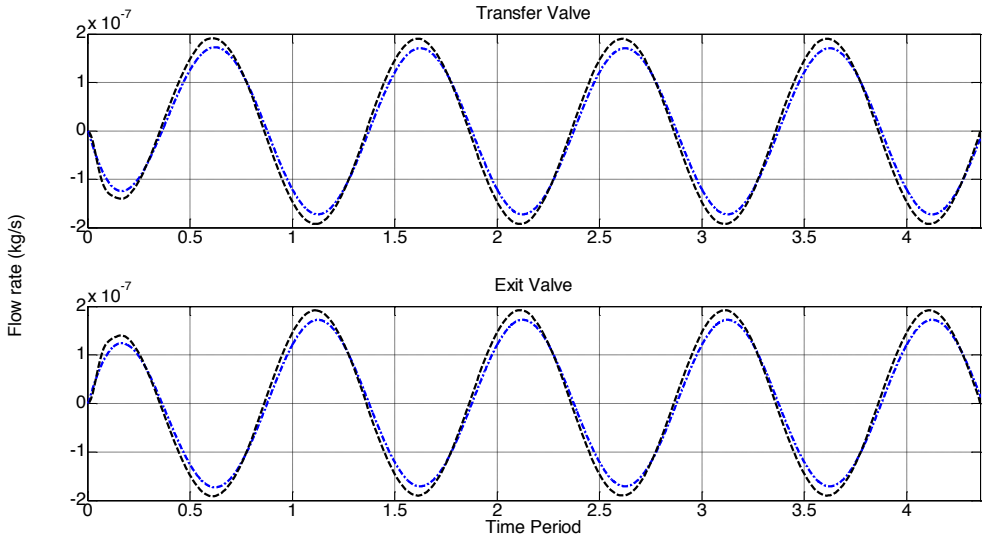

Figure 5.25: Comparison of the flow rate, through the transfer and exit valves between the reduced order model and CFD shown by blue and black lines respectively**.** Operation of the pump membrane at 3.488 kHz with valves opened.

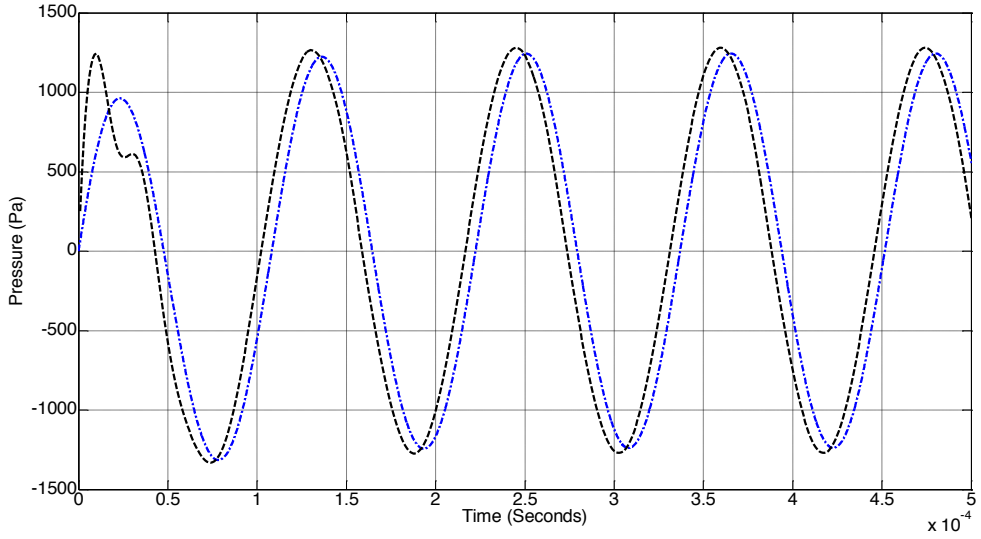

Figure 5.26: Comparison of the pressure in the cavity between the reduced order model and CFD shown by blue and black lines respectively**.** Operation of the pump membrane at 8.722 kHz with valves opened.

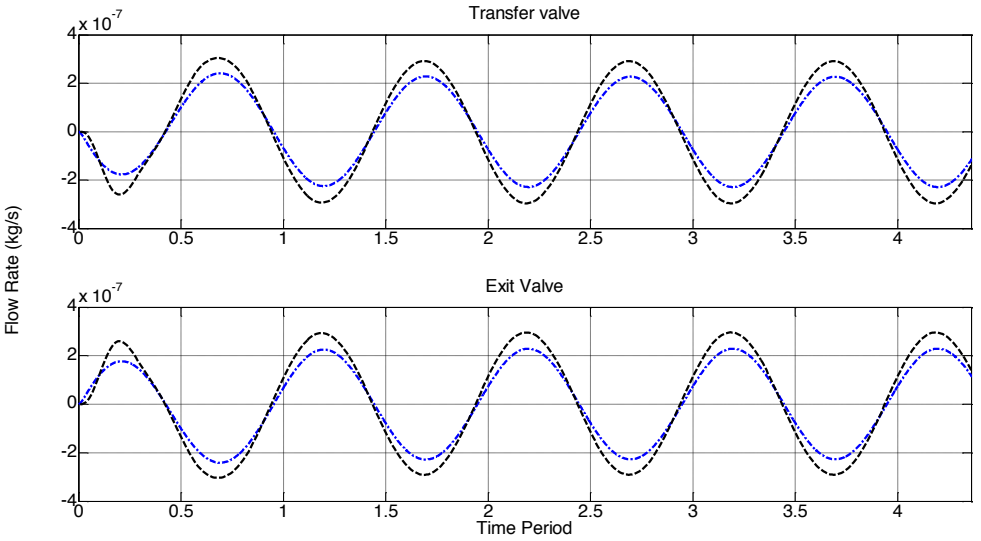

Figure 5.27: Comparison of the flow rate, through the transfer and exit valves, between the reduced order model and CFD shown by blue and black lines respectively**.** Operation of the pump membrane at 8.722 kHz with valves opened.

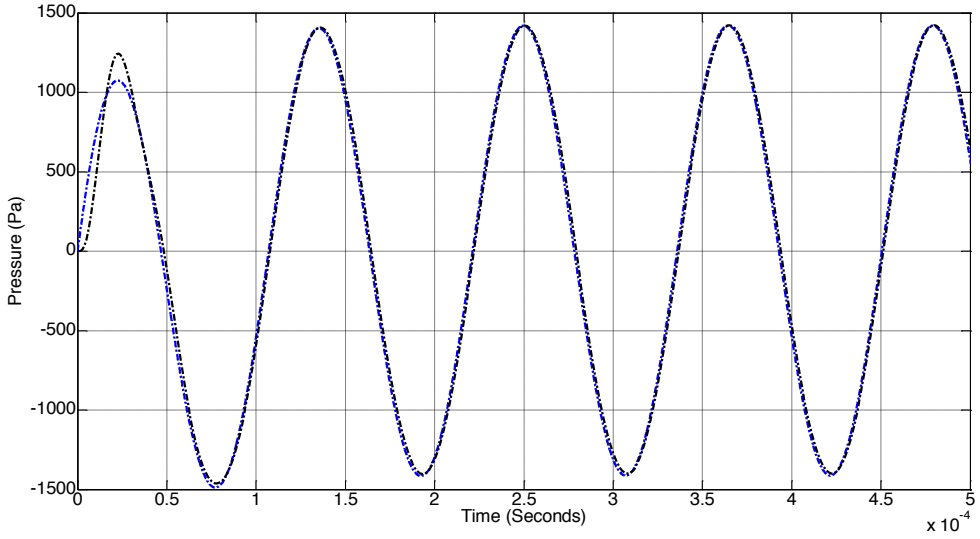

Figure 5.28: Comparison of the pressure in the cavity between the reduced order model (polytropic constant 1.4) and CFD shown by blue and black lines respectively**.** Operation of the pump membrane at 8.722 kHz with valves opened.

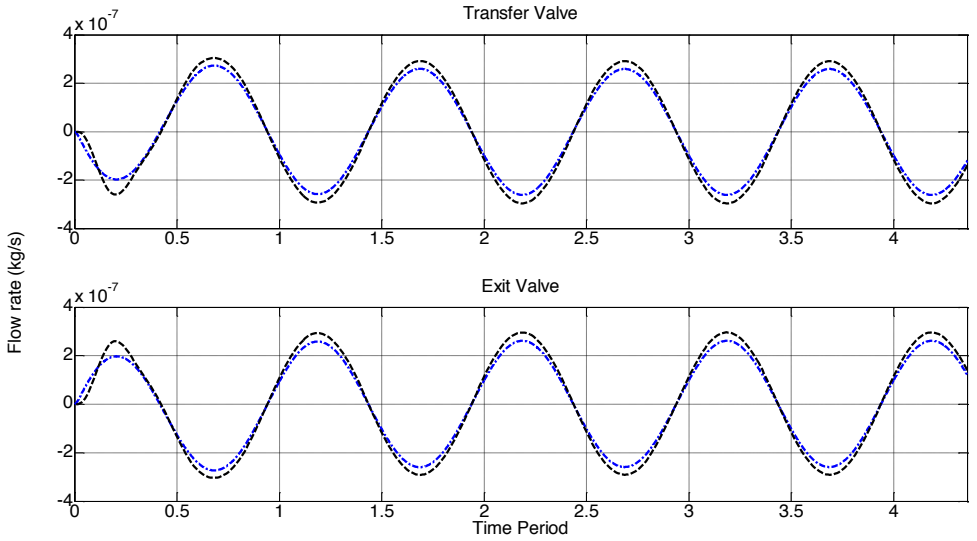

Figure 5.29: Comparison of the flow rate, through the transfer and exit valves, between the reduced order model (polytropic constant 1.4) and CFD shown by blue and black lines respectively**.** Operation of the pump membrane at 8.722 kHz with valves opened.

When the polytropic constant is increased to 1.4, the pressure and flow rate performance predicted by the reduced order model is nearly the same as CFD (shown in Figure 5.28 and Figure 5.29). This suggests that the polytropic constant needs to be increased to achieve nearly the exact performance predicted by CFD as the operating frequency approaches the acoustic frequency. However, since the reduced order model serves as a first order tool, a polytropic constant of 1 predicts nearly the same performance as that shown by CFD.

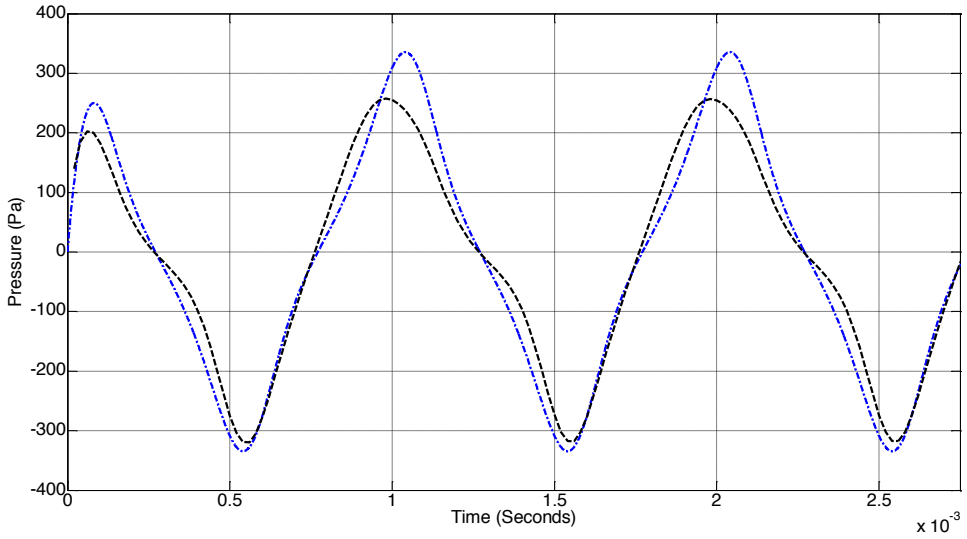

Figure 5.30: Comparison of the pressure in the cavity between the reduced order model and CFD shown by blue and black lines respectively**.** The pump and valve membranes are operated at 1 kHz with a time varying displacement shown in Figure 5.11 using the valve electrode with 196 holes.

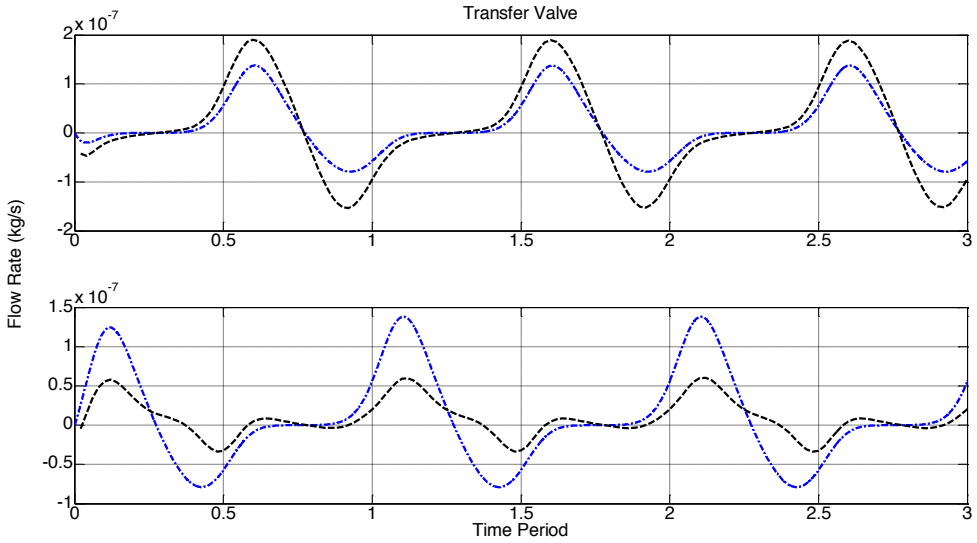

Figure 5.31: Comparison of the flow rate through the transfer and exit valves between the reduced order model and CFD shown by blue and black lines respectively**.** The pump and valve membranes are operated at 1 kHz with a time varying displacement as shown in Figure 5.11using the valve electrode with 196 holes.

Figure 5.30 and Figure 5.31 compare the pressure and flow rate when the pump and valve membranes are operated at 1 kHz with a displacement as shown in Figure 5.11. The pressure in the cavity predicted by the reduced order model follows the same trend as that predicted by CFD. However, the magnitude is slightly higher for the reduced order model. The flow rate predicted by CFD through the transfer valve is higher than that predicted by the reduced order model while the flow rate predicted by CFD through the exit valve is lower than that predicted by the reduced order model. This is due to the pressure build up as explained in the previous section. When the number of holes on the valve electrode is increased to ~1000 CFD, the reduced order model predicts nearly the same performance for the pressure and flow rate as shown in Figure 5.32 and Figure 5.33 respectively.

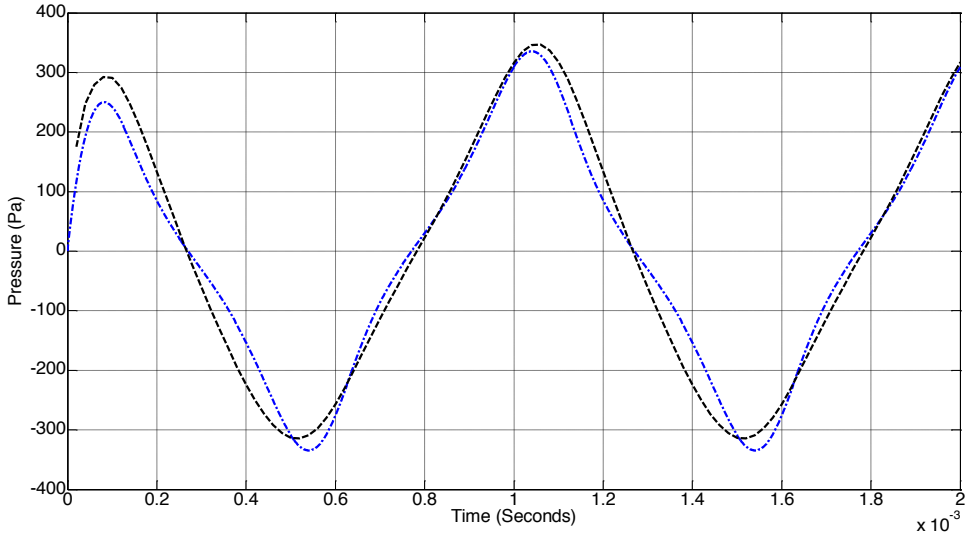

Figure 5.32: Comparison of the pressure in the cavity between the reduced order model and CFD shown by blue and black lines respectively**.** The pump and valve membranes are operated at 1 kHz with a time varying displacement shown in Figure 5.11, using valve electrode with ~1000 holes.

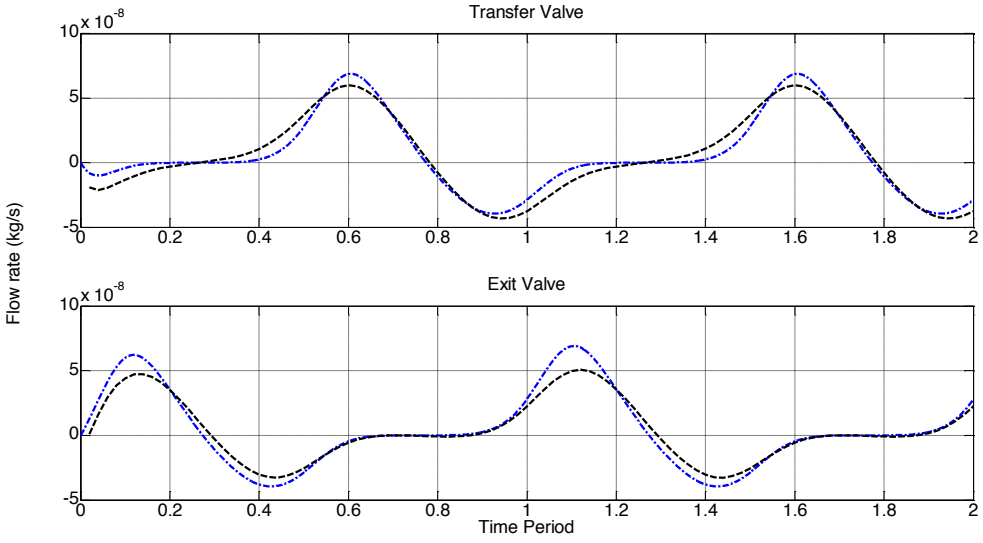

Figure 5.33: Comparison of the flow rate, through the transfer and exit valves, between the reduced order model and CFD shown by blue and black lines respectively**.** The pump and valve membranes are operated at 1 kHz with a time varying displacement shown in Figure 5.11 using valve electrode with ~1000 holes.

Comparing CFD with the reduced order model suggests that the assumptions of uniform pressure distribution, quasi steady state and ignoring hexagonal shape of cavity are valid. The pressure in the gap between the membranes and the electrode for the pump and valves is nearly the same as the pressure in the cavity. Hence, the assumption of the lack of damping due to this gap is valid. The predicted resistance and inertial length models are valid for the cases studied.

Chapter 6

Summary, Contributions & Recommendations

Summary

Review from literature suggests that very few or no applicable models exist to estimate the performance of any electrostatic micropump. Most of the mathematical tools developed apply only for pumps operated at low frequencies. These tools, in general, model the effect of the pumping membrane and not the valve membrane and are hence unable to capture the multiple resonant performances observed in measured results. These models cannot be used to analyze the micropump proposed at the University of Michigan. This utilizes a single electrode, active checkerboard microvalves, hexagonal modular and multistage design.

A hierarchy of models has been developed. A thermodynamic model proposed by Astle et al. (2003) is used to estimate the volume ratio necessary across each stage to achieve a target vacuum. Volume ratios for three different designs are proposed for a 16-stage design to achieve a desired vacuum of 250 Torr. The equal pressure and modular design showed similar and improved performance over the equal volume ratio design. The drawback of the equal volume ratio design is that the stages closer to the outlet perform extensively when compared to stages further away. A reduced order model

developed by Astle et al. (2003) is extended for multistage and transient applications. The tool confirmed the advantage of using the modular or the equal pressure design. The modular design is the most effective design for easier fabrication and better performance. The reduced order model suggests decrease in operating frequency when the inlet pressure decreases from atmospheric pressure to vacuum. A 16-stage micropump showed the decrease in operating frequency from 50 to 20 kHz. The effect of valve timing on the performance of the pump was also evaluated. To achieve maximum performance, a new control system (DVT) is proposed which could theoretically improve the performance by nearly 40%. The effect of leakage on the transient performance is evaluated and the minimum necessary sealing factor for the design proposed is estimated to be $2x10^6$ Pa/sccm. This resistance is exceedingly high. To compensate for this, a study was carried out to evaluate the effect of volume ratio and leakage. Transient studies showed that the volume ratio should be decreased to overcome losses due to leakage. The studies allow the user to choose the volume ratio based on the estimated leakage.

A multiphysics model is developed by combining the models proposed by Astle et al. (2003) and Müller et al. (2000). A nonlinear model for the structural membrane deflection is estimated using COMSOL. The advantages of using a single electrode design are evaluated using a 4-stage vacuum micropump. It was observed that a minimum voltage and optimum operating frequency produces maximum performance due to maximum achievable displacement of the membrane. Realizing that the valves affect the behavior equally, a new model is proposed to study the performance of a 4-stage micropump. New resistance and inertial models are developed using CFD analysis on a section of the valves. Two new designs are proposed for the holes on the valve

system. The resistance and inertial lengths for the two designs are found to be nearly equal. The viscous length varies inversely with the cube of the gap between the electrode and membrane while the inertial length varies inversely with the square root of the gap. The novelty of this model exists in its prediction of the existence of three resonant frequencies. These frequencies are due the cavity and membrane resonance. For the first time, the pumping due to valves is estimated and found to be significant. The model developed by Astle et al. (2003) required experimentally estimated inertial lengths while the model here estimates the resonant peaks accurately using the corresponding actuating waveforms.

A new experimental setup that allows easy measurement of the performance of the pump has been developed. Laser vibrometer results suggest that maximum displacement of a membrane in a 24-stage pump is estimated to be in the range of 4-10 kHz. Maximum flow performance was estimated in this range. Leakage performance of a 4-stage pump was measured and found to be double the predicted resistance. This difference is due to the resistance introduced by the capillary tube and particles present in the valve holes. The flow performance of 4, 12 and 24 stage micropumps are evaluated. The 4 and 12 stage micropumps show the existence of the three resonant peaks. Theoretical models are compared for the 4-stage micropump and are found to predict these peaks with an accuracy of 7-21%. While the theoretical model overestimates the flow rate, the estimation of these peaks allows easy experimentation of these devices. The low performance of these pumps is attributed to the curved electrodes and low sealing. The 4 and 12 stage pumps show a greater sensitivity to valve timing in comparison with the 24-stage micropump. Maximum flow rate was estimated using the 24-stage

micropump. The developed theoretical model can now be used to first mathematically control the pump more effectively before experimentally analyzing the device. Analysis using this model showed that valves produced nearly equal or greater pumping than the pump membrane. Based on this, a new valve only pumping design is proposed and its performance is measured.

Computational fluid dynamics using STARCCM+ suggests that the acoustic reduced order model produces similar performance for a single cavity having only transfer and exit valves. Acoustic effects due to the valve and pump motion are compared with the theoretical model. The estimated resistance and inertial models for flow through the valves produce similar pressures in the cavity and flow rate through each valve. The assumptions of uniform pressure, no damping between the membranes and the electrode and the absence of hexagonal effects are validated through CFD analysis.

Contributions

- Theoretical Models
    - Extended reduced order model for multistage and transient applications
    - Analytical models for estimation of leakage
    - Multiphysics models for single electrode design and active valve pumping
- New multistage micropump and controlling designs
    - Proposed three new multistage designs to achieve desired vacuum
    - Methodology for transient performance evaluation for multistage micropumps
    - Proposed dynamic valve timing to operate the pump more efficiently
- Valve Modeling
    - Resistance and inertial length estimation for two valve designs
    - Viscous and inertial lengths vary inversely with the cube and square of the gap respectively
- Theoretical Validations
    - Predicted the performance resonant peaks with an accuracy of 7-21% for a 4-stage micropump
    - Estimation of viscous length compares with measured results

- Theoretical analysis using estimated resistance and inertial models for flow through valves produce comparable performance as CFD

- Computational fluid dynamic Modeling
  - Pressure in the gap between the valve/pump membrane and electrode is equal to the distribution in the cavity, suggesting little or no damping
  - Holes on the valve electrode prevent pressure build up and produce efficient pumping.

- Valve Pumping – New Discovery
  - Theoretical models suggest that the performance is due to the valves and not the pump membranes
  - A new valve only design for a high flow rate application is proposed and is found to produce flow comparable to that of the micropumps.

Future Work and Recommendations

Through the course of this work, new strategies and ideas need to be developed to improve two main sections, 1) Modeling and 2) Experimentation. These two are however believed to be dependent on each other.

Nonlinear models need to be developed for the estimation of the membrane deflection. When the membrane releases from the electrode, the assumed sinusoidal shape of the membrane may not be preserved due to more significant vibrating modes.

Measurements of the membrane deflection using the laser vibrometer give an insight into the membrane deflection, but the pattern on its surface could produce erroneous results. New methods need to be developed to characterize the membrane deflection accurately and instantaneously. Damping due to blockage of the membrane holes can produce detrimental effects. Hence, new techniques to characterize the flow through the micropumps need to be developed.

For the current micropump design, it is important to implement DVT. Decrease in inlet pressure could significantly affect the performance of the pump with fixed valve timing. Instantaneous measurements of the membrane deflection will allow efficient implementation of DVT.

Theoretical models suggest that the valves contribute significantly to pumping. Hence, new designs should incorporate smaller valve area and optimized gap. A decrease in performance will occur if the gap is too small. The theoretically proven concept of

valve only pumping should be further explored for high flow rate devices. A parallel arrangement of these devices will be able to generate significantly larger flow rate.

APPENDIX

Multiphysics Code For Valve and Pump membrane Deflection Studies

```
function main
clear all
clc
close all

%*********************************************************************
****
tD=1.85e-6;                                 %Thickness of membrane
Am=4e-6;                                    %Area of membrane
rhoD=7.210e+003;                            %desnity of membrane
homem=4e-6;                                 %distance between
electrode
                                            %and pump membrane
hoio=4e-6;                                  %distance between
electrode
                                            %and inlet valve membrane
hotb=4e-6;                                  %distance between
electrode
                                            %and transfer valve
membrane
epsilon=8.85e-12;                           %permitivity of air
hg=4e-6;                                    %electrode gap
V=0.93;                                     %volume ratio
E=55;                                       %Eo= maximum voltage
Temp=298;                                   %Temperature
gamma=1.4;                                  %specific heat of air
alpha=(gamma*287*Temp)^.5;                  %speed of sound
n=1;
CavityVolume(1) = 1.1021e-9/90*65;          %Cavity Volume at the top
CavityVolume(2) = 1.1021e-9;                %Cavity Volume at the
bottom
pin=1;
M=2;                                        %Number of Stages = M*2
Vload=CavityVolume*M*2;                     %Volume of Inlet
Le = 200e-6;                                %Inertial Length
Lv=30e-6;                                   %Viscous Length
inlet=0;                                    %Condition of steady state
                                            %inlet = 0 else 1
Poutlet=101300;                             %Pressure of the outlet
rhooutlet=(Poutlet)/(287*Temp);             %Density of the outlet
mu=1.8e-5;                                  %viscosity
numberofholes=169;                          %number of holes through
valve
Lehole=20e-6;                               %electrode side length
Ae=Lehole^2*numberofholes;                  %area of all holes
%*********************************************************************
```

```
****
risetimeio=0.015;
risetimetb=0.015;
voltagetb=75;
voltageio=75;

%*********************************************************************
****

folder = ['sine','E',num2str(E),'V',num2str(V(1)),...
    'pump',num2str(M),'pin',num2str(pin)];
mkdir(folder);

filename_1 = (['volumetime.dat']);
filename_2 = (['error.dat']);
filename_3 = (['iter.dat']);
filename_4 = (['time.dat']);
fvolt = fopen(filename_1,'w');
ferror = fopen(filename_2,'w');
ftime = fopen(filename_4,'w');
fiter = fopen(filename_3,'w');
%*********************************************************************
****
%                        Initial Conditions
%*********************************************************************
****

%*********************************************************************
****
f=7000;
vopio=0.24;
voptb=0.24;
vclio=0;
vcltb=0.06;
%carrying out frequency analysis
for freq=1:length(f)
    %loading initial conditions
    y=zeros(M*14+6,1);
    [IC] =load_IC(y,M,1,pin,homem,hoio,hotb);
    i=1;
    check=1;
    p1old(1:M)=101300;
    p2old(1:M)=101300;
    fprintf('iter=%d\n',i);
    while check==1
        tsol=[];
        t=[(i-1)/f(freq) i/f(freq)];
        tcheck=0;
        loadcheck=1;
        while(tcheck==0)
            %initializing the evevnt solver for ODE45
            options=odeset('Events',@events,'MaxStep',1/f(freq)/1000);
            %Calling ODE45 SOlver
            [time,y]=ode45(@equation,t,IC,options,rhoD,tD,...
                Am,E,epsilon,CavityVolume,alpha,gamma,n,hg,...
                Le,Lv,inlet,Poutlet,rhooutlet,Vload,mu,Ae,f(freq),...
                M,vopio,vclio,risetimeio,voptb,vcltb,...
```

```
            risetimetb,voltageio,voltagetb,homem,hoio,hotb);
        %end of time cycle
        if(time(end)==t(2))
            tcheck=1;
            [IC] =load_IC(y,M,2,pin,homem,hoio,hotb);
            tsol=[tsol time'];
            %End of first time cycle
            if(loadcheck==1)
                [displ,displt,displio,displtio,displtb,...
                    displttb,displex,displtex,pinlet,p1,...
                    p2,rhoinlet,rho1,rho2,uin,utb,...
                    uex,volin,voltb,volex]=load_ar1(y,M);
                loadcheck=2;
            %after second cycle
            else
                [displ,displt,displio,displtio,displtb,...
                    displttb,displex,displtex,pinlet,p1,...
                    p2,rhoinlet,rho1,rho2,uin,utb,...
                    uex,volin,voltb,volex]=load_ar2(y,M,...
                    displ,displt,displio,displtio,...
                    displtb,displttb,displex,displtex,...
                    pinlet,p1,p2,rhoinlet,rho1,rho2,uin,...
                    utb,uex,volin,voltb,volex);
            end
        %Elctrode found...Initializing conditions
        else
            [IC] =load_IC(y,M,3,pin,homem,hoio,hotb);
            t=[time(end) t(2)];
            tsol=[tsol time'];
            %First Cycle
            if(loadcheck==1)
                [displ,displt,displio,displtio,displtb,...
                    displttb,displex,displtex,pinlet,...
                    p1,p2,rhoinlet,rho1,rho2,uin,utb,...
                    uex,volin,voltb,volex]=load_ar1(y,M);
                loadcheck=2;
            %after loading first time
            else
                [displ,displt,displio,displtio,displtb,...
                    displttb,displex,displtex,pinlet,p1,...
                    p2,rhoinlet,rho1,rho2,uin,utb,...
                    uex,volin,voltb,volex]=load_ar2(y,M,...
                    displ,displt,displio,displtio,...
                    displtb,displttb,displex,...
                    displtex,pinlet,p1,p2,rhoinlet,rho1,...
                    rho2,uin,utb,uex,volin,...
                    voltb,volex);
            end
        end
    end

    for stage = 1:M
        if(stage==1)
            fprintf('%3.6f\t',volin(end)*60e6*f(freq)/1.22);
        end
        fprintf('%3.6f\t',voltb(end,stage)*60e6*f(freq)/1.22);
        if(stage==M)
            fprintf('%3.6f\n',volex(end,stage)*60e6*f(freq)/1.22);
```

```
    else
        fprintf('%3.6f\t',volex(end,stage)*60e6*f(freq)/1.22);
    end
end

A(1:length(tsol)) =-3.99e-6;

Eio=zeros(length(tsol),1);
Etb=zeros(length(tsol),1);
E1=zeros(length(tsol),1);
for t_e = 1:length(tsol)
    Eio(t_e) = valveiotimig(f(freq),vopio,vclio,voltageio,...
        risetimeio,tsol(t_e));
    Etb(t_e) = valvetbtimig(f(freq),voptb,vcltb,voltagetb,...
        risetimetb,tsol(t_e));
    E1(t_e)=valveiotimig(f(freq),0,0.25,130,0.1,tsol(t_e));
end

%calcualting error
er =1;
for stage =1:M
    error(er)=abs(p1(end,stage)-p1old(stage))/p1(end,stage);
    p1old(stage)=p1(end,stage);
    fprintf('%f\t',error(er));
    er=er+1;
    error(er)=abs(p2(end,stage)-p2old(stage))/p2(end,stage);
    p2old(stage)=p2(end,stage);
    fprintf('%f\t',error(er));
    er=er+1;
end
for stage =1:er-1
    if(error<1e-5)
        check=0;
    else
        check=1;
    end
end
%plotting Displacement
f1=figure(1);
subplot(4,1,1)
A(1:length(tsol)) =-homem+0.01e-6;
plot(tsol/(1/f),displ)
subplot(4,1,2)
A(1:length(tsol)) =-hoio+0.01e-6;
plot(tsol/(1/f),displio)

subplot(4,1,3)
A(1:length(tsol)) =-hotb+0.01e-6;
plot(tsol/(1/f),displtb)

subplot(4,1,4)
A(1:length(tsol)) =-hoio+0.01e-6;
plot(tsol/(1/f),displex)

saveas(f1,'displ1','fig');
%plotting pressure
f2=figure(2);
```

```
        subplot(2,1,1)
        plot(tsol/(1/f),p1)
        subplot(2,1,2)
        plot(tsol/(1/f),p2)

        saveas(f2,'pressure1','fig');
        %plotting velocity
        f3=figure(3);
        subplot(3,1,1)
        plot(tsol/(1/f),uin)

        subplot(3,1,2)
        plot(tsol/(1/f),utb)

        subplot(3,1,3)
        plot(tsol/(1/f),uex)

        saveas(f3,'velocity1','fig');

        i=i+1;
        fprintf('iter=%d\n',i);
        if(i==100)
            check=0;
        end
        %Writing flow Data
        if(check==0)
            for stage = 1:M
                if(stage==1)

fprintf(fvolt,'%3.6f\t',volin(end)*60e6*f(freq)/1.22);
                end

fprintf(fvolt,'%3.6f\t',voltb(end,stage)*60e6*f(freq)...
                    /1.22);

fprintf(fvolt,'%3.6f\t',volex(end,stage)*60e6*f(freq)...
                    /1.22);
            end
            fprintf(fvolt,'\n');
            fvolcount=1;
            for stage=1:M
                fprintf(ferror,'%f\t%f\t',error(fvolcount),...
                    error(fvolcount+1));
                fvolcount=fvolcount+2;
            end
            fprintf(ferror,'\n');
            fprintf(fiter,'\%d\n',i);
            fprintf(ftime,'%f\t%f\t%f\t%f\n',vopio,vclio,voptb,vcltb);

%fprintf('************************************************************
************');
        end

        clear tsol A
        clear displ displt displio displtio displtb displttb displex
        clear displtex pinlet p1 p2 rhoinlet rho1 rho2 uin utb uex
volin
```

```
        clear voltb volex

    end
end

%ODE 45 SOLVER
function[dy]=equation(t,y,rhoD,tD,Am,E,epsilon,CavityVolume,...

alpha,gamma,n,hg,Le,Lv,inlet,Poutlet,rhooutlet,Vload,mu,Ae,f,M,topio,..
.

tclio,risetimeio,toptb,tcltb,risetimetb,voltageio,voltagetb,homem,hoio,
hotb)

%*********************************************************************
***
%                            Electric Input
%*********************************************************************
***
E=E*sin(2*pi*f*t);
Eio = valveiotimig(f,topio,tclio,voltageio,...
    risetimeio,t);
Etb = valvetbtimig(f,toptb,tcltb,voltagetb,...
    risetimetb,t);

%*********************************************************************
%                        Loading Variables
%*********************************************************************
[hmem,htmem,hio,htio,htb,httb,hex,htex,Pinlet,P1,P2,rhoinlet,rho1,rho2,
...
    uin,utb,uex,volin,voltb,volex...
    ]=loadvariables(y,M);

%*********************************************************************
%                        Volume Calculation
%*********************************************************************
[Vol1,dVol1,Vol2,dVol2,rhoin,rhotb,rhoex]=volumedensity(CavityVolume,..
.

hmem,htmem,hio,htio,htb,httb,hex,htex,M,uin,utb,uex,rhoinlet,rho1,...
    rho2,rhooutlet,Am,homem,hoio,hotb);
%*********************************************************************
%                             Equations
%*********************************************************************
count=1;
for stage=1:M
    [LvIN,LvEX,LvTB,LeIN,LeEX,LeTB]=valvetiming(hio,...
        htb(stage),hex(stage),hoio,hotb);

%*********************************************************************
    %               Membrane Deflection for Pump Membrane

%*********************************************************************
    %if membrane is collapsed on the electrode
    if(hmem(stage)==-homem+0.01e-6 && htmem(stage)==0)

force=membranedef(rhoD,tD,Am,hmem(stage),P1(stage),P2(stage),E,homem,..
```

```
.
            epsilon);
        %if the force is large enough to pull the membrane towards the
        %electrode
        if(force<0)
            dhmem(stage)=0;dy(count)=dhmem(stage);count=count+1;
            dhtmem(stage)=0;dy(count)=dhtmem(stage);count=count+1;
        else
            %displacement of the membrane

dhmem(stage)=htmem(stage);dy(count)=dhmem(stage);count=count+1;

dhtmem(stage)=membranedef(rhoD,tD,Am,hmem(stage),P1(stage),...
                P2(stage),E,homem,epsilon);
            dy(count)=dhtmem(stage);count=count+1;
        end
    else
        if(hmem(stage)<=-homem+0.01e-6)

dhmem(stage)=htmem(stage);dy(count)=dhmem(stage);count=count+1;
            dhtmem(stage)=membranedef(rhoD,tD,Am,-homem+0.01e-
6,P1(stage),...
                P2(stage),E,homem,epsilon);
            dy(count)=dhtmem(stage);count=count+1;
        else

dhmem(stage)=htmem(stage);dy(count)=dhmem(stage);count=count+1;

dhtmem(stage)=membranedef(rhoD,tD,Am,hmem(stage),P1(stage),...
                P2(stage),E,homem,epsilon);
            dy(count)=dhtmem(stage);count=count+1;
        end
    end

%**********************************************************************
    %               Membrane Deflection for I/o Valve

%**********************************************************************
    if(stage==1)
        if(hio(stage)==-hoio+0.01e-6 && htio(stage)==0)

force=membranedefio(rhoD,tD,Am,hio(stage),P1(stage),Pinlet,...
                Eio,hoio,epsilon);
            if(force<0)
                dhio(stage)=0;dy(count)=dhio(stage);count=count+1;
                dhtio(stage)=0;dy(count)=dhtio(stage);count=count+1;
            else

dhio(stage)=htio(stage);dy(count)=dhio(stage);count=count+1;

dhtio(stage)=membranedefio(rhoD,tD,Am,hio(stage),P1(stage),...
                    Pinlet,Eio,hoio,epsilon);
                dy(count)=dhtio(stage);count=count+1;
            end
        else
            if(hio(stage)<=-hoio+0.01e-6)

dhio(stage)=htio(stage);dy(count)=dhio(stage);count=count+1;
```

```
                dhtio(stage)=membranedefio(rhoD,tD,Am,-hoio+0.01e-
6,P1(stage),...
                    Pinlet,Eio,hoio,epsilon);
                dy(count)=dhtio(stage);count=count+1;
            else

dhio(stage)=htio(stage);dy(count)=dhio(stage);count=count+1;

dhtio(stage)=membranedefio(rhoD,tD,Am,hio(stage),P1(stage),...
                    Pinlet,Eio,hoio,epsilon);
                dy(count)=dhtio(stage);count=count+1;
            end
        end
    end

%**********************************************************************
    %               Membrane Deflection for TB Valve

%**********************************************************************
    if(htb(stage)==-hotb+0.01e-6 && httb(stage)==0)

force=membranedeftb(rhoD,tD,Am,htb(stage),P1(stage),P2(stage),Etb,hotb,
...
            epsilon);
        if(force<0)
            dhtb(stage)=0;dy(count)=dhtb(stage);count=count+1;
            dhttb(stage)=0;dy(count)=dhttb(stage);count=count+1;
        else

dhtb(stage)=httb(stage);dy(count)=dhtb(stage);count=count+1;

dhttb(stage)=membranedeftb(rhoD,tD,Am,htb(stage),P1(stage),...
                P2(stage),Etb,hotb,epsilon);
            dy(count)=dhttb(stage);count=count+1;
        end
    else
        if(htb(stage)<=-hotb+0.01e-6)

dhtb(stage)=httb(stage);dy(count)=dhtb(stage);count=count+1;
            dhttb(stage)=membranedeftb(rhoD,tD,Am,-hotb+0.01e-
6,P1(stage),...
                P2(stage),Etb,hotb,epsilon);
            dy(count)=dhttb(stage);count=count+1;
        else

dhtb(stage)=httb(stage);dy(count)=dhtb(stage);count=count+1;

dhttb(stage)=membranedeftb(rhoD,tD,Am,htb(stage),P1(stage),...
                P2(stage),Etb,hotb,epsilon);
            dy(count)=dhttb(stage);count=count+1;
        end
    end

%**********************************************************************
    %               Membrane Deflection for Exit Valve

%**********************************************************************
    if(stage==M)
```

```
        if(hex(stage)==-hoio+0.01e-6 && htex(stage)==0)

force=membranedefio(rhoD,tD,Am,hex(stage),Poutlet,P2(stage),Eio,hoio,..
.
                epsilon);
            if(force<0)
                dhex(stage)=0;dy(count)=dhex(stage);count=count+1;
                dhtex(stage)=0;dy(count)=dhtex(stage);count=count+1;
            else

dhex(stage)=htex(stage);dy(count)=dhex(stage);count=count+1;

dhtex(stage)=membranedefio(rhoD,tD,Am,hex(stage),Poutlet,...
                    P2(stage),Eio,hoio,epsilon);
                dy(count)=dhtex(stage);count=count+1;
            end
        else
            if(hex(stage)<=-hoio+0.01e-6)

dhex(stage)=htex(stage);dy(count)=dhex(stage);count=count+1;
                dhtex(stage)=membranedefio(rhoD,tD,Am,-hoio+0.01e-
6,Poutlet,...
                    P2(stage),Eio,hoio,epsilon);
                dy(count)=dhtex(stage);count=count+1;
            else

dhex(stage)=htex(stage);dy(count)=dhex(stage);count=count+1;

dhtex(stage)=membranedefio(rhoD,tD,Am,hex(stage),Poutlet,...
                    P2(stage),Eio,hoio,epsilon);
                dy(count)=dhtex(stage);count=count+1;
            end
        end
    else
        if(hex(stage)==-hoio+0.01e-6 && htex(stage)==0)

force=membranedefio(rhoD,tD,Am,hex(stage),P1(stage+1),P2(stage),Eio,hoi
o,...
                epsilon);
            if(force<0)
                dhex(stage)=0;dy(count)=dhex(stage);count=count+1;
                dhtex(stage)=0;dy(count)=dhtex(stage);count=count+1;
            else

dhex(stage)=htex(stage);dy(count)=dhex(stage);count=count+1;

dhtex(stage)=membranedefio(rhoD,tD,Am,hex(stage),P1(stage+1),...
                    P2(stage),Eio,hoio,epsilon);
                dy(count)=dhtex(stage);count=count+1;
            end
        else
            if(hex(stage)<=-hoio+0.01e-6)

dhex(stage)=htex(stage);dy(count)=dhex(stage);count=count+1;
                dhtex(stage)=membranedefio(rhoD,tD,Am,-hoio+0.01e-
6,P1(stage+1),...
                    P2(stage),Eio,hoio,epsilon);
                dy(count)=dhtex(stage);count=count+1;
```

```
            else

dhex(stage)=htex(stage);dy(count)=dhex(stage);count=count+1;

dhtex(stage)=membranedefio(rhoD,tD,Am,hex(stage),P1(stage+1),...
                    P2(stage),Eio,hoio,epsilon);
                dy(count)=dhtex(stage);count=count+1;
            end
        end
    end


%*********************************************************************
    %                       Pressure Calculations

%*********************************************************************
    if(stage==1)
        %Pressure Inlet
        if(inlet==1)
            dPinlet=-
rhoin*alpha^2*n/gamma*uin*Ae/Vload;dy(count)=dPinlet;
            count=count+1;
        else
            dPinlet=0;dy(count)=dPinlet;count=count+1;
        end
    end
    if(stage==1)
        %pressure in cavity 1 solution
        dP1(stage)=
pressure(alpha,n,gamma,Ae,rhoin,rhotb(stage),uin,...
            utb(stage),rho1(stage),Vol1(stage),dVol1(stage));
        dy(count)=dP1(stage);count=count+1;
    else
        %pressure in cavity 1 solution
        dP1(stage)= pressure(alpha,n,gamma,Ae,rhoex(stage-1),...
            rhotb(stage),uex(stage-
1),utb(stage),rho1(stage),Vol1(stage),...
            dVol1(stage));
        dy(count)=dP1(stage);count=count+1;
    end
    %Pressure in Cavity 2
    dP2(stage)= pressure(alpha,n,gamma,Ae,rhotb(stage),rhoex(stage),...
        utb(stage),uex(stage),rho2(stage),Vol2(stage),dVol2(stage));
    dy(count)=dP2(stage);count=count+1;

%*********************************************************************
    %                       Density Calculations

%*********************************************************************
    if(stage==1)
        drhoinlet=density(gamma,alpha,n,dPinlet);
        dy(count)=drhoinlet;count=count+1;
    end
    drho1(stage)=density(gamma,alpha,n,dP1(stage));     %Density in
Cavity 1
    dy(count)=drho1(stage);count=count+1;
    drho2(stage)=density(gamma,alpha,n,dP2(stage));     %Density in
Cavity 2
```

```
    dy(count)=drho2(stage);count=count+1;

%*********************************************************************
    %                          Velocity Calculations

%*********************************************************************
    %Velcoity through the Inlet Valve
    if(stage==1)
        duin=velocity(LeIN,mu,hg,LvIN,Pinlet,P1(stage),rhoin,uin);
        dy(count)=duin;count=count+1;
    end
    %Velocity through the top bottom Valve

dutb(stage)=velocity(LeTB,mu,hg,LvTB,P1(stage),P2(stage),rhotb(stage),.
..
        utb(stage));
    dy(count)=dutb(stage);count=count+1;
    %Velocity through the exit Valve
    if(stage==M)
        duex(stage)=velocity(LeEX,mu,hg,LvEX,P2(stage),Poutlet,...
            rhoex(stage),uex(stage));
        dy(count)=duex(stage);count=count+1;
    else
        duex(stage)=velocity(LeEX,mu,hg,LvEX,P2(stage),P1(stage+1),...
            rhoex(stage),uex(stage));
        dy(count)=duex(stage);count=count+1;
    end
    if(stage==1)
        dvolin=volumeflow(rhoin,uin,Ae);
        dy(count)=dvolin;count=count+1;
    end
    dvoltb(stage)=volumeflow(rhotb(stage),utb(stage),Ae);
    dy(count)=dvoltb(stage);count=count+1;
    dvolex(stage)=volumeflow(rhoex(stage),uex(stage),Ae);
    dy(count)=dvolex(stage);count=count+1;
end
dy=dy';

%*********************************************************************
%               Terminate Ode solver if electrode reached
%*********************************************************************

function[value,isterminal,direction]=events(t,y,rhoD,tD,Am,E,...

epsilon,CavityVolume,alpha,gamma,n,hg,Le,Lv,inlet,Poutlet,rhooutlet,...
    Vload,mu,Ae,f,M,topio,tclio,risetimeio,toptb,tcltb,risetimetb,...
    voltageio,voltagetb,homem,hoio,hotb)

%pump membrane stage 1
value=[y(1)+homem-0.01e-6];
isterminal=[1];
direction=[-1];
%inlet membrane stage 1
value=[value y(3)+hoio-0.01e-6];
isterminal=[isterminal 1];
direction=[direction -1];
%transfer membrane stage 1
value=[value y(5)+hotb-0.01e-6];
```

```
isterminal=[isterminal 1];
direction=[direction -1];
%exit membrane stage 1
value=[value y(7)+hoio-0.01e-6];
isterminal=[isterminal 1];
direction=[direction -1];

count=1+20;
for stage = 2:M
    %pump membrane stage2
    value=[value y(count)+homem-0.01e-6];
    isterminal=[isterminal 1];
    direction=[direction -1];
    %TB membrane stage 2
    value=[value y(count+2)+hotb-0.01e-6];
    isterminal=[isterminal 1];
    direction=[direction -1];
    %Exit Membrane stage 2
    value=[value y(count+4)+hoio-0.01e-6];
    isterminal=[isterminal 1];
    direction=[direction -1];
    count=count+14;
end


%density in the cavity
function [rho]=density(gamma,alpha,n,P)
rho=gamma/(alpha^2*n)*P;

%loading the arrays for further computation - First Time
function [displ,displt,displio,displtio,displtb,displttb,displex,...
    displtex,pinlet,p1,p2,rhoinlet,rho1,rho2,uin,utb,uex,...
    volin,voltb,volex]=...
    load_ar1(y,M)

count=1;
for stage=1:M
    displ(:,stage) = y(:,count);count=count+1;
    displt(:,stage)= y(:,count);count=count+1;
    if(stage==1)
        displio(:,stage) = y(:,count);count=count+1;
        displtio(:,stage)= y(:,count);count=count+1;
    end
    displtb(:,stage) = y(:,count);count=count+1;
    displttb(:,stage)= y(:,count);count=count+1;
    displex(:,stage) = y(:,count);count=count+1;
    displtex(:,stage)= y(:,count);count=count+1;
    if(stage==1)
        pinlet(:,1)= y(:,count);count=count+1;
    end
    p1(:,stage)= y(:,count);count=count+1;
    p2(:,stage)= y(:,count);count=count+1;
    if(stage==1)
        rhoinlet(:,1)= y(:,count);count=count+1;
    end
    rho1(:,stage)= y(:,count);count=count+1;
    rho2(:,stage)= y(:,count);count=count+1;
    if(stage==1)
```

```
        uin(:,1)= y(:,count);count=count+1;
    end
    utb(:,stage)= y(:,count);count=count+1;
    uex(:,stage)= y(:,count);count=count+1;
    if(stage==1)
        volin(:,1) = y(:,count);count=count+1;
    end
    voltb(:,stage)=y(:,count);count=count+1;
    volex(:,stage)=y(:,count);count=count+1;
end


%laoding arrays subsequently
function [displ,displt,displio,displtio,displtb,displttb,displex,...
    displtex,pinlet,p1,p2,rhoinlet,rho1,rho2,uin,utb,uex,...
    volin,voltb,volex]=load_ar2(y,M,displ,displt,displio,displtio,...
    displtb,displttb,displex,displtex,pinlet,p1,p2,rhoinlet,...
    rho1,rho2,uin,utb,uex,volin,voltb,volex)


initial =length(pinlet)+1;
final = length(pinlet)+length(y(:,1));
count=1;
for stage=1:M
    displ(initial:final,stage) = y(:,count);count=count+1;
    displt(initial:final,stage)= y(:,count);count=count+1;
    if(stage==1)
        displio(initial:final,stage) = y(:,count);count=count+1;
        displtio(initial:final,stage)= y(:,count);count=count+1;
    end
    displtb(initial:final,stage) = y(:,count);count=count+1;
    displttb(initial:final,stage)= y(:,count);count=count+1;
    displex(initial:final,stage) = y(:,count);count=count+1;
    displtex(initial:final,stage)= y(:,count);count=count+1;
    if(stage==1)
        pinlet(initial:final)= y(:,count);count=count+1;
    end
    p1(initial:final,stage)= y(:,count);count=count+1;
    p2(initial:final,stage)= y(:,count);count=count+1;
    if(stage==1)
        rhoinlet(initial:final)= y(:,count);count=count+1;
    end
    rho1(initial:final,stage)= y(:,count);count=count+1;
    rho2(initial:final,stage)= y(:,count);count=count+1;
    if(stage==1)
        uin(initial:final)= y(:,count);count=count+1;
    end
    utb(initial:final,stage)= y(:,count);count=count+1;
    uex(initial:final,stage)= y(:,count);count=count+1;
    if(stage==1)
        volin(initial:final,1) = y(:,count);count=count+1;
    end
    voltb(initial:final,stage)=y(:,count);count=count+1;
    volex(initial:final,stage)=y(:,count);count=count+1;
end

%*********************************************************************
```

```
****
%                          Loading Initial Conditions
%*************************************************************************
****


function[IC]=load_IC(y,M,type,pin,homem,hoio,hotb)


if(type==1)
    count=1;
    %initially loading data
    for stage=1:M
        IC(count)=0;count=count+1;
        IC(count)=0;count=count+1;
        if(stage==1)
            IC(count)=0;count=count+1;
            IC(count)=0;count=count+1;
        end
        IC(count)=0;count=count+1;
        IC(count)=0;count=count+1;
        IC(count)=0;count=count+1;
        IC(count)=0;count=count+1;
        if(stage==1)
            IC(count)=101300*pin;count=count+1;
        end
        IC(count)=101300;count=count+1;
        IC(count)=101300;count=count+1;
        if(stage==1)
            IC(count)=(101300)*pin/(287*298);count=count+1;
        end
        IC(count)=(101300)/(287*298);count=count+1;
        IC(count)=(101300)/(287*298);count=count+1;
        if(stage==1)
            IC(count)=0;count=count+1;
        end
        IC(count)=0;count=count+1;
        IC(count)=0;count=count+1;
        if(stage==1)
            IC(count)=0;count=count+1;
        end
        IC(count)=0;count=count+1;
        IC(count)=0;count=count+1;
    end
else
    count=1;
    for stage =1:M
        hmem(stage) = y(end,count);count=count+1;
        htmem(stage)=y(end,count);count=count+1;
        if(stage==1)
            hio(stage) = y(end,count);count=count+1;
            htio(stage)=y(end,count);count=count+1;
        end
        htb(stage) = y(end,count);count=count+1;
        httb(stage)=y(end,count);count=count+1;
        hex(stage) = y(end,count);count=count+1;
        htex(stage)=y(end,count);count=count+1;
```

```
    if(stage==1)
        Pinlet=y(end,count);count=count+1;
    end
    P1(stage) = y(end,count);
    count=count+1;
    P2(stage) = y(end,count);
    count=count+1;
    if(stage==1)
        rhoinlet=y(end,count);count=count+1;
    end
    rho1(stage)=y(end,count);count=count+1;
    rho2(stage)=y(end,count);count=count+1;
    if(stage==1)
        uin=y(end,count);count=count+1;
    end
    utb(stage)=y(end,count);count=count+1;
    uex(stage)=y(end,count);count=count+1;
    if(stage==1)
        volin = y(end,count);count=count+1;
    end
    voltb(stage)=y(end,count);count=count+1;
    volex(stage)=y(end,count);count=count+1;
end
%loading data at the end of the cycle
if(type==2)
    count=1;
    for stage=1:M
        IC(count)=hmem(stage);count=count+1;
        IC(count)=htmem(stage);count=count+1;
        if(stage==1)
            IC(count)=hio(stage);count=count+1;
            IC(count)=htio(stage);count=count+1;
        end
        IC(count)=htb(stage);count=count+1;
        IC(count)=httb(stage);count=count+1;
        IC(count)=hex(stage);count=count+1;
        IC(count)=htex(stage);count=count+1;
        if(stage==1)
            IC(count)=Pinlet;count=count+1;
        end
        IC(count)=P1(stage);count=count+1;
        IC(count)=P2(stage);count=count+1;
        if(stage==1)
            IC(count)=rhoinlet;count=count+1;
        end
        IC(count)=rho1(stage);count=count+1;
        IC(count)=rho2(stage);count=count+1;
        if(stage==1)
            IC(count)=uin;count=count+1;
        end
        IC(count)=utb(stage);count=count+1;
        IC(count)=uex(stage);count=count+1;
        if(stage==1)
            IC(count)=0;count=count+1;
        end
        IC(count)=0;count=count+1;
        IC(count)=0;count=count+1;
    end
```

```
    %If electrode found
    elseif(type==3)
        count=1;
        for stage=1:M
            if(abs(hmem(stage)+(homem-0.01e-6))<1e-10)
                IC(count)=-(homem-0.01e-6);count=count+1;
                IC(count)=0;count=count+1;
            else
                IC(count)=hmem(stage);count=count+1;
                IC(count)=htmem(stage);count=count+1;
            end
            if(stage==1)
                if(abs(hio(stage)+(hoio-0.01e-6))<1e-10)
                    IC(count)=-(hoio-0.01e-6);count=count+1;
                    IC(count)=0;count=count+1;
                else
                    IC(count)=hio(stage);count=count+1;
                    IC(count)=htio(stage);count=count+1;
                end
            end
            if(abs(htb(stage)+(hotb-0.01e-6))<1e-10)
                IC(count)=-(hotb-0.01e-6);count=count+1;
                IC(count)=0;count=count+1;
            else
                IC(count)=htb(stage);count=count+1;
                IC(count)=httb(stage);count=count+1;
            end
            if(abs(hex(stage)+(hoio-0.01e-6))<1e-10)
                IC(count)=-(hoio-0.01e-6);count=count+1;
                IC(count)=0;count=count+1;
            else
                IC(count)=hex(stage);count=count+1;
                IC(count)=htex(stage);count=count+1;
            end
            if(stage==1)
                IC(count)=Pinlet;count=count+1;
            end
            IC(count)=P1(stage);count=count+1;
            IC(count)=P2(stage);count=count+1;
            if(stage==1)
                IC(count)=rhoinlet;count=count+1;
            end
            IC(count)=rho1(stage);count=count+1;
            IC(count)=rho2(stage);count=count+1;
            if(stage==1)
                IC(count)=uin;count=count+1;
            end
            IC(count)=utb(stage);count=count+1;
            IC(count)=uex(stage);count=count+1;
            if(stage==1)
                IC(count)=volin;count=count+1;
            end
            IC(count)=voltb(stage);count=count+1;
            IC(count)=volex(stage);count=count+1;
        end
    end
end
```

```
%loading the data obtained from the ODE45 SOlver
function[hmem,htmem,hio,htio,htb,httb,hex,htex,Pinlet,P1,P2,rhoinlet,rh
o1,rho2,uin,utb,uex,volin,voltb,...
  volex]=loadvariables(y,M)

count=1;
for stage =1:M
    hmem(stage) = y(count);count=count+1;
    htmem(stage)=y(count);count=count+1;
    if(stage==1)
        hio=y(count);count=count+1;
        htio=y(count);count=count+1;
    end
    htb(stage) = y(count);count=count+1;
    httb(stage)=y(count);count=count+1;
    hex(stage) = y(count);count=count+1;
    htex(stage)=y(count);count=count+1;
    if(stage==1)
        Pinlet=y(count);count=count+1;
    end
    P1(stage) = y(count);
    count=count+1;
    P2(stage) = y(count);count=count+1;
    if(stage==1)
        rhoinlet=y(count);count=count+1;
    end
    rho1(stage)=y(count);count=count+1;
    rho2(stage)=y(count);count=count+1;
    if(stage==1)
        uin=y(count);count=count+1;
    end
    utb(stage)=y(count);count=count+1;
    uex(stage)=y(count);count=count+1;
    if(stage==1)
        volin = y(count);count=count+1;
    end
    voltb(stage)=y(count);count=count+1;
    volex(stage)=y(count);count=count+1;
end

%to study the membrane deflection
function[ht]=membranedef(rhoD,tD,Am,h,P1,P2,E,ho,epsilon)

mass = (pi^2/(4*rhoD*tD*Am));
kx_non = (5.330e+017*h^3+4.34e+008*h)*Am;
elec = (Am-3183*20e-6^2)*epsilon/2*(E/ho)^2/(1+(h/ho))^0.846;

ht = -mass*kx_non + mass*(-elec-P1*Am+P2*Am);


%Study the Inlet Valve Membrane Deflection
function[ht]=membranedefio(rhoD,tD,Am,h,P1,P2,E,ho,epsilon)

mass = (pi^2/(4*rhoD*tD*Am));
kx_non = ( 4.711123923837595e+17*h^3+4.193633444909403e+08*h)*Am;
elec = (Am-3183*20e-6^2)*epsilon/2*(E/ho)^2/(1+(h/ho))^0.846;
```

```
ht = -mass*kx_non + mass*(-elec-P1*Am+P2*Am);
```

```
%Transfer Valve membrane Deflection
function[ht]=membranedeftb(rhoD,tD,Am,h,P1,P2,E,ho,epsilon)

mass = (pi^2/(4*rhoD*tD*Am));
kx_non = ( 4.711123923837595e+17*h^3+4.193633444909403e+08*h)*Am;
elec = (Am-3183*20e-6^2)*epsilon/2*(E/ho)^2/(1+(h/ho))^0.846;

ht = -mass*kx_non + mass*(-elec-P1*Am+P2*Am);

function [E] = valveiotimig(frequency,top,tcl,amplitude,risetime,t)

x = t/(1/frequency)-floor(t/(1/frequency));
if(top==0)
    if(x<=risetime)
        slope = amplitude*frequency/risetime;
        E=+slope*(t-(floor(t/...
            (1/frequency)))*1/frequency);
    elseif(x>risetime && x<=tcl+risetime)
        E=amplitude;
    elseif(x>tcl+risetime && x<=tcl+2*risetime)
        slope = -amplitude*frequency/(risetime);
        E=amplitude+slope*(t-(tcl+risetime+floor(t/...
            (1/frequency)))*(1/frequency));
    elseif(x>tcl+risetime && x<=0.5)
        E=0;
    elseif(x>0.5 && x<=0.5+risetime)
        slope = -amplitude*frequency/risetime;
        E=slope*(t-((0.5)+floor(t/...
            (1/frequency)))*(1/frequency));
    elseif(x>0.5+risetime && x<=0.5+risetime+tcl)
        E=-amplitude;
    elseif(x>0.5+risetime+tcl && x<0.5+risetime+tcl+risetime)
        slope = amplitude*frequency/risetime;
        E=-amplitude+slope*(t-((0.5+risetime+tcl)+floor(t/...
            (1/frequency)))*1/frequency);
    else
        E=0;
    end
else
    if(x<=tcl)
        E = amplitude;
    elseif(x>tcl && x<=tcl+risetime)
        slope = -amplitude*frequency/(risetime);
        E=amplitude+slope*(t-(tcl+floor(t/...
            (1/frequency)))*(1/frequency));
    elseif(x> tcl+risetime && x < 0.5- top-risetime)
        E=0;
    elseif(x>=0.5- top-risetime && x<0.5- top)
        slope = -amplitude*frequency/risetime;
        E=slope*(t-((0.5- top-risetime)+floor(t/...
            (1/frequency)))*(1/frequency));
```

```
    elseif(x>=0.5- top && x< 0.5+tcl)
        E=-amplitude;
    elseif(x>= 0.5+tcl && x<0.5+tcl+risetime)
        slope = amplitude*frequency/risetime;
        E=-amplitude+slope*(t-((0.5+tcl)+floor(t/...
            (1/frequency)))*1/frequency);
    elseif(x>=0.5+tcl+risetime && x <1-top-risetime)
        E=0;
    elseif(x >=1-top-risetime &&x <1-top)
        slope=amplitude*frequency/risetime;
        E=slope*(t-((1-top-risetime)+floor(t/...
            (1/frequency)))*1/frequency);
    else
        E=amplitude;
    end
end


%timing of the transfer valves

function [E] = valvetbtimig(frequency,top,tcl,amplitude,risetime,t)


x = t/(1/frequency)-floor(t/(1/frequency));
if(top==0)
    if(x<0.5-(risetime+tcl+risetime))
        E=0;
    elseif(x>=0.5-(risetime+tcl+risetime) && x<0.5-(risetime+tcl))
        slope = amplitude*frequency/risetime;
        E=+slope*(t-((0.5-(risetime+tcl+risetime))+floor(t/...
            (1/frequency)))*1/frequency);
    elseif(x>=0.5-(risetime+tcl) && x<0.5-(risetime))
        E=amplitude;
    elseif(x>=0.5-(risetime) && x<0.5)
        slope = -amplitude*frequency/risetime;
        E=amplitude+slope*(t-(0.5-(risetime)+...
            floor(t/(1/frequency)))*(1/frequency));
    elseif(x>=0.5 && x<1-(risetime+tcl+risetime))
        E=0;
    elseif(x>=1-(risetime+tcl+risetime) && x<1-(risetime+tcl))
        slope = -amplitude*frequency/risetime;
        E=slope*(t-((1-(risetime+tcl+risetime))+floor(t/...
            (1/frequency)))*(1/frequency));
    elseif(x>=1-(risetime+tcl) && x<1-(risetime))
        E=-amplitude;
    elseif(x>1-(risetime))
        slope = amplitude*frequency/risetime;
        E=-amplitude+slope*(t-((1-(risetime))+floor(t/...
            (1/frequency)))*1/frequency);
    end

elseif(tcl+risetime>0.25 && tcl<0.25)
    slope=amplitude*frequency/risetime;
    amps=-amplitude+slope*(1/frequency-(((0.75+tcl))+...
        floor(0/(1/frequency)))*(1/frequency));
    if(x<=(tcl+risetime)-0.25)
        slope=amplitude*frequency/risetime;
```

```
        E=amps+slope*(t-(((0))+...
            floor(t/(1/frequency)))*(1/frequency));
    elseif(x>(tcl-0.25)+risetime && x<=0.25-top-risetime)
        E=0;
    elseif(x>0.25-top-risetime && x<=0.25-top)
        slope = amplitude*frequency/(risetime);
        E=slope*(t-((0.25-top-risetime)+floor(t/...
            (1/frequency)))*(1/frequency));
    elseif(x> 0.25 -top && x <= 0.25+tcl)
        E=amplitude;
    elseif(x>0.25+ tcl && x<0.25+ tcl+risetime)
        slope = -amplitude*frequency/risetime;
        E=amplitude+slope*(t-((0.25+tcl)+...
            floor(t/(1/frequency)))*(1/frequency));
    elseif((x>=0.25+tcl+risetime && x< 0.75-top-risetime))
        E=0;
    elseif(x>= 0.75-top-risetime && x<0.75-top)
        slope = -amplitude*frequency/risetime;
        E=slope*(t-((0.75-top-risetime)+...
            floor(t/(1/frequency)))*(1/frequency));
    elseif(x>=0.75-top && x <=0.75+tcl)
        E=-amplitude;
    elseif(x>0.75+tcl && x<=1)
        slope=amplitude*frequency/risetime;
        E=-amplitude+slope*(t-(((0.75+tcl))+...
            floor(t/(1/frequency)))*(1/frequency));
    end
elseif(tcl>=0.25)
    if(x<=tcl-0.25)
        E=-amplitude;
    elseif(x>tcl-0.25&& x<=(tcl-0.25)+risetime)
        slope=amplitude*frequency/risetime;
        E=-amplitude+slope*(t-(((tcl-0.25))+...
            floor(t/(1/frequency)))*(1/frequency));
    elseif(x>(tcl-0.25)+risetime && x<=0.25-top-risetime)
        E=0;
    elseif(x>0.25-top-risetime && x<=0.25-top)
        slope = amplitude*frequency/(risetime);
        E=slope*(t-((0.25-top-risetime)+floor(t/...
            (1/frequency)))*(1/frequency));
    elseif(x> 0.25 -top && x <= 0.25+tcl)
        E=amplitude;
    elseif(x>0.25+ tcl && x<0.25+ tcl+risetime)
        slope = -amplitude*frequency/risetime;
        E=amplitude+slope*(t-((0.25+tcl)+...
            floor(t/(1/frequency)))*(1/frequency));
    elseif((x>=0.25+tcl+risetime && x< 0.75-top-risetime))
        E=0;
    elseif(x>= 0.75-top-risetime && x<0.75-top)
        slope = -amplitude*frequency/risetime;
        E=slope*(t-((0.75-top-risetime)+...
            floor(t/(1/frequency)))*(1/frequency));
    elseif(x>=0.75-top && x <=1)
        E=-amplitude;
    end

else
    if(x<=0.25-top-risetime)
```

```
        E = 0;
    elseif(x>0.25-top-risetime && x<=0.25-top)
        slope = amplitude*frequency/(risetime);
        E=slope*(t-((0.25-top-risetime)+...
            floor(t/(1/frequency)))*(1/frequency));
    elseif(x> 0.25 -top && x <= 0.25+tcl)
        E=amplitude;
    elseif(x>0.25+ tcl && x<0.25+ tcl+risetime)
        slope = -amplitude*frequency/risetime;
        E=amplitude+slope*(t-((0.25+tcl)+...
            floor(t/(1/frequency)))*(1/frequency));
    elseif(x>=0.25+tcl+risetime && x< 0.75-top-risetime)
        E=0;
    elseif(x>= 0.75-top-risetime && x<0.75-top)
        slope = -amplitude*frequency/risetime;
        E=slope*(t-((0.75-top-risetime)+...
            floor(t/(1/frequency)))*(1/frequency));
    elseif(x>=0.75-top && x <0.75+tcl)
        E=-amplitude;
    elseif(x >=0.75+tcl &&x <0.75+tcl+risetime)
        slope=amplitude*frequency/risetime;
        E=-amplitude+slope*(t-((0.75+tcl)+...
            floor(t/(1/frequency)))*(1/frequency));
    else
        E=0;
    end
end

%velocity through each valve
function[u]=velocity(Le,mu,hg,Lv,P1,P2,rho,u)

u=1/Le*(P1-P2)/rho-8*mu/rho*u/hg^2*Lv/Le;

%estimation of volume change in the vacity due to valve and pump
membrane
%motion and choice of appropriate density based on flow direction
function[Vol1,dVol1,Vol2,dVol2,rhoin,rhotb,rhoex]...

=volumedensity(CavityVolume,hmem,htmem,hio,htio,htb,httb,hex,htex,...
    M,uin,utb,uex,rhoinlet,rho1,rho2,...
    rhooutlet,Am,homem,hoio,hotb)

for stage=1:M
    if(stage==1)
        Vol1(stage) = CavityVolume(1)-4*Am/pi^2*hmem(stage)-...
            4*Am/pi^2*hio(stage)-4*Am/pi^2*htb(stage);
        dVol1(stage)=-4*Am/pi^2*htmem(stage)-4*Am/pi^2*htio(stage)-...
            4*Am/pi^2*httb(stage);
    else
        Vol1(stage) = CavityVolume(1)-4*Am/pi^2*hmem(stage)-...
            4*Am/pi^2*hex(stage-1)-4*Am/pi^2*htb(stage);
        dVol1(stage)=-4*Am/pi^2*htmem(stage)-...
            4*Am/pi^2*htex(stage-1)-4*Am/pi^2*httb(stage);
    end
    Vol2(stage) = (CavityVolume(2)+homem*Am)+4*Am/pi^2*hmem(stage)+...
        4*Am/pi^2*htb(stage)+4*Am/pi^2*hex(stage)+hotb*Am+hoio*Am;
    dVol2(stage)=4*Am/pi^2*htmem(stage)+4*Am/pi^2*httb(stage)+...
```

```
        4*Am/pi^2*htex(stage);

%*********************************************************************
    %                Density Calculation through the valves

%*********************************************************************
    if(stage==1)
        if(uin(stage)>0)
            rhoin = rhoinlet;
        else
            rhoin = rho1(stage);
        end
    end
    if(utb(stage)>0)
        rhotb(stage) = rho1(stage);
    else
        rhotb(stage) = rho2(stage);
    end
    if(stage==M)
        if(uex(stage)>0)
            rhoex(stage) = rho2(stage);
        else
            rhoex(stage) = rhooutlet;
        end
    else
         if(uex(stage)>0)
            rhoex(stage) = rho2(stage);
        else
            rhoex(stage) = rho1(stage+1);
        end
    end
end

%Flow rate COmputation
function[vol]=volumeflow(rho,u,A)

vol=rho*u*A;
```

BIBLOGRAPHY

Allen, D. G. & M. V. Sefton (1986) A model of insulin delivery by a controlled release micropump. *Ann Biomed Eng,* 14**,** 257-76.

Astle, A., L. P. Bernal, H. Kim, K. Najafi & P. D. Washabaugh. 2005. Theoretical and Experimental Performance of a High Frequency Micropump. ASME.

Astle, A., L. P. Bernal, P. Washabaugh, H. Kim & K. Najafi. 2003. Dynamic modeling and design of a high frequency micro vacuum pump. ASME.

Astle, A., A. Paige, L. P. Bernal, J. Munfakh, H. Kim & K. Najafi. 2002. Analysis and design of multistage electrostatically-actuated micro vacuum pumps. ASME.

Astle, A. A. (2006) Analysis, design and experimental characterization of electrostatically actuated gas micropumps.

Besharatian, A., K. Kumar, R. L. Peterson, L. P. Bernal & K. Najafi. 2012. A scalable, modular, multi-stage, peristaltic, electrostatic gas micro-pump. In *Micro Electro Mechanical Systems (MEMS), 2012 IEEE 25th International Conference on*, 1001-1004. IEEE.

Bogue, R. (2007) MEMS sensors: past, present and future. *Sensor Review,* 27**,** 7-13.

Bourouina, T. & J. P. Grandchamp (1999) Modeling micropumps with electrical equivalent networks. *Journal of Micromechanics and Microengineering,* 6**,** 398.

Bruschi, P., A. Diligenti & M. Piotto (2002) Micromachined gas flow regulator for ion propulsion systems. *Aerospace and Electronic Systems, IEEE Transactions on,* 38**,** 982-988.

Cabuz, C., W. R. Herb, E. I. Cabuz & S. T. Lu. 2001. The dual diaphragm pump. In *Micro Electro Mechanical Systems, 2001. MEMS 2001. The 14th IEEE International Conference on*, 519-522. IEEE.

Coll, J. L., P. Chollet, E. Brambilla, D. Desplanques, J. P. Behr & M. Favrot (1999) In vivo delivery to tumors of DNA complexed with linear polyethylenimine. *Hum Gene Ther,* 10**,** 1659-66.

Dash, A. K. & G. C. Cudworth, 2nd (1998) Therapeutic applications of implantable drug delivery systems. *J Pharmacol Toxicol Methods,* 40**,** 1-12.

De Bock, H. P. J., J. L. Jackson, B. P. Whalen & P. Chamarthy. 2012. Experimental Flow Performance Evaluation of novel miniaturized Advanced Piezoelectric Dual Cooling Jet. In *Journal of Physics: Conference Series*, 012035. IOP Publishing.

Gerlach, T. 1997. Pumping gases by a silicon micro pump with dynamic passive valves. In *Solid State Sensors and Actuators, 1997. TRANSDUCERS'97 Chicago., 1997 International Conference on*, 357-360. IEEE.

Goldschmidtböing, F., A. Doll, M. Heinrichs, P. Woias, H. J. Schrag & U. T. Hopt (2005) A generic analytical model for micro-diaphragm pumps with active valves. *Journal of Micromechanics and Microengineering,* 15**,** 673.

Hanseup, K., W. H. Steinecker, S. Reidy, G. R. Lambertus, A. A. Astle, K. Najafi, E. T. Zellers, L. P. Bernal, P. D. Washabaugh & K. D. Wise. 2007. A Micropump-Driven High-Speed MEMS Gas Chromatography System. In *Solid-State Sensors, Actuators and Microsystems Conference, 2007. TRANSDUCERS 2007. International*, 1505-1508.

Kim, H., A. A. Astle, L. P. Bernal, K. Najafi & P. D. Washabaugh. 2006. Directional pumping performance of an electrostatic checkerboard microvalve. ASME.

Kim, H., A. A. Astle, K. Najafi, L. P. Bernal & P. D. Washabaugh. 2007. A fully integrated high-efficiency peristaltic 18-stage gas micropump with active microvalves. In *Micro Electro Mechanical Systems, 2007. MEMS. IEEE 20th International Conference on*, 131-134. IEEE.

Kim, H. T., J. W. Park & H. Kim. 2011. All-electric peristaltic vacuum pump utilizing electromagnetic and hydraulic actuation with a highly flexible latex membrane. In *Solid-State Sensors, Actuators and Microsystems Conference (TRANSDUCERS), 2011 16th International*, 2454-2457. IEEE.

Koch, M., N. Harris, R. Maas, A. G. R. Evans, N. M. White & A. Brunnschweiler (1999) A novel micropump design with thick-film piezoelectric actuation. *Measurement Science and Technology,* 8**,** 49.

Lee, S., S. Y. Yee, A. Besharatian, H. Kim, L. P. Bernal & K. Najafi. 2009. Adaptive gas pumping by controlled timing of active microvalves in peristaltic micropumps. In *Solid-State Sensors, Actuators and Microsystems Conference, 2009. TRANSDUCERS 2009. International*, 2294-2297. IEEE.

Lin, Q., B. Yang, J. Xie & Y. C. Tai (2006) Dynamic simulation of a peristaltic micropump considering coupled fluid flow and structural motion. *Journal of Micromechanics and Microengineering,* 17**,** 220.

Lozano, P. & D. Courtney. 2010. On the development of high specific impulse electric propulsion thrusters for small satellites. In *Proceedings of the Symposium on Small Satellite Systems and Services, Funchal Madeira, Portugal*.

Lung-Jieh, Y. & L. Tzu-Yuan (2011) A PDMS-based thermo-pneumatic micropump with Parylene inner walls. *Microelectron. Eng.,* 88**,** 1894-1897.

Micci, M. M. & A. D. Ketsdever. 2000. *Micropropulsion for small spacecraft*. Aiaa.

Müller, M. O., L. P. Bernal, R. P. Moran, P. D. Washabaugh, B. A. Parviz, T. A. Chou, C. Zhang & K. Najafi (2000) Thrust performance of micromachined synthetic jets. *Ann Arbor,* 1001**,** 48109-2140.

Müller, M. O., L. P. Bernal, P. D. Washabaugh, T. K. A. Chou, H. S. Kim & K. Najafi. 2002. Acoustically Generated Micromachined Jet Arrays for Micropropulsion Applications. ASME.

Nabity, J. (2004) Modeling an electrostatically actuated MEMS diaphragm pump. *ASEN 5519 Fluid-Structures Interactions*.

Naveen, K. G. a. S. A. a. Y. B. G. (2012) A Si-micromachined 48-stage Knudsen pump for on-chip vacuum. *Journal of Micromechanics and Microengineering,* 22**,** 105026.

Naveen, K. G. a. Y. B. G. (2011) Porous ceramics for multistage Knudsen micropumps—modeling approach and experimental evaluation. *Journal of Micromechanics and Microengineering,* 21**,** 095029.

Nisar, A., N. Afzulpurkar, B. Mahaisavariya & A. Tuantranont (2008) MEMS-based micropumps in drug delivery and biomedical applications. *Sensors and Actuators B: Chemical,* 130**,** 917-942.

Pan, T., S. J. McDonald, E. M. Kai & B. Ziaie (2005) A magnetically driven PDMS micropump with ball check-valves. *Journal of Micromechanics and Microengineering,* 15**,** 1021.

Qiao Lin and Bozhi Yang and Jun Xie and Yu-Chong, T. (2007) Dynamic simulation of a peristaltic micropump considering coupled fluid flow and structural motion. *Journal of Micromechanics and Microengineering,* 17**,** 220.

Santiago, D. J. L. a. J. G. (2004) A review of micropumps. *Journal of Micromechanics and Microengineering,* 14**,** R35.

Smits, J. G. (1990) Piezoelectric micropump with three valves working peristaltically. *Sensors and Actuators A: Physical,* 21**,** 203-206.

thinXXs (2008)
http://www.thinxxs.com/fileadmin/website/pdf/MicroPump_mdp1304_v2.1.pdf

Wiberg, D., B. Eyre, K. Shcheglov, V. White & V. Garkanian (2001) Progress toward highly miniaturized vacuum pumps 2nd Workshop on Harsh-Environment Mass Spectrometry (St. Petersburg, FL).

Woias, P. (2005) Micropumps—past, progress and future prospects. *Sensors and Actuators B: Chemical,* 105**,** 28-38.

Zellers, E. T., S. Reidy, R. A. Veeneman, R. Gordenker, W. H. Steinecker, G. R. Lambertus, H. Kim, J. A. Potkay, M. P. Rowe & Q. Zhong. 2007. An integrated micro-analytical system for complex vapor mixtures. In *Solid-State Sensors, Actuators and Microsystems Conference, 2007. TRANSDUCERS 2007. International*, 1491-1496. IEEE.

Zengerle, R. & M. Richter (1999) Simulation of microfluid systems. *Journal of Micromechanics and Microengineering,* 4**,** 192.

Zhang, L., J. M. Koo, L. Jiang, M. Asheghi, K. E. Goodson, J. G. Santiago & T. W. Kenny (2002) Measurements and modeling of two-phase flow in microchannels with nearly constant heat flux boundary conditions. *Microelectromechanical Systems, Journal of,* 11**,** 12-19.